CTR 3-5-79-2

EVALUATION OF THE FATIGUE PERFORMANCE OF BUTT-WELDED SPLICES

Antonio J. F. P. Leite, Karl H. Frank,
and Joseph A. Yura

RESEARCH REPORT 247-3

PROJECT 3-5-79-247

CENTER FOR TRANSPORTATION RESEARCH
BUREAU OF ENGINEERING RESEARCH
THE UNIVERSITY OF TEXAS AT AUSTIN
AUGUST 1982

AUGUST 1982

247-3

EVALUATION OF THE FATIGUE PERFORMANCE
OF BUTT-WELDED SPLICES

Leite, Frank,
and Yura

PARTIAL LIST OF REPORTS PUBLISHED BY THE CENTER FOR TRANSPORTATION RESEARCH

This list includes some of the reports published by the Center for Transportation Research and the organizations which were merged to form it: the Center for Highway Research and the Council for Advanced Transportation Studies. Questions about the Center and the availability and costs of specific reports should be addressed to: Director; Center for Transportation Research; ECJ 2.5; The University of Texas at Austin; Austin, Texas 78712.

7-1 “Strength and Stiffness of Reinforced Concrete Rectangular Columns Under Biaxially Eccentric Thrust,” by J. A. Desai and R. W. Furlong, January 1976.

7-2F “Strength and Stiffness of Reinforced Concrete Columns Under Biaxial Bending,” by V. Mavichak and R. W. Furlong, November 1976.

16-1F “Oil, Grease, and Other Pollutants in Highway Runoff,” by Bruce Wiland and Joseph F. Malina, Jr., September 1976.

23-1 “Prediction of Temperature and Stresses in Highway Bridges by a Numerical Procedure Using Daily Weather Reports,” by Thaksin Thepchatri, C. Philip Johnson, and Hudson Matlock, February 1977.

23-2 “Analytical and Experimental Investigation of the Thermal Response of Highway Bridges,” by Kenneth M. Will, C. Philip Johnson, and Hudson Matlock, February 1977.

23-3F “Temperature Induced Stresses in Highway Bridges by Finite Element Analysis and Field Tests,” by Atalay Yargicoglu and C. Philip Johnson, July 1978.

29-2F “Strength and Behavior of Anchor Bolts Embedded Near Edges of Concrete Piers,” by G. B. Hasselwander, J. O. Jirsa, J. E. Breen, and K. Lo, May 1977.

114-4 “Durability, Strength, and Method of Application of Polymer-Impregnated Concrete for Slabs,” by Piti Yimprasert, David W. Fowler, and Donald R. Paul, January 1976.

114-5 “Partial Polymer Impregnation of Center Point Road Bridge,” by Ronald Webster, David W. Fowler, and Donald R. Paul, January 1976.

114-6 “Behavior of Post-Tensioned Polymer-Impregnated Concrete Beams,” by Ekasit Limsuwan, David W. Fowler, Ned H. Burns, and Donald R. Paul, June 1978.

114-7 “An Investigation of the Use of Polymer-Concrete Overlays for Bridge Decks,” by Huey-Tsann Hsu, David W. Fowler, Mickey Miller, and Donald R. Paul, March 1979.

114-8 “Polymer Concrete Repair of Bridge Decks,” by David W. Fowler and Donald R. Paul, March 1979.

114-9F “Concrete-Polymer Materials for Highway Applications,” by David W. Fowler and Donald R. Paul, March 1979.

118-9F “Observation of an Expansive Clay Under Controlled Conditions,” by John B. Stevens, Paul N. Brotcke, Dewaine Bogard, and Hudson Matlock, November 1976.

123-30F “Overview of Pavement Management Systems Developments in the State Department of Highways and Public Transportation,” by W. Ronald Hudson, B. Frank McCullough, Jim Brown, Gerald Peck, and Robert L. Lytton, January 1976 (published jointly with the Texas State Department of Highways and Public Transportation and the Texas Transportation Institute, Texas A&M University).

172-1 “Axial Tension Fatigue Strength of Anchor Bolts,” by Franklin L. Fischer and Karl H. Frank, March 1977.

172-2F “Fatigue of Anchor Bolts,” by Karl H. Frank, July 1978.

176-4 “Behavior of Axially Loaded Drilled Shafts in Clay-Shales,” by Ravi P. Aurora and Lymon C. Reese, March 1976.

176-5F “Design Procedures for Axially Loaded Drilled Shafts,” by Gerardo W. Quiros and Lymon C. Reese, December 1977.

177-1 “Drying Shrinkage and Temperature Drop Stresses in Jointed Reinforced Concrete Pavement,” by Felipe Rivero-Vallejo and B. Frank McCullough, May 1976.

177-3 “A Study of the Performance of the Mays Ride Meter,” by Yi Chin Hu, Hugh J. Williamson, and B. Frank McCullough, January 1977.

177-4 “Laboratory Study of the Effect of Nonuniform Foundation Support on Continuously Reinforced Concrete Pavements,” by Enrique Jimenez, B. Frank McCullough, and W. Ronald Hudson, August 1977.

177-6 “Sixteenth Year Progress Report on Experimental Continuously Reinforced Concrete Pavement in Walker County,” by B. Frank McCullough and Thomas P. Chesney, April 1976.

177-7 “Continuously Reinforced Concrete Pavement: Structural Performance and Design/Construction Variables,” by Pieter J. Strauss, B. Frank McCullough, and W. Ronald Hudson, May 1977.

177-9 “CRCP-2, An Improved Computer Program for the Analysis of Continuously Reinforced Concrete Pavements,” by James Ma and B. Frank McCullough, August 1977.

177-10 “Development of Photographic Techniques for Performing Condition Surveys,” by Pieter Strauss, James Long, and B. Frank McCullough, May 1977.

177-11 “A Sensitivity Analysis of Rigid Pavement Overlay Design Procedure,” by B. C. Nayak, W. Ronald Hudson, and B. Frank McCullough, June 1977.

177-12 “A Study of CRCP Performance: New Construction Vs. Overlay,” by James I. Daniel, W. Ronald Hudson, and B. Frank McCullough, April 1978.

177-13 “A Rigid Pavement Overlay Design Procedure for Texas SDHPT,” by Otto Schnitter, W. R. Hudson, and B. F. McCullough, May 1978.

177-15 “Precast Repair of Continuously Reinforced Concrete Pavement,” by Gary Eugene Elkins, B. Frank McCullough, and W. Ronald Hudson, May 1979.

177-16 “Nomographs for the Design of CRCP Steel Reinforcement,” by C. S. Noble, B. F. McCullough, and J. C. M. Ma, August 1979.

177-17 “Limiting Criteria for the Design of CRCP,” by B. Frank McCullough, J. C. M. Ma, and C. S. Noble, August 1979.

177-18 “Detection of Voids Underneath Continuously Reinforced Concrete Pavements,” by John W. Birkhoff and B. Frank McCullough, August 1979.

183-7 “Permanent Deformation Characteristics of Asphalt Mixtures by Repeated-Load Indirect Tensile Test,” by Joaquin Vallejo, Thomas W. Kennedy, and Ralph Haas, June 1976.

(Continued inside back cover)

TECHNICAL REPORT STANDARD TITLE PAGE

1. Report No. FHWA/TX-82/27+247-3	2. Government Accession No.	3. Recipient's Catalog No.
4. Title and Subtitle EVALUATION OF THE FATIGUE PERFORMANCE OF BUTT-WELDED SPLICES		5. Report Date August 1982 6. Performing Organization Code
7. Author(s) Antonio J. F. P. Leite, Karl H. Frank, and Joseph A. Yura		8. Performing Organization Report No. Research Report 247-3
9. Performing Organization Name and Address Center for Transportation Research The University of Texas at Austin Austin, Texas 78712-1075		10. Work Unit No. 11. Contract or Grant No. Research Study 3-5-79-247 13. Type of Report and Period Covered Interim
12. Sponsoring Agency Name and Address Texas State Department of Highways and Public Transportation; Transportation Planning Division P. O. Box 5051 Austin, Texas 78763		14. Sponsoring Agency Code

15. Supplementary Notes

Study conducted in cooperation with the U. S. Department of Transportation, Federal Highway Administration. Research Study Title: "Evaluation of the Fatigue Life of Structural Steel Bridge Details"

16. Abstract

The fatigue performance of flange transition butt-welded splices has been evaluated. Analytical solutions for the stress gradient correction, F_G , are generated using a finite element method. The 1 to 2-1/2 slope transition recommended by the AASHTO Specifications is compared with the 1 to 5 slope transition used in the bridge being investigated. The 1 to 5 slope increases the estimated fatigue by a factor of 2 and is recommended for future construction.

The data generated under normal speed traffic in the field study of the bridge show the significance of the induced-vibration cycles superimposed to each major cycle due to a single truck. The dynamic vibrations have amplitudes of the same order of magnitude as the static stress range.

Solutions for the fatigue life of surface, corner, and interior cracks are presented in tabular form. These solutions can be applied to any desired stress range and initial flaw size.

The results of the analytical fracture mechanics study and the field study of the bridge indicate that quite large initial flaw sizes would be required to produce a fatigue failure in the butt welds of the bridge. Such large initial flaws would be unlikely in the welds due to the radiographic inspection required in fabrication. Therefore, no fatigue cracking is likely to occur at the flange butt welds used in the bridge.

17. Key Words fatigue performance, flange transition, butt-welded splice, finite element, bridge, induced vibration	18. Distribution Statement No restrictions. This document is available to the public through the National Technical Information Service, Springfield, Virginia 22161.

19. Security Classif. (of this report) Unclassified	20. Security Classif. (of this page) Unclassified	21. No. of Pages 224	22. Price

Form DOT F 1700.7 (8-69)

EVALUATION OF THE FATIGUE PERFORMANCE OF BUTT-WELDED SPLICES

by

Antonio J.F.P. Leite
Karl H. Frank
and
Joseph A. Yura

Research Report 247-3

Research Project 3-5-79-247
Evaluation of the Fatigue Life of Structural
Steel Bridge Details

Conducted for

Texas
State Department of Highways and Public Transportation

In cooperation with the
U.S. Department of Transportation
Federal Highway Administration

by

CENTER FOR TRANSPORTATION RESEARCH
BUREAU OF ENGINEERING RESEARCH
THE UNIVERSITY OF TEXAS AT AUSTIN

August 1982

PREFACE

This is an interim report on Research Project 3-5-79-247 entitled "Evaluation of the Fatigue Life of Structural Steel Bridge Details." The study described was conducted as a part of the overall research program at The University of Texas at Austin, Center for Transportation Research. The work was sponsored jointly by the Texas State Department of Highways and Public Transportation and the Federal Highway Administration.

The authors are indebted to the Laboratory staff members: Mr. Dan Perez and Mr. Richard Marshall in charge of the electronic instrumentation, Mrs. Laurie Golding for her assistance in purchasing, Mr. Jeff Horowitz for the drafting of figures, and Mrs. Maxine DeButts for the careful typing of the manuscript.

Sincere thanks are given to the Research Assistants David Platten and Ashok Gupta for their assistance with the data acquisition system and the field tests.

Mr. Frank Endres developed most of the computer programs necessary to analyze the field data and the authors are also indebted to him.

Liaison with the Texas Department of Highways and Public Transportation was maintained through the contact representatives Bob Reed and Gerry Fox. Their cooperation in the field testing was invaluable. Mr. Randy Losch was the contact representative for the Federal Highway Administration.

ABSTRACT

The fatigue performance of flange transition butt-welded splices has been evaluated. Analytical solutions for the stress gradient correction, F_G, are generated using a finite element method. The 1 to 2-1/2 slope transition recommended by the AASHTO Specifications is compared with the 1 to 5 slope transition used in the bridge being investigated. The 1 to 5 slope increases the estimated fatigue by a factor of 2 and is recommended for future construction.

The data generated under normal speed traffic in the field study of the bridge shows the significance of the induced-vibration cycles superimposed to each major cycle due to a single truck. The dynamic vibrations have amplitudes of the same order of magnitude as the static stress range.

Solutions for the fatigue life of surface, corner, and interior cracks are presented in tabular form. These solutions can be applied to any desired stress range and initial flaw size.

The results of the analytical fracture mechanics study and the field study of the bridge indicate that quite large initial flaw sizes would be required to produce a fatigue failure in the butt welds of the bridge. Such large initial flaws would be unlikely in the welds due to the radiographic inspection required in fabrication. Therefore, no fatigue cracking is likely to occur at the flange butt welds used in the bridge.

IMPLEMENTATION

The results of the analytical study of the fatigue performance of butt welded joints indicate that the use of a lower slope in thickness transition butt welds than the 2-1/2 to 1 slope in the AASHTO Specification can greatly increase fatigue performance. The 5 to 1 slope (measured slope) employed on the bridge studied increases the fatigue life by a factor of 2 over the steeper 2-1/2 to 1 slope. The present Texas Standard Specification for Construction of Highways, Streets, and Bridges in Sec. 448.4 states that the slope of such a transition should be no greater than a 1 in 4 slope. This is a good requirement. The gradual slope found on the bridge, 1 in 5, in conjunction with the radiographic inspection and low measured stresses, alleviated fatigue cracking as a cause for concern in the butt welds in the bridge.

CONTENTS

LIST OF TABLES

LIST OF FIGURES

CHAPTER 1

INTRODUCTION

1.1 Objectives

The fracture mechanics approach to designing of structures is now being used as a quantitative method of controlling fatigue failures in bridges.

The great majority of steel highway and railroad bridges has been performing satisfactorily. The few failures reported in the literature did not encourage a better understanding of the possibility of brittle fracture until the catastrophic collapse of the Point Pleasant Bridge. In 1967, that eye-bar suspension bridge failed without warning, claiming 46 lives [1].*

Since then, an extensive research effort has been undertaken to understand the effects of repetitive loads on cracking of steel bridges. Using the concepts of fracture mechanics, the relationship of material behavior (resistance to fracture), design (actual stress range on a particular detail), and fabrication (built-in flaws, weld defects, detail geometry, etc.) upon fatigue can be quantified.

The 1974 AASHTO Fatigue Specifications [2] represent the new approach to the problem and are a result of the research carried out in the past decade [3-6].

Many steel bridges which were designed prior to use of current specifications may have details with potentially low fatigue resistance. A research study is now being conducted at The

---

*Numbers in brackets refer to the References.

University of Texas at Austin, sponsored by the Texas State Department of Highways and Public Transportation. The steel bridges that are being investigated include part of IH 345, a major complex in the Dallas, Texas, area.

The objective of this report, as part of the research study, is to predict the fatigue life of the field flange and web splices and the shop flange splice details. The flange splices are full penetration butt welds, with the reinforcement removed. This is a very common detail in a welded steel bridge; consequently, its performance is of major concern to other bridges.

Analytical stress intensity factor solutions for the crack-like defects in the flange thickness transition details have been generated. The measured stress ranges are used in the analytical solutions to predict the crack growth rate and number of cycles to failure. Before introducing the aspects of the research, a brief review of fatigue and fracture in steel will be presented.

1.2 Fatigue Behavior of Weldments

The life of structural components subjected to repetitive, cyclic loading, is governed by the rate of crack propagation. The possible existence of welding imperfections or defects undetected during fabrication inspections requires the designer to disregard the crack initiation portion of the fatigue life and to assume the presence of the largest crack-like flaw that can be missed by the nondestructive inspection method used. In Fig. 1.1, the effect of flaw size on the fatigue life is schematically shown. That typical fatigue crack propagation curve is for a detail under constant amplitude cyclic loading. Most of the fatigue life of cracked specimens is spent when the crack is relatively small, as is inferred from the flat portion, or low growth rate, da/dN, of the fatigue crack growth curve. A decrease in the initial crack size, a_i, from improved fabrication methods and reliability of inspection procedures

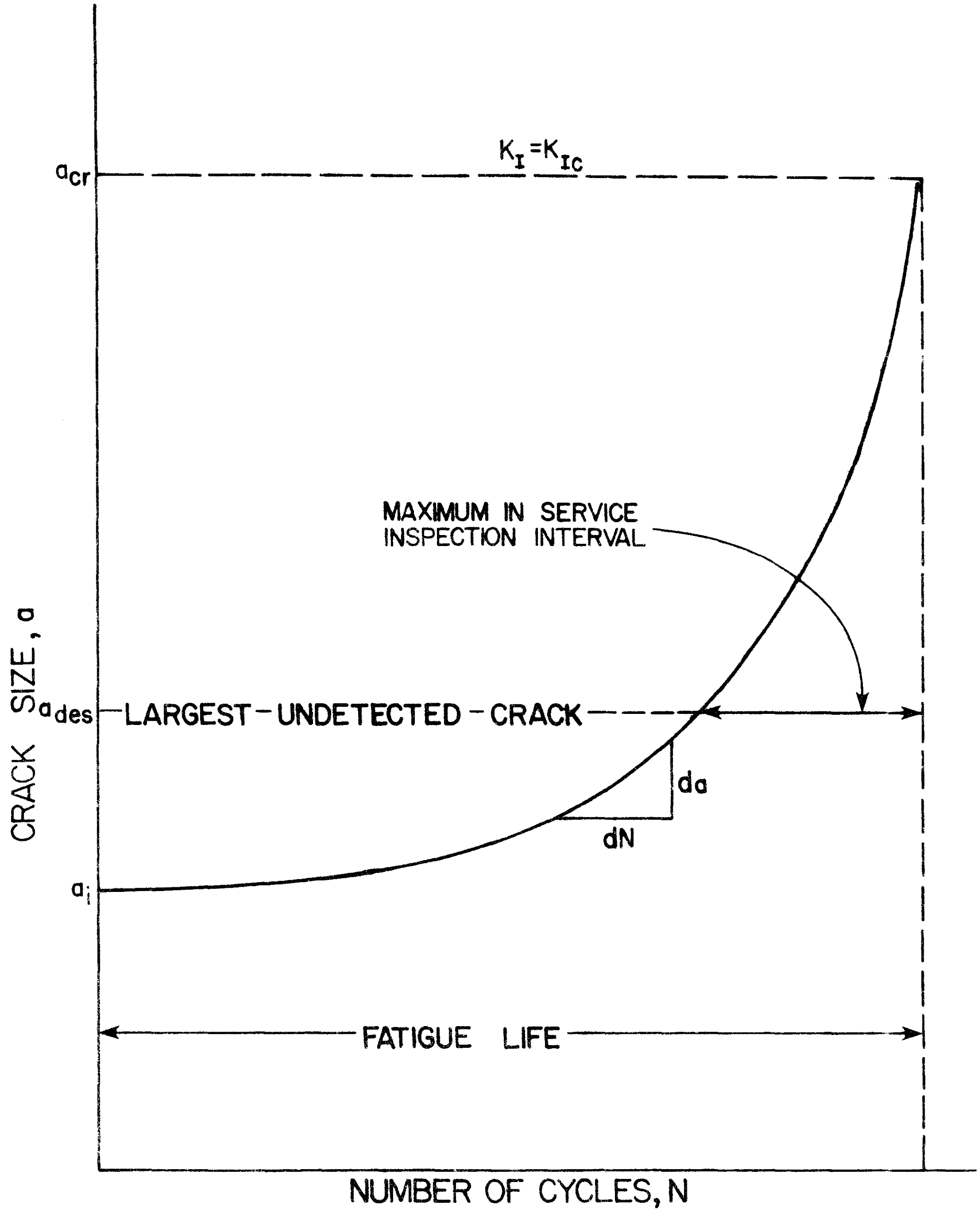

Fig. 1.1 Crack growth under constant amplitude cyclic loading

will represent a much greater increase in the number of cycles, N, than an equivalent increase in the critical flaw size, a_{cr}, from improved material toughness.

The effect of the stress range, S_r, is reflected on the variation of the crack growth rate, da/dN. Figure 1.2(b) shows a family of curves that can be measured for the same initial crack size and geometry under various stress ranges, where stress range, S_r, is defined as $S_r = S_{max} - S_{min}$ and is represented in Fig. 1.2(a) with other stress parameters.

The geometry of the detail introduces a state of stresses compatible with that geometry. A stress concentration factor, λ, occurring on a particular detail directly affects the local stress range, S_r, and the previous discussion can be interpreted in terms of a factored stress range, λS_r.

The change in critical crack size, a_{cr}, is directly proportional to the material toughness, K_{Ic}. The relative trade-offs among critical crack size, a_{cr}, initial crack size, a_i, and stress range, S_r, is represented in Fig. 1.3. The improvement in life from a larger critical crack size is accomplished through an increase in material toughness. The loading conditions factored by the local stress concentration directly affects the improvement in life due to a lower stress range and the fabrication procedures and reliability of nondestructive inspection determines the improvement in the life from a smaller initial flaw size. The relative improvements are shown schematically in Fig. 1.3 as I, II, and III, in decreasing effectiveness. The greatest increase in fatigue occurs by decreasing the initial flaw size. Reducing the stress range produces the next best improvement in life and if it yields ΔK values less than ΔK_{TH} (refer to Fig. 1.11) crack growth will not occur. The critical crack size produces very little increase in life.

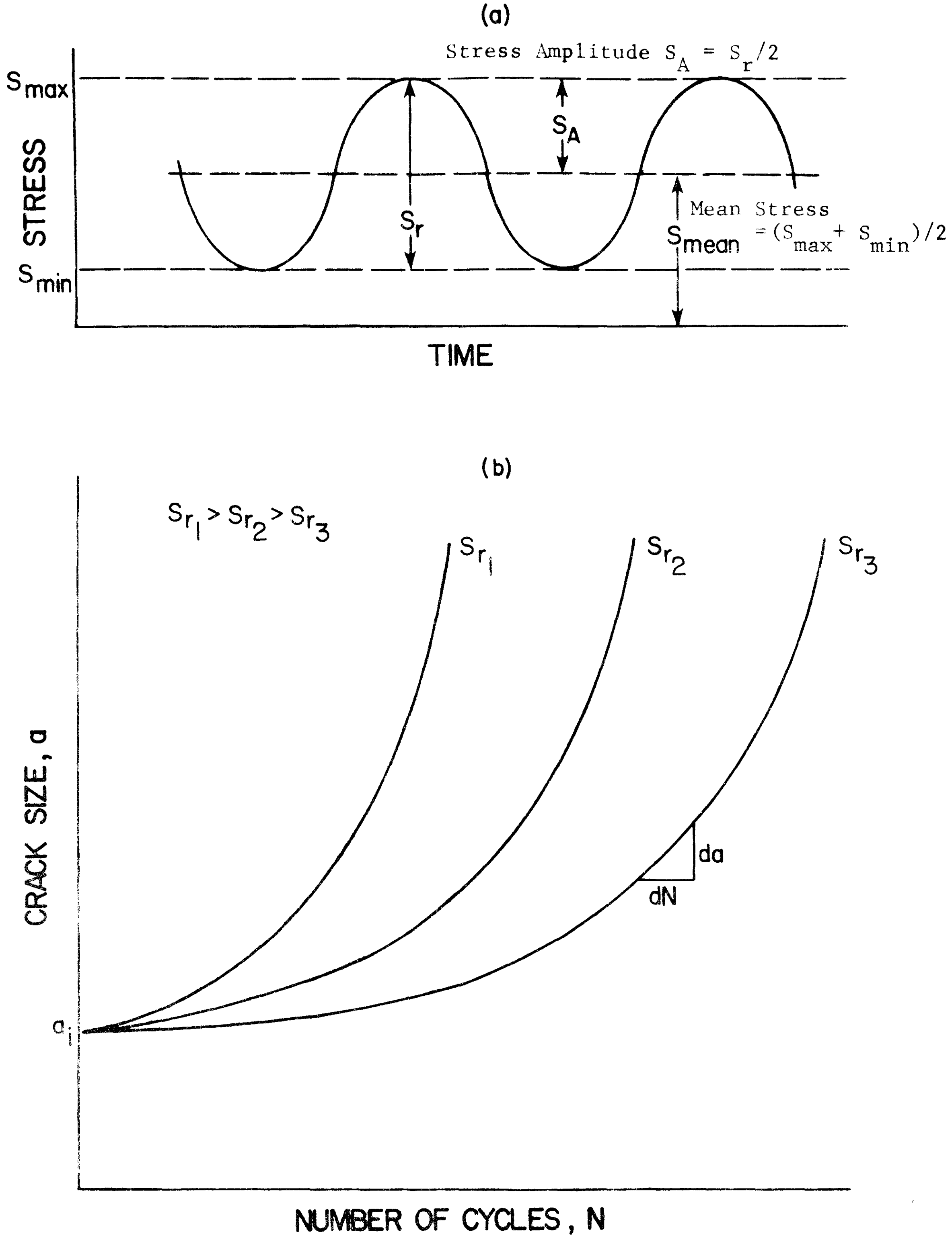

Fig. 1.2 (a) Stress parameters; (b) Crack growth for various stress ranges

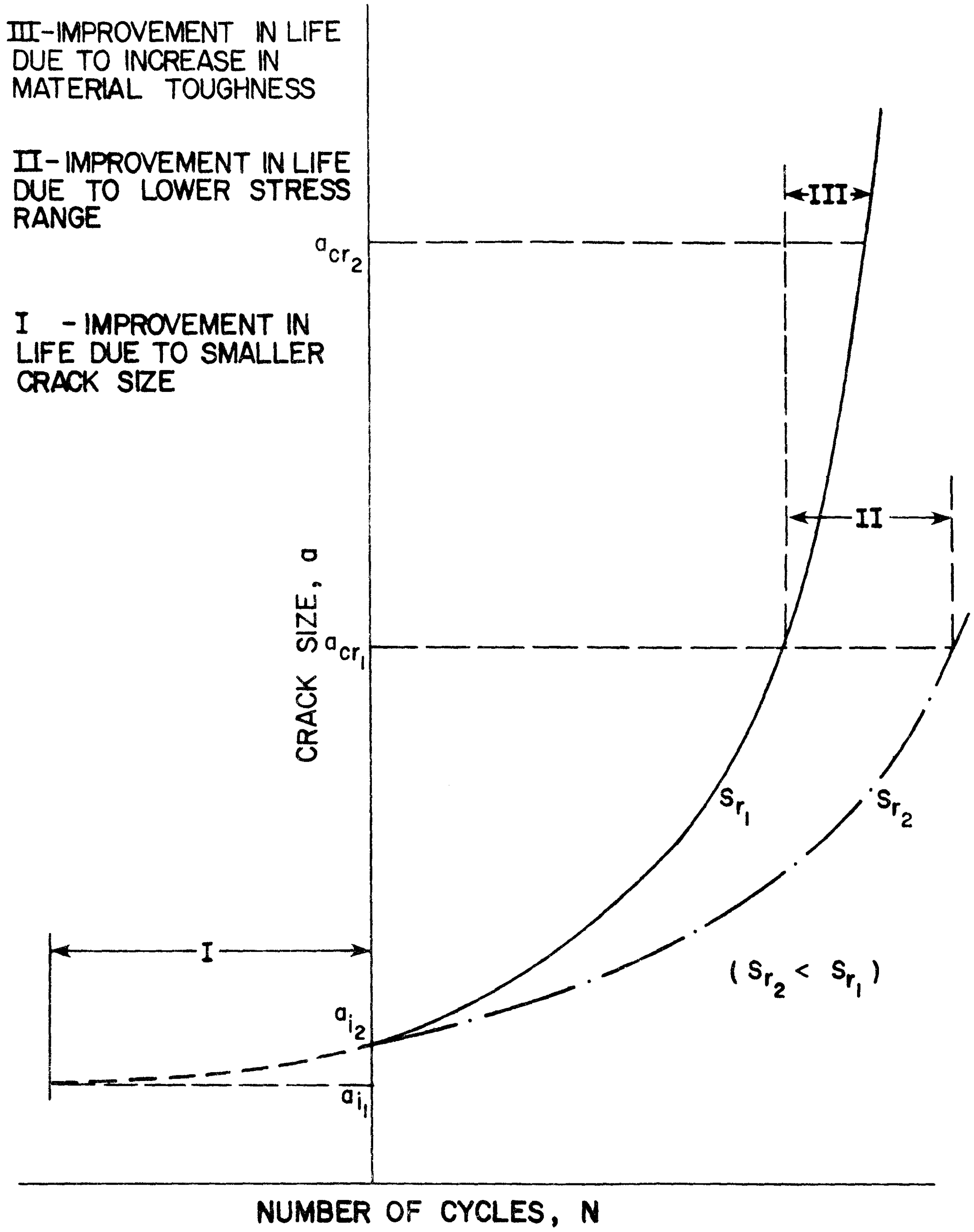

Fig. 1.3 Relative improvement on fatigue life for a_i, S_r, and K_{Ic}

1.3 Fracture Toughness

Linear-elastic fracture mechanics is based on analytical studies that relate the stress intensity factor, K_I, to the nominal stress, σ, applied to the structure and the crack or crack-like defect, a. The stress intensity factor, K_I, is the dominant term on the elastic stress field distribution at the crack tip [7]. The equations in Fig. 1.4 show that the distribution of the elastic stress field at the crack tip is invariant of material properties and the intensity of the stress field is a function of a single parameter, K_I. The basic relationship can be described as

$$K_I = C \sigma \sqrt{\pi a} \tag{1}$$

where K_I is in units of ksi $\sqrt{in.}$ (MN/m$^{3/2}$), for Mode I displacements, in which the fracture surfaces are displaced symmetrically with respect to the x-y and x-z planes, as shown in Fig. 1.5. C is a nondimensional correction function for the crack size, shape, orientation, and specimen geometry (typical values of C are shown in Fig. 1.6). σ is the nominal applied stress in units of ksi (MPa); and a is the crack size in inches (m). These three basic factors establish the conditions for crack instability or fracture which occurs when the stress intensity factor, K_I, equals the material fracture toughness, K_{Ic}.

The material toughness or critical stress intensity factor, K_{Ic}, is a material property that can be described as the ability to carry load in the presence of a crack. The effect of the material toughness on the critical crack size, a_{cr}, is shown in Fig. 1.7. A reduction in toughness decreases the critical crack size and its effect on the fatigue life is indicated in Fig. 1.3.

The major factors influencing the fracture toughness of structural steels are the loading rate, the plate thickness, and the temperature. The material toughness, K_{Ic}, refers to a static

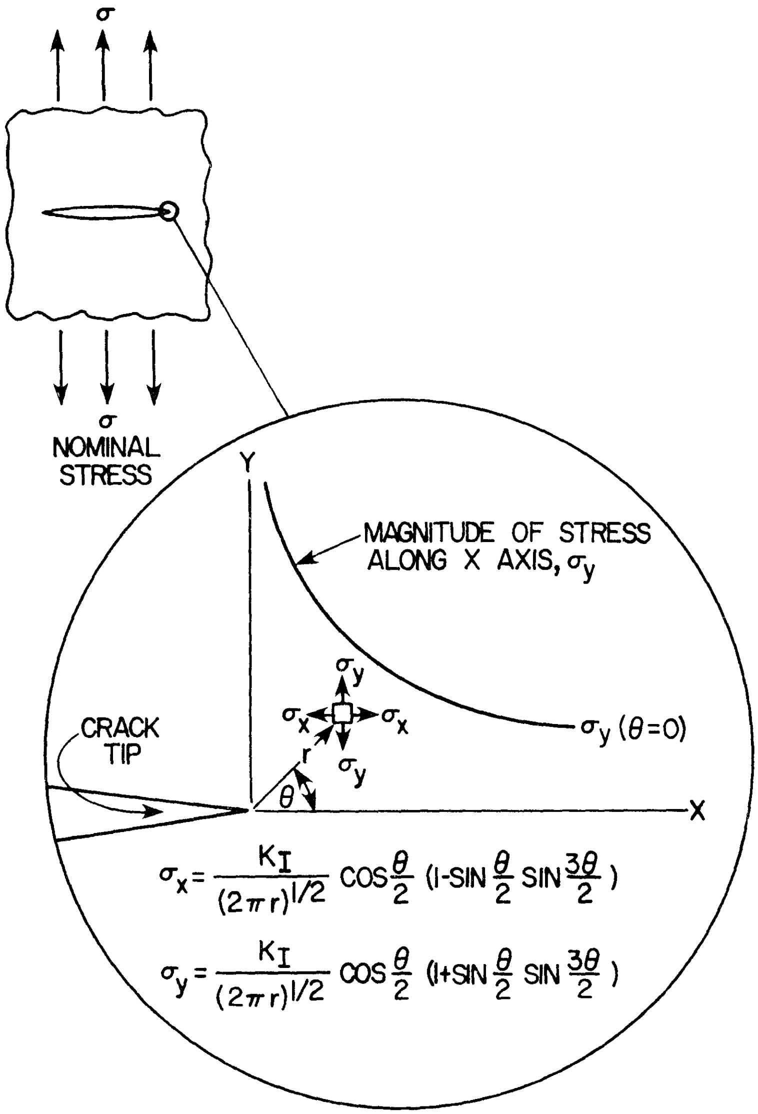

Fig. 1.4 Elastic stress field distribution at the crack tip (Mode I)

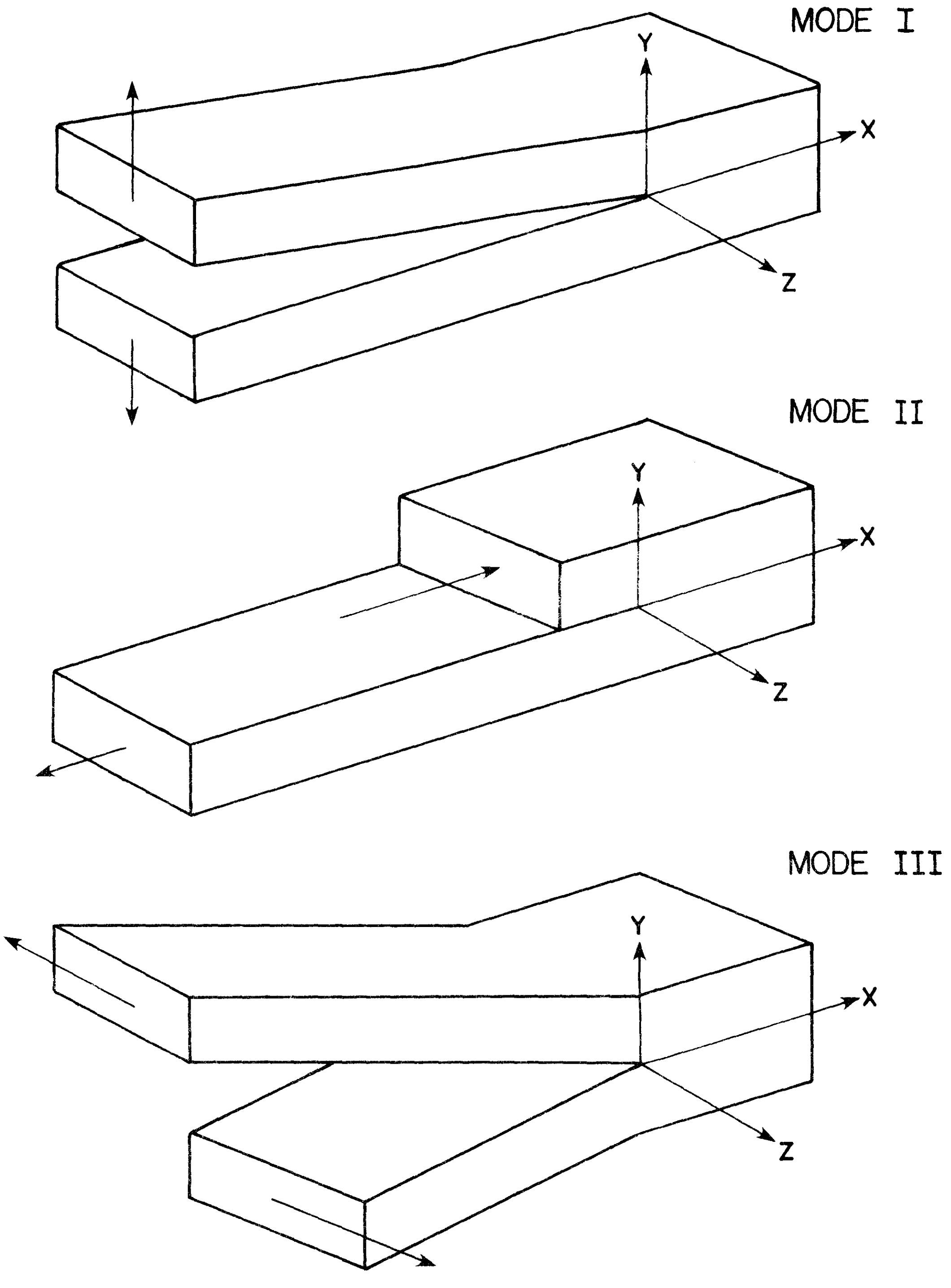

Fig. 1.5 Basic modes of crack surface displacement (Ref. 15)

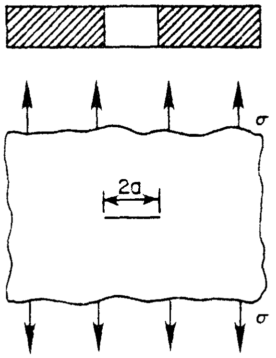

(a) Through thickness crack on an infinite plate

$C = 1$

$K_I = \sigma\sqrt{\pi a}$

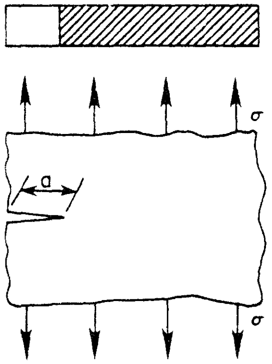

(b) Edge crack on an infinite plate

$C = 1.12$

$K_I = 1.12\,\sigma\sqrt{\pi a}$

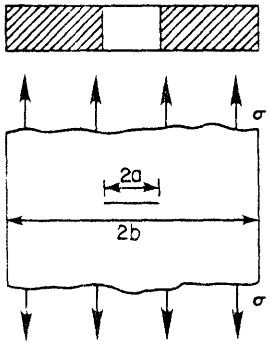

(c) Through thickness crack on a finite width plate

$$C = \left(\frac{2b}{\pi a}\tan\frac{\pi a}{2b}\right)^{1/2}$$

$$K_I = \sigma\left[\pi a\left(\frac{2b}{\pi a}\tan\frac{\pi a}{2b}\right)\right]^{1/2}$$

Fig. 1.6 C values for common crack geometries

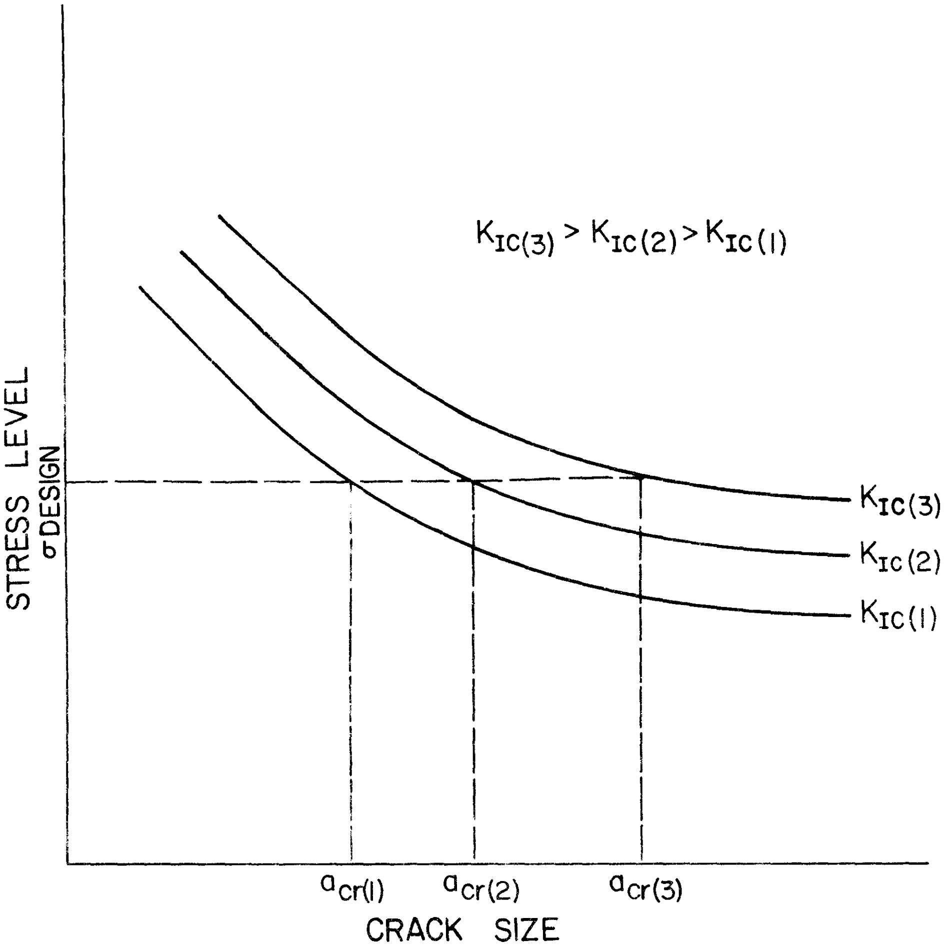

Fig. 1.7 Influence of material toughness on critical crack size

loading rate and a state of plane strain in a Mode I displacement for a given temperature.

There is a significant decrease in fracture toughness from a static or slow loading rate, K_{Ic}, to a dynamic loading rate fracture toughness, K_{Id}, as is shown in Fig. 1.8. Actual bridge test results [8] indicate that the maximum loading rates observed in bridges are closer to slow loading rates than to dynamic loading rates.

The lateral constraint at the crack tip increases with plate thickness and produces a state of plane strain for thick plates with a triaxial state of stress at the crack tip. The triaxial state of stress at the crack tip reduces the material's fracture toughness. The effect of plate thickness on the fracture toughness is shown in Fig. 1.9. The limiting thickness to ensure a plane strain behavior established by the ASTM standard fracture toughness test method [10] is given by $t \geq 2.5(K_{Ic}/\sigma_{ys})^2$, where t is the plate thickness and σ_{ys} is the static tensile yield strength.

The fracture toughness of structural steels increases with increasing temperatures. The effect of increasing temperatures and decreasing loading rates on the K_{Ic} behavior has been determined to be directly related to the Charpy V-notch (CVN) impact test results. That is shown in Fig. 1.10 from various fracture toughness tests.

The cost of a K_{Ic} test under ASTM Standard test methods makes it impractical as a quality control test for bridge steels. One of the tests most widely used is the Charpy V-notch (CVN) impact test. For the same temperature, the dynamic fracture toughness, K_{Id}, can be calculated from CVN test results by

$$K_{Id} = 12.5\sqrt{CVN} \qquad (2)$$

where CVN is in ft-lb and K_{Id} is in ksi $\sqrt{in.}$ for structural steels with Young's modulus of 29000 ksi. The temperature shift from the

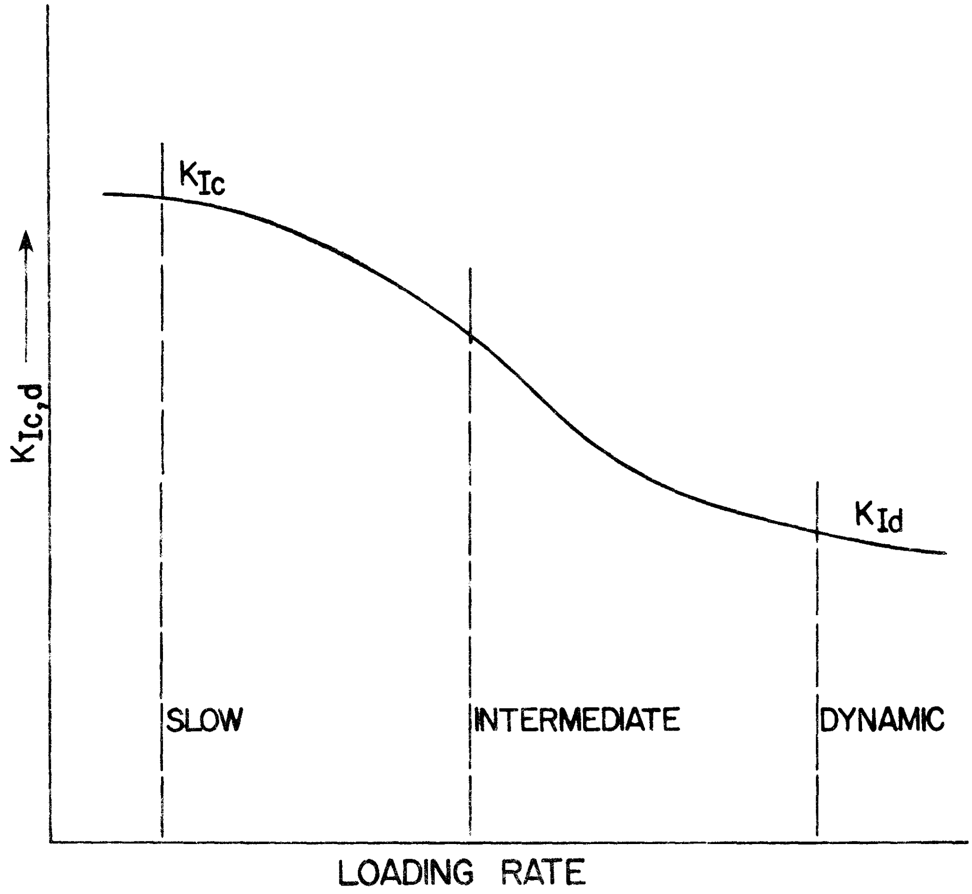

Fig. 1.8 Change in material toughness due to loading rate

1 in. = 25.4 mm.
1 Ksi $\sqrt{\text{in.}}$ = 1.1 MN/m$^{3/2}$

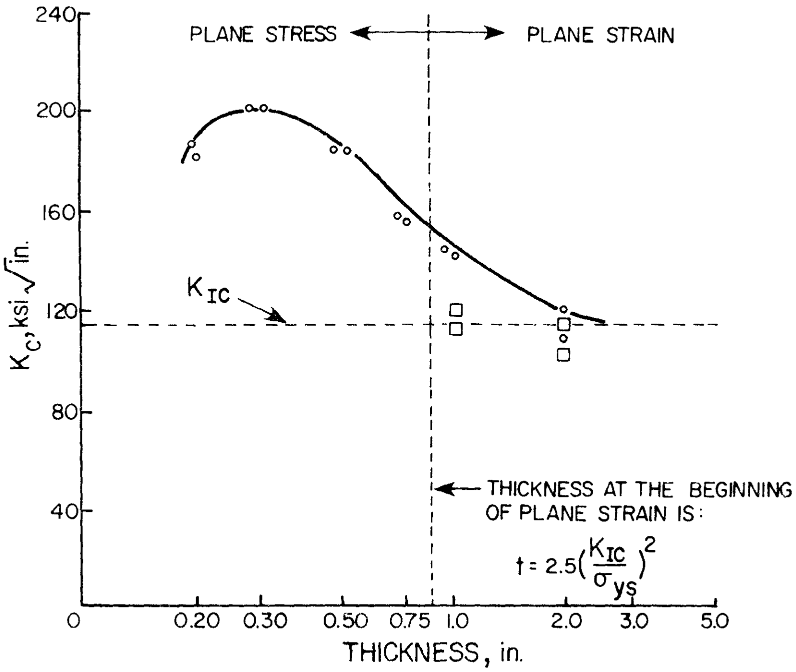

Fig. 1.9 Effect of thickness on K_c behavior (From Ref. 9)

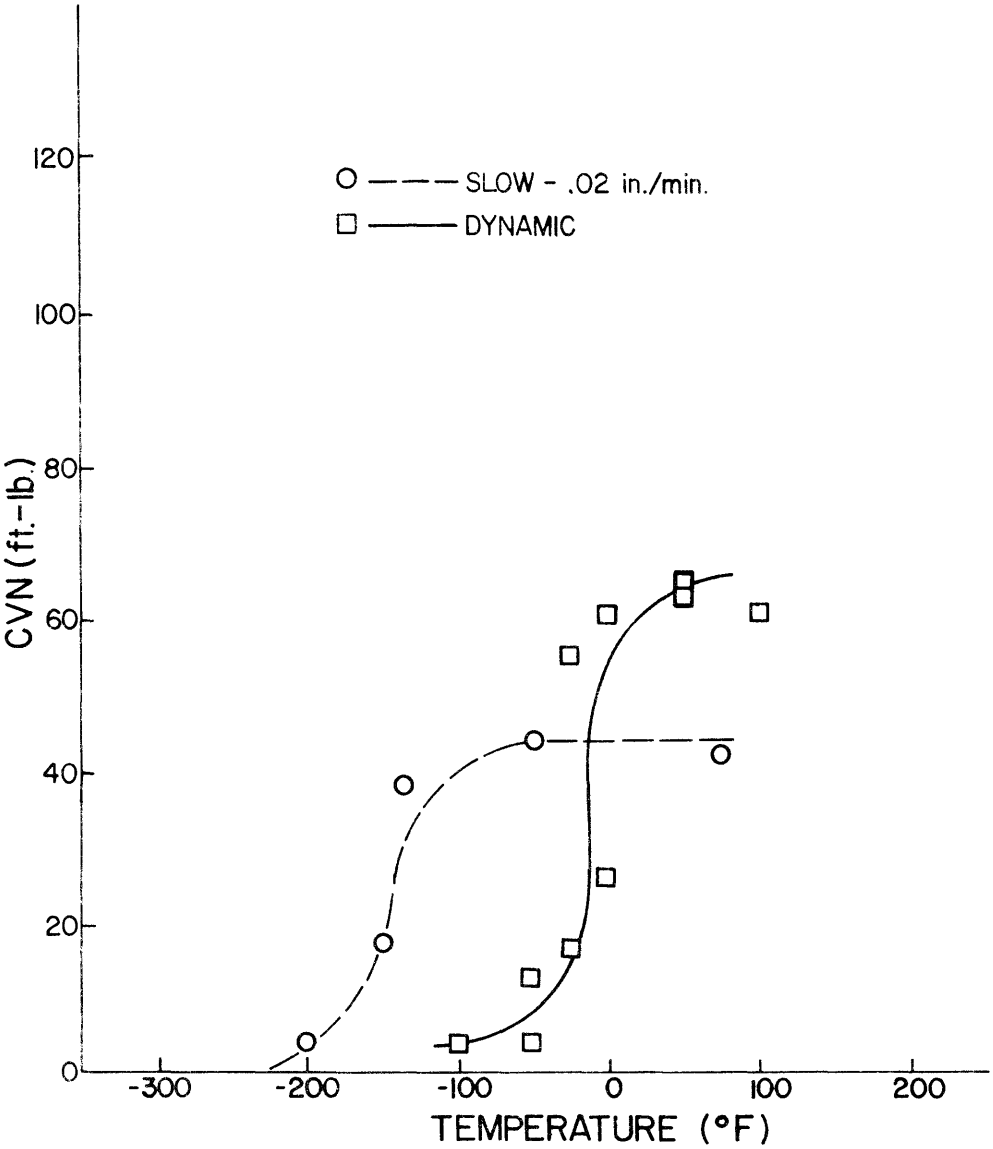

Fig. 1.10 Effect of temperature on fracture toughness (From Ref. 5)

K_{Id} to the K_{Ic} curve can be estimated by

$$T_{shift} = 215 - 1.5\ \sigma_{ys} \qquad (3)$$

for 36 ksi $< \sigma_{ys} <$ 140 ksi and the temperature in degrees Fahrenheit (°F) [9].

1.4 Crack Growth under Cyclic Loading

The curves in Fig. 1.2(b) can be reduced to a single curve representing the crack growth rate per cycle of loading, da/dN, as a function of the stress intensity factor range, ΔK where

$$\Delta K = C\ S_r \sqrt{\pi a} \qquad (4)$$

In the log da/dN versus log ΔK_I plot, Fig. 1.11, there are three distinct regions of crack growth behavior. Region I is characterized by a fatigue threshold stress intensity factor range, ΔK_{TH}, below which cracks do not propagate. For structural steels, where the ratio of minimum stress to maximum stress, $R = S_{min}/S_{max}$, is greater than +0.1, a lower bound estimate of ΔK_{TH} can be predicted from [9]

$$\Delta K_{TH} = 6.4(1 - 0.85R) \qquad (5)$$

where ΔK_{TH} is in ksi $\sqrt{\text{in.}}$

Region II in Fig. 1.11 represents the fatigue crack propagation behavior and it is defined as

$$da/dN = A(\Delta K_I)^n \qquad (6)$$

where A and n are constants and function of the material properties. Region II defines the useful life of the structure. For positive stress ratios, the fatigue crack propagation can be modeled by Eq. (7) [9]:

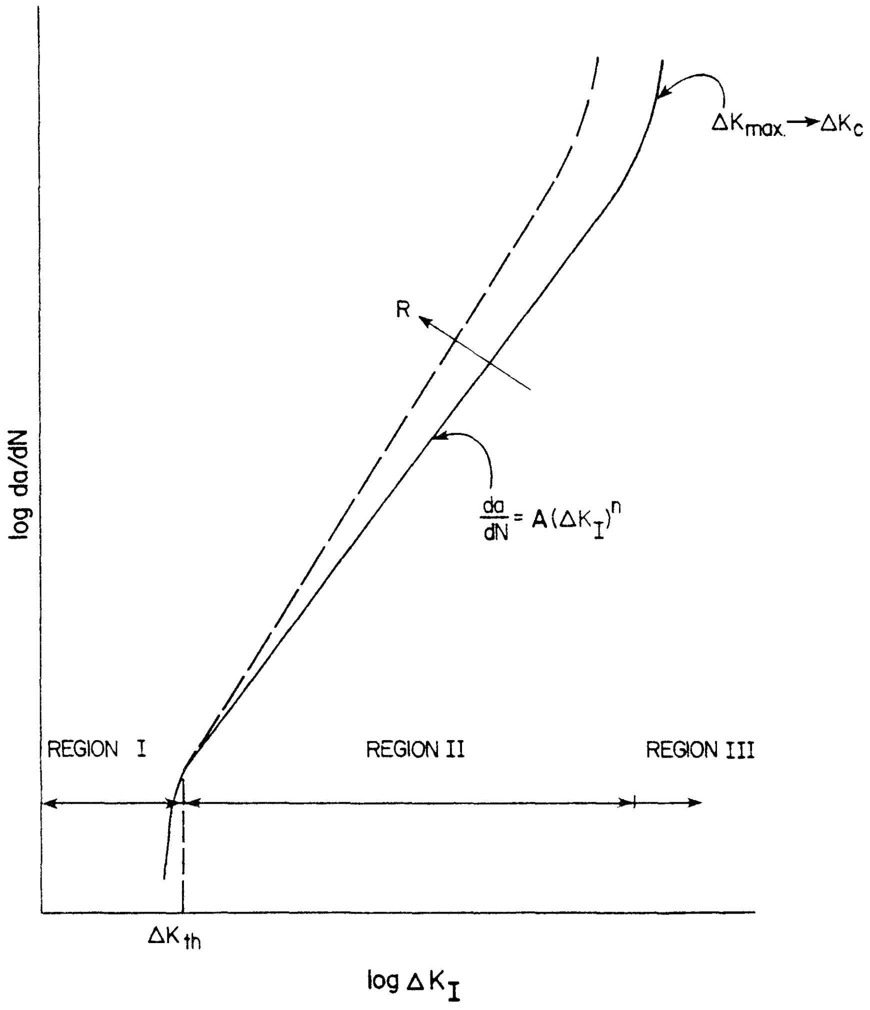

Fig. 1.11 Fatigue crack propagation behavior

$$da/dN = \frac{A(\Delta K_I)^n}{(1 - R)^{1/2}} \tag{7}$$

The increase in the crack propagation rate with increasing R is indicated in this equation. However, the influence of R is usually small and can be disregarded.

Region III corresponds to the onset of acceleration in fatigue crack growth rates as K_{max} in the fatigue cycle approaches the fracture toughness of the materials. For large initial flaws, the corresponding large values of ΔK from Eq. (4) will yield very short fatigue life when we are in Region III. Such a large defect would not be acceptable under the bridge fatigue specifications. For small initial defects, the difference in life is negligible if we disregard the Region III contribution to fatigue life.

The constants A and n for various yield strength structural steels have been estimated experimentally [11] and are compared with the crack growth rate material constants for E70 weld metal [12] in Table 1.1. The crack growth rate for the weld metal gives an upper bound band to the base metal. The usual practice of using the base metal constants is conservative and a simple approach. The heat affected zones also show fatigue crack growth rates less than or equal to the base metal; therefore, the base metal material properties will be used in this study.

Those residual stress zones due to the welding often are equal to the yield stresses of the material. They affect the magnitude of ΔK_{TH} and also of ΔK_{max}, but the effect on Region II is significant only due to a major change in R.

TABLE 1.1 CRACK GROWTH RATE PARAMETERS (for ΔK in ksi $\sqrt{\text{in.}}$ and da/dN in in./cycle)

Material	n	A
E70 Weld Metal	5.8	0.27×10^{-13}
Martensitic Steels	2.28	0.66×10^{-8}
Ferrite-Pearlite Steels	3.0	0.36×10^{-9}
Austenitic Stainless Steels	3.25	0.30×10^{-9}

1.5 Application of Fracture Mechanics to the Flange Splice Details

For a given material and a constant C, Eq. (6) and Eq. (4) can be combined and solved for dN as

$$\int dN = \Delta N = A' S_n^{-n}(a_i^{-\alpha} - a_f^{-\alpha}) \qquad (8)$$

where ΔN is the elapsed fatigue crack growth life in cycles, A' is a function of the material constants A and n and geometry correction C, and $\alpha = (n/2) - 1$. For large crack sizes at failure $a_f^{-\alpha}$ will be negligible compared to $a_i^{-\alpha}$ for $\alpha > 0$ (α is equal to 0.5 for structural steels with $n = 3$). For materials with low fracture toughness, the final crack size may be relevant in Eq. (8) and can be calculated from Eq. (4) using the proper C correction for the particular detail and the appropriate value of the material's fracture toughness.

The initial flaw size present in the structural detail can be assumed conservatively to be the greatest size that could be missed by the nondestructive inspection procedure used. This is a conservative assumption in the design, but as we have seen in Figs. 1.1 and 1.3, the importance of a_i cannot be overemphasized.

The stress range is another major factor as it is raised to a third power for structural steels and inversely proportional to the fatigue life. The usual fatigue tests are performed under constant amplitude loading, but the bridge structures are subjected to variable amplitude random-stress loading.

Based on a cumulative damage theory, the effective stress range, S_{re}, from a variable amplitude random-stress loading can be calculated and used in place of S_r in Eq. (8). A detailed examination of the effective stress range estimation will be presented later.

Assuming conservative values of a_i, using analytical and measured S_{re}, and with available ΔK_I relationships, the fatigue life of the butt-welded flange splices can be estimated.

CHAPTER 2

ASSESSMENT OF STRESS RANGE AND INITIAL FLAW SIZE ON FATIGUE LIFE

The flange splice is one of the most common welded details found in bridge girders. When the reinforcement is removed, the detail is considered as Category B in the AASHTO Fatigue Specification [2]. This is the same category as plain welded beams which fail in fatigue from the web to flange fillet weld. If the reinforcement is left in place, the resulting stress concentration at the weld toe due to the abrupt change in geometry causes a more severe detail. The stress concentration and the coupled internal discontinuities in the transverse butt weld decrease the fatigue life. This detail is classified as a Category C detail. The width or thickness transition in the AASHTO Specification is limited to a 1 to 2-1/2 slope in order to provide a gradual stress flow, minimizing the stress concentration at the weld toe. The 1 to 2-1/2 slope is a requirement to place the thickness or width transition under the Category B provisions if the reinforcement is also removed.

2.1 Experimental Results

2.1.1 Flange Splice Width Transition. As part of an extensive research program directed to a better understanding of welded details' fatigue performance, 84 beams with width transition flange splices were tested at Lehigh University and Drexel Institute of Technology [3].

Details of the test beams are shown in Fig. 2.1. One of the splices in each beam was a 2 ft-0 in. (609.6-mm) radius transition and the other was a 1 to 2-1/2 straight transition. The flange welds were ground flush in both transition details. Three types of steel were tested: A36 steel, with 36 ksi (248.2 MPa) yield point; A441 steel, with 50 ksi (344.7 MPa) yield point; and A514 steel, with yield point of 100 ksi (689.4 MPa). The depth of the beams was selected in such a way to give a representative depth-to-span ratio of beams used in highway bridges. The stress variables were the minimum stress, the maximum stress, and the stress range.

The longitudinal fillet weld used to join the web to the flange in the width transition was the same used for plain welded beams with constant width. The results from the plain welded beams and the flange splice beams yielded similar lives, but the failure locations for the splice beams were concentrated in a small region close to the splices where for the plain welded beams they were distributed over all the applied constant moment region. Both the plain welded beams and the flange splice beams were grouped together as Category B under the proposed specification.

The fatigue failures observed in the flange splice beams were caused by the change in geometry and consequent change in moment resistance of the section coupled with the stress concentration at the fusion line, by the flaws caused by the mechanical grinding process and also by the flaws within the longitudinal fillet weld connecting the web to the flange, which were usually gas pockets caused by gas trapped in the weldment. No failures caused by internal flaw within the butt weld splices were reported.

Two distinct types of fatigue failures were reported in Ref. 3. The Type 1 refers to the failures caused by porosity flaws within the longitudinal fillet welds. These flaws had round

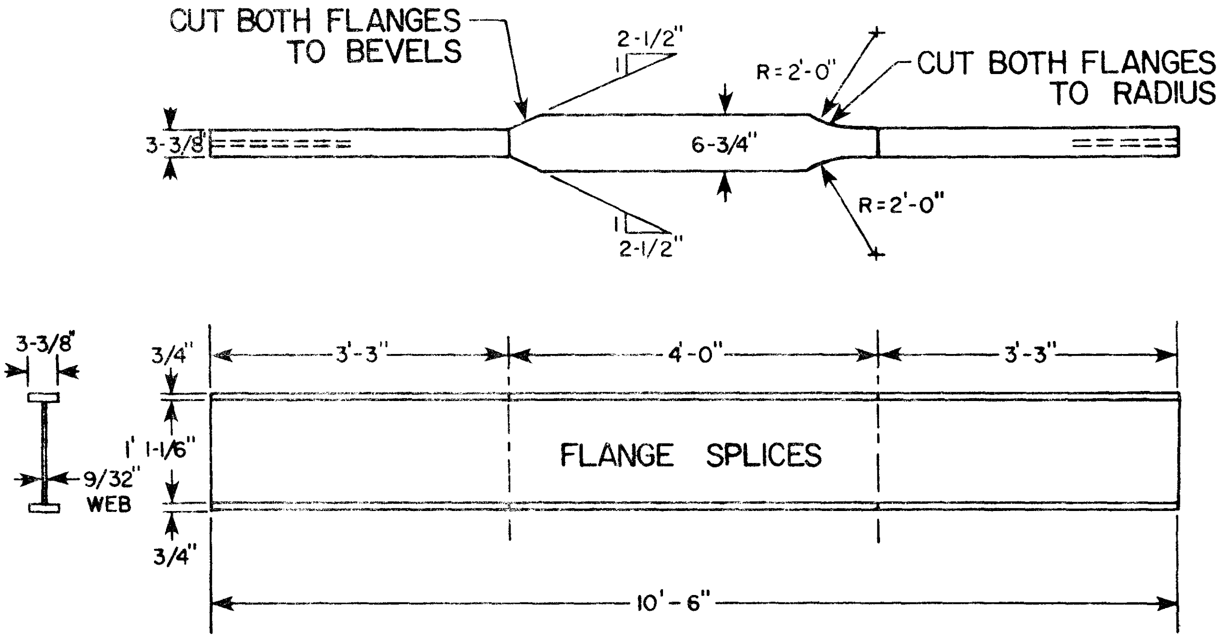

Fig. 2.1 Details of beams with flange splices (from Ref. 3)

or wormhole shapes formed from gas trapped in the weldment. They propagated as a penny-shape flaw, as shown schematically in Fig. 2.2. It is worth mentioning that Type 1 failures accounted for 80 percent of all the failures observed in the plain welded and flange spliced beams. The Type 2 failures initiated in the butt weld surface and were caused by notches from the grinding operation. Those defects which were located on the edge of the flange grew as corner quarter-circular cracks and those on the flange surface grew as semi-elliptical cracks. The fatigue failures which initiated from surface flaws generally yielded shorter lives than those failing from the web-to-flange fillet weld defects.

When a surface crack propagated through the flange thickness, most of the fatigue life had been exhausted. The remaining life to final failure accounted for 10 to 20 percent of the total life of the specimen.

The only significant variable to predict the fatigue failure was found to be the stress range, S_r. In Fig. 2.3, all the spliced beam and the plain welded beam test results are plotted with the mean regression curve for plain welded beams and the 95 percent confidence limits for 95 percent survival. The scatter of the data can be attributed to the variation in the initial flaw size. The majority of the data points falling below the 95 percent confidence limit curve of Fig. 2.3 were from the A514 steel beams with manual straight tapered transition butt welds. Curved transition is specified for this high strength steel, due to the lower fatigue life exhibited by the straight tapered transition.

The 95 percent confidence limit for 95 percent survival was approximately equal to twice the standard deviation from the mean regression line. This level was recommended for design of

TYPE 1-FAILURE MODE

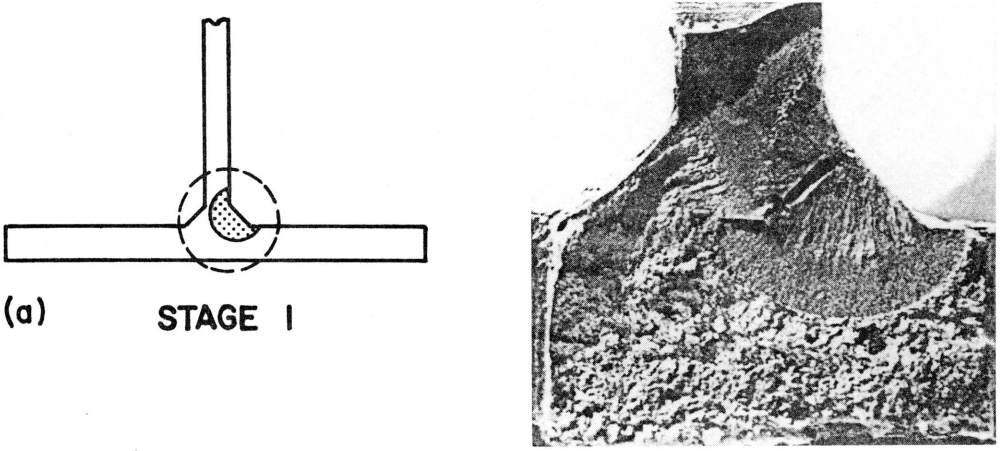

(a) STAGE 1

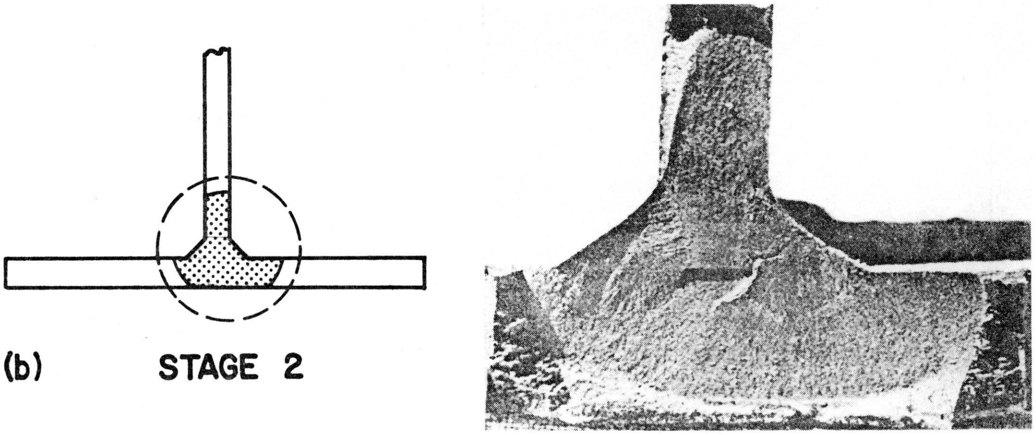

(b) STAGE 2

TYPE 2-FAILURE MODE

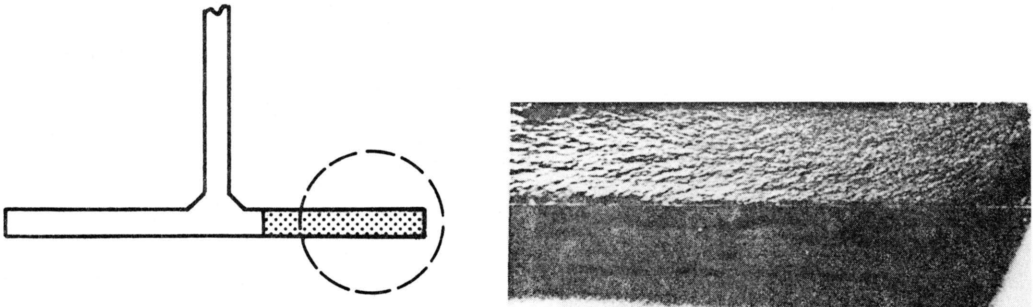

(c) CRACK INITIATION AT FLANGE TIP

Fig. 2.2 Crack growth in welded beams (from Ref. 3)

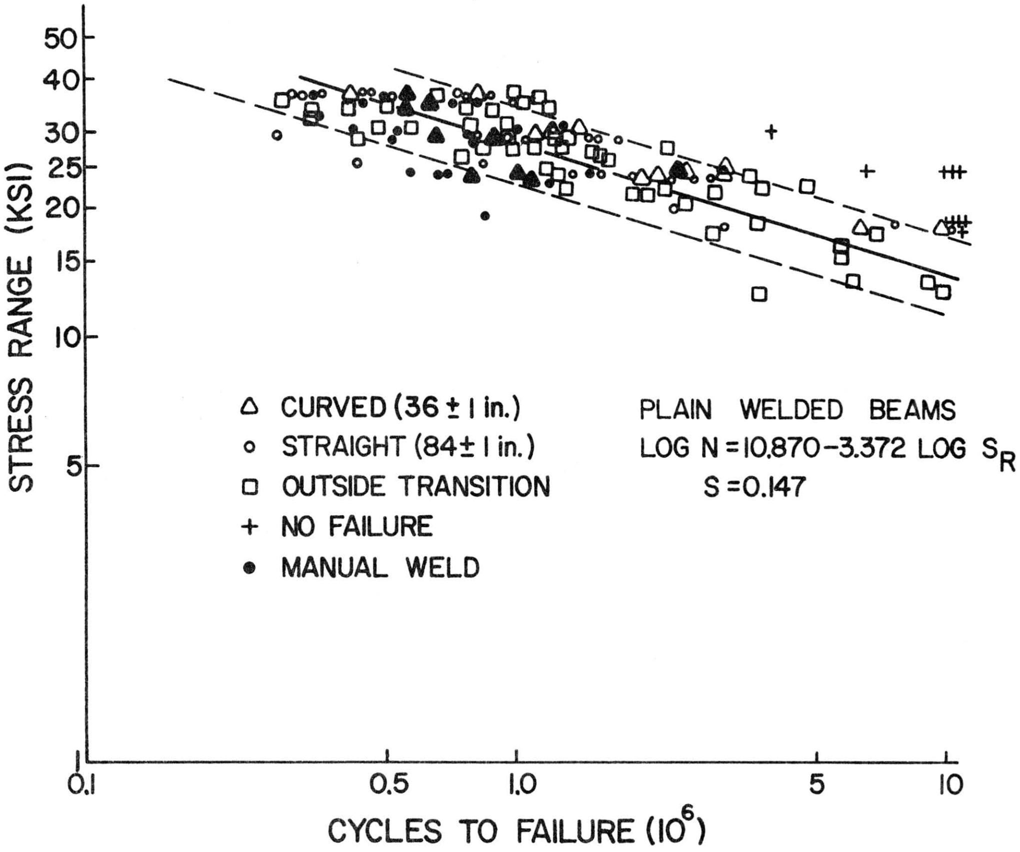

Fig. 2.3 Plain welded and flange spliced S-N tests (from Ref. 3)

plain welded and flange spliced beams, the Category B of the fatigue specifications [2].

Constant stress cycles were used throughout the tests reported in Ref. 3. The variable amplitude cyclic loading can be correlated using Miner's linear cumulative fatigue damage theory [13]. Miner's theory implies the variable stress cycle damage is accumulated in proportion to the relative frequency of occurrence of each level of stress range. The effective stress range, S_{re}, calculated from variable amplitude cyclic loading can be used to predict fatigue life from a constant cycle S-N plot.

2.1.2 Flange Splice Thickness Transition--Full Size Beam Tests. Full size beams with welded details conforming to various categories given in the AASHTO Fatigue Specification were tested [5]. Six of the twenty-four beams tested were welded beams with a 1 to 2-1/2 slope flange thickness transition. The geometrical details of the flange spliced beams are shown in Fig. 2.4. The steels tested were A36, A588, and A514.

The outside faces of the thinner flanges were tested under a maximum stress of 0.55 σ_{ys} and a stress range of 18 ksi (124.1 MPa), the Category B design stress range for a fatigue life of 2 million cycles.

The fatigue cracks at the flange transition details started as corner cracks at the flange tip that grew into edge cracks. The final crack sizes for the beams at fracture are shown in Fig. 2.5, with the respective number of cycles shown in the lower right corner.

Figure 2.6 shows the mean S-N curve and its 95 percent confidence limit for 95 percent survival for the Category B details. The test results for the full size beams are shown on the same figure as open figures for the elapsed cycles, N, at which the fatigue cracks were first observed, and as closed figures for N at

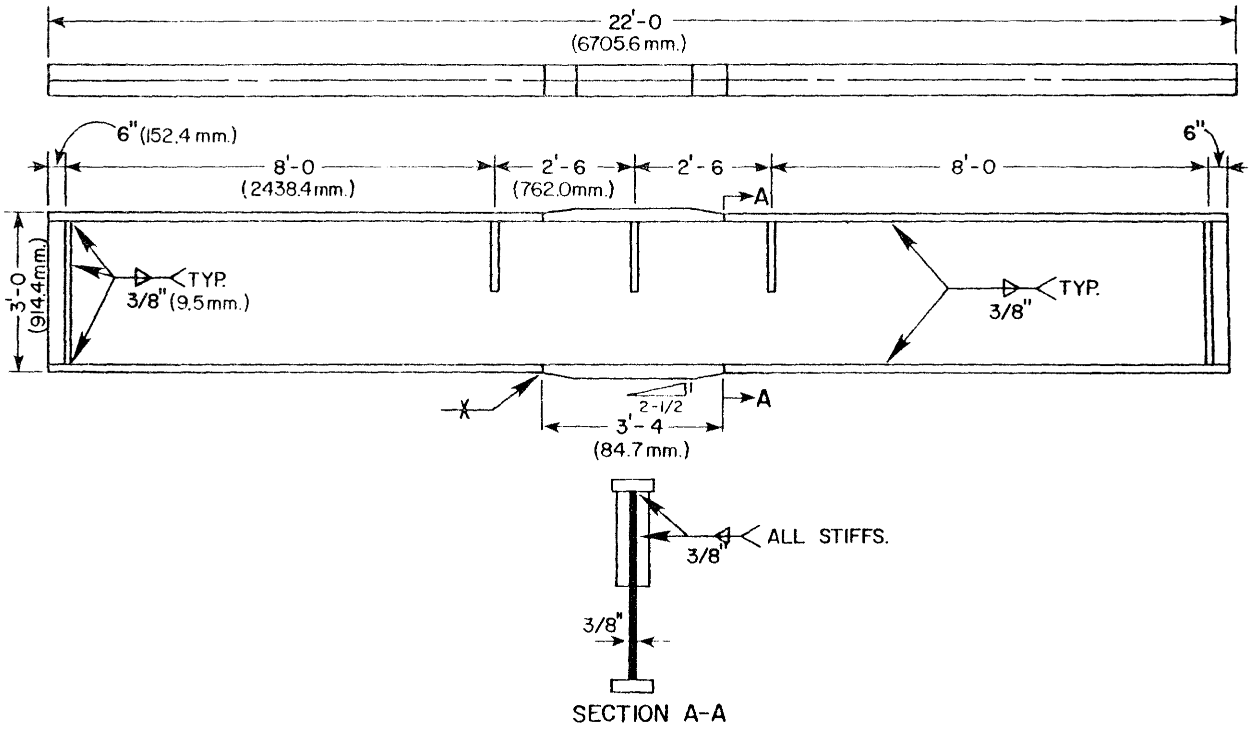

Fig. 2.4 Typical full size spliced beam (from Ref. 5)

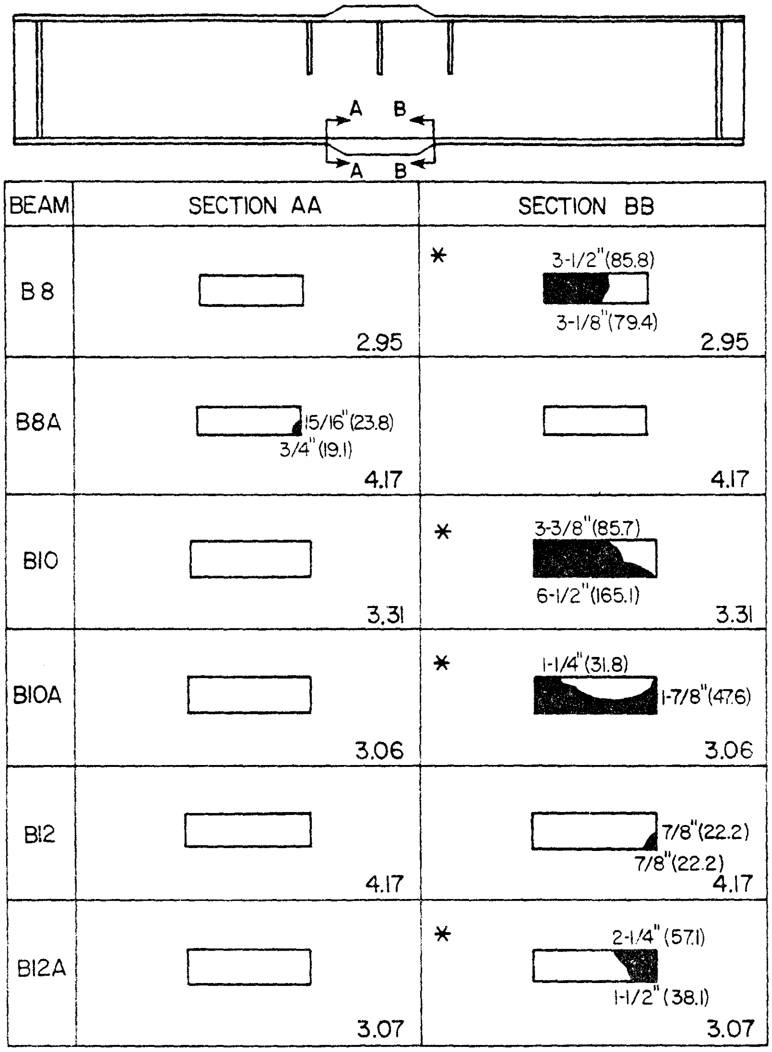

TABLE SCALE 1-1/2" = 1'-0"
MEASUREMENTS TAKEN AT CYCLES LISTED AT BOTTOM
OF CROSS SECTION (IN MILLIONS OF CYCLES)
* BEAM FRACTURED AT THIS SECTION
FATIGUE CRACK PRIOR TO LAST FRACTURE TEST
MEASUREMENTS IN BRACKETS, mm

Fig. 2.5 Fatigue cracks prior to last fracture test (from Ref. 5)

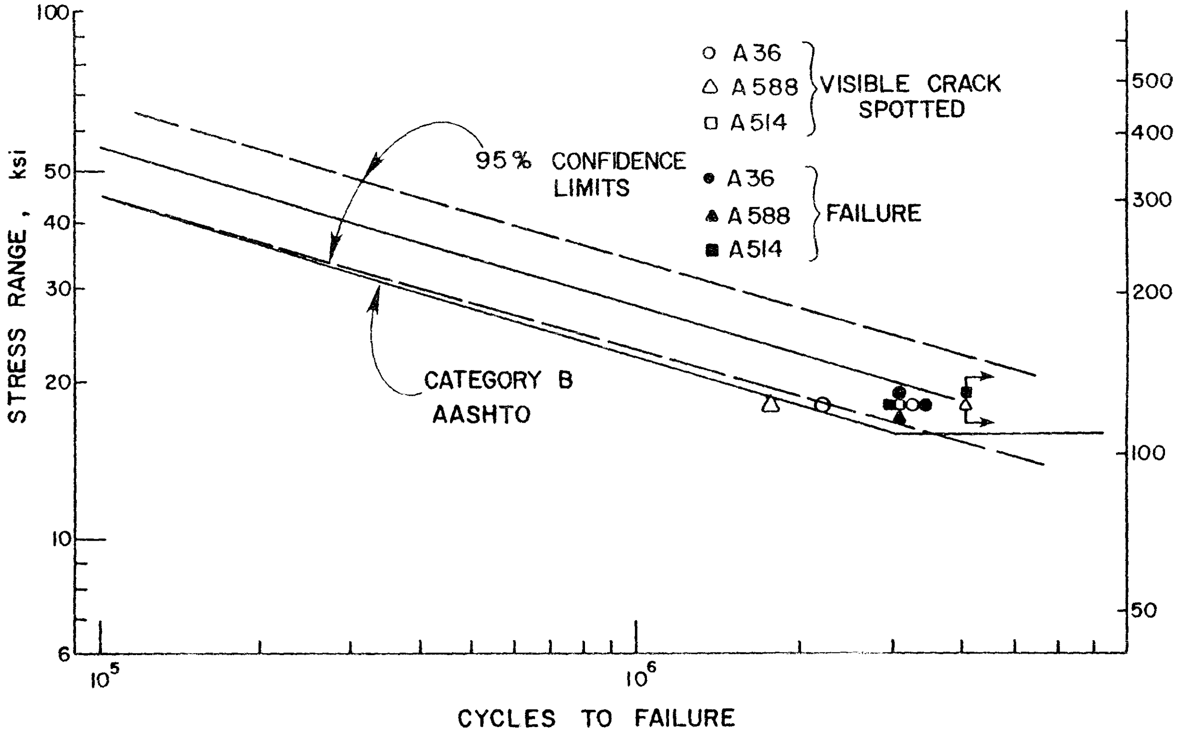

Fig. 2.6 Category B S-N plot, flange transition (from Ref. 5)

fracture. Beams B8A and B12 did not fracture and the tests were interrupted after 4 million cycles. The lower bound S-N curve used as AASHTO Category B for fatigue life prediction gives a conservative estimate for the full size flange splice beams. At fracture, the points fall within the mean S-N line and its lower bound 95 percent confidence limit.

2.2 Computation of the Effects of Initial Flaw Size on Fatigue Life for Various Flaw Shapes, Sizes, and Locations

The fatigue-crack-propagation behavior was defined by Eq. (6) as

$$\frac{da}{dN} = A(\Delta K_I)^n \qquad (6)$$

where A and n are constants and function of the material. Substituting the value of the stress intensity factor, ΔK_I, given by Eq. (4) and rearranging Eq. (6), yields

$$\Delta N = \int_{N_i}^{N_f} dN = \frac{1}{A} \int_{a_i}^{a_f} \frac{da}{CS_r\sqrt{\pi a}} \qquad (8a)$$

where the subscripts i and f stand for initial and final and ΔN is the elapsed fatigue life in cycles. C is a function of the geometric detail, crack shape, size, and location. Assuming the function C is known for a particular detail, the solution for the right-hand side of Eq. (8a) has the form of

$$\Delta N = A' \; S_r^{-n} \; a_i^{-\alpha} \left[1 - \left(\frac{a_i}{a_f}\right)\right]^{\alpha} \qquad (8b)$$

For large crack sizes at failure, the term a_i/a_f vanishes, since α is equal to 1/2 for most structural steels. Equation (8b) could then be written as

$$\Delta N = A' \; S_r^{-n} \; a_i^{-\alpha} \tag{8c}$$

2.2.1 Analytical Solutions for C. The fluctuation of the stress intensity factor ΔK_I for a central through crack of length 2a in an infinite width sheet under uniaxial tension is given by

$$\Delta K_I = S_r \sqrt{\pi a} \tag{4a}$$

The value of C for this geometry is a constant and equal to one. For typical finite dimension details and various crack shapes, locations, or sizes, the value of C can be subdivided into a series of correction factors. The approximation involved assumes the factors are independent of one another and are superimposed as appropriate [14]. We can write Eq. (4) as

$$\Delta K_I = (F_S F_W F_E F_G F_P) \times S_r \sqrt{\pi a} \tag{4b}$$

where

$$F_S F_W F_E F_G F_P = C \tag{a}$$

F_S, the front free surface, is the correction associated with a free surface as in Fig. 1.6b. F_W, the finite width correction, is associated with the free surface away from the crack tip, as in Fig. 1.6c. F_E is the flaw shape correction, F_G is the stress gradient correction which models the stress gradient caused by bending or the stress concentration caused by detail geometry along the crack path, and F_P is the plastic zone correction which accounts for the plastic zone ahead of the crack tip.

2.2.1.1 Semi-elliptical Surface Cracks. The surface fatigue cracks usually encountered in the first stages of crack growth have a semi-elliptical shape. A schematic view of such a crack on the plate thickness transition being studied is shown in Fig. 2.7.

Irwin's solution for an edge crack on a semi-infinite plate yields a front free surface correction, F_S, equal to 1.12, as shown in Fig. 1.6. For a semi-elliptic crack on a semi-infinite plate, the approximate solution suggested by Paris and Sih [15] yields

$$F_S = 1 + 0.12(1 - a/c) \qquad (9)$$

where a is the crack length and the semi-ellipse semiminor diameter and c is the semimajor diameter. There are better approximations reported in the literature [16], but that yield results within 5 percent of Eq. (9). F_s is shown in Fig. 2.8 as a function of a/c, so we can graphically visualize its linear variation, changing from 1.12 for a/c equal to zero or an edge crack, to 1.00 for a/c equal to 1 or a circular crack.

For a plate that is not subjected to bending, as the flange can be modeled, the finite width correction for a through edge crack can be approximated by [17]

$$F_W = \sqrt{\sec\left(\frac{\pi a}{2t}\right)} \qquad (10)$$

where a is the crack length and t is the plate thickness. A plot of F_W versus a/t is given in Fig. 2.9. The "secant" solution is known to be accurate for an edge crack, or a semi-elliptical crack with a/c tending to zero. The elliptical shape correction is an additional reduction factor that should then be applied with the finite width correction, F_W, for other a/c values.

The solution for an elliptical crack in an infinite body subjected to uniform tension was obtained by Irwin [18] and it is given by

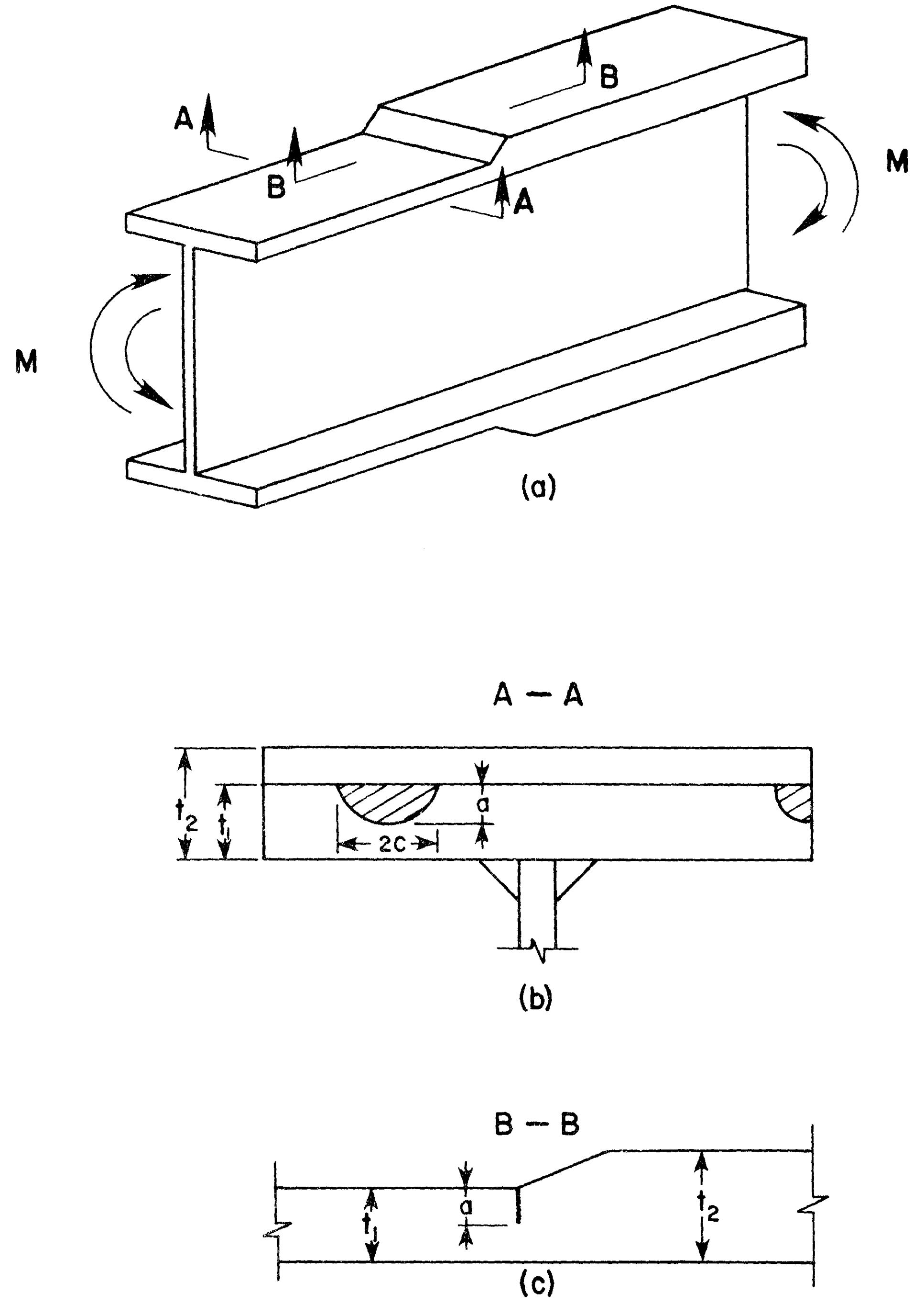

Fig. 2.7 Semi-elliptical surface crack and corner crack on flange thickness transition

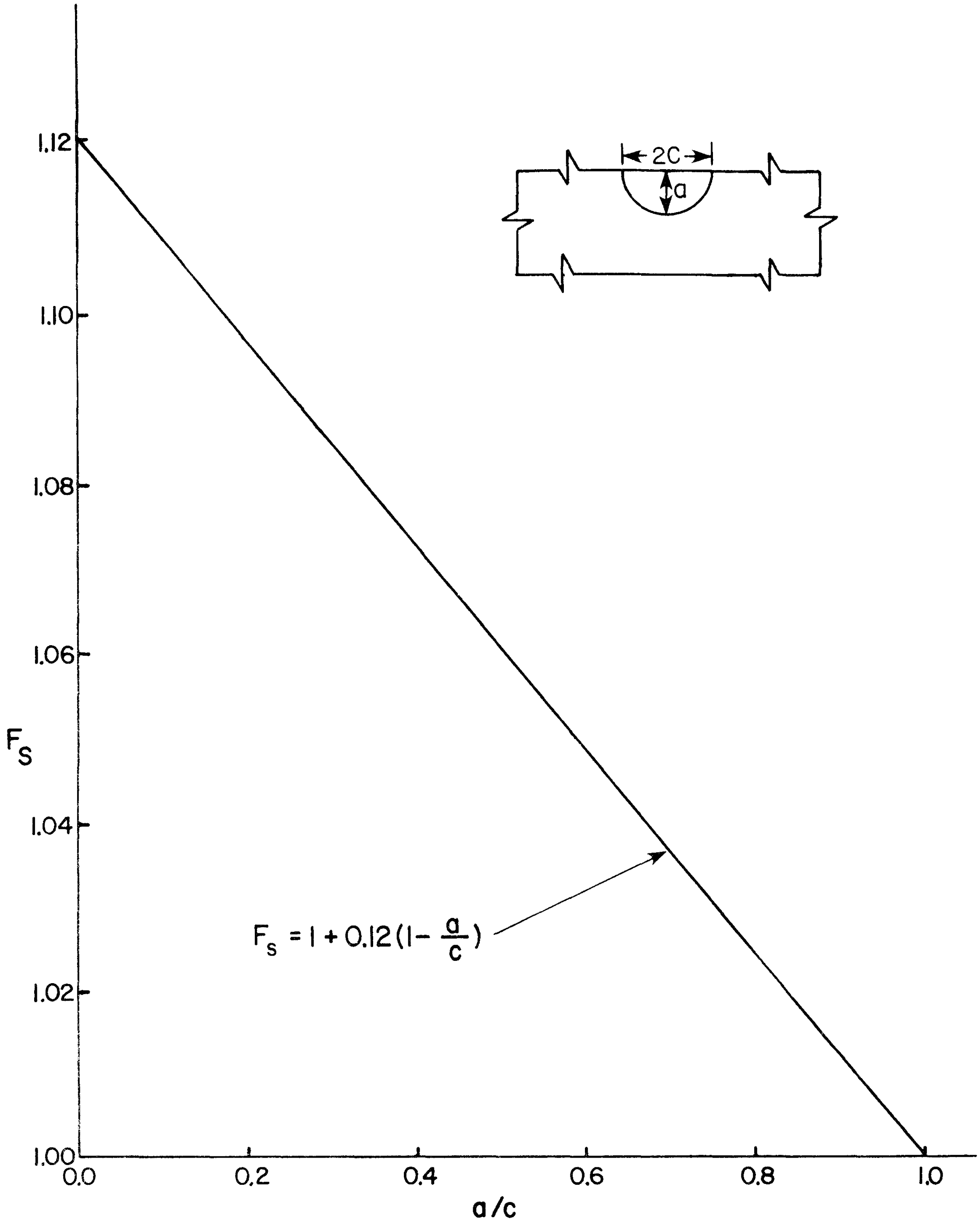

Fig. 2.8 Front free surface correction

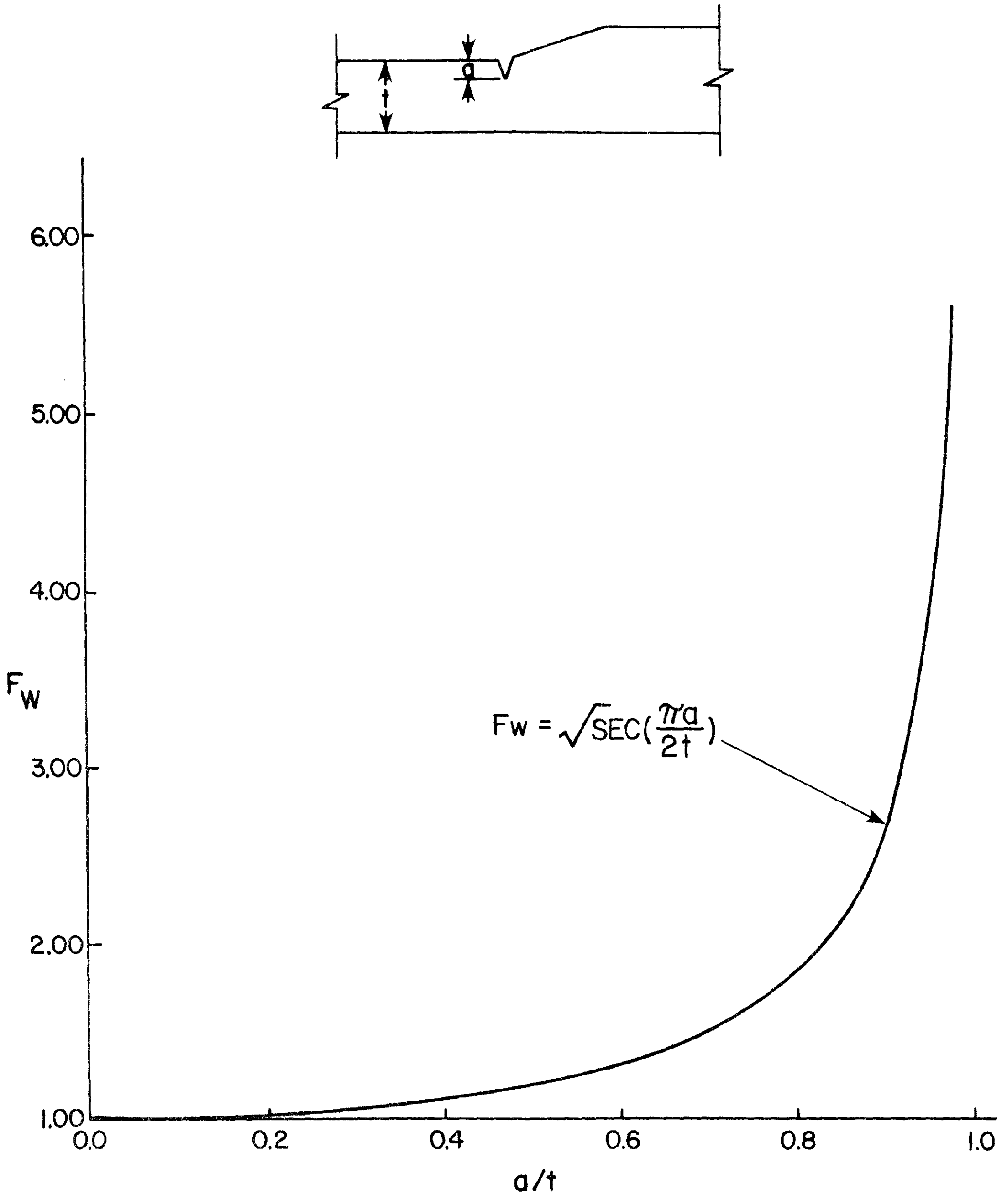

Fig. 2.9 Finite width correction

$$K_I = \frac{\sigma\sqrt{\pi a}}{E_K}\left(\sin^2 \beta + \frac{a^2}{c^2}\cos^2 \beta\right)^{1/4} \tag{11}$$

where the angle β describes the desired location anywhere on the crack border and E_K is the complete elliptical integral of the second kind given by

$$E_K = \int_0^{\pi/2} \left[1 - \left(\frac{c^2 - a^2}{c^2}\right)\sin^2 \theta\right]^{1/2} d\theta \tag{12}$$

As it has been defined before, c and a are the semimajor and the semiminor diameters, respectively. Solutions for the above integral can be found in many mathematical tables.

From Eq. (11), we conclude that our main concern will be for a value of β equal to $\pi/2$, where the stress intensity factor, K_I, will be greatest. Equation (11) for that particular location will be

$$K_I = \frac{\sigma\sqrt{\pi a}}{E_K} \tag{13}$$

where the elliptical shape correction, F_E, is defined from Eq. (13) as

$$F_E = \frac{1}{E_K} \tag{14}$$

with E_K defined by Eq. (12). The variation of F_E as a function of a/c is given in Fig. 2.10.

Abrupt changes in geometry cause severe local stress gradients which have a significant effect on the stress intensity factor. This effect is properly accounted for by the stress gradient correction F_G. The value F_G can be calculated using a

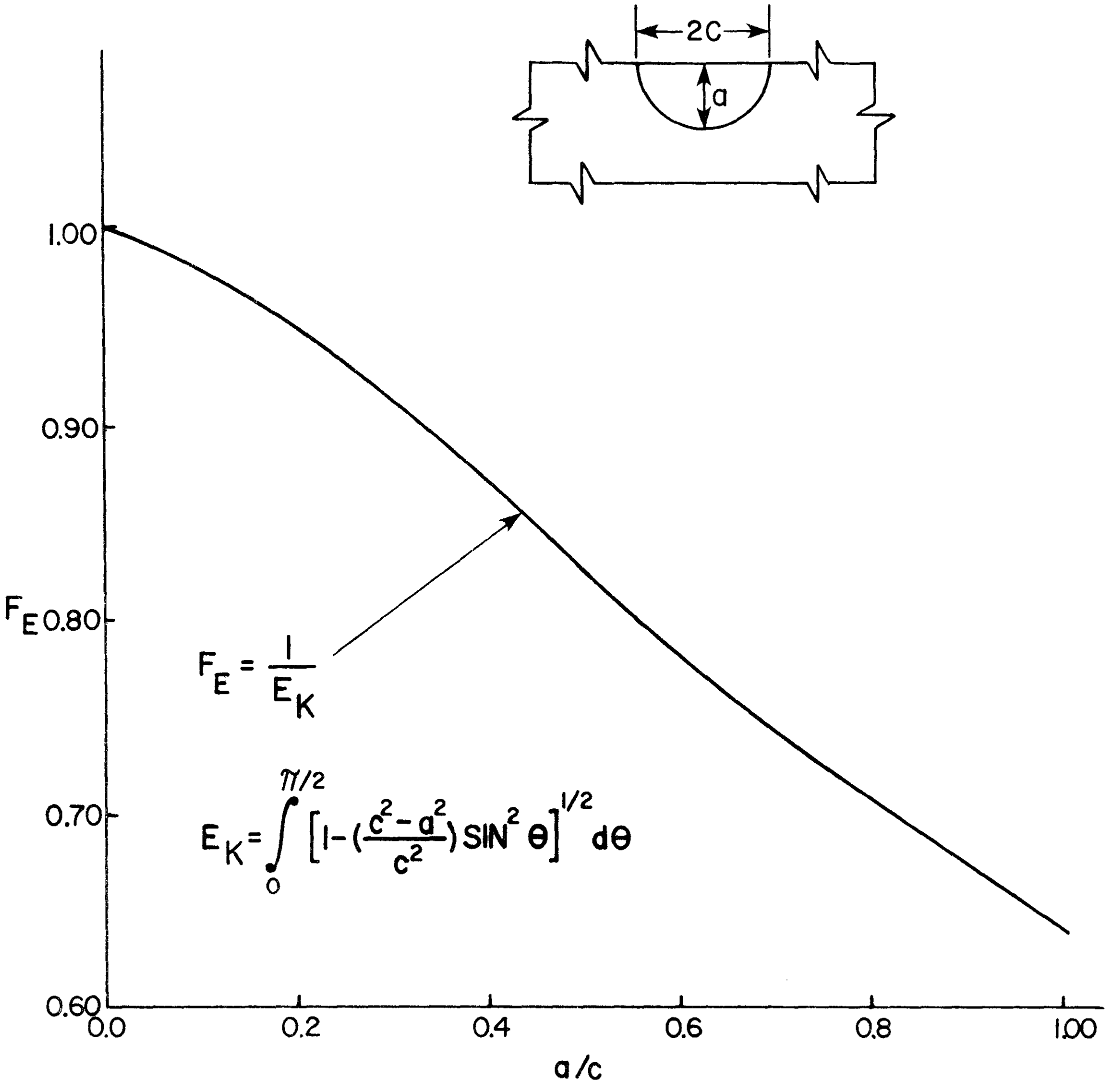

Fig. 2.10 Elliptical shape correction

procedure proposed by Albretcht, et al. [14]. This approach was used to determine the value of F_G for the flange thickness transition weldment. The stresses along the line where the crack shall be inserted are computed using a finite element program [19] and the stress gradient as derived in Ref. 14 from the closed form integral solution is

$$F_G = \frac{2}{\pi} \sum_{i=1}^{n} \frac{\sigma_{b_i}}{\sigma} \left(\text{arc sin } \frac{b_{i+1}}{a} - \text{arc sin } \frac{b_i}{a}\right) \qquad (15)$$

where σ_{b_i}/σ comes from the finite element solution, a is the crack length, and b_i and b_{i+1} are dimensions defined in Fig. 2.11. The approximation involved in using the summation in place of the closed form integral solution yields sufficient accuracy when the value of b is sufficiently small.

A typical model used in the finite element analysis of the flange thickness transition detail is presented in Fig. 2.12. The section of interest is the one at the beginning of the thickness transition where the stress gradient and the stress concentration factor, SCF, will be highest. This location is shown by the arrow in Fig. 2.12. The accuracy of the stress concentration factor at that point depends on the mesh size and also on the type of element used in the finite element model. The triangular element does not yield the same precision as the two quadrilateral ones that are connected at that node. The meshes used had values of element size, ℓ, over flange thickness, t, varying from 0.1250 to 0.0214 at the location shown by the arrow in Fig. 2.12. The quadrilateral elements at the neighborhood of the point of interest were subdivided using a built-in program feature. The node displacements from the coarse solution are used to interpolate imposed displacements at the finer mesh exterior boundaries of specified elements and the program gives automatically the solution for the finer mesh along with the

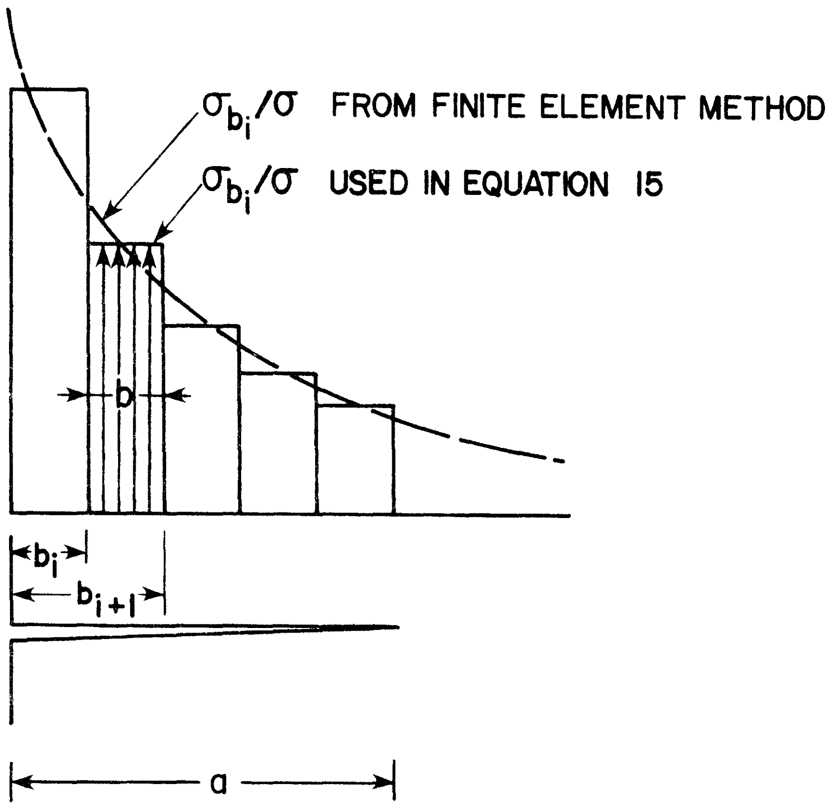

Fig. 2.11 Stress gradient distribution used in F_G calculation

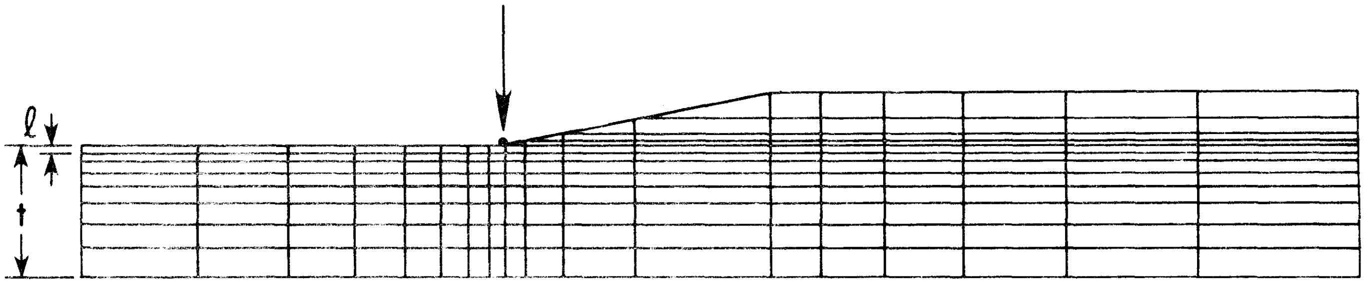

Fig. 2.12 Typical finite element model

coarse mesh solution. The elements at the neighborhood of the highest SCF had each dimension subdivided five times to give the desired resolution. A more detailed discussion of the finite element solution and F_G determination is given in Appendix A.

F_G was calculated from Eq. (15) for all the mesh size solutions in order to establish the convergence and the desired level of refinement. The SCF did not converge for the refined mesh sizes but the F_G decay did converge for acceptable values of crack size over plate thickness, a/t. The value of F_G is shown in Fig. 2.13 for various mesh sizes. The values of F_G for a/t equal to 0.01 for the two finer meshes were within 5 percent of each other. This level of accuracy was considered to be acceptable. The ℓ/t mesh size equal to 0.0043 was used to calculate the F_G function. A larger horizontal scale was used in the Fig. 2.13 detail to distinguish the rapid convergence of F_G for values of a/t of the order of 0.01 to 0.05. The dashed area represents the difference from the two finite element solutions which converge from a 5 percent difference to about 0 percent in the range of a/t from 0.01 to 0.05.

The calculated value of F_G is compared in Fig. 2.14 with similar solutions reported in the literature. For the full size beams reported in Ref. 5, the stress gradient correction was predicted using an empirical correlation derived primarily for attachment details and adapted to the flange thickness transition. An assumed value of r of 0.50 (see Fig. 2.14) is used in Ref. 5 to get a SCF equal to 2.15. When the reinforcement is removed, the grinding operation will not leave a sharp edge as it was modeled in the finite element solution, but that is the most critical situation and its solution an upper bound. The SCF from the finite element solution was equal to 2.24. The maximum value for the stress concentration factor from photoelastic analysis [20] for the same r used in Ref. 5 was found to be 2.10, which compares very well with

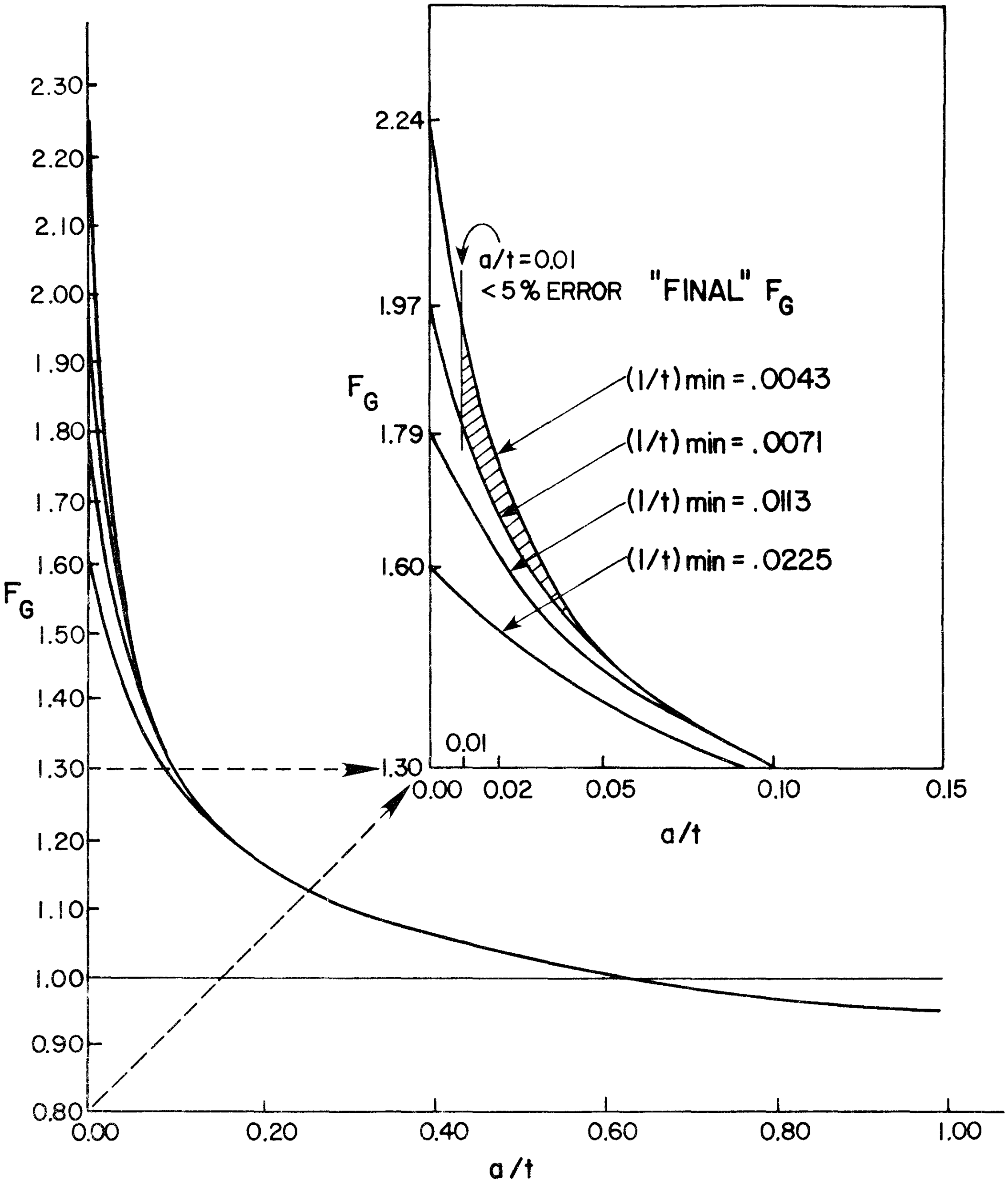

Fig. 2.13 Stress gradient correction decay - 1 to 2-1/2 slope

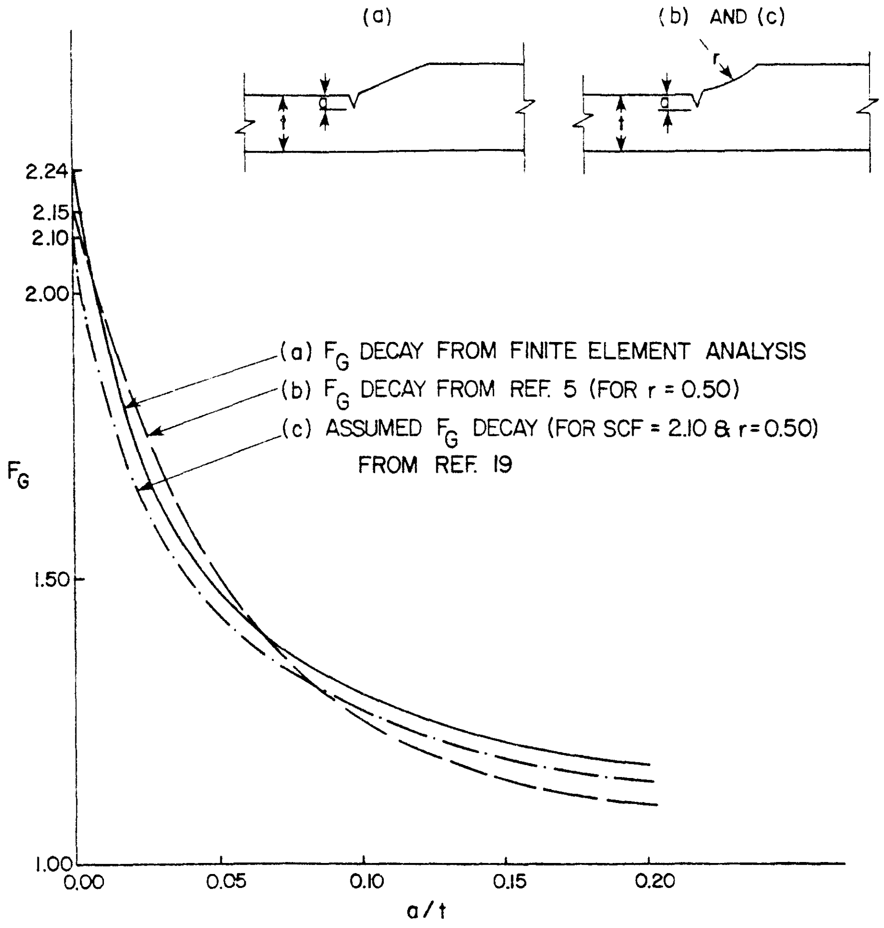

Fig. 2.14 Stress gradient correction solutions - 1 to 2-1/2 slope

the value of 2.15 reported in that study. The F_G decay for the SCF of 2.10 was assumed to follow the trend shown in Fig. 2.14 and it should give a lower bound estimate of the F_G decay.

The same procedure described above for the AASHTO 1 to 2-1/2 slope was used to provide a solution for the 1 to 5 transition slope in the bridge studied in this investigation. A value of F_G was also established for the 1 to 5 transition slope using the same 5 percent convergence tolerance. The solution is presented in Fig. 2.15. The convergence for the 1 to 5 transition slope is shown in Fig. 2.15 to be more rapid and it was only necessary to use two mesh refinements to reach the established convergence tolerance.

The plasticity near the crack tip has significance only for large a/t values, when the crack length approaches the plate thickness. For the region of interest, the stress field near the maximum K_I is of triaxial restrain, or plain strain, and the plastic zone should then be small. In the fatigue crack subjected to cyclic loading, the reversed plastic flow at the crack tip increases the effective yield stress and the value of the plastic zone correction is given by

$$F_P = \left[1 + \frac{1}{24}\left(\frac{\sigma}{\sigma_{ys}}\right)^2\right]^{1/2} \qquad (16)$$

As we can see, the value of F_P for fatigue crack growth will generally be small and can be disregarded.

For the semi-elliptical surface cracks, the total correction C, from the superposition of the various correction factors, is plotted as a function of the crack length to plate thickness ratio, a/t, in Figs. 2.16 and 2.17. Figure 2.16 shows the family of curves for the 1 to 2-1/2 slope for various semiminor diameter to semimajor diameter ratios, a/c, varying from zero to 1.0. The correction C for a/t tending to zero ranges from 1.43 to 2.51.

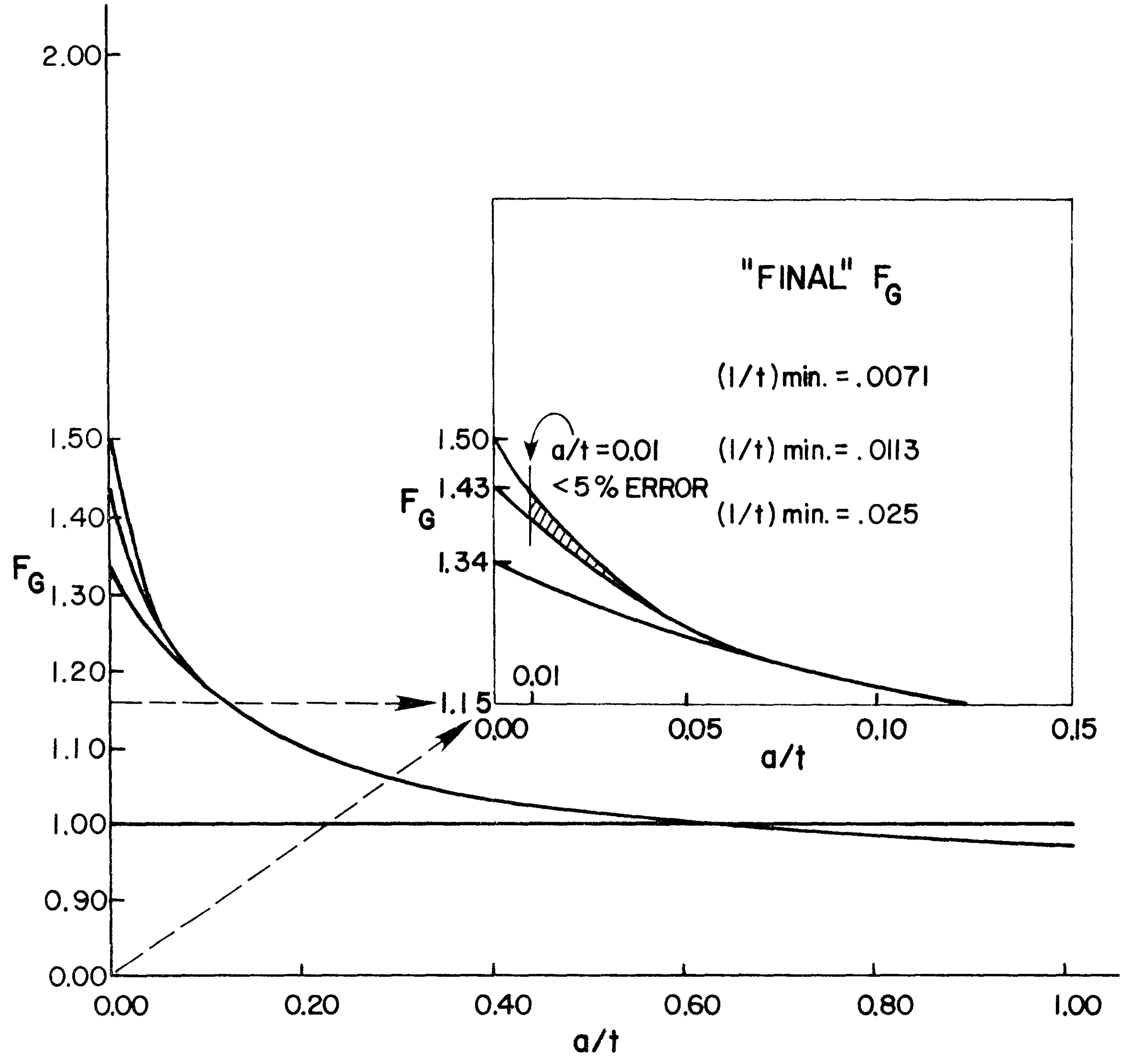

Fig. 2.15 Stress gradient correction decay - 1 to 5 slope

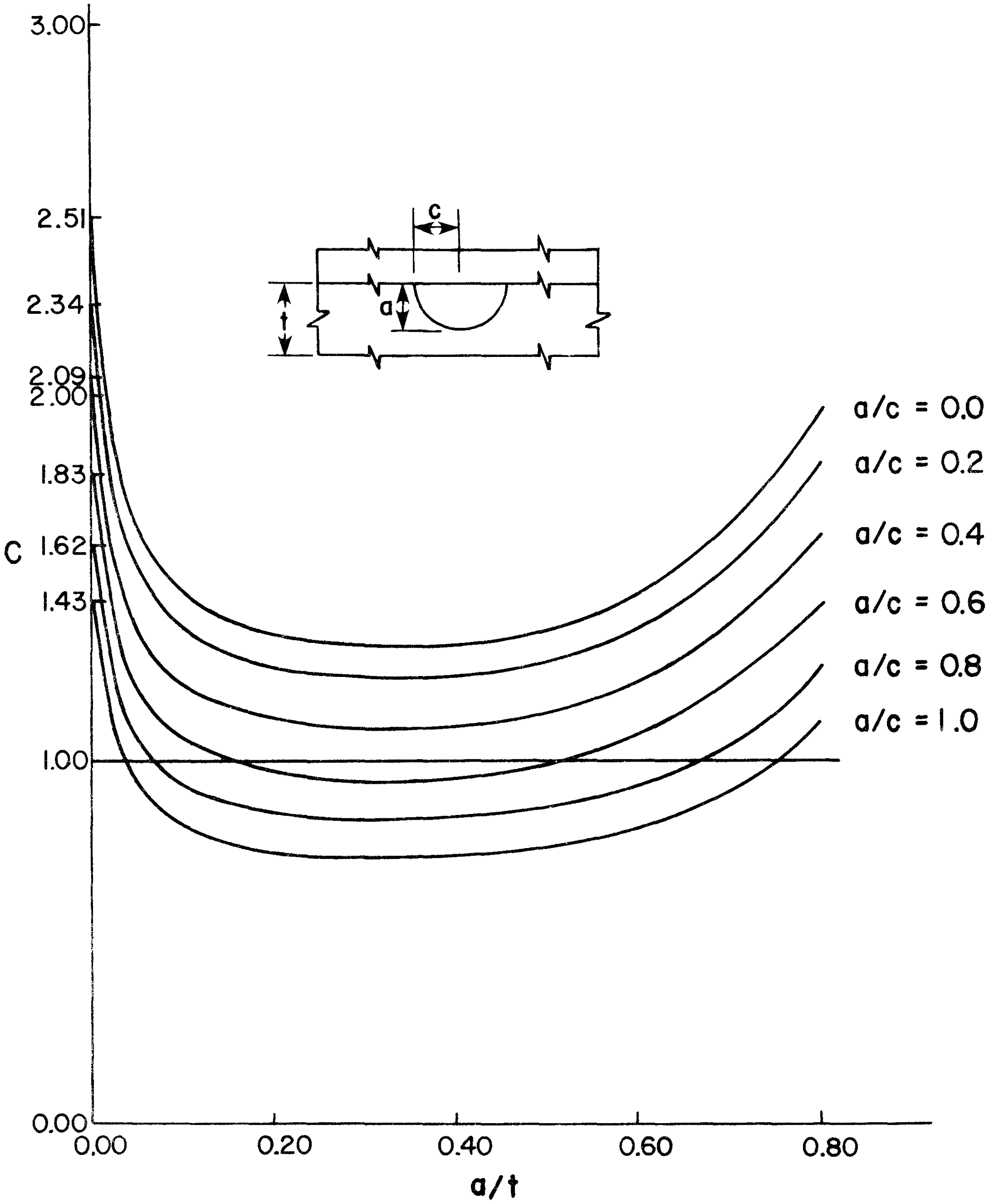

Fig. 2.16 Final correction factor, semi-elliptical crack - 1 to 2-1/2 slope

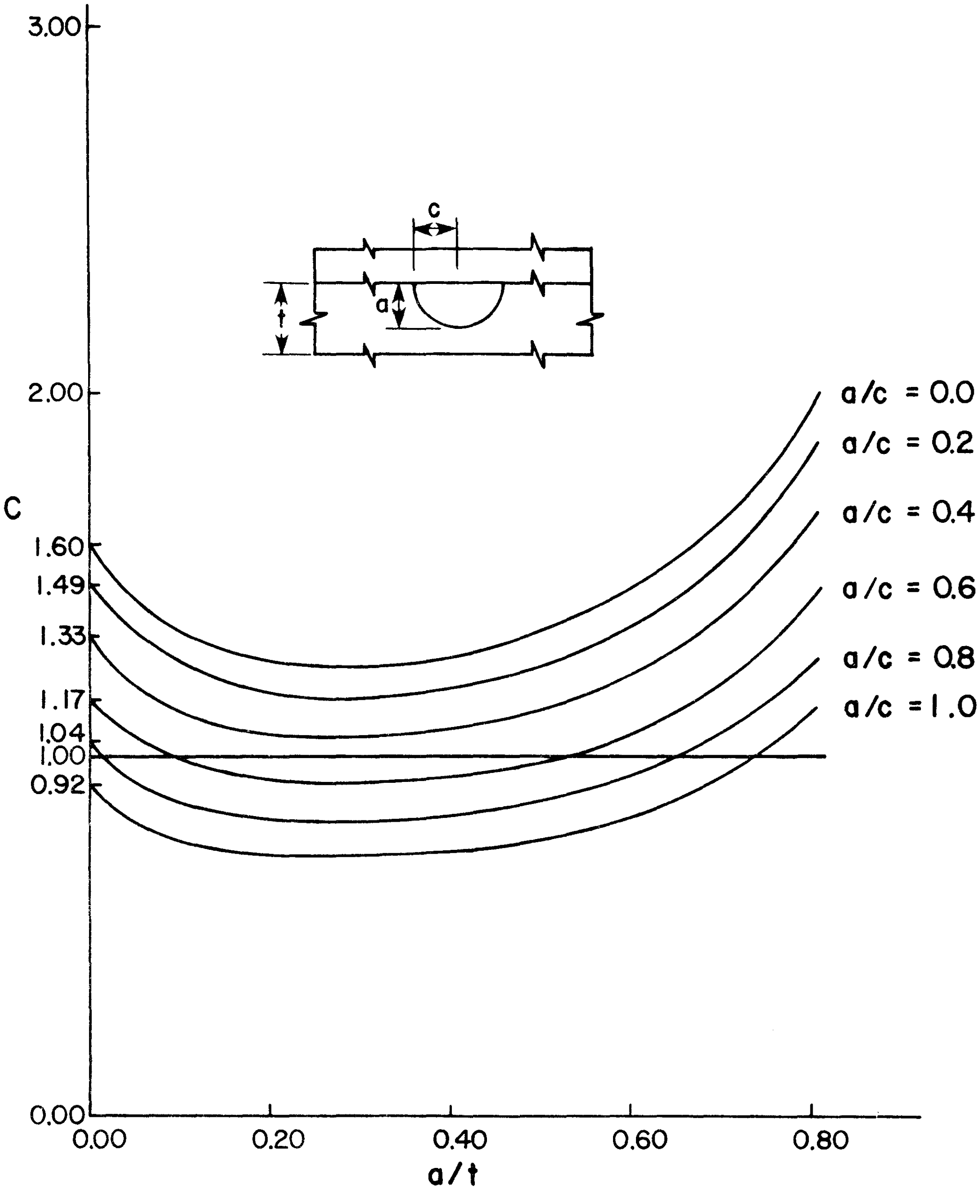

Fig. 2.17 Final correction factor, semi-elliptical crack - 1 to 5 slope

The a/c ratio from observed cracks is usually close to 0.6. For that a/c curve the C correction value is 1.83 for a/t equal to zero. It decreases rapidly to 1.07 for a/t equal to 0.1, and stays close to 1.0 for values of a/t up to 0.6 when the back surface correction makes C increase rapidly for higher values of a/t. Figure 2.17 shows a family of curves for the 1 to 5 transition slope. For a/t equal to zero, C ranges from 0.92 to 1.60, a considerable improvement compared to the 1 to 2-1/2 transition slope. For a/c equal to 0.6, the C correction is 1.17 for a/t equal to zero and decreases to 1.03 for a/t equal to 0.05. It stays close to 1.0 for most of the thickness and for a/t greater than 0.6 it starts to increase due to F_W. The values of the various correction factors as a function of a/c or a/t and the values of the total correction C are given in Tables 2.1, 2.2, 2.3, 2.4, and 2.5.

2.2.1.2 Semi-circular Corner Cracks. Cracks emanating from a 90° external corner of the flange usually result from notches during the grinding operation, but may be due to other surface weld defects. Exact closed form solutions for these cracks are not available, but the approximate solutions which will be used correlate very well with measured stress intensity factors [21].

The crack can be considered as a corner crack in a quarter infinite solid, as shown in Fig. 2.18. For this case, the finite width correction, F_W, becomes unity. The flaw can be considered as a surface flaw having two front free surfaces, one at θ equal to 0° and the other at θ equal to 90°. It is often observed that corner cracks have a semi-circular shape which gives a value of F_E equal to $2/\pi$ from Eqs. (12) and (14). The semi-circular shape of corner cracks was observed in the full size tests from Ref. 5 and and the corner cracks will be treated as semi-circular in this study.

TABLE 2.1 FRONT FREE SURFACE CORRECTION AND ELLIPTICAL CORRECTION

a/c	0.0	0.2	0.4	0.6	0.8	1.0
F_S	1.12	1.10	1.07	1.05	1.02	1.00
F_E	1.00	0.95	0.87	0.78	0.71	0.64

TABLE 2.2 FINITE WIDTH CORRECTION AND STRESS GRADIENT CORRECTION - 1 to 2-1/2 SLOPE

a/t	F_W	F_G
0	1.00	2.24
0.05	1.00	1.46
0.1	1.01	1.29
0.2	1.03	1.17
0.3	1.06	1.11
0.4	1.11	1.06
0.5	1.19	1.03
0.6	1.30	1.01
0.7	1.48	0.98
0.8	1.80	0.97

TABLE 2.3 SURFACE FLAW CORRECTION FACTOR C - 1 TO 2-1/2 SLOPE, SEMI-ELLIPTICAL CRACK

a/t \ a/c	0.0	0.2	0.4	0.6	0.8	1.0
0	2.51	2.34	2.09	1.83	1.12	1.43
0.05	1.64	1.53	1.36	1.20	1.06	0.93
0.1	1.46	1.36	1.21	1.07	0.94	0.83
0.2	1.35	1.26	1.12	0.99	0.87	0.77
0.3	1.32	1.23	1.10	0.96	0.85	0.75
0.4	1.32	1.23	1.10	0.96	0.85	0.75
0.5	1.37	1.28	1.14	1.00	0.89	0.78
0.6	1.47	1.37	1.22	1.08	0.95	0.84
0.7	1.62	1.52	1.35	1.19	1.05	0.93
0.8	1.96	1.82	1.63	1.43	1.26	1.12

TABLE 2.4 STRESS GRADIENT CORRECTION -
1 TO 5 SLOPE

a/t	F_G
0	1.43
0.05	1.26
0.1	1.19
0.2	1.10
0.3	1.07
0.4	1.04
0.5	1.02
0.6	1.01
0.7	1.00
0.8	0.99

TABLE 2.5 SURFACE FLAW CORRECTION FACTOR C - 1 TO 5 SLOPE, SEMI-ELLIPTICAL CRACK

a/t \ a/c	0.0	0.2	0.4	0.6	0.8	1.0
0	1.60	1.49	1.33	1.17	1.04	0.92
0.05	1.41	1.32	1.17	1.03	0.91	0.81
0.1	1.35	1.26	1.12	0.98	0.87	0.77
0.2	1.27	1.18	1.05	0.93	0.82	0.73
0.3	1.27	1.19	1.06	0.93	0.82	0.73
0.4	1.29	1.21	1.07	0.95	0.84	0.74
0.5	1.36	1.27	1.13	0.99	0.88	0.78
0.6	1.47	1.37	1.22	1.08	0.95	0.84
0.7	1.66	1.55	1.38	1.21	1.07	0.95
0.8	2.00	1.86	1.66	1.46	1.29	1.14

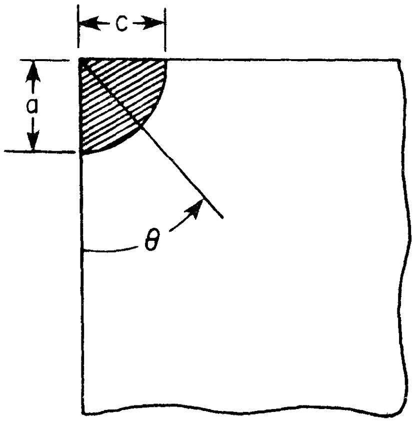

Fig. 2.18 Corner crack in a quarter infinite space (Ref. 21)

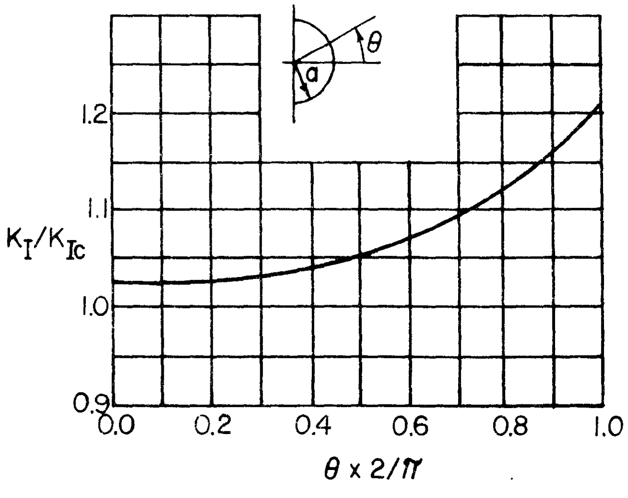

Fig. 2.19 Free surface solution for a semi-circular surface flaw (Ref. 16)

Adopting Smith, et al. [16] front free surface solution for a semi-circular surface flaw, we have $F_S(0°)$ equal to 1.03 and $F_S(90°)$ equal to 1.22. These are shown in Fig. 2.19. The stress gradient correction will be the same used for the surface semi-elliptical crack. The final expression for the stress intensity factor is

$$\Delta K_I = F_E \times F_S(0°) \times F_S(90°) \times F_G \, S_r \sqrt{\pi a} \tag{17}$$

where the values of F_E, $F_S(0°)$, and $F_S(90°)$ have been defined and the values of F_G can be obtained from Figs. 2.13 and 2.15. The semi-circular corner cracks correction C for 1 to 2-1/2 and 1 to 5 transition slopes is plotted in Figs. 2.20 and 2.21. The change in slope gives a change in the value of C from 1.79 for the 1 to 2-1/2 slope to 1.14 for the 1 to 5 slope for a/t equal to zero. It decreases rapidly for both slopes and is less than one for a/t from about 0.15 to 1.0.

If we consider a semi-circular crack embedded in an infinite solid, the exact solution given by Sneddon [22] is

$$K_I = \frac{2}{\pi} \sigma \sqrt{\pi a} \tag{18}$$

Cutting the circle twice and applying the front free surface correction of 1.12 for each cut, we get approximately the same values as Eq. (17) when we superimpose F_G.

2.2.1.3 Internal Penny-Shaped Cracks. The most common failures reported in Ref. 3 were caused by cracks originated from a flaw in the web-flange fillet weld. Those flaws were caused by entrapped gas in the weldment and they could be present in the butt weld splices as well as in the web-flange fillet welds. The gas pocket may have elliptical or wormhole shape, but the crack generated from those discontinuities will have almost no deviation

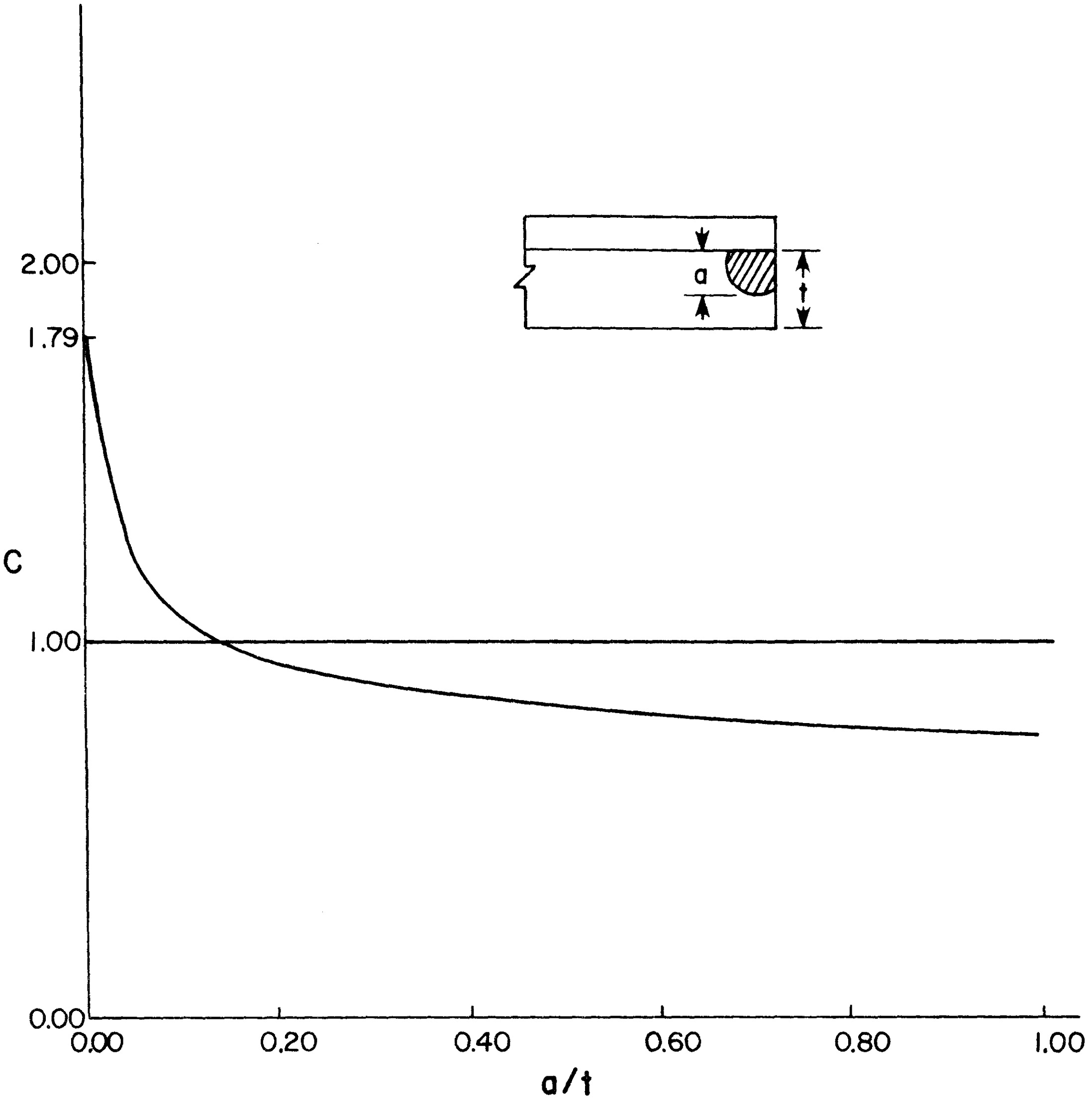

Fig. 2.20 Final correction factor, corner crack - 1 to 2-1/2 slope

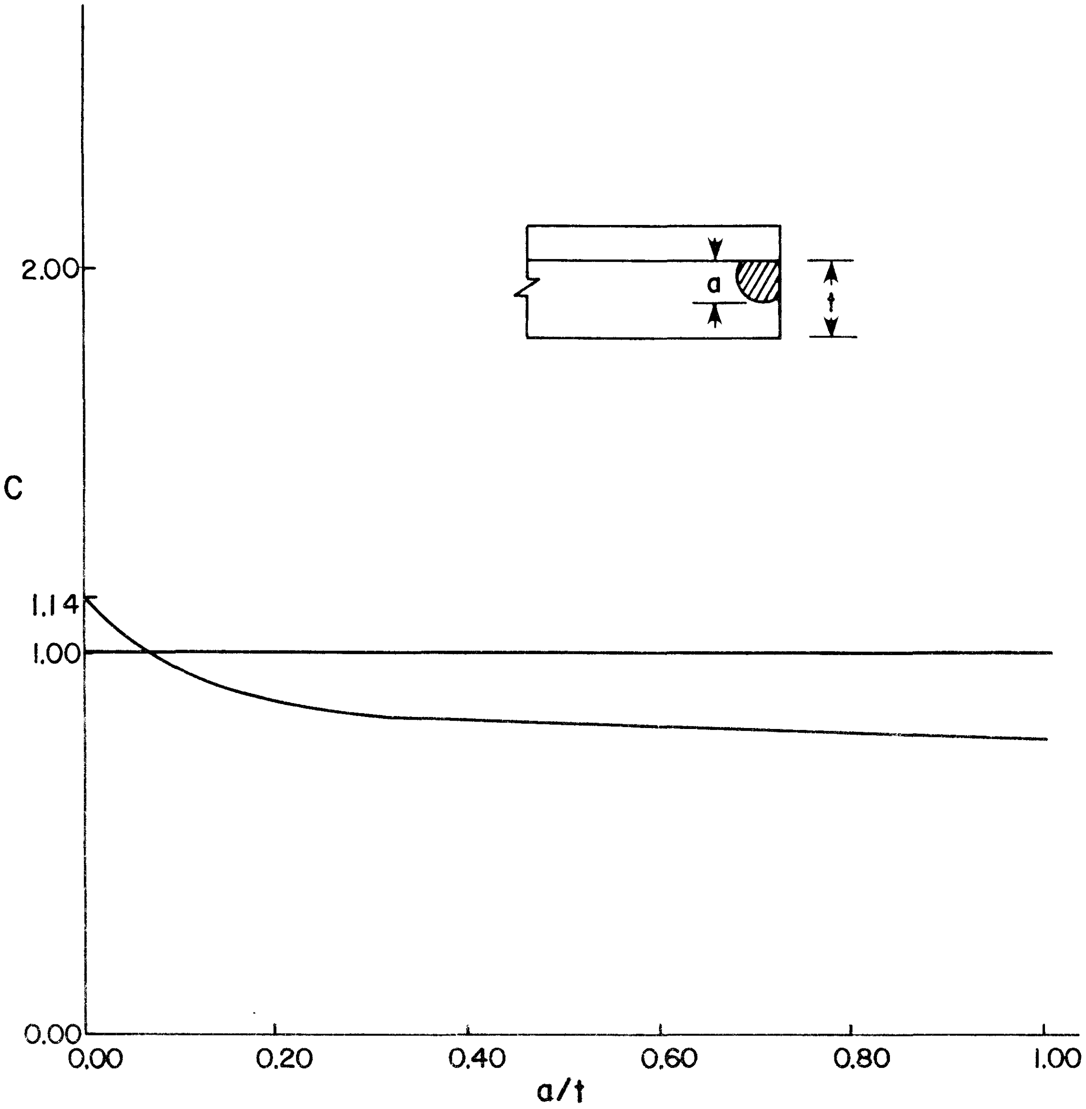

Fig. 2.21 Final correction factor, corner crack, 1 to 5 slope

from a circular shape. Two examples of such a crack are shown in Fig. 2.2 and a schematic view of crack growth stages for such a crack is presented in Fig. 2.22.

The analytical model used to compute the stress intensity factor for such a penny-shaped crack is based on the solution for a circular crack embedded in an infinite body. The actual penny-shaped crack seems not influenced by the free surfaces. The front free surface and the finite width correction become unity and the elliptical shape correction for a circular crack becomes $2/\pi$ as presented before from Eqs. (12) and (14).

In the regions likely to have internal defects, the stress gradient gives values lower than the nominal stress and the corresponding F_G correction can be disregarded. Stress gradients for the 1 to 2-1/2 and 1 to 5 transition slopes from the final finite element solution and used to calculate F_G for the surface cracks are plotted in Figs. 2.23 and 2.24. For internal defects over almost anywhere within the thickness of the plate, F_G calculated from the stress gradient would yield values less than one. For internal defects closer to the surface the F_G would be applicable but those defects would probably develop as surface cracks and will be treated as such.

For the penny-shaped internal crack, the solution for the stress intensity factor will be Eq. (18)

$$\Delta K_I = \frac{2}{\pi} S_r \sqrt{\pi a} \tag{18a}$$

where C is a constant and assume the value of $2/\pi$ and S_r replaces σ.

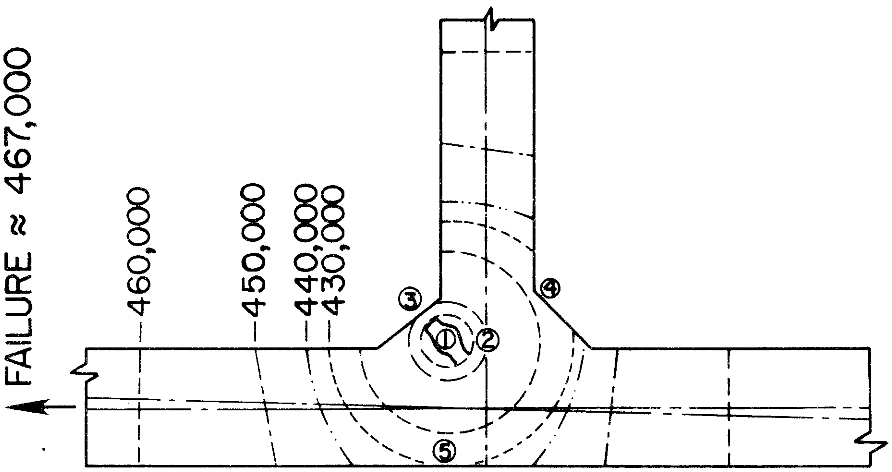

Fig. 2.22 Crack growth stages for a penny-shaped flaw (Ref. 23)

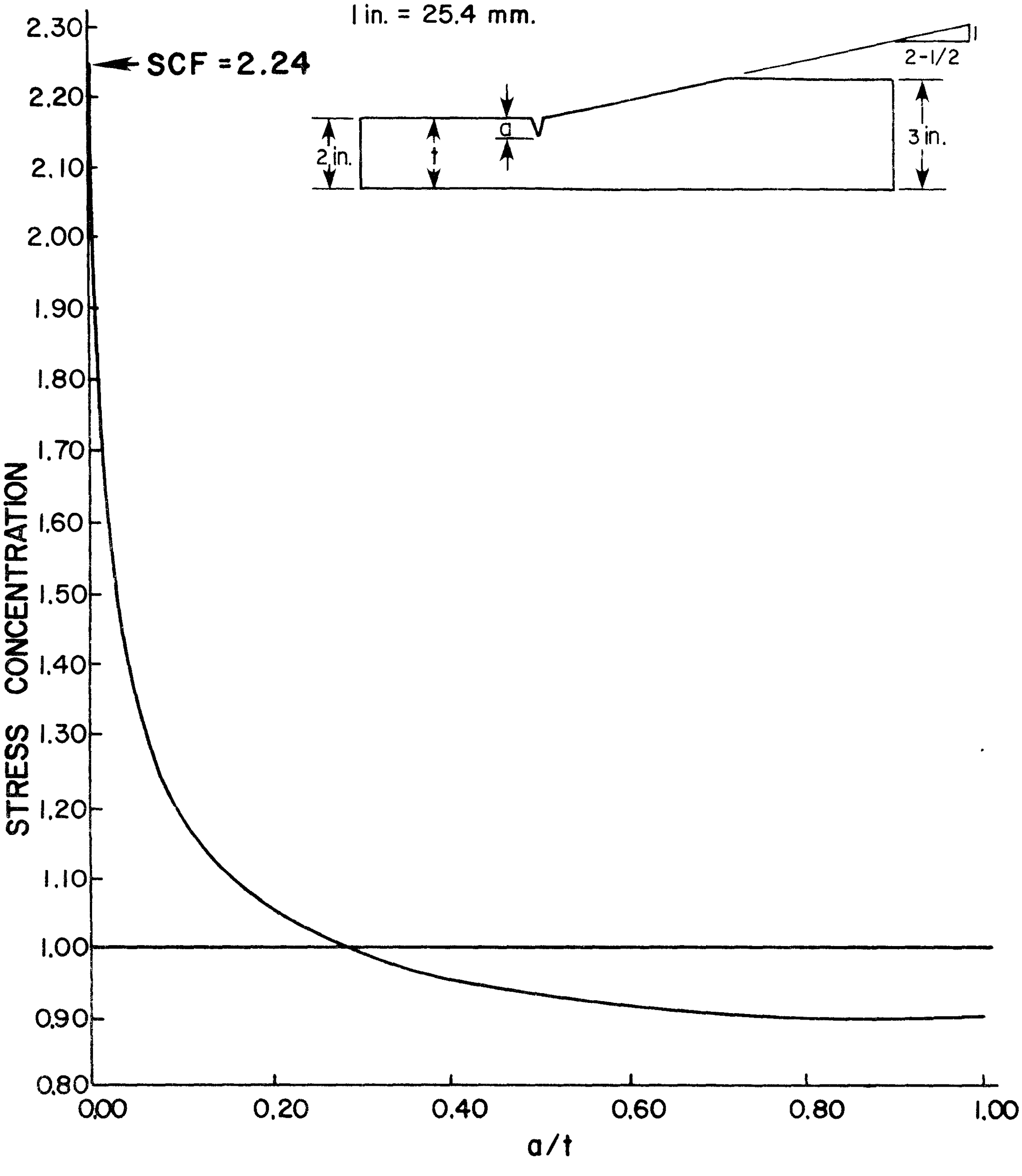

Fig. 2.23 Stress concentration decay - 1 to 2-1/2 slope $\ell_1/\ell_8 = 16$

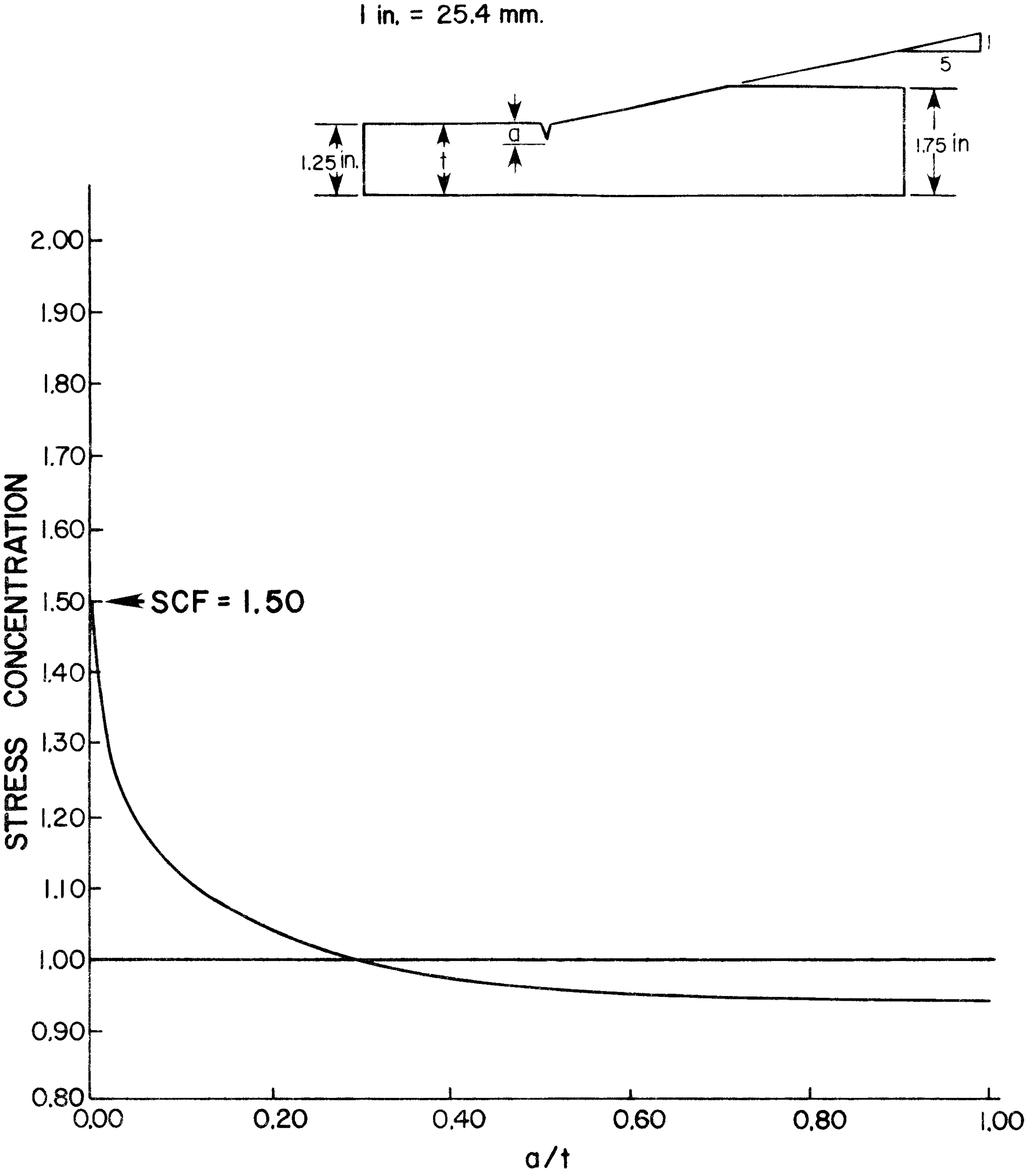

Fig. 2.24 Stress concentration decay - 1 to 5 slope $\ell_1/\ell_8 = 8$

CHAPTER 3

ESTIMATION OF STRESS RANGES

The stress range along with the initial flaw size and the material fracture toughness are the designer's first concern in the fatigue behavior of structures. The increase in fatigue life due to an increased material toughness has been shown not to be of major significance compared to proportional decreases in the initial flaw size or stress range. The initial flaw size is a parameter dependent upon fabrication procedures, workmanship, etc., and it is quantified through the level of reliability of the nondestructive inspection method used. The approach adopted in this study assumes the presence of the biggest flaw that can be missed by the inspection method being used. Hopefully, this will build in an extra conservatism in the estimation of the initial crack size. On the other hand, there is a much greater control by the designer in the analytical evaluation of the stress range for a specified moving load. Since most of the fatigue damage is caused by the heavier trucks, the sections should be checked against these heavier loads.

When the stress range is close to the allowable stress range for a certain category (Ref. 2, Tables 1.7.2A1 and 1.7.2A2), a better knowledge of the probable number of load cycles is required to establish the inspection interval. The importance of the stress range upon the allowable flaw sizes and inspection intervals will be shown in the next chapter.

3.1 Analytical Stress Range

The choice of the bridge to be investigated was based upon two primary factors. The first was related to a well-defined structural system, without curved members, nonaligned piers, or any other feature that could cause secondary effects on the bridge response. In that first phase of the investigation, the reliability of the data acquisition system was established. The special details were studied later. The second factor was to combine a well-defined structural system bridge with a short span bridge with a corresponding high live load to dead load ratio in order to yield significant fatigue stress.

Bridge unit 18S, of the interchange being studied, was selected for field testing. It is a five-span bridge with four lanes of traffic and two extra lanes for disabled vehicles. The two exterior end spans instrumented have span lengths of 70 ft (~ 21 m) and 100 ft (~ 30 m). The structural system of the bridge as well as for most of the IH 345 interchange bridges consists of a 10-1/2-in. (266.7-mm) thick post-tensioned slab supported on transverse steel beams usually spaced 20 ft (6.10 m) apart. The transverse steel beams are then supported on two plate girders forming a nonredundant load path to transmit the loads to the piers. The main girders rest on elastomeric pads on the interior supports and on hangers on the exterior ones. The girders do not have any direct contact with the post-tensioned slab and the transverse floor beams are designed noncompositely. Each side of the concrete deck supported by the floor beams overhangs the main girders approximately 15 ft (~ 5 m). A schematic of the structure is shown in Fig. 3.1 and the photos in Fig. 3.2 show the structural system.

Various truck lengths, axle spacings and axle loads were investigated to determine what type of loading would present the

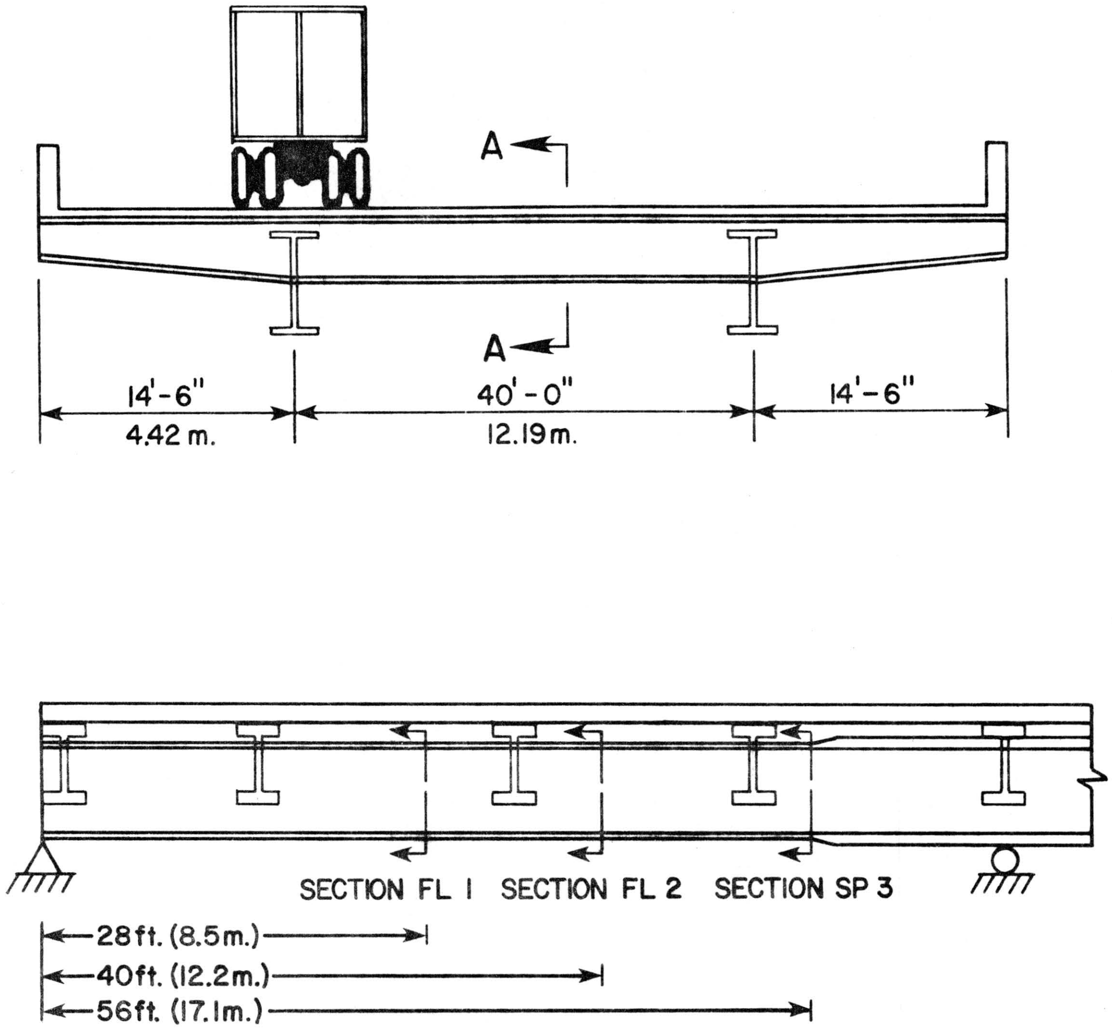

SECTION AA

Fig. 3.1 Structural system

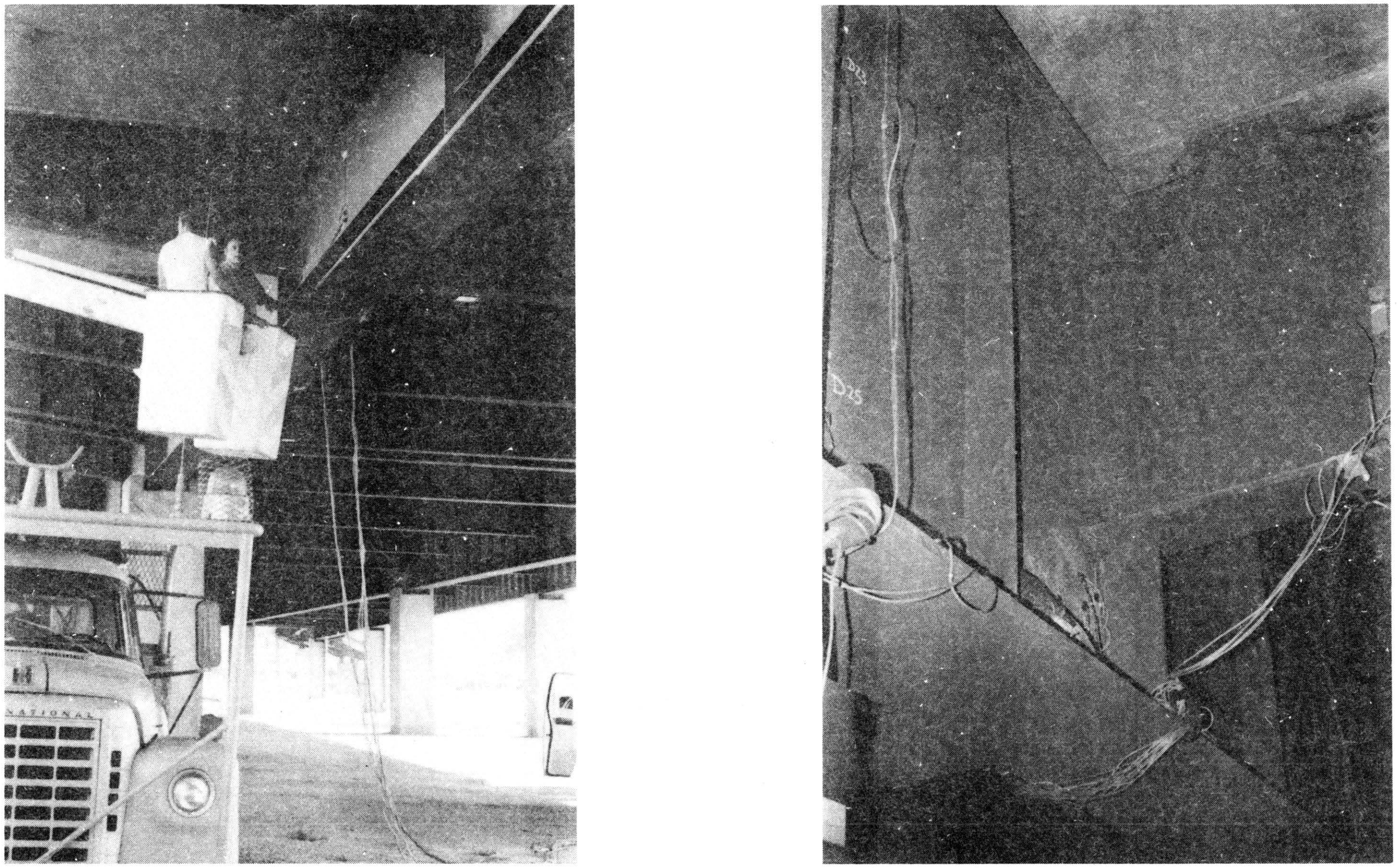

(a) Overall view

(b) Floor-beam-girder connection

Fig. 3.2 Unit 18S structural system

highest stress ranges. The results showed that the shorter distance between axles yielded higher stress ranges, as would be expected for the short span length of the bridge. The loading used in the actual field measurement and reproduced in the analytical study was a dump truck loaded with sand with a distance between axles of 15 ft, 7 in. (4.75 m). The total load of the truck was approximately 55 kips (244.6 MN), with 15 kips (66.7MN) on the front axle and 40 kips (177.9 MN) on the dual rear axles.

In order to calculate the stress envelopes for the longitudinal girder sections, the total load was placed on one single girder assuming no redistribution. The load was placed directly on the girder and not through the slab and floor beams. Based on the stress envelopes, two sections at 28 ft (8.5 m) and 40 ft (12.2 m) away from the end support of the last span, were chosen to be investigated. The sections FL1 and FL2 are shown schematically in Fig. 3.1 with the splice section, SP3, 56 ft (17.1 m) away from the exterior support. A more precise analytical determination of the stress influence lines for any section of the girder needs to consider the load positioned on the slab and not directly over the girder. If we cut a free body diagram at any section, the total moment will be the resultant from the moment in the girder and in the slab. When the load is applied close to the midspan of the slab between the floor beams, the slab moment generated may amount to as much as 20 percent of the total moment acting on the section.

The bridge girder-slab system was modeled using a frame analysis program where the load was applied at various slab locations. The transverse floor beams were modeled as pin-ended vertical members transmitting the load from the slab to the main girder. The computer program was used to solve for the girder and slab moments for successive load positions. A node was located at each of the sections of interest to give directly the moment values.

3.1.1 Member Properties. The welded girder is formed by two 24 in. × 1-1/4 in. (609.6 mm × 31.8 mm) flange plates welded to a 72 in. × 3/8 in. (1828.8 mm × 9.5 mm) web plate in the positive moment region. The flange thickness is increased to 1-3/4 in. (44.5 mm) and to 2 in. (50.8 mm) over the interior pier supports. The moment of inertia for the positive moment region was calculated to be 92,160 $in.^4$ (3.836×10^{10} mm^4). For the negative moment regions, the moments of inertia were 125,900 $in.^4$ (5.240×10^{10} mm^4) and 143,120 $in.^4$ (5.957×10^{10} mm^4), respectively, for the 1-3/4-in. (44.5-mm) flange section and for the 2-in. (50.8-mm) flange section. The girder dimensions and respective geometric properties are shown in Fig. 3.3. The longitudinal stiffeners used throughout all spans were not taken into account in the calculation of the geometric properties of the sections. The 10.5-in. (266.7-mm) slab was assumed to have an effective width in bending of 10 times its thickness, which provided a moment of inertia of 10,000 $in.^4$ (4.162×10^9 mm^4). When half of the bridge deck was considered to act as the slab's effective width, the moment of inertia increased 4 times, but the change in the girder moments was not significant. The smaller slab thickness was felt to be more realistic. The Young's modulus, E_c, was considered to be equal to 4,000 ksi (27,560 MPa).

3.1.2 Calculated Influence Lines. The influence line for section FL1 is plotted in Fig. 3.4 for the 55-kip (244.6 MN) dump truck. The truck front axle load was always placed facing the exterior hanger support, as sketched in Fig. 3.4. The largest positive stress occurs when the resultant of truck load was positioned at a distance of 30 ft (9.1 m) from the exterior hanger support, 2 ft (0.61 m) away from the section FL1. It has a value of 2.68 ksi (18.26 MPa). Placing the truck on the second span at a distance of 110 ft (37.5 m) from the exterior hanger support

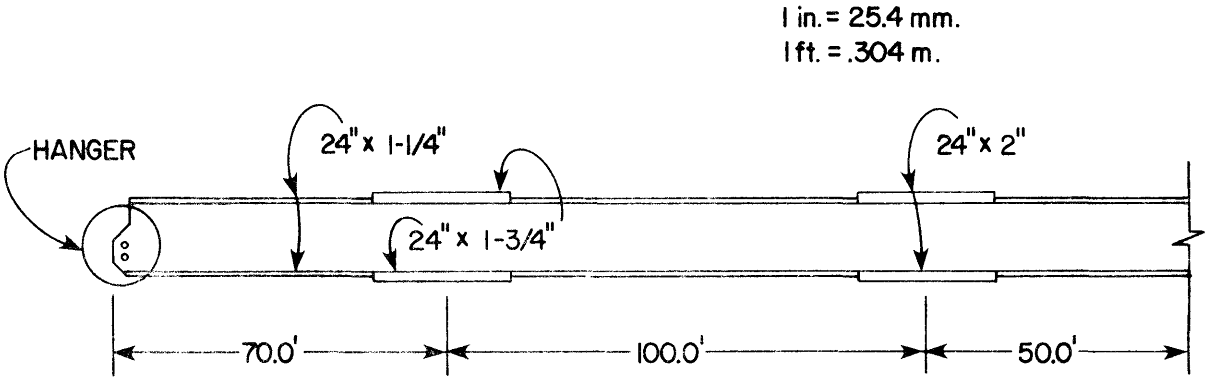

Fig. 3.3 Girder dimensions

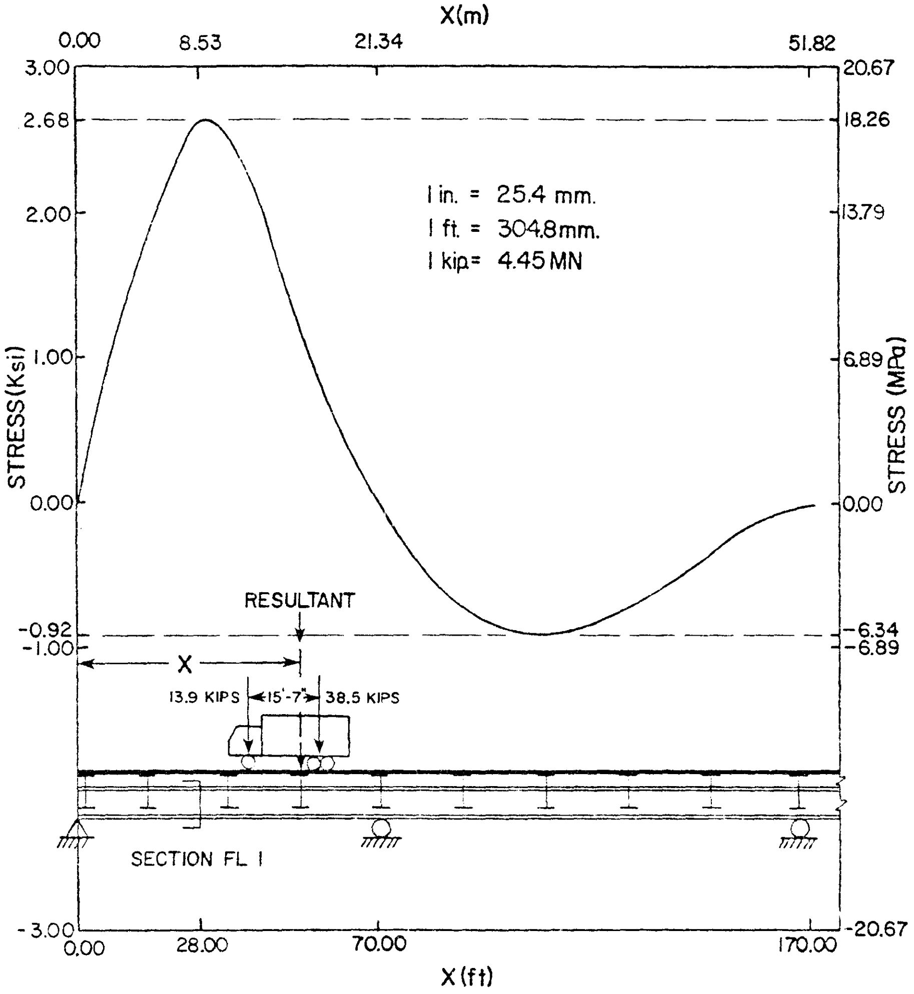

Fig. 3.4 Stress influence line for section FL1 - analytical solution

produces the largest negative stress of 0.92 ksi (6.34 MPa). The resulting maximum stress range is 3.60 ksi (24.60 MPa) for this section. Placing the load on the other spans farther from the section did not produce higher stresses. As our main interest is the maximum stress range, only the loading in the gaged end span and the adjacent span are relevant.

The bottom flange stress influence line for section FL2 is plotted in Fig. 3.5. For section FL2, the highest tension stress occurred for the resultant load placed at 35 ft (10.7 m) from the exterior hanger support, 5 ft (1.5 m) away from the section FL2; this stress was 2.41 ksi (16.60 MPa). The highest absolute compression stress was equal to 1.31 ksi (9.03 MPa) and occurred when the resultant load was 105 ft (32.0 m) from the left hanger support. The resulting stress range was equal to 3.72 ksi (25.63 MPa).

At the flange thickness transition, section SP3, the bottom stress influence line was calculated for the 1-1/4-in. (31.8-mm)-thick flange which yields the highest nominal stresses. The maximum absolute stress value for this section occurs when the resultant load is on the second span, 105 ft (32.0 m) from the left support. This bottom flange compression stress for this load location equals 1.84 ksi (12.68 MPa). The highest tension stress is equal to 1.19 ksi (8.20 MPa) when the load is 48 ft (16.4 m) from the left hanger support. The resulting stress range is 3.03 ksi (28.88 MPa). The bottom flange stress influence line for the section SP3 is plotted in Fig. 3.6 and all the stress values used for the sections under discussion can be found in Table 3.1.

3.2 Measured Stress Range

The field test data were recorded on a VIDAR high speed digital data acquisition system. The system is capable of scanning up to 40 channels of information at a frequency of 10,000 channels

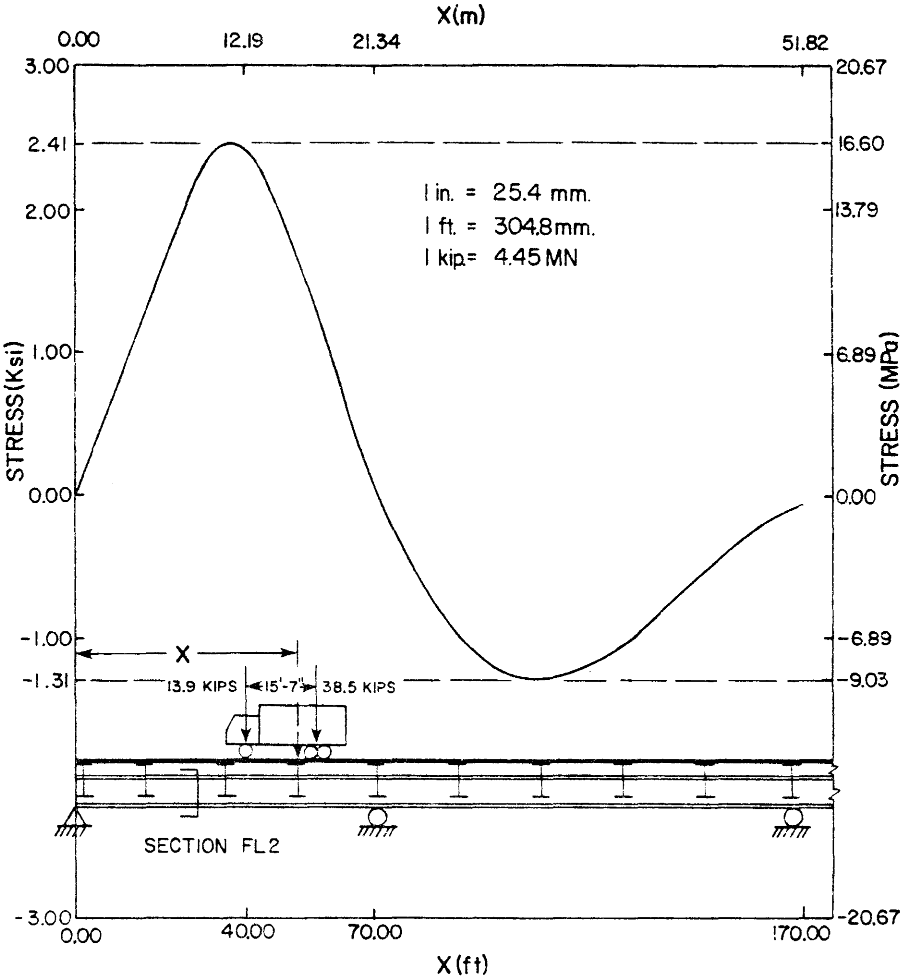

Fig. 3.5 Stress influence line for section FL2 - analytical solution

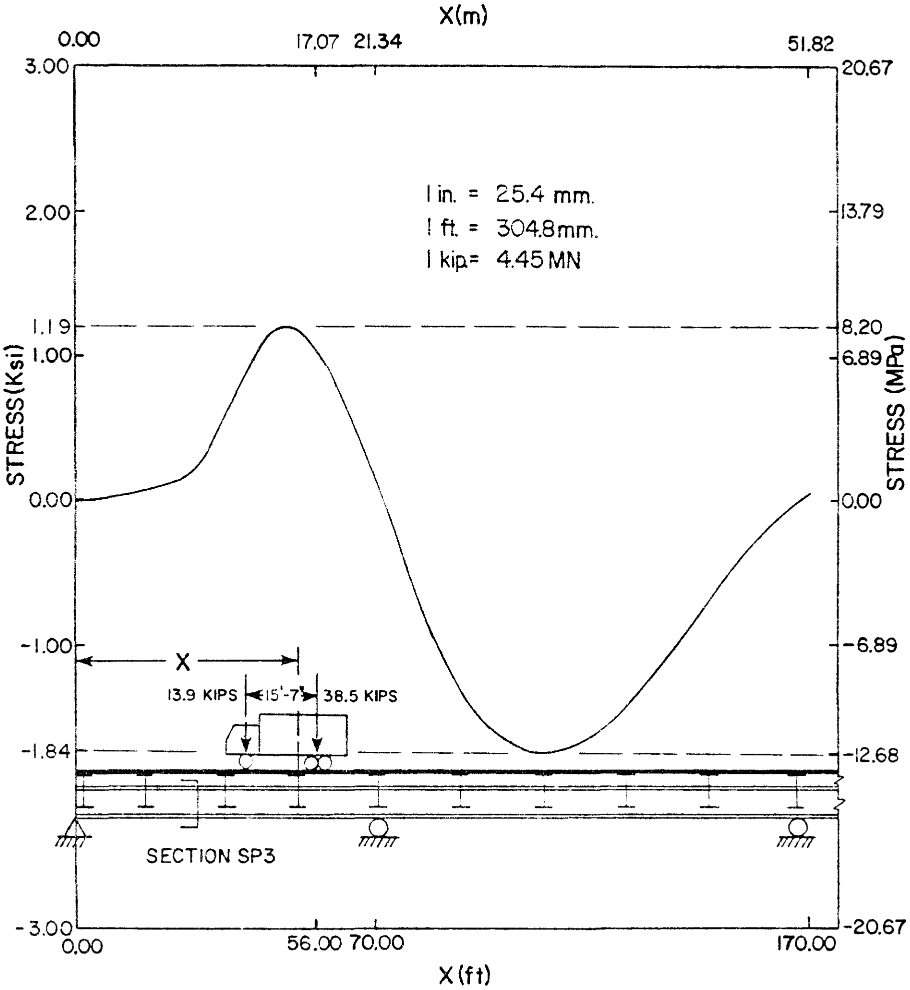

Fig. 3.6 Stress influence line for section SP3 - analytical solution

TABLE 3.1 STRESS INFLUENCE LINE FROM ANALYTICAL SOLUTION

x* (ft)	Stresses (ksi) Section FL1	 Section FL2	 Section SP3
6	0.93	0.47	0.02
12	1.45	0.84	0.02
17	1.97	1.28	0.04
21	2.38	1.74	0.08
27	2.63	2.12	0.18
30	2.68	2.29	0.29
35	2.57	2.41	0.56
40	2.27	2.36	0.86
45	1.87	2.15	1.10
48	1.60	1.95	1.19
53	1.18	1.56	1.16
58	0.78	1.11	0.95
63	0.44	0.65	0.61
66	0.26	0.39	0.36
71	-0.01	-0.01	-0.07
76	-0.25	-0.36	-0.51
81	-0.45	-0.65	-0.91
85	-0.60	-0.87	-1.21
90	-0.73	-1.05	-1.48
95	-0.83	-1.19	-1.66
100	-0.89	-1.27	-1.78
105	-0.92	-1.31	-1.84
110	-0.92	-1.31	-1.84
115	-0.89	-1.28	-1.79
120	-0.85	-1.21	-1.70
125	-0.79	-1.13	-1.59
130	-0.72	-1.02	-1.43
135	-0.63	-0.90	-1.26
140	-0.53	-0.76	-1.07
144	-0.44	-0.63	-0.89
149	-0.34	-0.49	-0.69
154	-0.25	-0.35	-0.49
159	-0.15	-0.22	-0.31
164	-0.07	-0.11	-0.15

*Distance from load CG to support as in Fig. 3.3.

1 ft = 0.3048 m
1 ksi = 6.89 MPa

per second, converting analog data into binary codes for recording on magnetic tape. The system is capable of operating in either of two modes. In Mode I a single scan of all channels is performed each time the system is started manually. In Mode II, the system scans all channels continuously. An electronic timing device is utilized to establish the time interval between scans. Computer programs were developed to reduce the recorded binary code to engineering units.

In a first stage of obtaining field data, the reliability of the system was checked using statics. The gage sections FL1 and FL2, and the girder reaction on the hanger supports allow this static check. Both girders had sections FL1 and FL2 monitored and also the respective hanger reactions. The sections FL1 and FL2 are defined in Figs. 3.4 and 3.5 and in Fig. 3.7 the girder sections and hanger are also shown. A dump truck with 14.24 kips (63.34 MN) front axle load and 40.38 kips (179.61 MN) rear axle load was positioned at 3 locations, 147 ft (44.8 m), 39 ft (11.9 m), and 29 ft (8.8 m), respectively, from the hanger support. The system was operated in Mode I and five different readings were taken for the truck in each of the above locations. The bridge had two lanes blocked, as shown in Fig. 3.8a, and the load truck was placed directly over the girder. The traffic was opened on the two opposite lanes over the "unloaded" girder but the static readings were taken only when light vehicles were crossing the bridge or when these lanes were clear of vehicles. Due to the vibration of the bridge, the static tests were reproducible only within a range. The dynamic tests with a single truck moving over one girder gave more complete and reliable information and the test results are presented in the next sections.

3.2.1 <u>5 MPH Dynamic Test</u>. The first dynamic test was performed with the truck going from North to South at a speed of

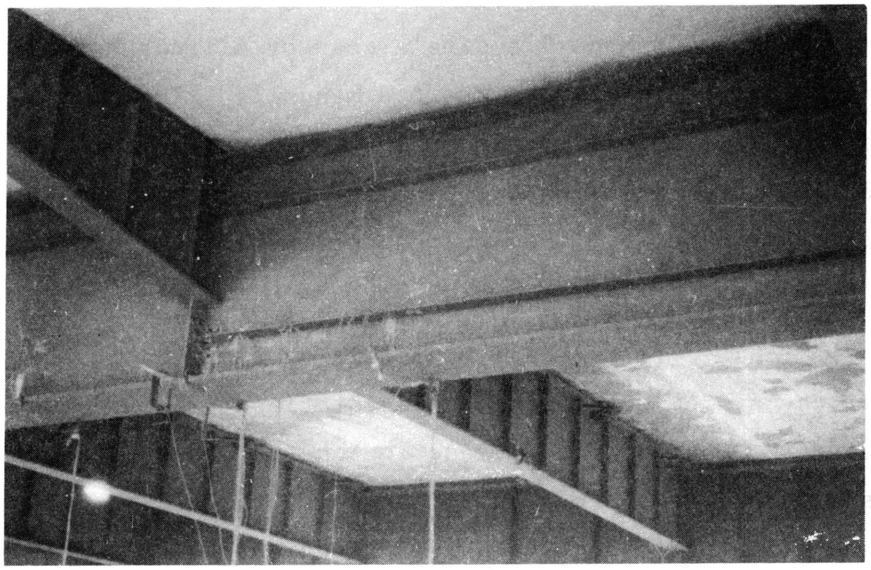

(a) Girder gage location

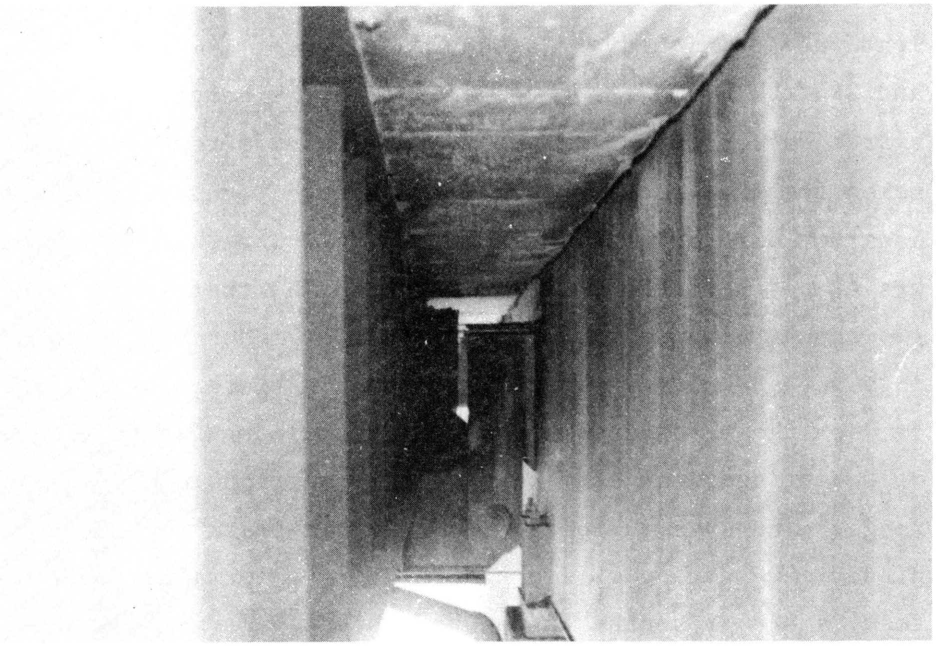

(b) Hanger support

Fig. 3.7 Monitored girder locations

(a) Two lanes blocked for testing

(b) Dump truck

Fig. 3.8 Typical test and load truck

5 mph (8 Km/h). The North to South direction is the same direction used to plot the influence lines of Figs. 3.4, 3.5, and 3.6. A bottom flange gage at section FL1 showed the stress response presented in Fig. 3.9. The maximum measured tensile stress amounts to 1.66 ksi (11.44 MPa) compared to the calculated 2.68 ksi (18.26 MPa), and the maximum measured compression stress is 0.80 ksi (5.51 MPa) compared to the calculated 0.92 ksi (6.34 MPa). It should be noticed that the calculated stresses assumed the total truck load was carried by one girder. In Fig. 3.9 the measured stresses from a smooth curve connecting the midpoint of the vibration wave is defined as static stress range and the maximum vibration stress range is also defined. A sketch of the bridge girder is also shown, with the measured influence line. In Fig. 3.10 the same gage section of the unloaded girder shows a higher amplitude vibration due to the presence of normal speed light vehicle traffic on the two open lanes. When the plots from Figs. 3.9 and 3.10 are superimposed, the general trend of the influence line pattern is apparent on the unloaded girder. When the truck is on the 100-ft (30.5-m) span, the maximum static compression stress on the loaded girder is approximately 0.60 ksi (3.79 MPa), 65 percent of the calculated 0.92 ksi (6.34 MPa) with no redistribution. The remaining 35 percent is carried by the unloaded girder and that is the trend shown in Fig. 3.10.

Figure 3.11 shows the stress response for the bottom flange gage at the section FL2. The maximum stresses are 2.28 ksi (15.67 MPa) tension and 1.10 ksi (7.58 MPa) compression, compared to the calculated 2.41 ksi (16.60 MPa) and 1.31 ksi (9.03 MPa), respectively. The measured static stress range was equal to 3.13 ksi (21.57 MPa) corresponding to 84 percent of the calculated stress range. The unloaded girder stress at the same section FL2 in Fig. 3.12 also shows the same influence line trend with again a higher amplitude vibration due to the light vehicles in the open

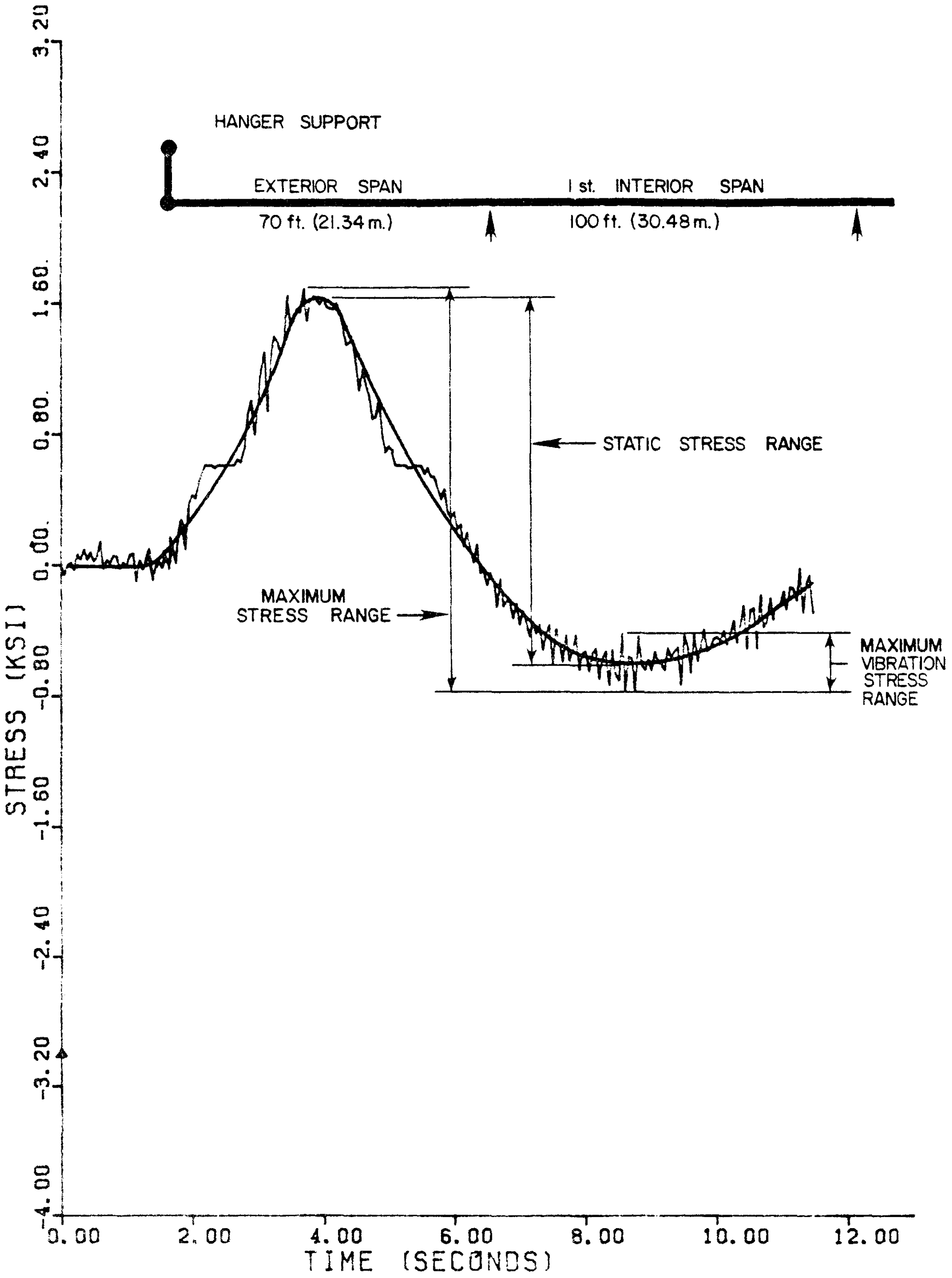

Fig. 3.9 Gauge FL1A period = .05HZ 5 MPH S-N

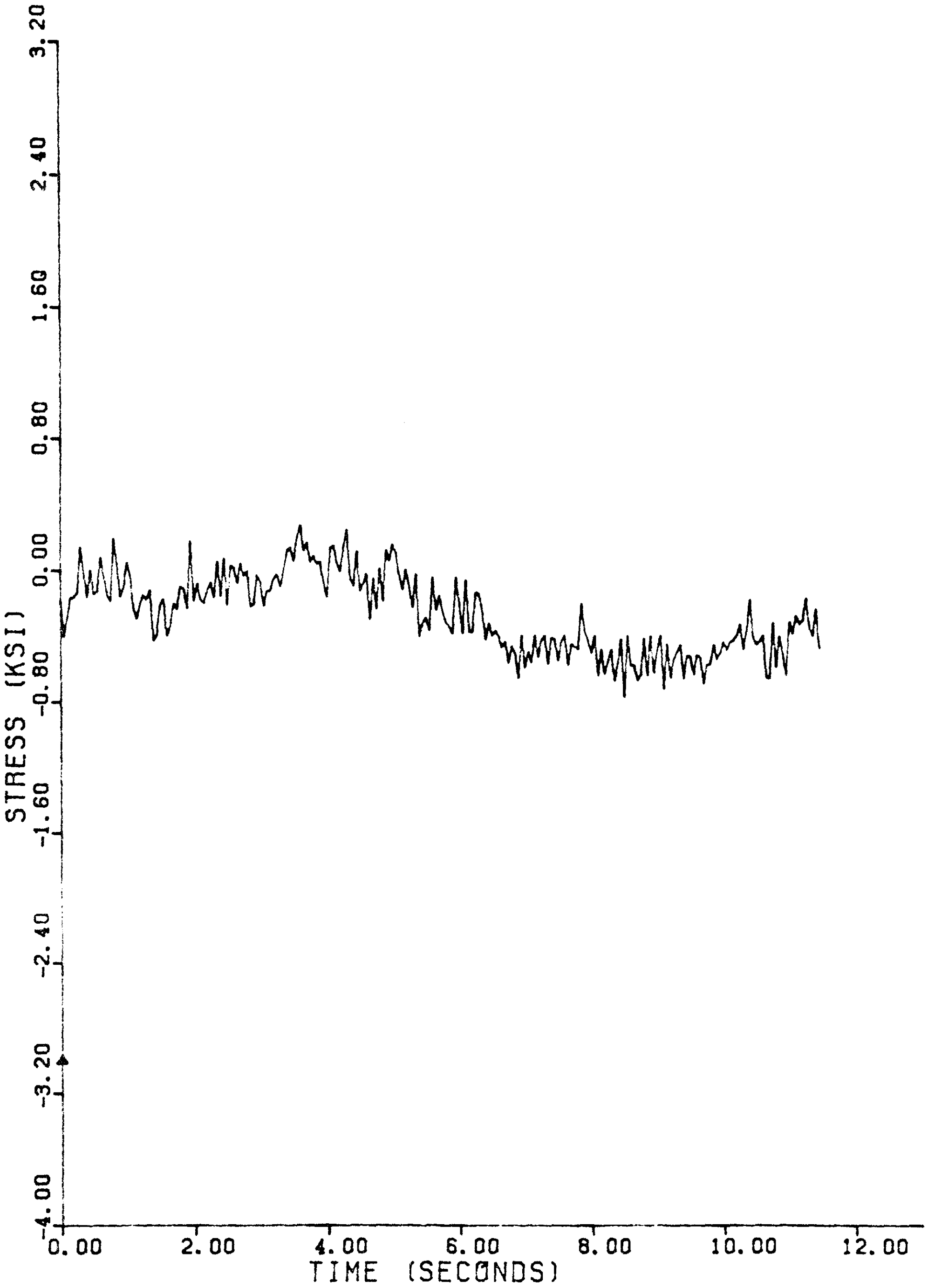

Fig. 3.10 FL1 unloaded girder P = .05HZ 5 MPH S-N

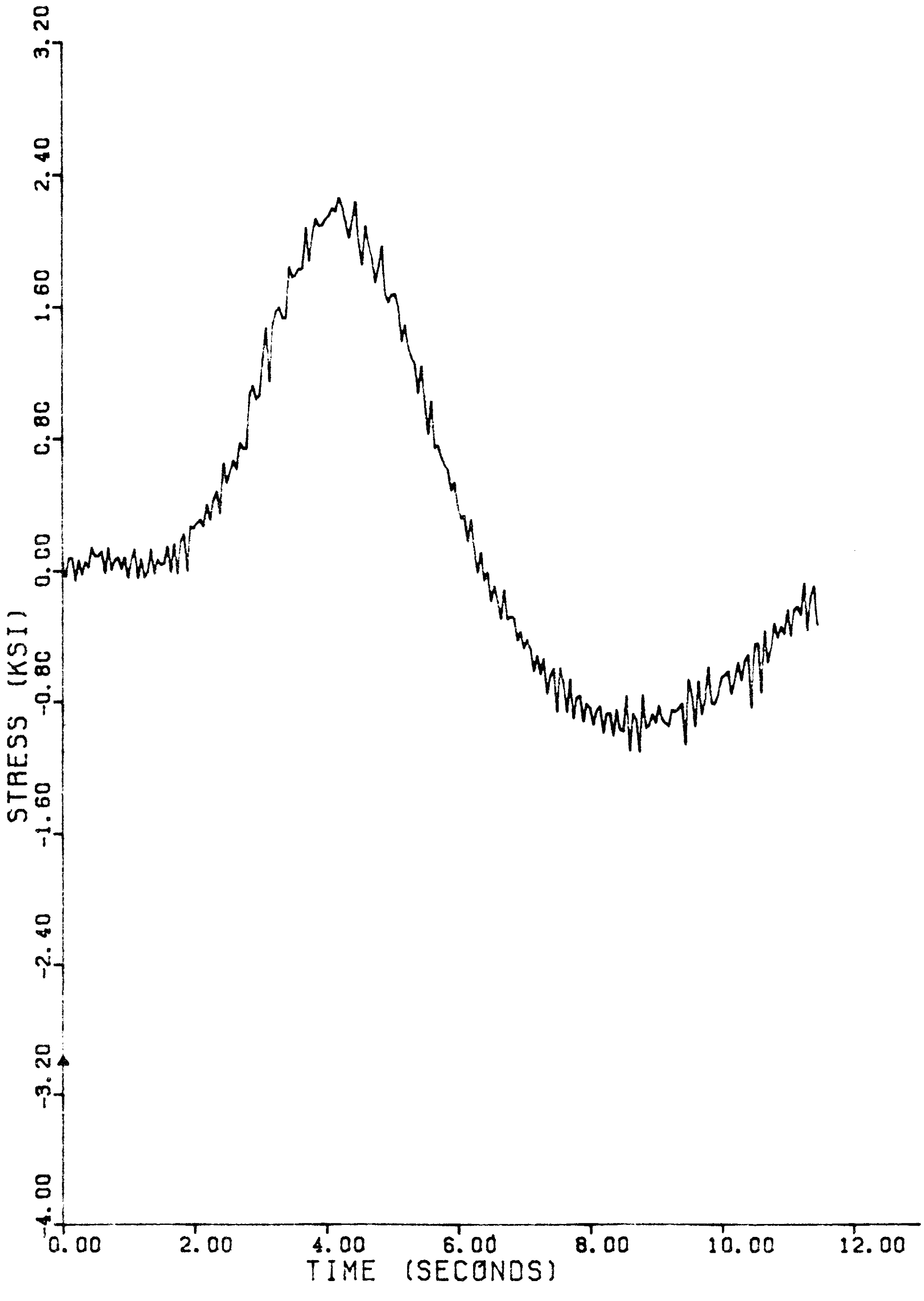

Fig. 3.11 Gauge FL2A period = .05HZ 5 MPH S-N

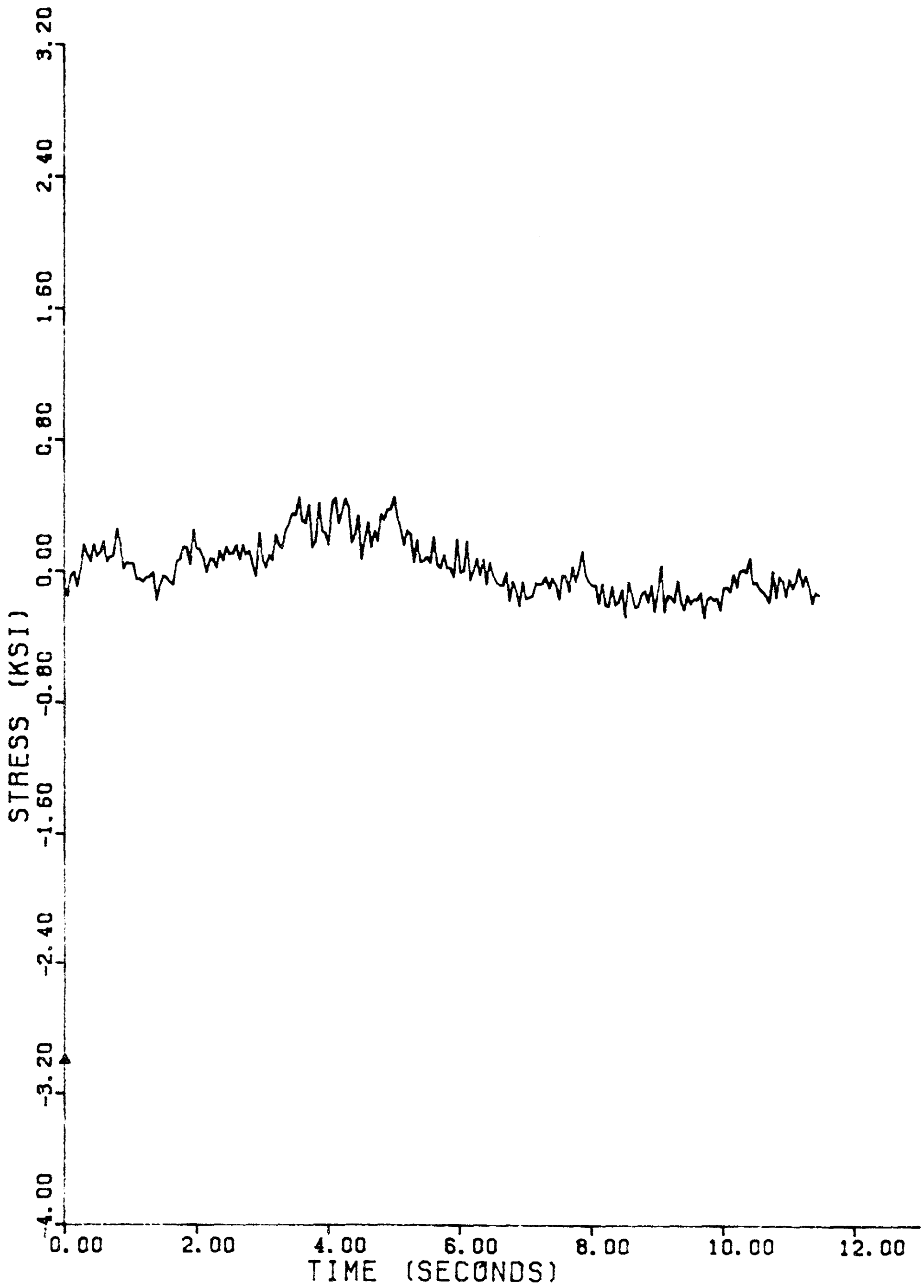

Fig. 3.12 FL2 unloaded girder P = .05HZ 5 MPH S-N

lanes traffic. At this section, however, the percentage of the load shared by the unloaded girder is the remaining 16 percent compared to the remaining 35 percent shared by the unloaded girder at section FL1. When the plots in Figs. 3.11 and 3.12 at section FL2 are superimposed and compared to the superimposed measured stresses at Section FL1, the respective percentages in each section give excellent agreement and they establish the reliability of the data acquisition system used. At sections FL1 and FL2 there were strain gages on both sides of each flange to monitor out-of-plane movement and the neutral axis location. In Fig. 3.13 the stresses on the bottom flange at the B locations, across the web from gage FL2A shown in Fig. 3.10,are within 10 percent of the measured FL2A stresses. This is within the limits of accuracy of the measurements and indicates no significant out-of-plane bending. The neutral axis location is determined by looking at the stress response from two opposite flange gages, as in Fig. 3.14. For the load on the gage location span, the maximum stresses differ by 22 percent, indicating the neutral axis is close to the middepth of the section. A higher vibration was recorded on the top flange gage when the load was over the 100-ft (30.5-m) span; however, that behavior was not reproduced on the other speed tests.

3.2.2 35 MPH Dynamic Test. The 35 MPH (56 Km/h) speed test was performed with the truck moving from North to South, the normal traffic direction, opposite to the direction used in Figs. 3.4, 3.5, and 3.6, the influence line plots. In Fig. 3.15, the bottom flange stress response at section FL1 is presented. The influence line is now opposite to the calculated influence line shown in Fig. 3.4. A schematic of the bridge is also shown in Fig. 3.15 for the 35 MPH measured stresses. The load is over the monitored section span just before it leaves the bridge at about the 13.20 sec mark in Fig. 3.15. The maximum stresses are

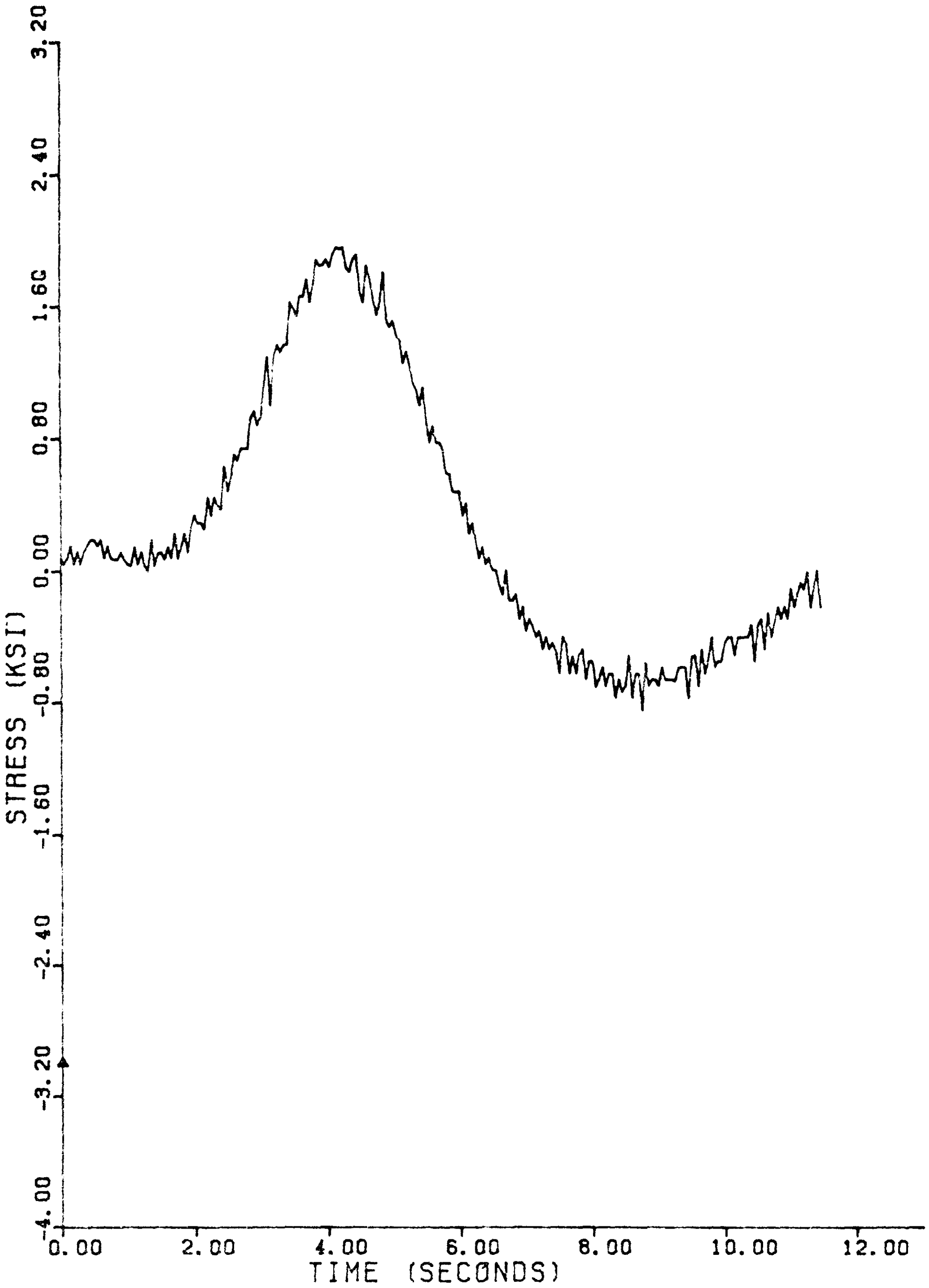

Fig. 3.13 Gauge FL2B period = .05HZ 5 MPH S-N

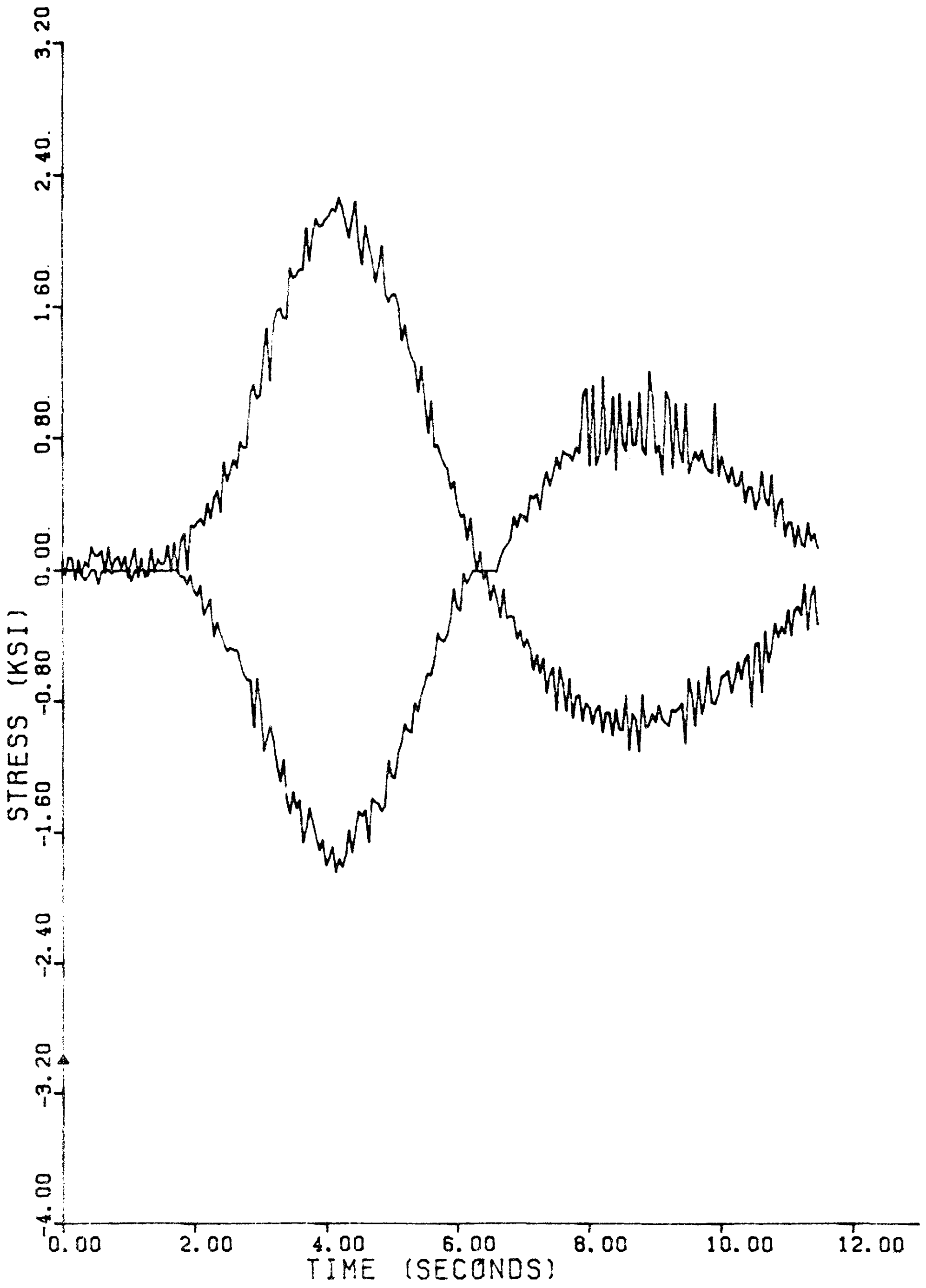

Fig. 3.14 FL2A flange gauges P = .05HZ 5 MPH S-N

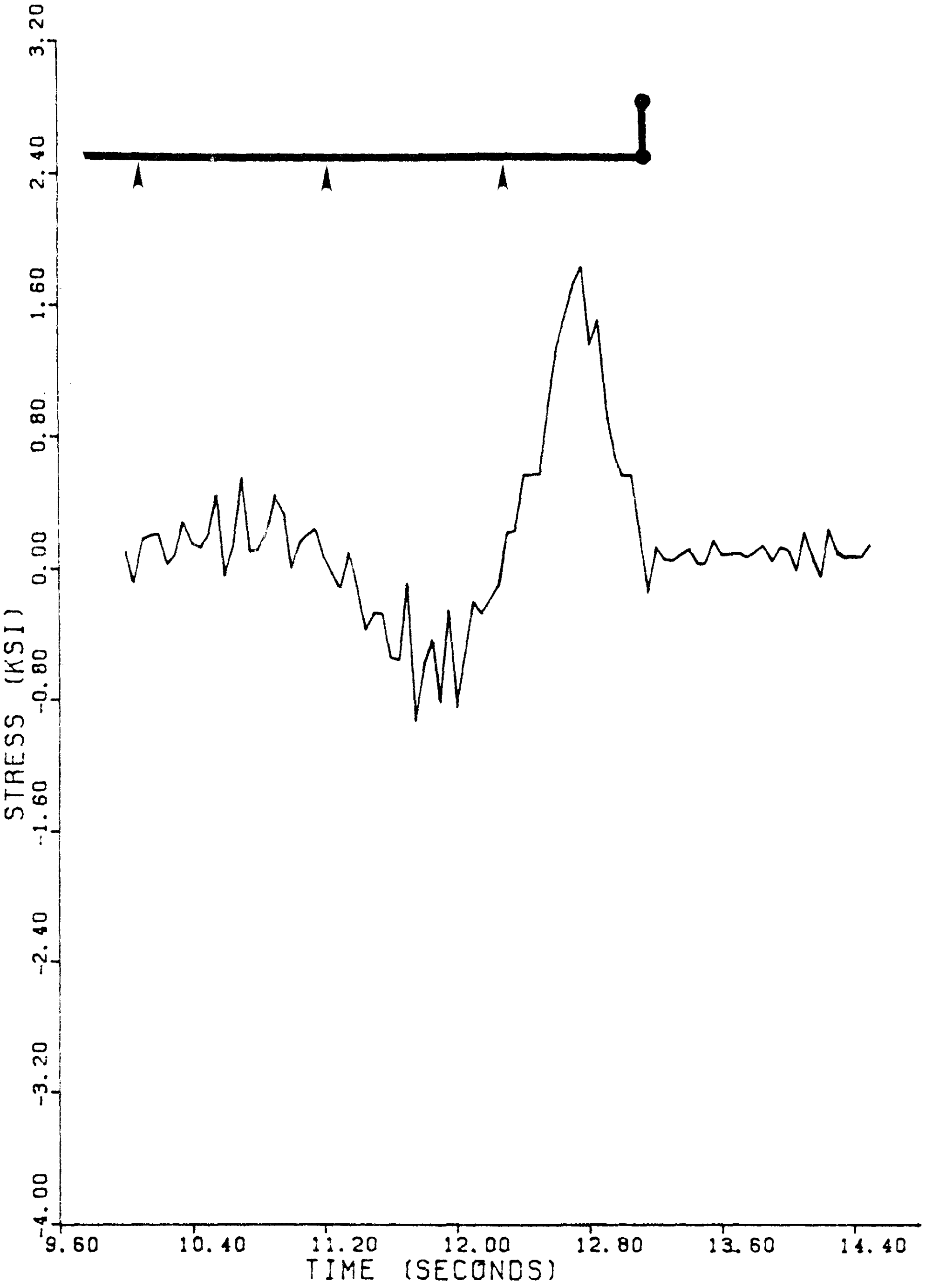

Fig. 3.15 Gauge FL1A period = .05HZ 35 MPH N-S

1.85 ksi (12.75 MPa) tension and 0.93 ksi (6.37 MPa) compression, respectively, 13 percent higher than the maximum stresses reported in the 5 MPH test. The measured static stresses are 1.70 ksi (11.71 MPa) tension and 0.60 ksi (4.13 MPa) compression, reproducing almost exactly the same values from the 5 MPH measured static stresses. The induced vibration cycles in the 35 MPH test had stress range amplitudes up to 0.85 ksi (5.86 MPa), 30 percent of the maximum stress range reported in the same test. The induced vibration cycles for the 5 MPH test usually had stress range amplitudes of 0.30 ksi (2.07 MPa) and they did not seem significant at that stage of the study. The unloaded girder in Fig. 3.16 stress response follows the same pattern reported in the 5 MPH test. The induced vibrations are of the same magnitude as those on the loaded girder. When both stress responses are superimposed, it is found that the induced stresses on both girders are due primarily to the test truck. No vehicles were present on the open lanes during the time the data were recorded.

The stress response for section FL2 is given in Figs. 3.17 and 3.18 from strain measurements at opposite sides of the bottom flange. The maximum stresses for gage FL2A are 2.13 ksi (14.64 MPa) tension and 1.35 ksi (9.30 MPa) compression. The measured static stresses give a stress range of 3.11 ksi (21.39 MPa), again reproducing almost exactly the measured static stress range in the 5 MPH test. The unloaded girder stress response is shown in Fig. 3.19 for the same FL2 section. In Figs. 3.20 and 3.21, top and bottom flange gages are plotted together for sections FL1 and FL2. The plots are almost mirror images of each other in terms of induced vibrations and also total response. Again, the data indicate that the neutral axis is located very close to the mid-depth of the girder section.

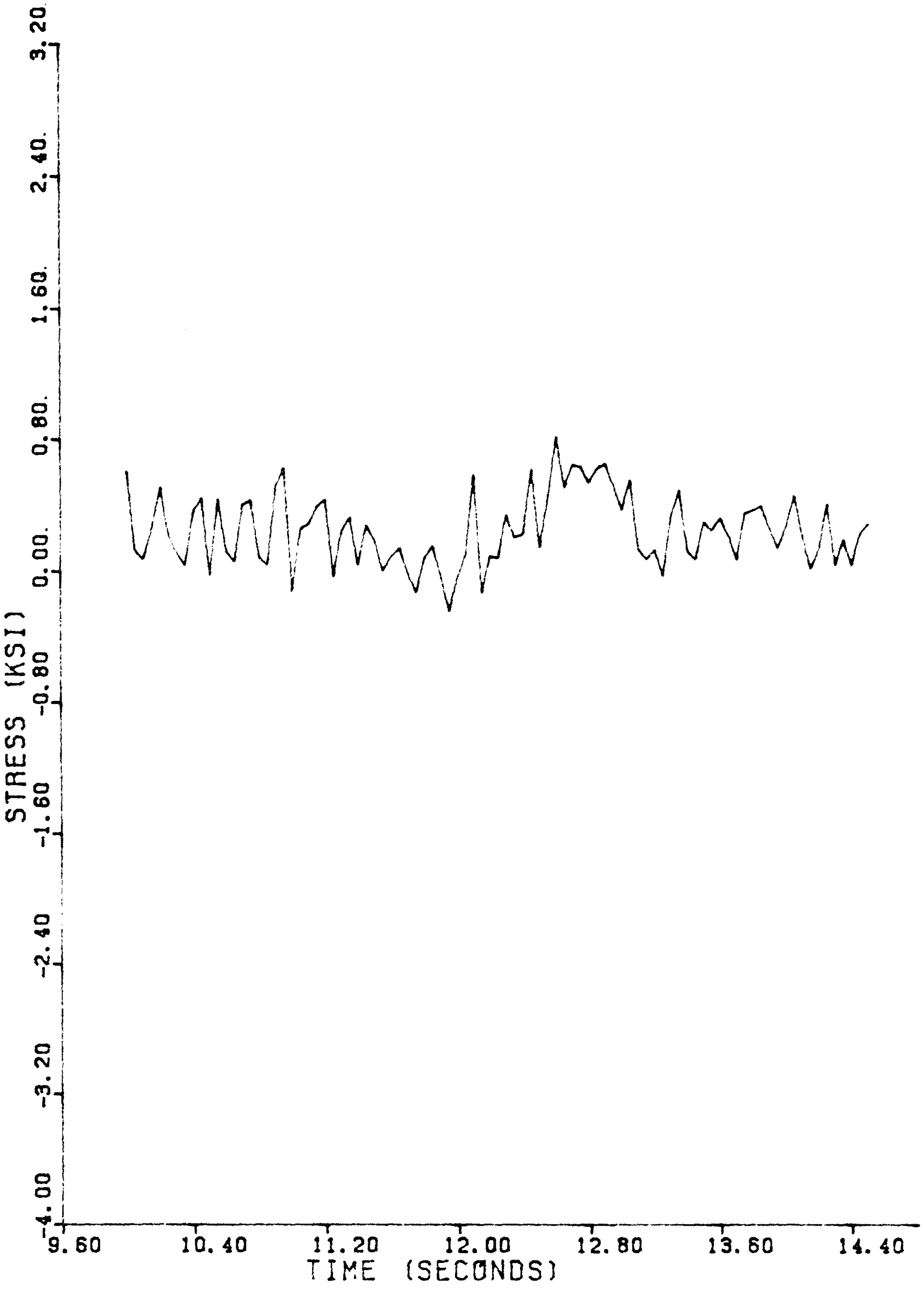

Fig. 3.16 FL1 unloaded girder P = .05HZ 35 MPH N-S

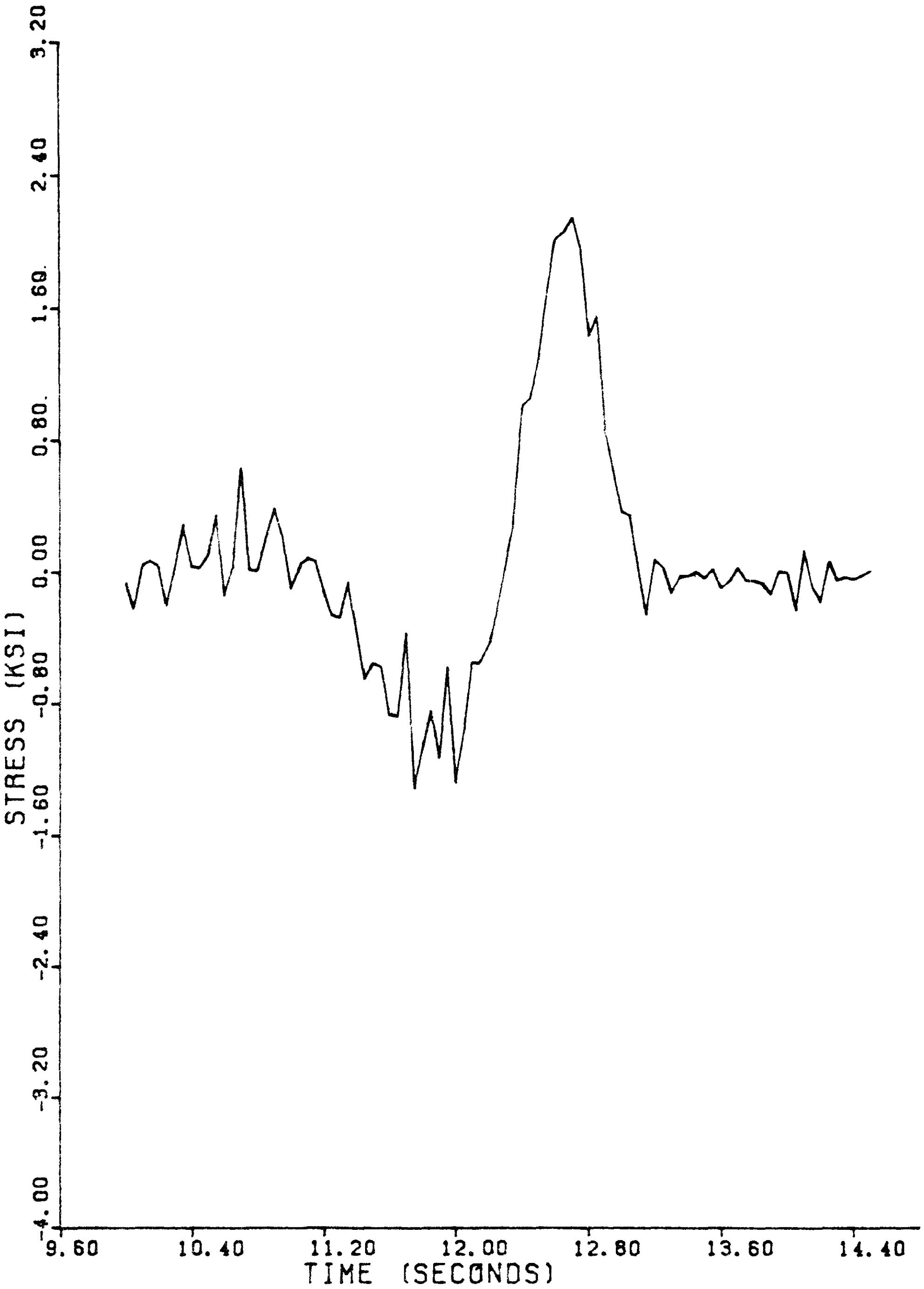

Fig. 3.17 Gauge FL2A period = .05HZ 35 MPH N-S

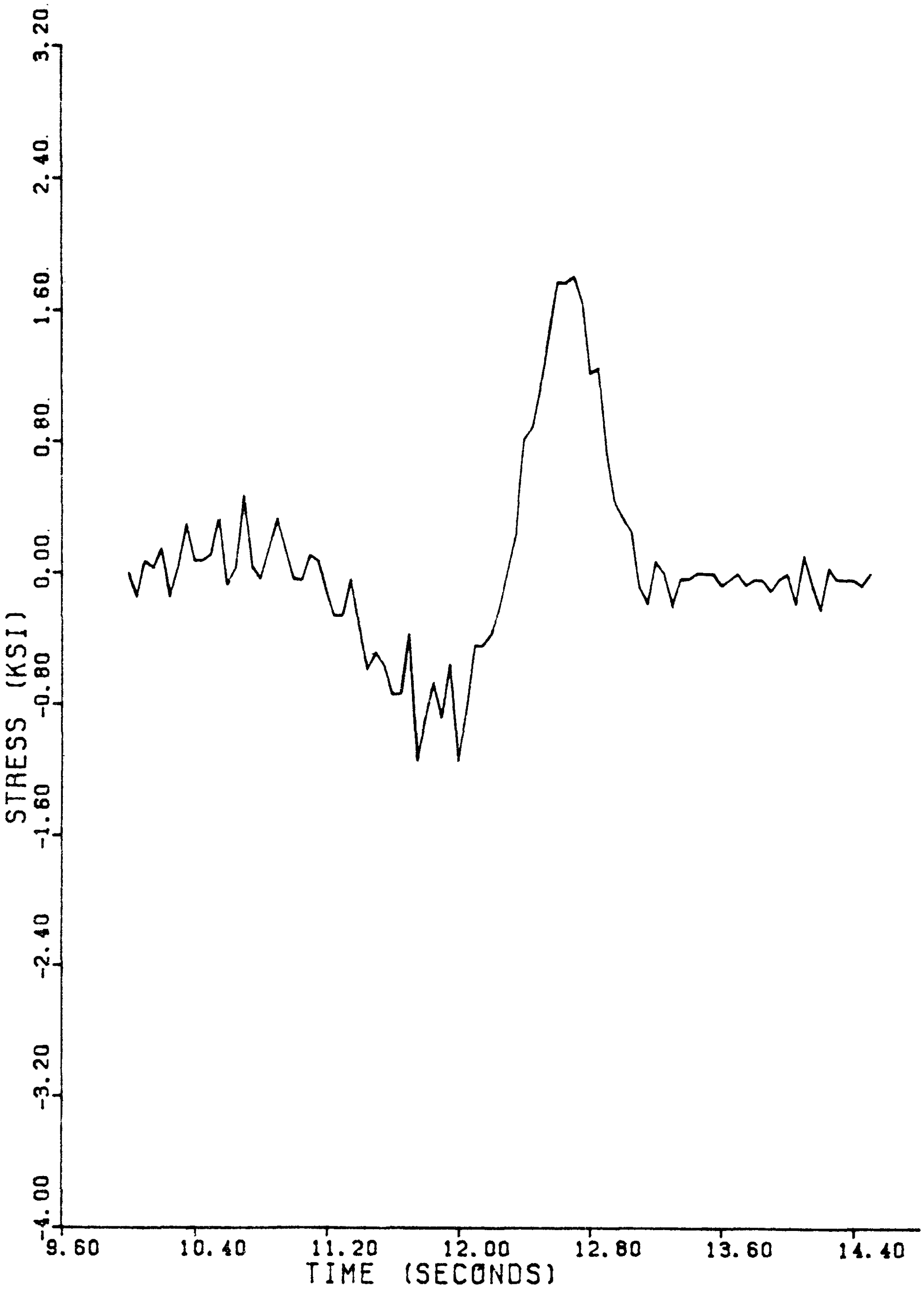

Fig. 3.18 Gauge FL2B period = .05HZ 35 MPH N-S

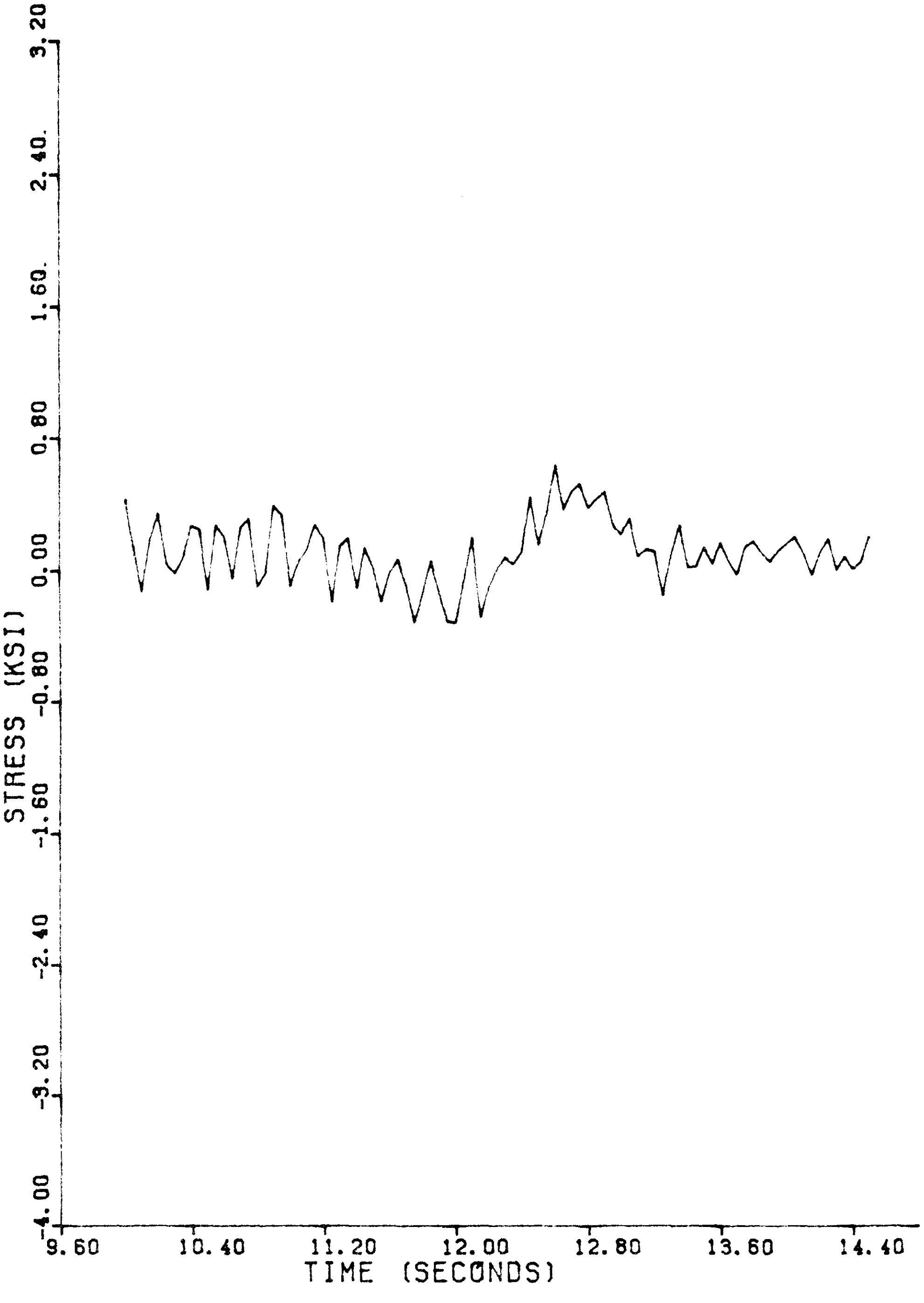

Fig. 3.19 FL2 unloaded girder P = .05HZ 35 MPH N-S

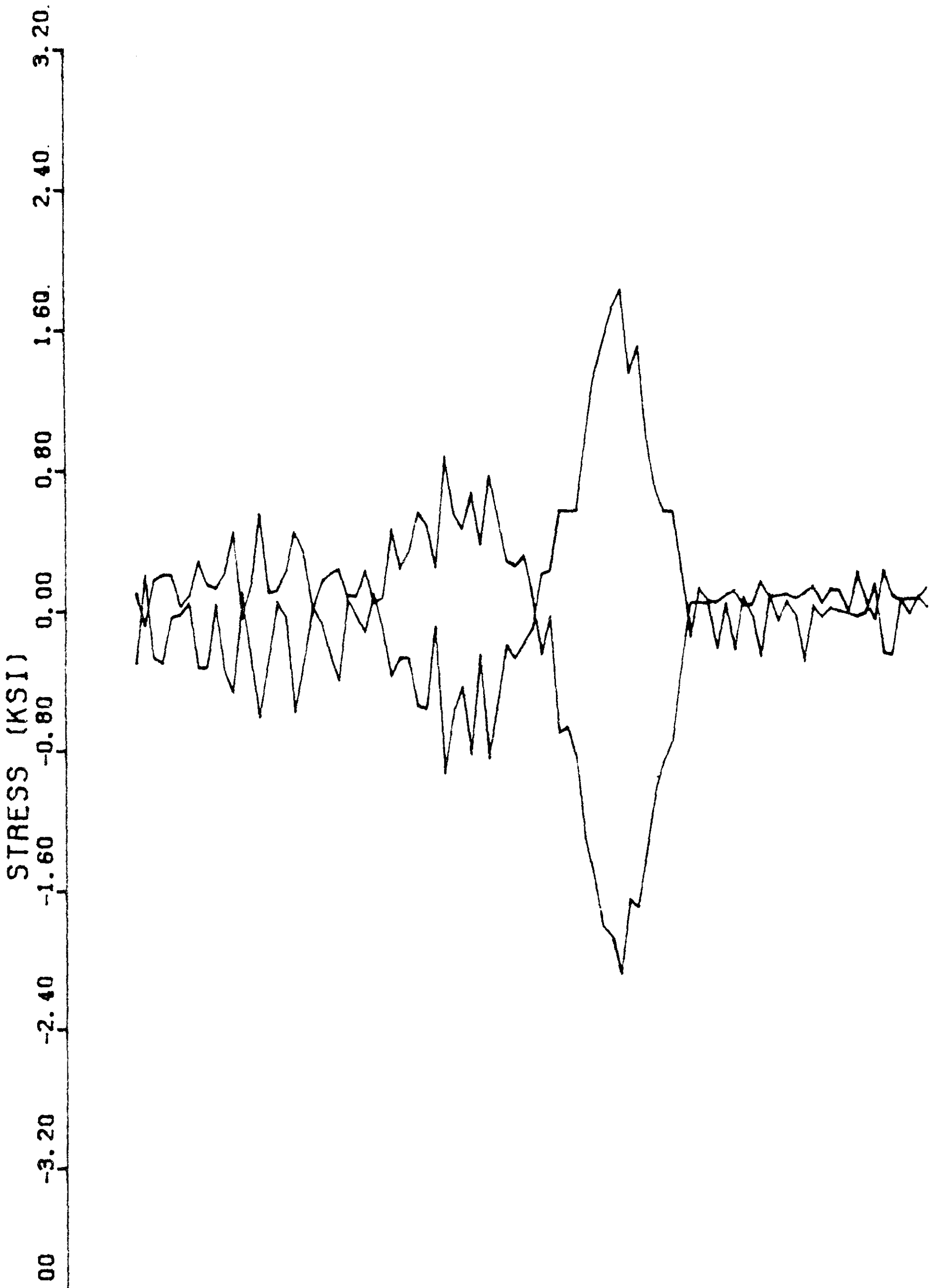

Fig. 3.20 FL1A flange gauges P = .05HZ 35 MPH N-S

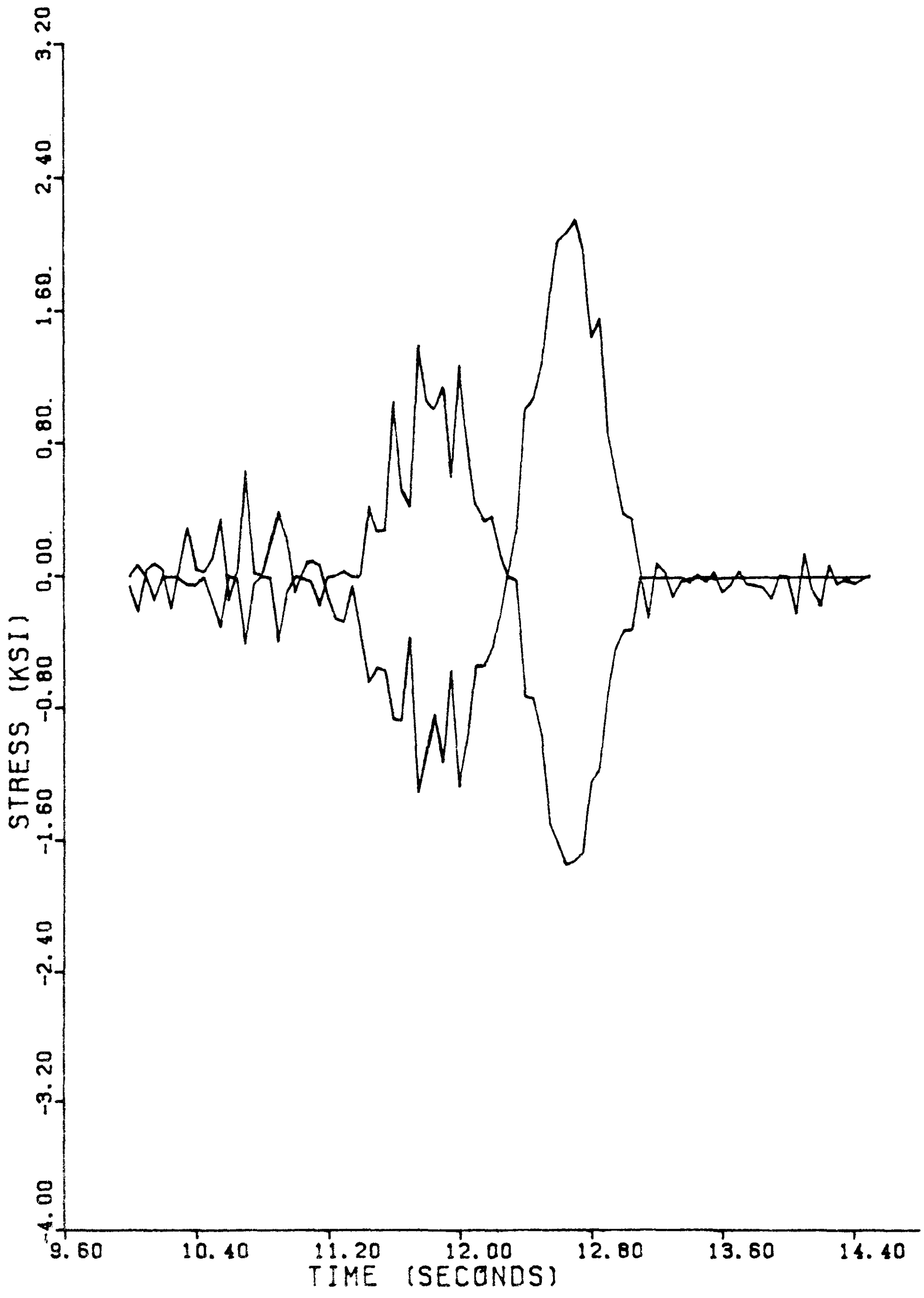

Fig. 3.21 FL2A flange gauges P = .05HZ 35 MPH N-S

3.2.3 <u>55 MPH Dynamic Test</u>. The normal speed test results gave an insight in bridge response that had not been found in the available literature. For this test,only the loaded girder was monitored. The splice section SP3 with the calculated influence line plotted in Fig. 3.6 was monitored at five distinct points in order to measure the stress field due to the change in geometry. Details of the gaged section, SP3, are shown in Fig. 3.22.

The stress response at section FL1 is presented in Fig. 3.23. The maximum measured stresses are 2.50 ksi (17.23 MPa) tension and 1.70 ksi (11.71 MPa) compression, representing a 60 percent increase in maximum stress range from the 5 MPH test. It should be emphasized that this increase is due solely to the induced vibration which reaches stress range amplitudes of up to 2.30 ksi (15.85 MPa), 55 percent of the maximum stress range and 93 percent of the measured static 5 MPH stress range. That is to say, from the midpoint vibration cycles, a plot can be drawn that will be approximately equal for any of the test speeds. The induced vibration does not damp out for a considerable amount of cycles after the truck has left the bridge. In Fig. 3.23, after the truck has crossed the last span at about the 6.50-second mark, up to 6 cycles can be counted until the recording system was turned off. Some of the last recorded cycles had stress ranges of the order of 1.70 ksi (11.71 MPa), 70 percent of the measured static 5 MPH stress range. In Fig. 3.24, the top and bottom flange strain gage responses are shown. They are seen to yield practically the same strains with opposite signs. The compression and tension dynamic stresses for the gages are always opposite, as they cross each other many times.

The section FL2 response is presented in Fig. 3.25. It shows a maximum stress range of 4.93 ksi (33.93 MPa) that is 50 percent higher than the measured 5MPH maximum stress range. The

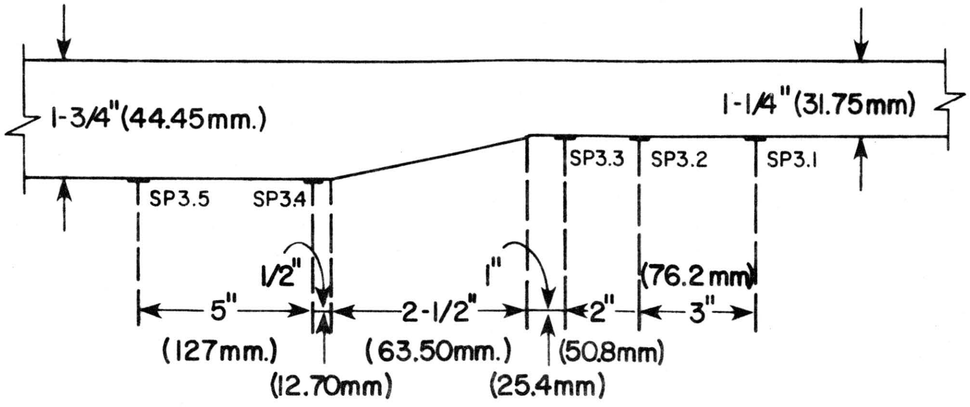

(a) Section SP3 strain gage locations

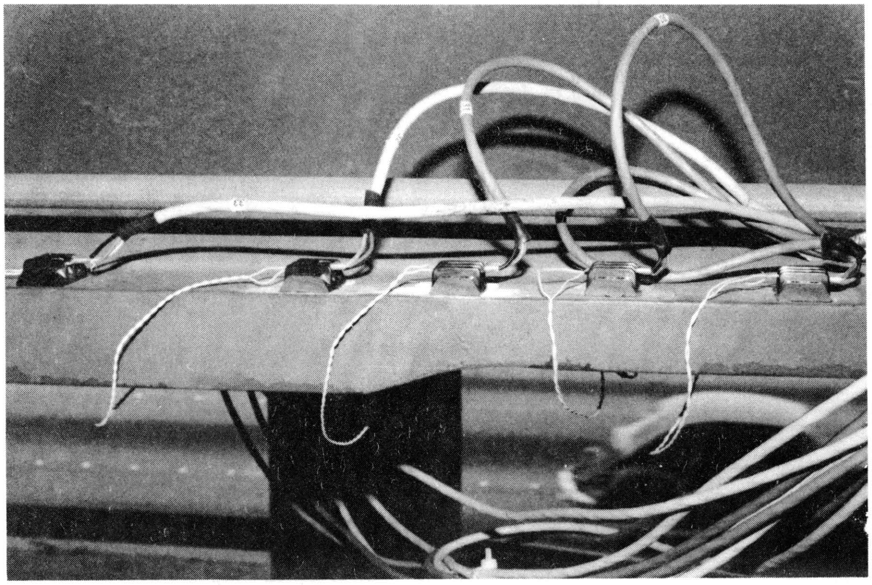

(b) Field monitoring of section SP3

Fig. 3.22 Flange splice SP3

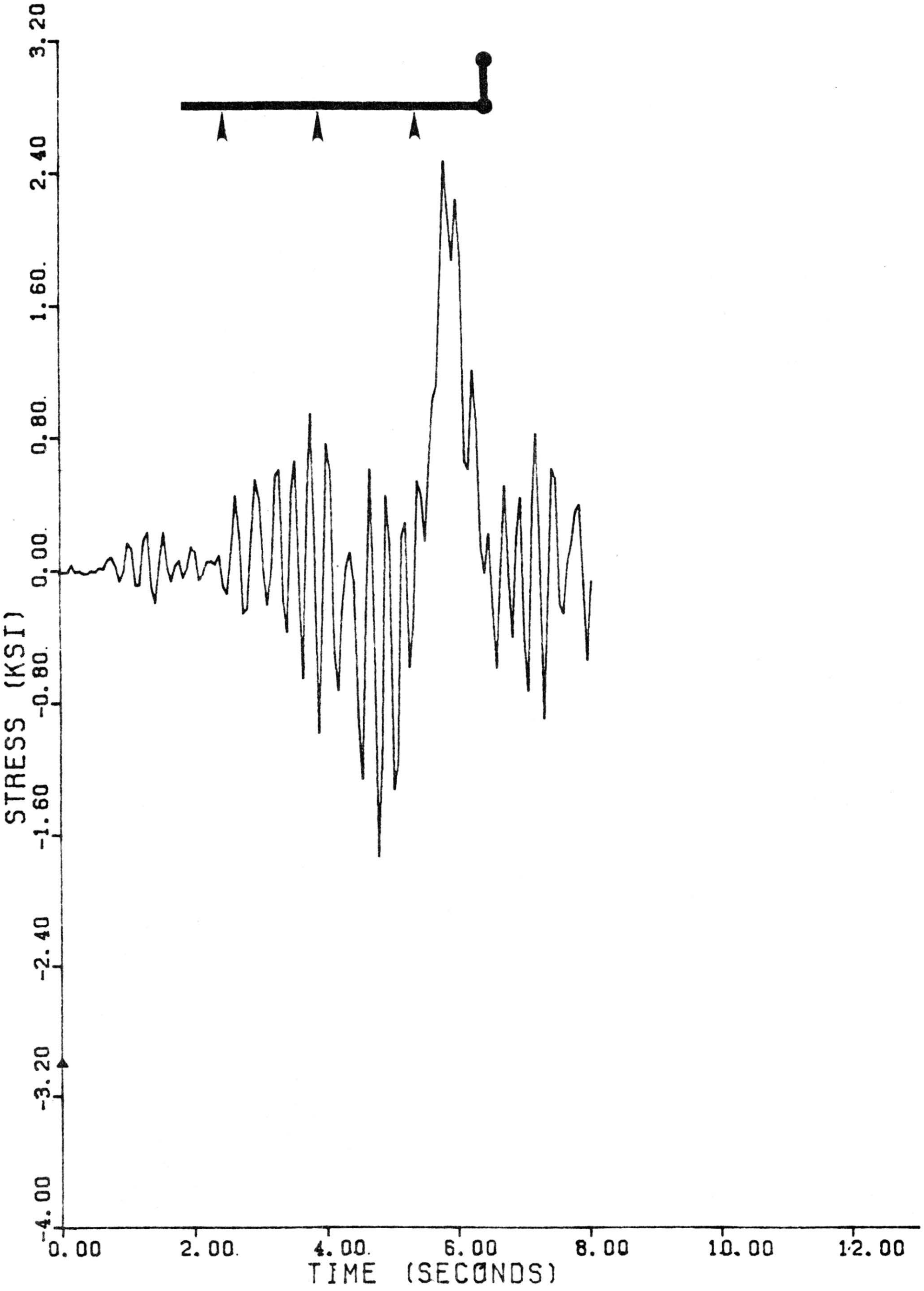

Fig. 3.23 Gauge FL1A period = .06HZ 55 MPH N-S

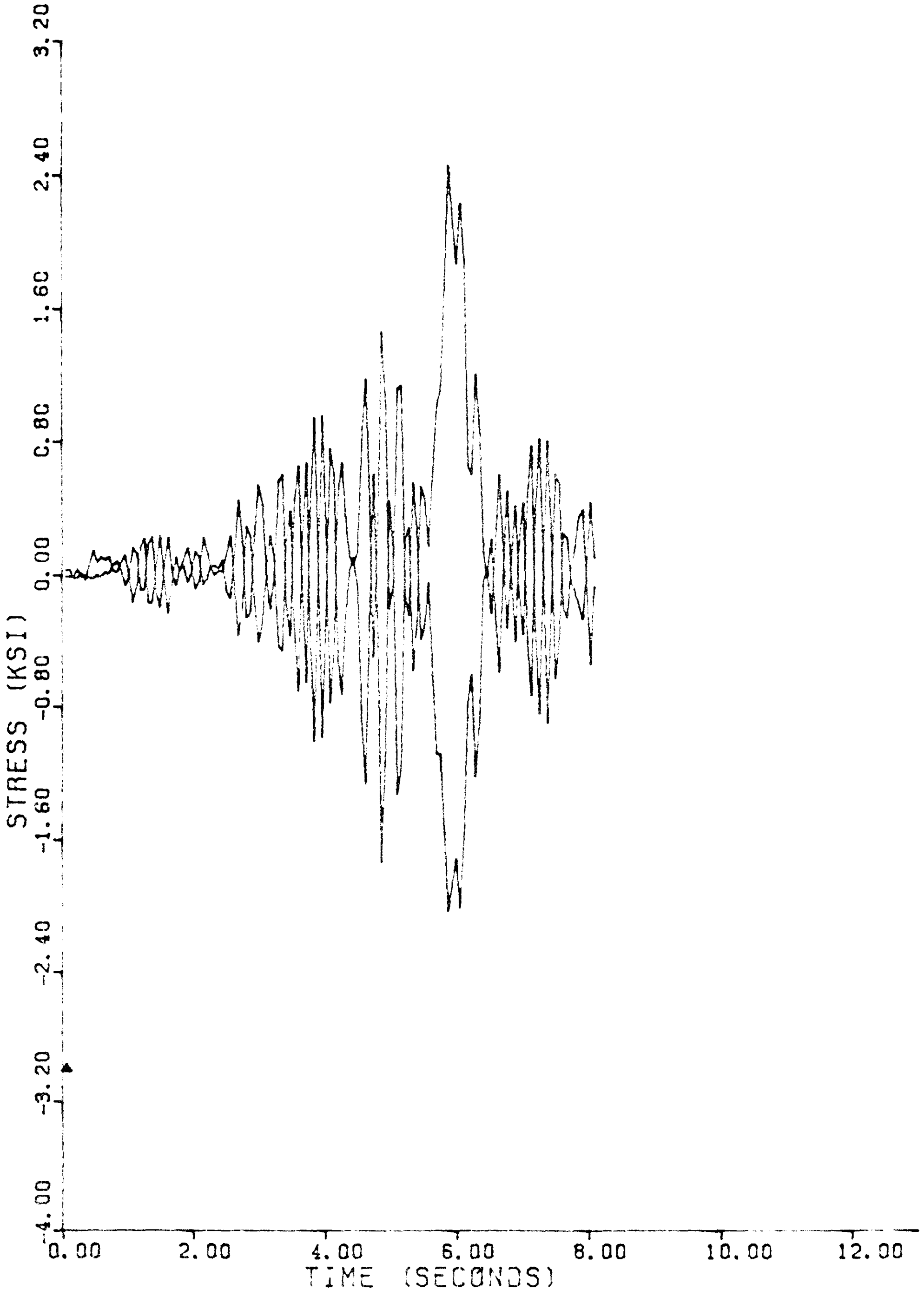

Fig. 3.24 FL1A flange gauges P = .06HZ 55 MPH N-S

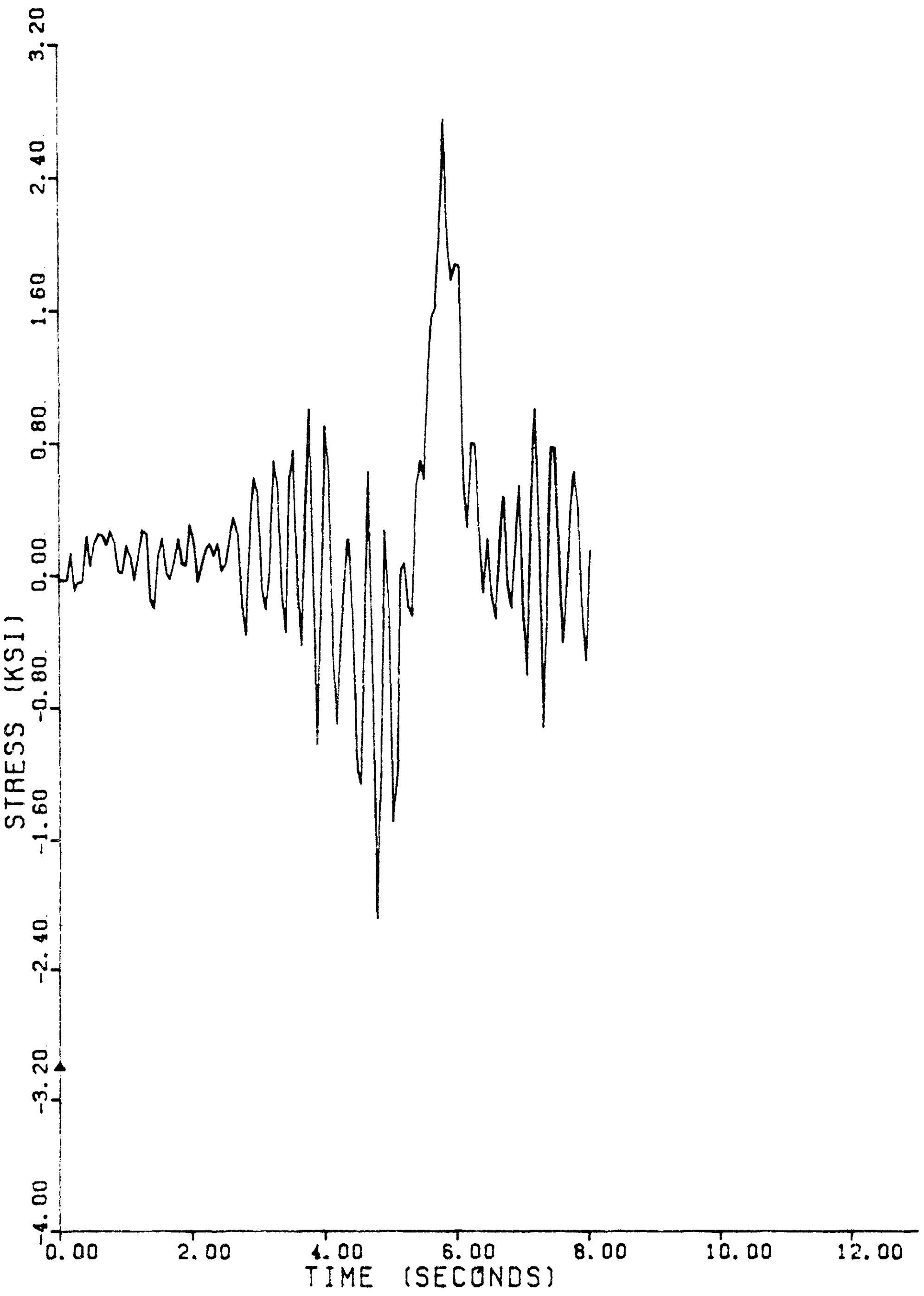

Fig. 3.25 Gauge FL2A period = .06HZ 55 MPH N-S

induced vibration cycles had showed a maximum stress range of 2.73 ksi (18.78 MPa), 55 percent of the maximum stress range and 10 percent higher than the measured static 5 MPH total stress range. The induced vibrations behavior is consistent for both sections FL1 and FL2 showing the stress response as a superposition of a constant cycle, a percentage of the calculated influence line values, and a dynamic induced vibration at the bridge's natural frequency. Those induced vibrations are proportional to the vehicle speed and amount to 55 percent of the maximum stress range for the 55 MPH test. Significant induced cycles are also present in Fig. 3.25 after the truck has left the bridge.

The SP3 section strain gage response at locations SP3.1 through SP3.5 are presented in Figs. 3.26 through 3.30. The locations are defined in Fig. 3.22. The strain gages were placed on the outside face of the bottom flange where the change in geometry actually is located. The maximum stress ranges recorded were 3.65 ksi (25.15 MPa), 3.63 ksi (24.98 MPa), 4.60 ksi (31.69 MPa), 1.40 ksi (9.65 MPa), and 1.65 ksi (11.37 MPa), respectively, for locations SP3.1 through SP3.5. The various locations show the same overall stress response with the difference in amplitude due to the stress concentration at the geometry change, 1 in. (25.4 mm) from SP3.3, and the reduced amplitude at the thicker flange locations SP3.4 and SP3.5.

The dynamic test responses are highly reproducible and the measured stress for two other 55 MPH tests at location SP3.3 are presented in Figs. 3.31 and 3.32. They give almost exactly the same cycles and respective amplitudes for the three different tests reported in Figs. 3.28, 3.31, and 3.32. The 55 MPH test in Fig. 3.33 was performed with the truck on one interior lane adjacent to the loaded girder lane. The maximum recorded stress range had a value of 3.15 ksi (21.70 MPa) compared to 4.30 ksi (29.63 MPa) recorded

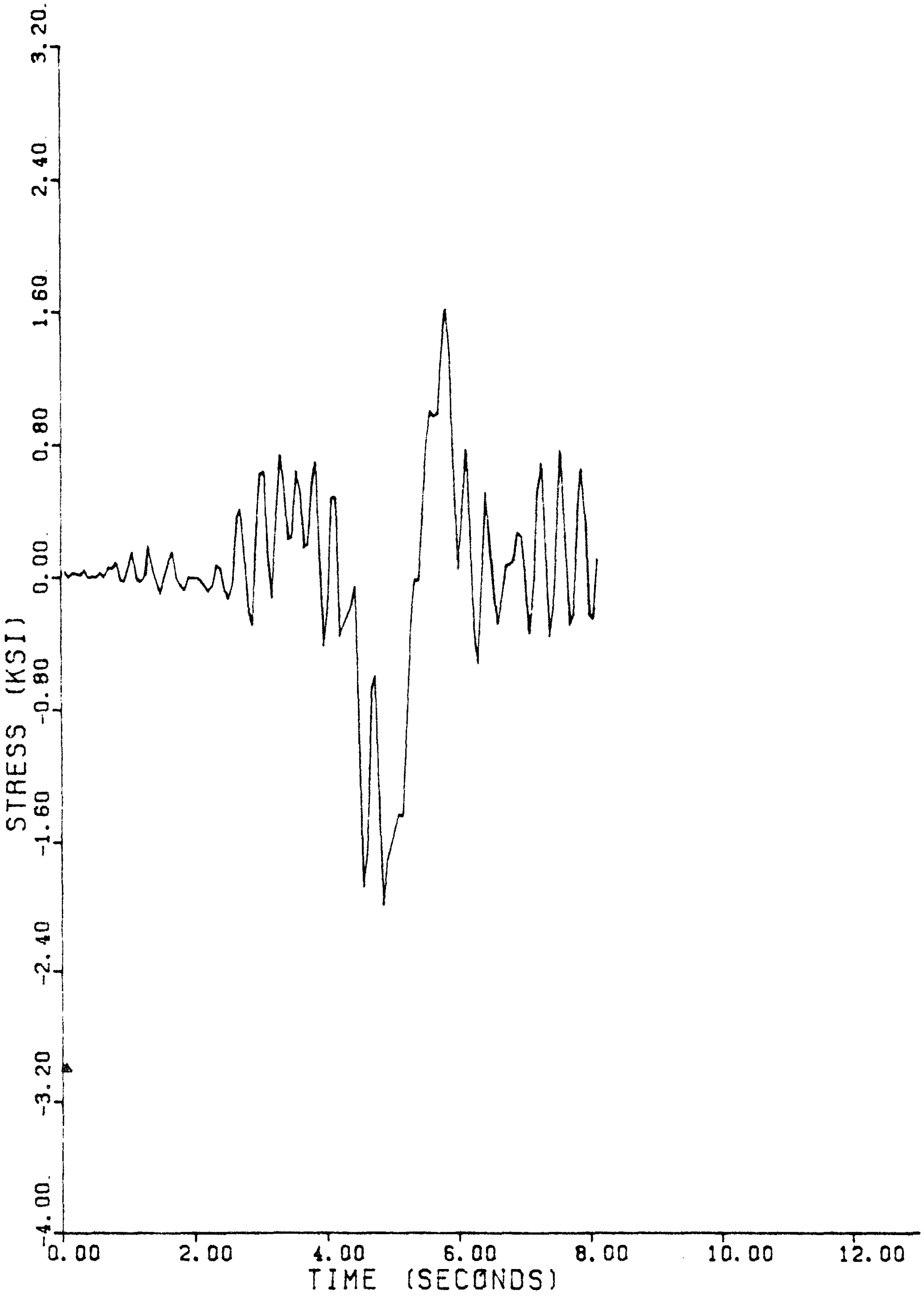

Fig. 3.26 Gauge SP3.1A period = .06HZ 55 MPH N-S

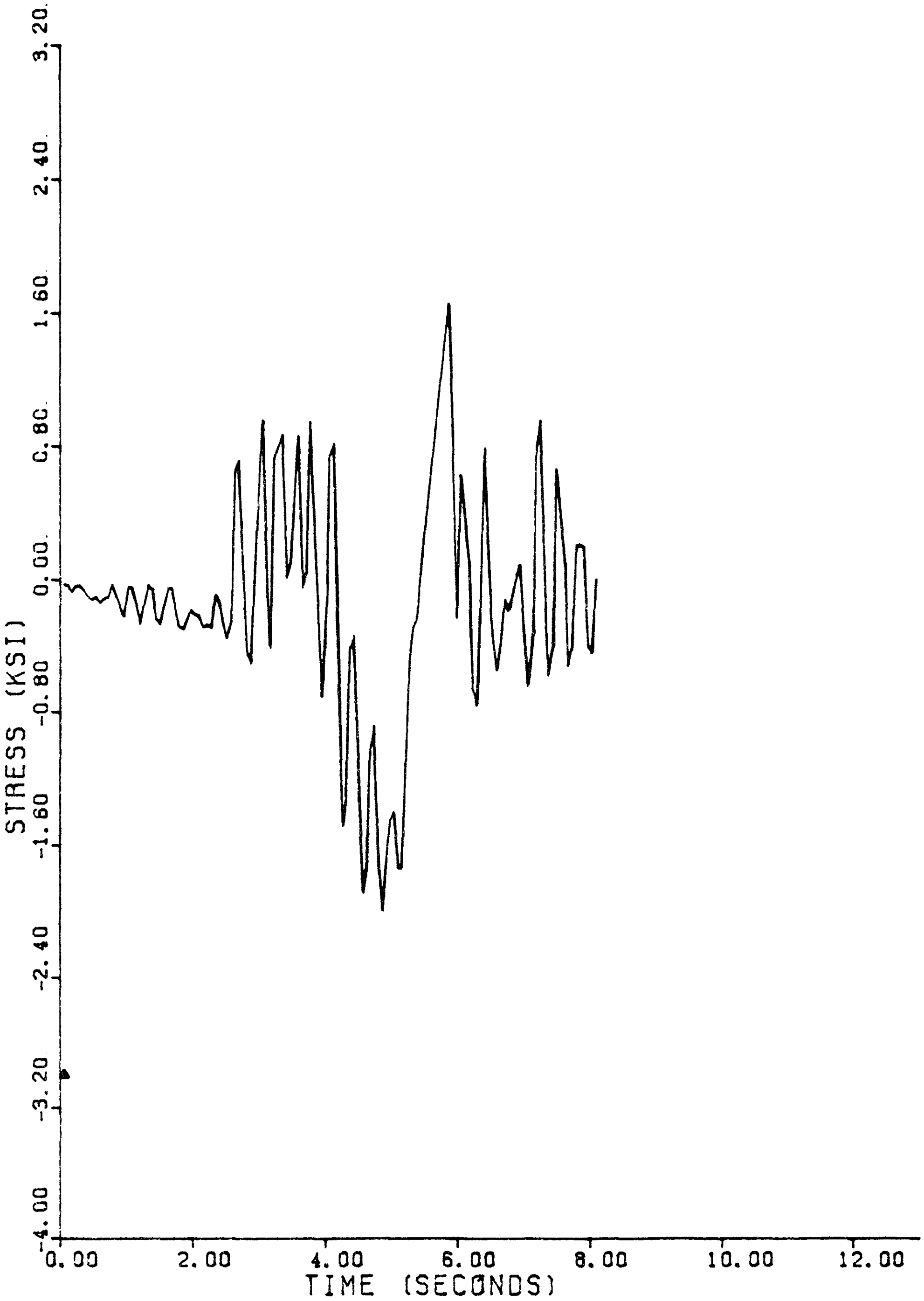

Fig. 3.27 Gauge SP3.2A period = .06HZ 55 MPH N-S

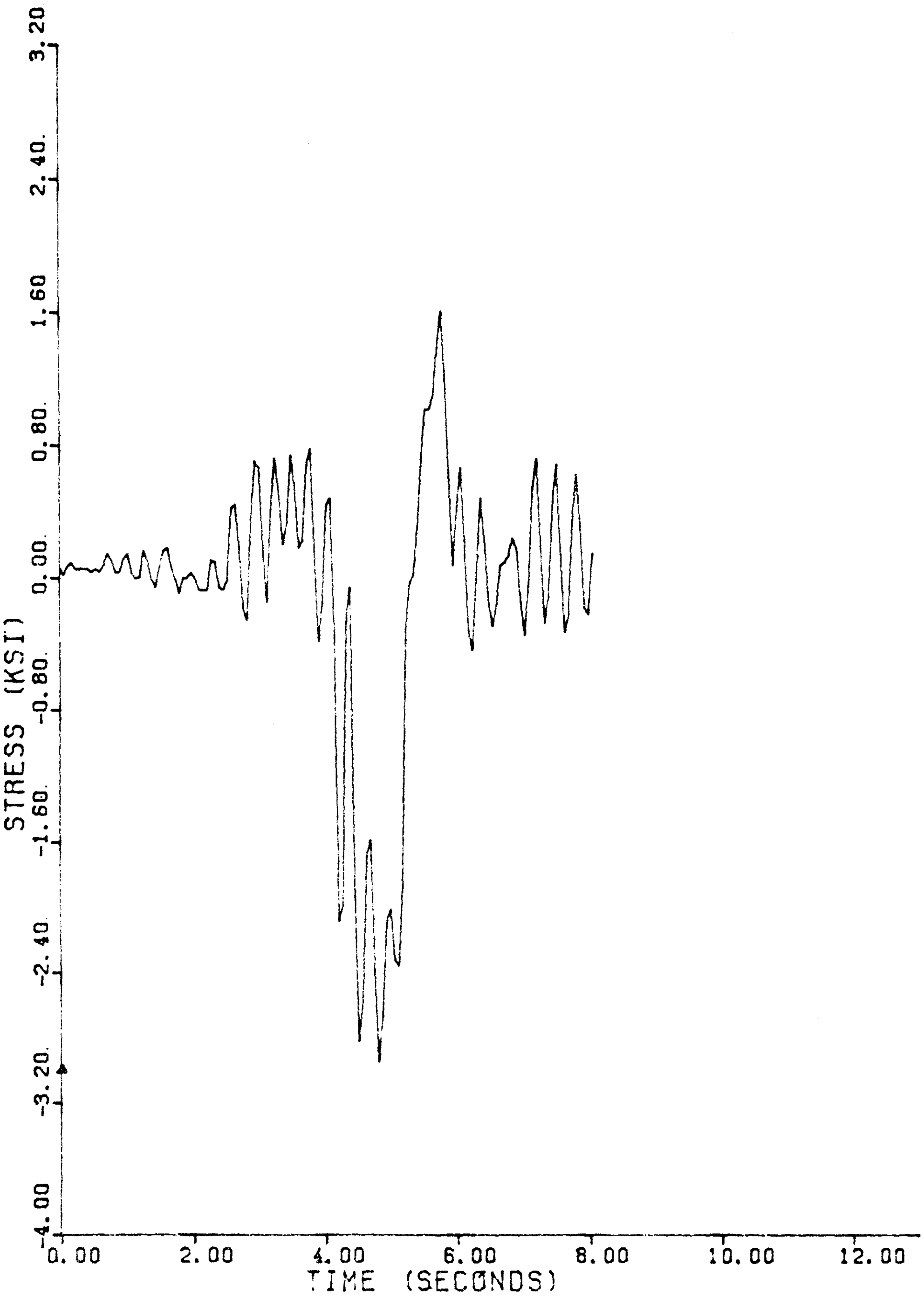

Fig. 3.28 Gauge SP3.3B period = .06HZ 55 MPH N-S

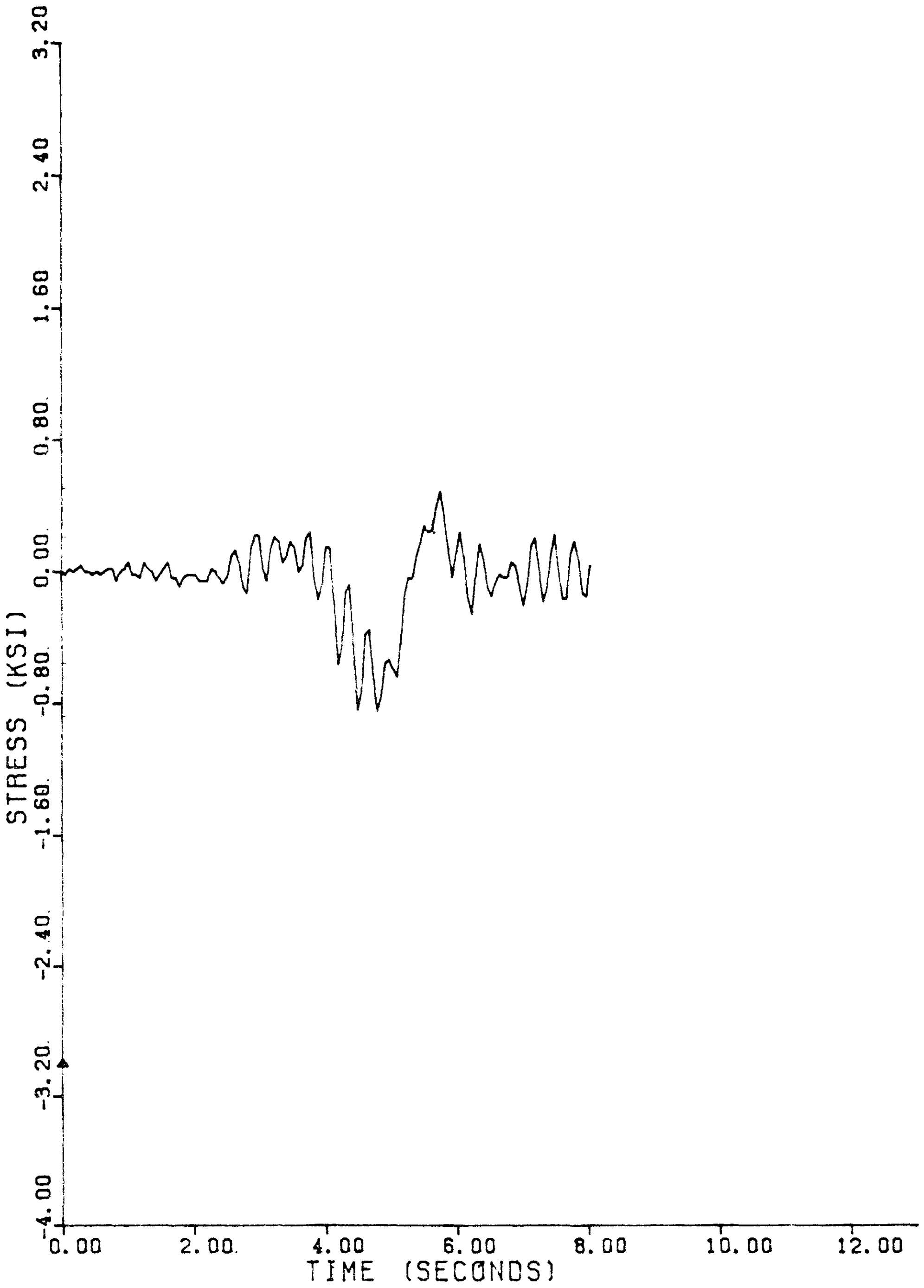

Fig. 3.29 Gauge SP3.4A period = .06HZ 55 MPH N-S

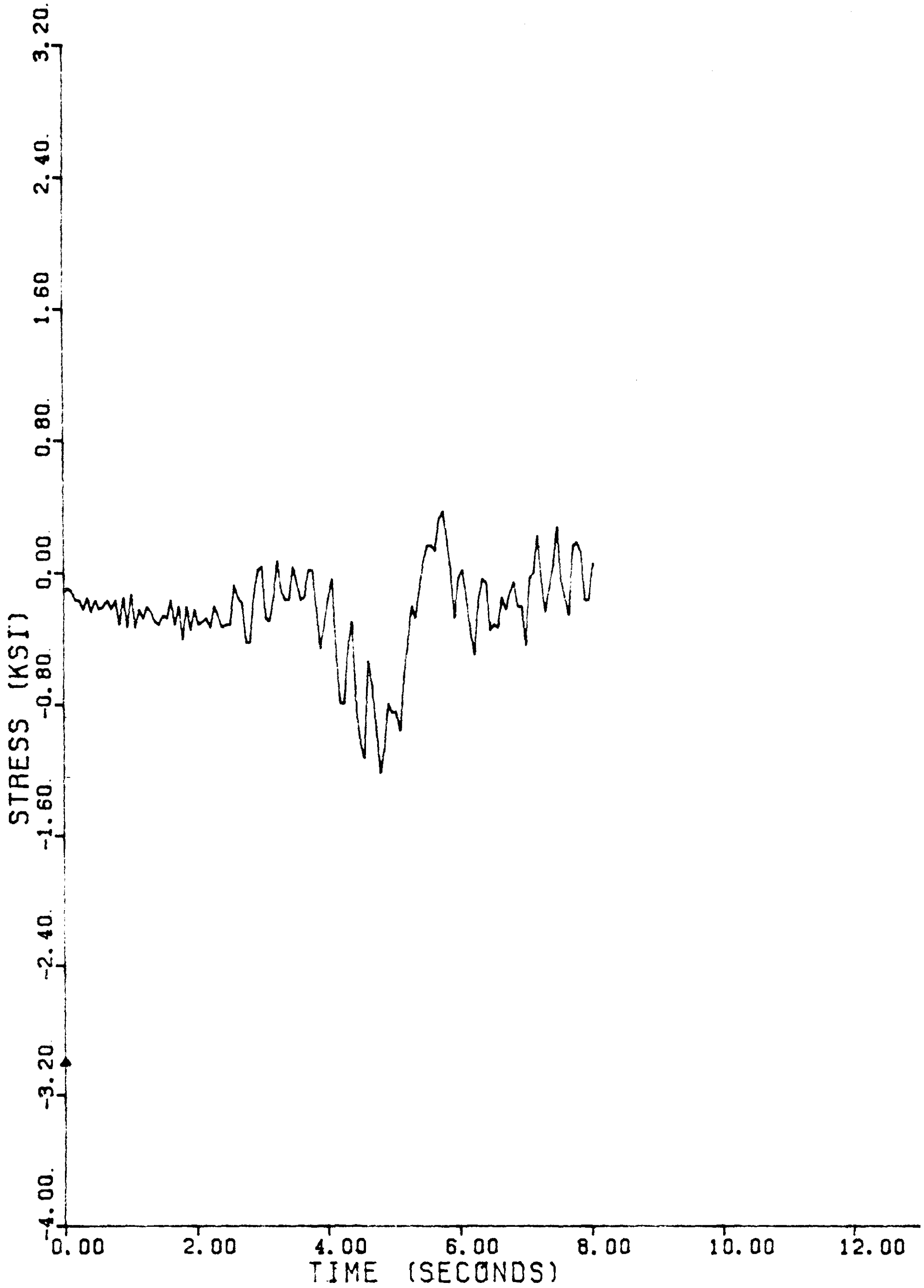

Fig. 3.30 Gauge SP3.5B period = .06HZ 55 MPH N-S

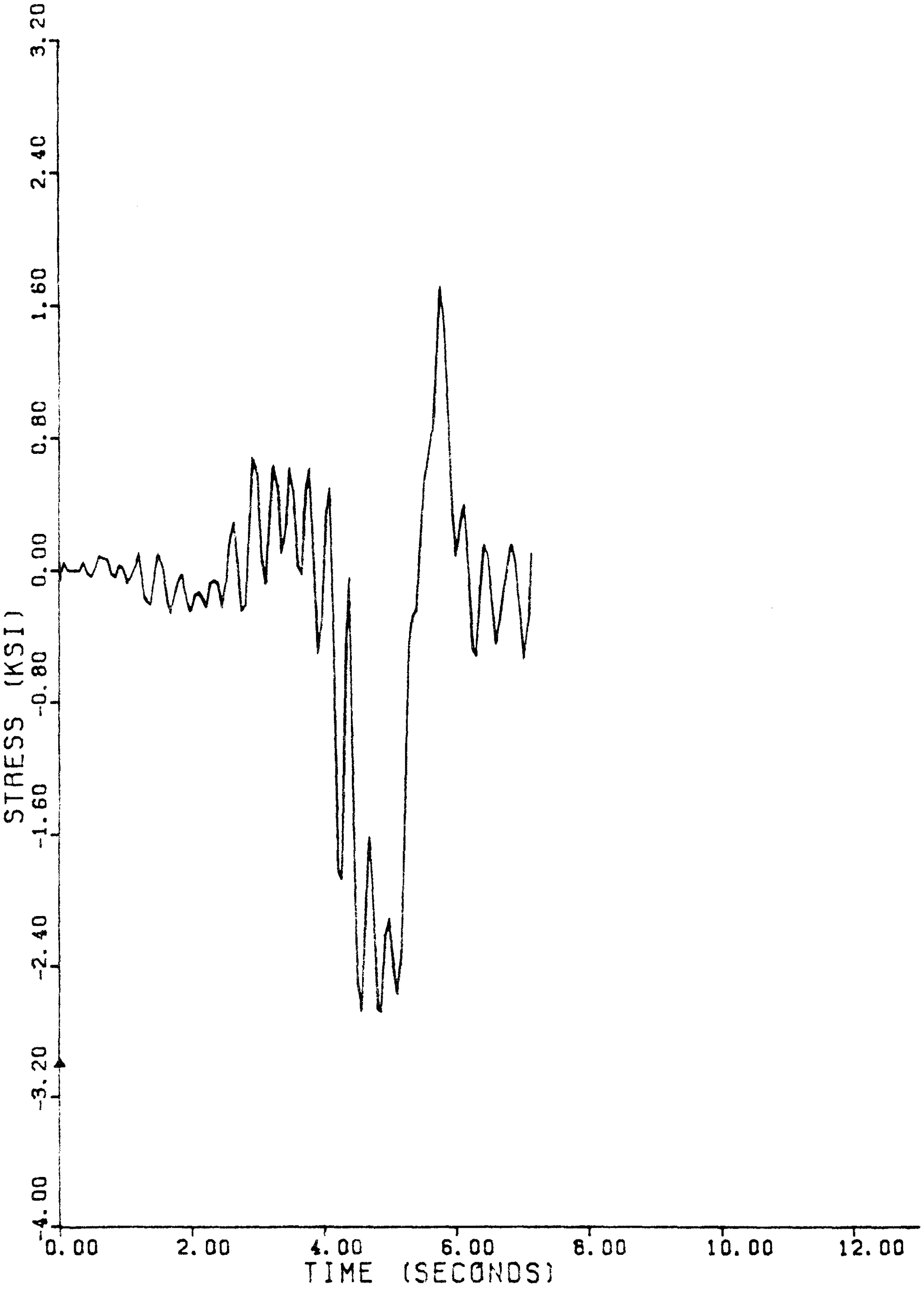

Fig. 3.31 Gauge SP3.3B period = .06HZ 55 MPH N-S

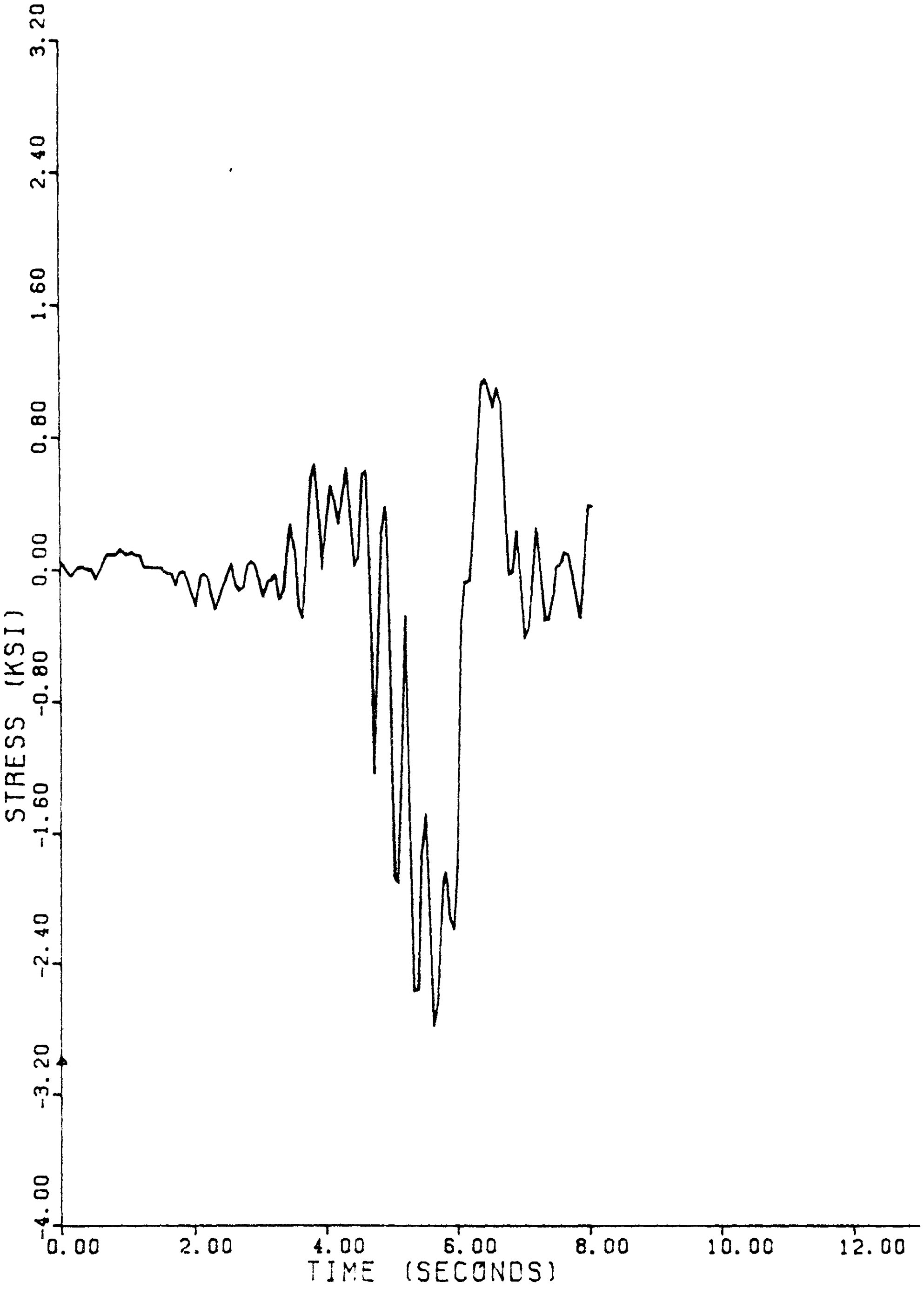

Fig. 3.32 Gauge SP3.3B period = .06HZ 55 MPH N-S

in Fig. 3.32 for the truck over the girder. Figure 3.33 also shows a very large amount of significant induced cycles after the truck has actually left the bridge. Up to twenty cycles can be counted before the system was turned off. They do not appear to damp out.

For the three distinct 55 MPH tests, there are available the stress responses for all the sections presented above. They show the tests are reproducible. An important insight into the actual field behavior under normal traffic, the measured stress responses introduce a very important variable that has not been properly accounted for; the large number of significant cycles induced by the moving load that are superimposed on the static influence line stress cycle.

A summary of the calculated stress ranges and the 5 MPH, 35 MPH, and 55 MPH measured stress ranges for section FL1 are presented in Table 3.2. The values in Table 3.2 show the significance of the induced vibrations superimposed to the static stress range.

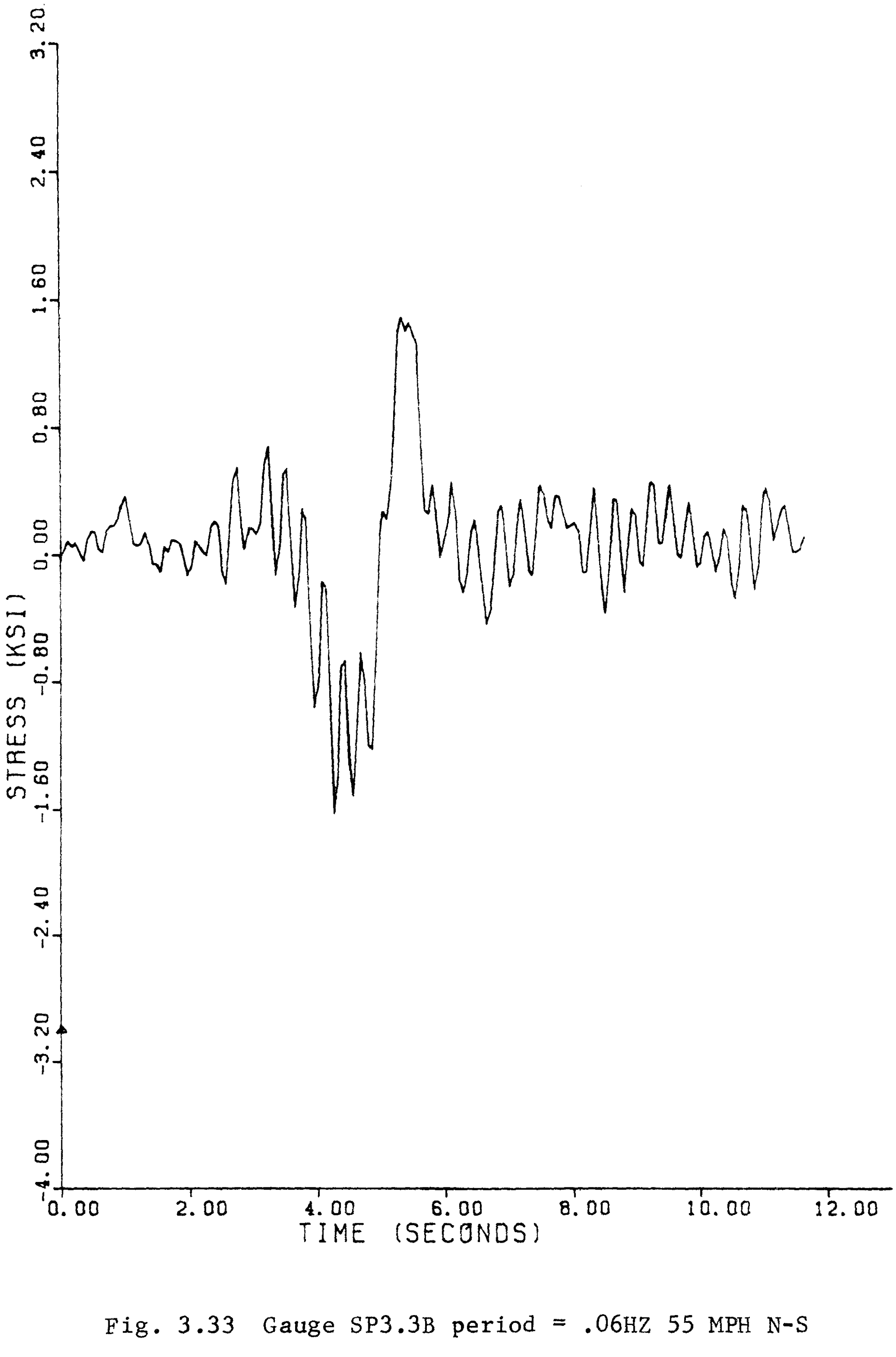

Fig. 3.33 Gauge SP3.3B period = .06HZ 55 MPH N-S

TABLE 3.2 SECTION FL1 STRESS RANGES

Stress Range (ksi)

	Static	Max.	Vibration
Calculated*	3.60	3.60	--
5 MPH	2.26	2.46	0.30
35 MPH	2.30	2.78	0.85
55 MPH	2.85	4.20	2.30

*All the load placed on the single girder

1 ksi = 6.89 MPa

CHAPTER 4

ESTIMATION OF FATIGUE BEHAVIOR

4.1 Effective Stress Range

Bridge structures are subjected to variable amplitude random stress loading due to traffic. In many specifications, the number of cycles to failure is computed based on the high stress levels caused by heavy design trucks. An estimated traffic survey is used to extrapolate the load history for the desired lifetime of the structural detail in question. The effective stress range and the number of cycles for the desired fatigue life will define a point that has to be over or above the appropriate S-N curve in order to be a safe design.

When the maximum stress range yields a ΔK_I value less than the material's threshold stress intensity factor, ΔK_{TH}, no fatigue crack growth will occur. That stress range establishes the limit for infinite life design.

Recently it has been seen that fatigue damage in bridges can occur from many cycles of low stress range. For a bridge with high volume of traffic, the low cyclic stresses produced by traffic can represent a significant portion of the fatigue damage. This is true even when the high stress cycles are responsible for the major portion of damage. That is the case for transverse members which are subjected to many stress cycles from the various axle loadings for each truck.

Many relationships between the design stress range and the actual stress from random traffic load have been studied [6]. A cumulative damage theory can be used to compare the damage from laboratory constant cycle loadings to variable cycle loadings.

The simplest of these procedures is known as Miner's theory [13] and it assumes the damage is accumulated linearly as

$$\Sigma \frac{n_i}{N_i} = 1 \tag{19}$$

where n_i is the number of cycles at a certain stress range, S_{r_i}, and N_i is the corresponding constant stress range fatigue life at S_{r_i}. From Eqs. (4) and (6), it can be seen that the fatigue life, N, is proportional to the stress range, S_r^{-n}, or

$$N_i \alpha \; S_{r_i}^{-n} \tag{20}$$

If we call the frequency of occurrence of S_{r_i}, γ_i, by definition

$$\Sigma n_i = \Sigma \gamma_i N \tag{21}$$

Combining Eqs. (19), (20), and (21) yields the relationship

$$S_{re(Miner)} = [\Sigma \gamma_i S_{r_i}^n]^{1/n} \tag{22}$$

where $S_{re(Miner)}$ is the effective stress range using Miner's linear cumulative damage theory. The value of n may be taken as 3 for most structural steels used in bridge construction. Alternatively, the root mean square stress range, RMS, is defined as

$$S_{re(RMS)} = [\Sigma \gamma_i S_{r_i}^2]^{1/2} \tag{23}$$

In Reference 6, the Miner's effective stress range using n equal to 3 and the RMS effective stress range are used to calculate the mean regression and the 95 percent confidence limit S-N lines for coverplated beams. The variable amplitude random loadings conform to a Rayleigh distribution which is shown schematically as Fig. 4.1. On Figs. 4.2 and 4.3 the S-N lines for the same coverplated beams under constant and variable amplitude loading are presented. The results compare very well within the limits of the experimental uncertainties. Either the $S_{re(Miner)}$ or $S_{re(RMS)}$ yields close agreements. Therefore, the effective stress range can be used to predict the total life, N, of a bridge subjected to random stress cycles from constant amplitude cyclic loading from laboratory generated data.

4.2 Stress Range due to Normal Traffic

Using the linear cumulative damage equation and the proportionality of fatigue life to stress range, Eqs. (19) and (20) respectively, a relationship between vehicle weight and fatigue life can be obtained. Reference 24 gives an equation of the form

$$\frac{(\alpha\beta)^3}{A''} (GVW)_D^3 (ADTT)(D_L) \Sigma\gamma_i\phi_i^3 = 1 \tag{24}$$

where α = ratio of actual stress range due to the passage of a design vehicle and the design stress range

β = elastic constant relating load and stress at a particular location on the structure

A'' = function of crack size and fatigue behavior of the detail

$(GVW)_D$ = design gross vehicle weight

$(ADTT)$ = average daily truck traffic

D_L = design life in days

ϕ_i = ratio of actual vehicle weight to design vehicle weight, $(GVW)_i/(GVW)_D$

γ_i = fraction of (ADTT) for $(GVW)_i$.

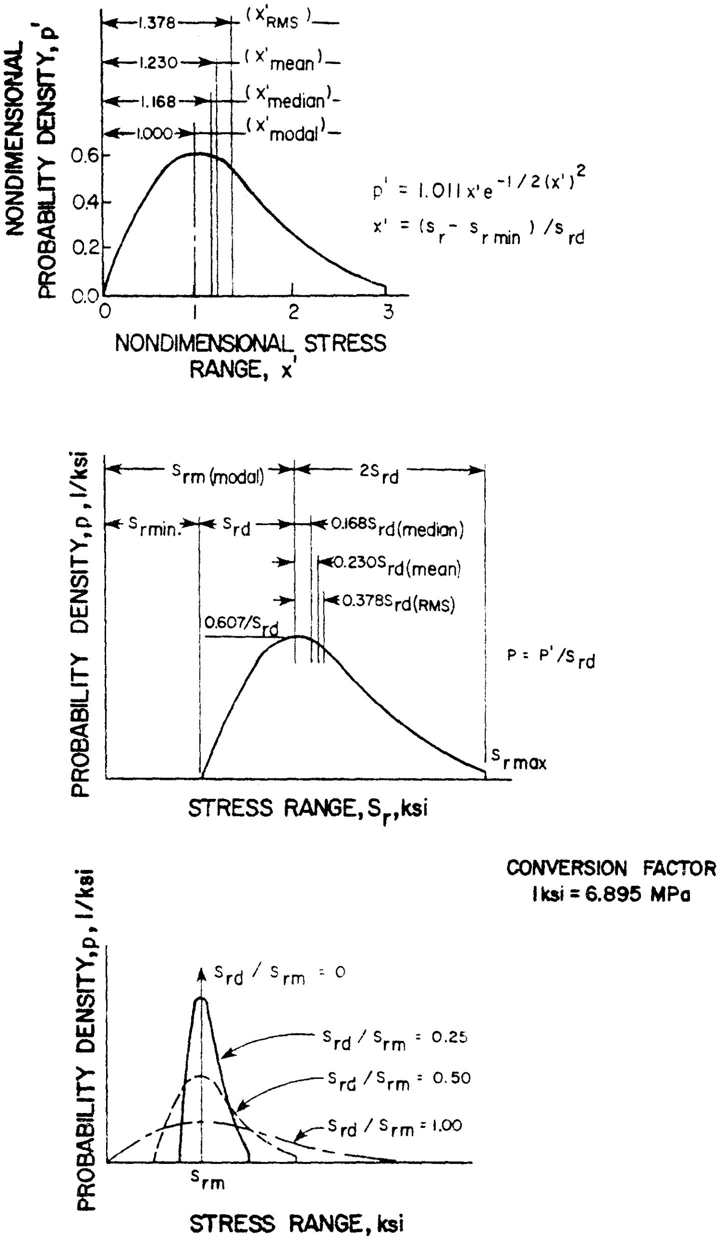

Fig. 4.1 Characteristics of Rayleigh probability curves (from Ref. 9)

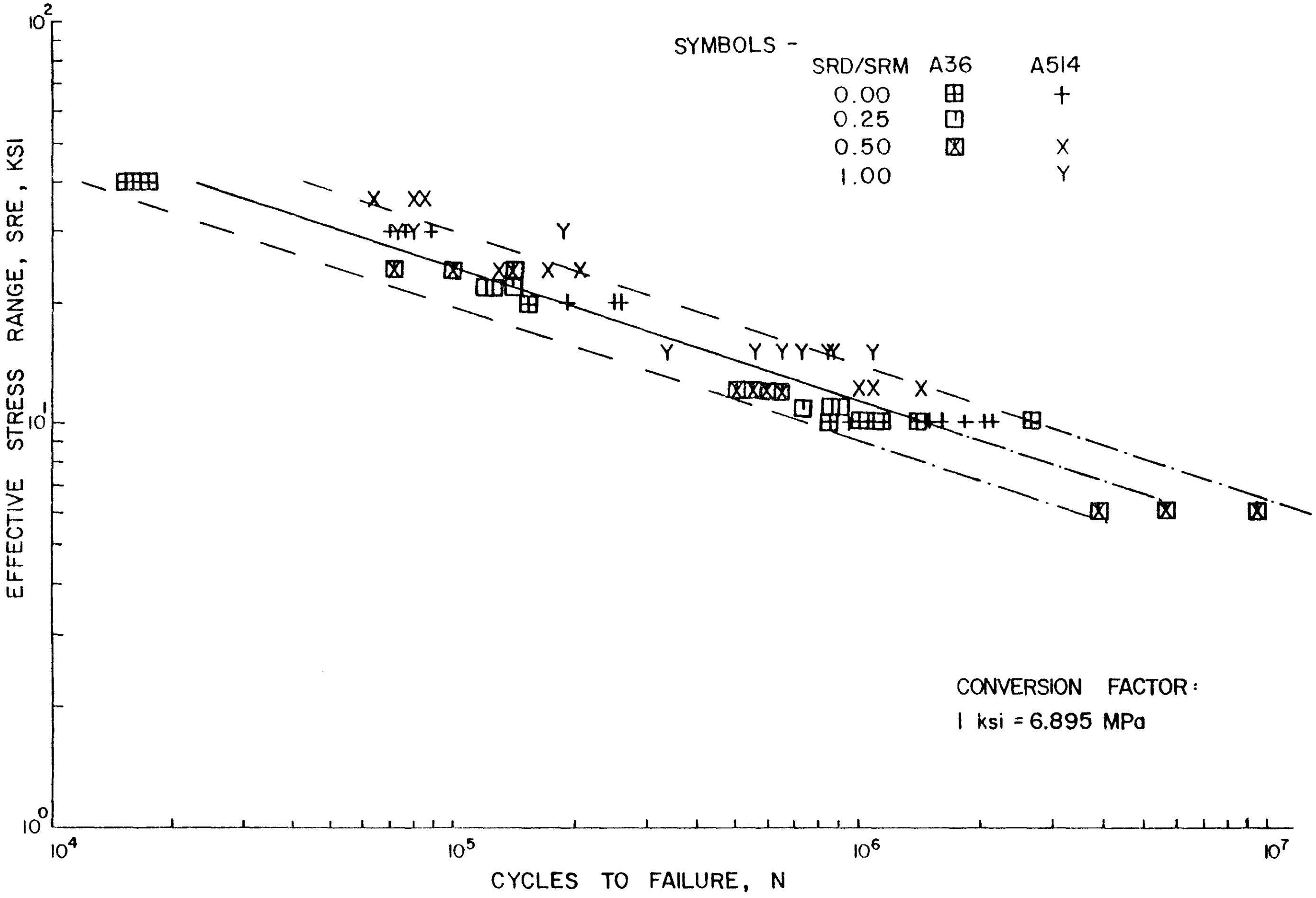

Fig. 4.2 Miner effective stress range vs fatigue life for cover-plate B and C beams (from Ref. 9)

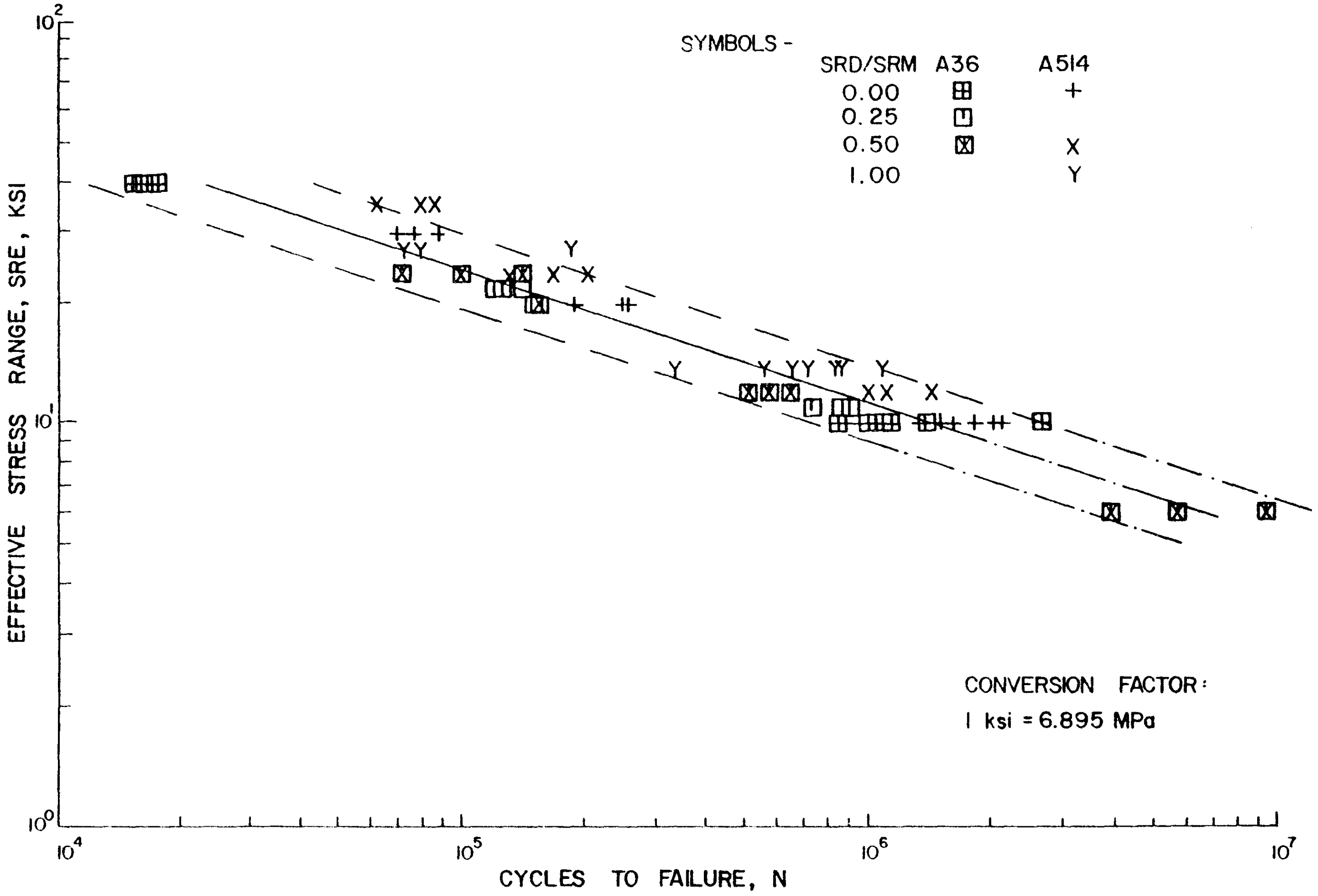

Fig. 4.3 RMS effective stress range vs fatigue life for cover-plate B and C beams (from Ref. 9)

From a loadmeter survey, the summation in Eq. (24) can be estimated. Using a gross vehicle weight frequency distribution from the 1970 FHWA Nationwide Loadmeter Survey, the summation $\gamma_i \phi_i^3$ was obtained as a function of the gross vehicle weight. This is shown in Fig. 4.4. The shape of the curve in Fig. 4.4b indicates that most of the fatigue damage is caused by trucks near the design vehicle weight and the area under the curve gives a value of the summation $\gamma_i \phi_i^3$ equal to 0.35. Using this value in Eq. (24), the relationship between the total number of trucks and stress cycles becomes [24]

$$\frac{(\mathrm{ADTT})D_L}{N} = \frac{2.85}{\alpha^3} \tag{25}$$

For an estimated (ADTT) value and a desired life expectancy, D_L, the value of N can be determined. The result is highly dependent upon the value assumed for α.

It has been assumed the factor α is always less than one. Field tests of bridges have shown that the measured stress range would be less than the design stress range, due to differences in load distribution not accounted for in design, impact, and other factors. When we measure the stresses in a particular location of the structure, we are actually determining the value of α. From the previous chapter, the 5 MPH test shows values of α equal to 0.55 for section FL1 and 0.73 for section FL2 when the measured stress range is divided by the calculated stress range incremented by the value of impact factor. To derive the (ADTT) of the AASHTO Fatigue Specification, values of α of 0.8 for transverse members and 0.7 for longitudinal members were used. Those values were assumed to be conservative estimates of α and they give good correlation with the measured 5 MPH. The 55 MPH measured stress ranges, however, show values of α equal to 0.93, 1.06, and 1.23 for sections FL1, FL2,

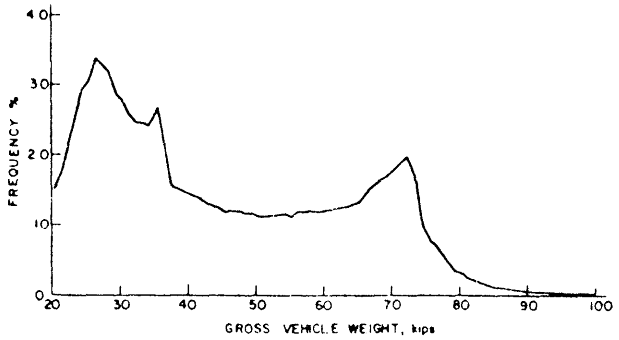

Gross vehicle weight distribution from 1970 FHWA Nationwide Loadometer Survey

(a)

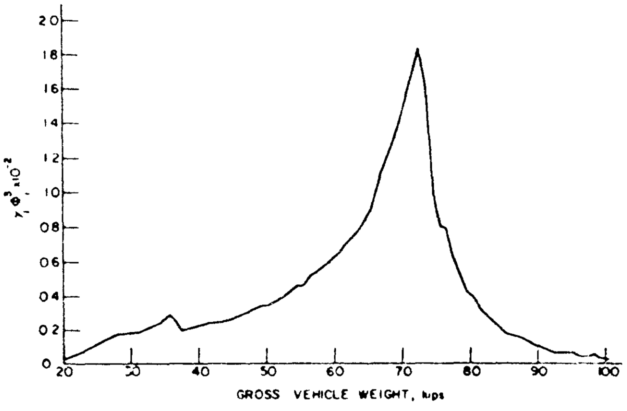

Probable damage caused by various truck weights

(b)

Fig. 4.4 Load frequency distribution and fatigue damage (from Ref. 24) and SP3, respectively. The ratio between the measured value of α equal to 1.23 and the assumed value of 0.7 when raised to the 3rd power as in Eq. [25] represents a decrease in fatigue life of about 5.4 for the same (ADTT). Notice the values of α in this study represent the ratio between the measured maximum or effective stress range and the calculated static stress range from one single truck incremented by the impact load and assuming no lateral load distribution.

If Miner's linear comulative damage theory is then used and Eq. (22) applied to the 55 MPH static stress range superimposed by the vibration cycles, an effective stress range can be predicted. Following this procedure, effective stress range values 10 percent higher than the maximum stress range are obtained. The effective value of α for the section SP3 will be equal to 1.35 and that represents a decrease in fatigue life by a factor of 7. The values of α for the various tests are presented in Table 4.1.

4.3 Defect Characterization

It is accepted that flaws exist in every welded detail. Those defects can be incomplete fusion, inadequate penetration, porosity, slag inclusion, undercutting or cracks caused by shrinkage in the weld and/or heat-affected zone. With the application of the fracture mechanics principles, the idea of removing the defects is replaced by a fatigue control plan in which the effective stress range due to cyclic loading, the fracture toughness of the material, and the inspection interval, all play a role in establishing the necessity or not of removing the defect.

The nondestructive inspection techniques are employed specifically to the type of flaws expected to be found from a certain welding procedure. The size of the defect present in the

TABLE 4.1 MEASURED VALUES OF α

Section	Calculated*	5 MPH		35 MPH		55 MPH	
	S_r**	S_r**	α	S_r**	α	S_r**	α
FL1	4.50	2.46	0.55	2.78	0.62	4.20	0.93
FL2	4.63	3.38	0.73	3.48	0.75	4.93	1.06
SP3	3.74					4.60	1.23

*The calculated S_r from static loadings was incremented using AASHTO impact formula I = 50/(L + 125), which for L equal to 70 ft and 100 ft gives values of I equal to 0.26 and 0.22, respectively.

**S_r in ksi, 1 ksi = 6.89 MPa

detail is assumed to be the greatest size that could be missed by such an inspection. This assumption provides an extra built-in conservatism as to the initial crack size.

In Fig. 4.5, the quantitative significance of various flaw shapes and locations is illustrated [25]. For a given applied stress, σ, the stress intensity factor for the infinitely long surface flaw (edge crack in Fig. 1.6b) is taken as the reference for comparison with a crack size, a, equal to the unity. As the surface defect becomes shorter, the depth for an equivalent stress intensity factor increases from 1 to 1.6 for a semi-elliptical surface crack with the major axis twice the minor axis; and from 1 to 2.4 for a semi-circular crack.

The internal defects follow the same trend showed above for the surface ones. The equivalent crack size for the infinitely long internal flaw is 2.4 times greater than the surface one. For the elliptical and circular internal flaws, the equivalent flaw size is respectively 3.9 and 5.8 greater than for the infinitely long surface crack. Surface cracks are more critical than the internal cracks and as their shape changes from circular to infinitely long, they also become more critical.

The types of flaws found by any of the nondestructive inspection methods used can have many different forms and can be anywhere from the surface to any other location within the material thickness. Many times some types of multiple defects may be present in a form of cloud of inclusions, weld porosity, or any other cluster of defects.

The ASME Boiler and Pressure Vessel Code, Section XI [26], has a conservative and sound approach to the stress intensity factor characterization of the flaws. The flaw shape in any case is circumscribed by an elliptical or circular area and treated as

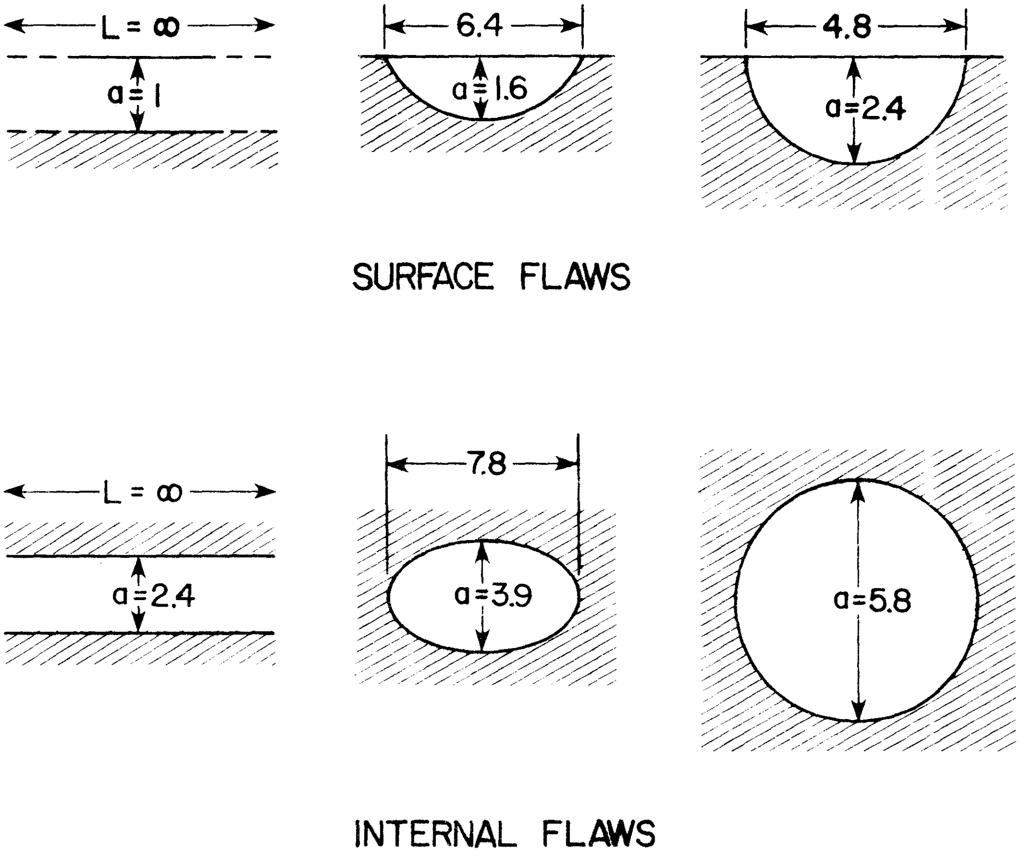

SURFACE FLAWS

INTERNAL FLAWS

Fig. 4.5 Equivalent critical crack size for different flaw geometries and location (Ref. 25) such in the analysis. Figure 4.6 from Ref. 25 shows how some typical defects would be modeled for analysis. Many other cases covering most of the range of defect sizes, location, and shape are found in the same reference. For a cluster of defects, the approach is to circumscribe the whole cluster. This is again a conservative approach but one that greatly simplifies the analysis. A more complex and detailed analysis of such a multiple defect could be employed if there is such a need, depending upon the various trade-offs of the complete fracture mechanics analysis.

Another built-in conservatism is the assumption of the sharpness of the edge of the defect. It is assumed to be of crack-like sharpness and in reality some part of the fatigue life is spent to "sharpen" the edge of the defect.

The defects found by an inspection can be treated conservatively as the shapes shown in Fig. 4.6. They will then be analyzed as surface, corner, or internal penny-shaped cracks using the appropriate correction presented in Chapter 2.

4.4 Remaining Fatigue Life

The analytical results from Chapter 2 were used to predict the remaining fatigue life of the flange splice detail as a function of the initial crack size (the biggest flaw missed by the inspection technique used). For the surface semi-elliptical crack, the predictions were based on a a/c ratio equal to 0.6, which is an upper bound of usual ranges of a/c reported in the literature [3]. Life predictions for the semi-elliptical surface cracks and for the corner cracks were derived using the total correction factor, C, for the most common 1 to 2-1/2 slope transition and also for the field-measured 1 to 5 slope transition. The penny-shaped interior cracks are in a zone not affected by the stress gradient and the same prediction applies for both transition slopes.

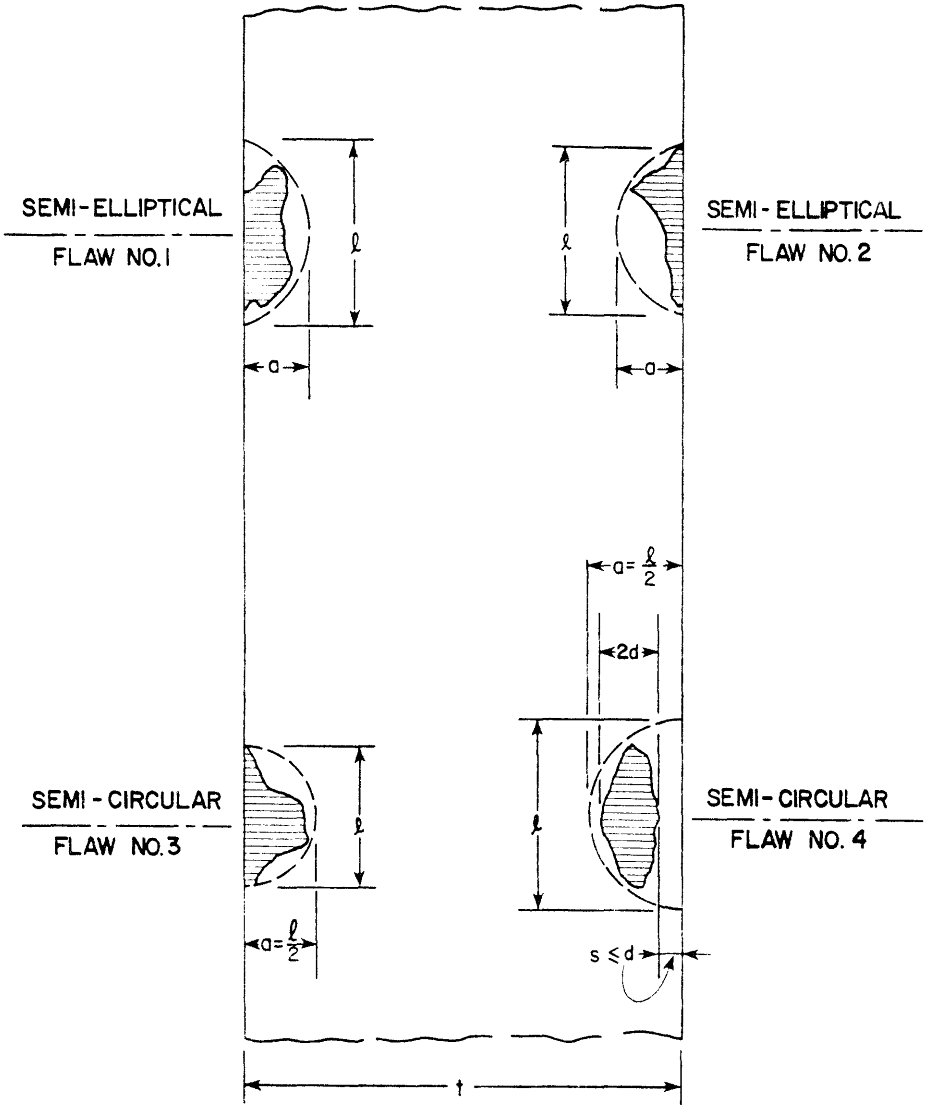

Fig. 4.6 Surface planar flaws oriented in plane normal to max. stress (Ref. 26)

The correction C for the 1 to 2-1/2 slope was calculated from the various correction factors and is presented in Table 4.2 as a function of the nondimensionalized crack size over flange thickness ratio, a/t. The total fatigue life for each crack growth interval, Δa, was computed for a specified effective stress range. The discrete crack interval Δa is the difference between a_f and a_o. Their average is used in place of the crack when we replace the integral in Eq. (8a) by a summation. The crack size interval, Δa, is very significant in the fatigue life calculation for small values of a. Therefore, the Δa values used increased with increasing crack size.

When the measured effective stress range is used, the factor α in Eq. (25) is by definition equal to the unity. For an (ADTT) equal to 2,500, it will take 6.25 years to reach a value of N equal to 2 million cycles when we solve Eq. (25) for α equal to 1. If we use a design stress range equal to 6 ksi (41.34 MPa) compared to the measured effective stress range equal to 4.10 ksi (28.25 MPa), α becomes 0.68 and it will take 20 years to reach the same 2 million cycles. The life consumed in various crack growth intervals is presented in Table 4.3 for a design stress range equal to 6 ksi (41.34 MPa) corresponding to a 20-year life period. For an initial semi-elliptical crack size of 0.60 in. (15.24 mm) in a 2-in. (50.8-mm) thick plate, which has surface length of 2 in. (50.8 mm), the fatigue life for the crack to penetrate the full thickness of the plate is over 2 million cycles (over 20 years assuming the loadmeter survey presented in Fig. 4.4 applies to this bridge and for an ADTT equal to 2,500). Such a crack is not likely to be missed in an inspection and for such a low effective stress range that detail should not present a problem. The procedure described above can be used to determine the inspection interval for any of

TABLE 4.2 SEMI-ELLIPTICAL CRACK CORRECTION - 1 TO 2-1/2 SLOPE

$C = F_S F_E F_W F_G$ (a/c = 0.6)

$F_S = 1.05$ $F_E = 0.78$ $F_W = \sqrt{\sec(\pi a/2t)}$ F_G from FEM solution

a (in.)	a/t	F_G	C
0.015	0.0075	1.98	1.62
0.025	0.0125	1.87	1.53
0.035	0.0175	1.78	1.46
0.045	0.0225	1.72	1.41
0.055	0.0275	1.66	1.36
0.07	0.035	1.60	1.31
0.09	0.045	1.49	1.22
0.15	0.075	1.34	1.10
0.25	0.125	1.25	1.03
0.35	0.175	1.19	0.99
0.45	0.225	1.15	0.97
0.55	0.275	1.12	0.96
0.65	0.325	1.09	0.96
0.75	0.375	1.07	0.96
0.85	0.425	1.05	0.97
0.95	0.475	1.04	0.99
1.10	0.55	1.02	1.03
1.30	0.65	0.99	1.12
1.50	0.75	0.96	1.27
1.70	0.85	0.97	1.64
1.90	0.95	0.96	2.82

1 in. = 25.4 mm

TABLE 4.3 FATIGUE LIFE - S_{re} = 6 ksi - SEMI-ELLIPTICAL CRACK 1 to 2-1/2 SLOPE

$$\Sigma N = [1/(3.6\times10^{-10})]\ \Sigma[CS_{re}\sqrt{\pi a_{avg}}\ ]^{-3} \times \Delta a$$

S_{re} = 6 ksi

a_o (in.)	a_f (in.)	a_{avg} (in.)	C	ΔK_I (ksi $\sqrt{\text{in.}}$)	ΔN (10^3 cycles)	ΣN (10^3 cycles)
1.80	2.00	1.90	2.82	42	7	7
1.60	1.80	1.70	1.64	23	47	55
1.40	1.60	1.50	1.27	17	122	177
1.20	1.40	1.30	1.12	14	221	399
1.00	1.20	1.10	1.03	12	366	766
0.90	1.00	0.95	0.99	11	257	1,023
0.80	0.90	0.85	0.97	10	322	1,346
0.70	0.80	0.75	0.96	9	401	1,747
0.60	0.70	0.65	0.96	9	498	2,246

1 in. = 25.4 mm

1 ksi $\sqrt{\text{in.}}$ = 1.1 $MN/m^{3/2}$

the cracks studied as long as the ADTT and the $\gamma_i \phi_i^3$ are available from a loadmeter survey.

The fatigue life for the allowable stress range of 16 ksi (110.24 MPa) of AASHTO specification for over 2 million cycles is presented in Table 4.4 for various crack growth intervals. For a 0.01-in. (0.25-mm) crack which represents a surface crack equal to 0.03 in. (0.85 mm), the remaining number of cycles for the crack to penetrate the full 2-in. (50.8-mm) thickness of the plate is about 1 million cycles. At this level of stress, the detail performance and inspection interval can be determined from Table 4.4. The initial crack size will be a function of the type of inspection used. The S-N plots for initial crack sizes equal to 0.01 in. (0.25 mm), 0.1 in. (2.54 mm), and 0.5 in. (12.7 mm) are shown in Fig. 4.7, along with the recommended Category B (AASHTO) provisions. The Category B implies no crack growth will occur for a maximum stress range less than 16 ksi (110.24 MPa). More research is necessary to determine the effect of a large number of low stress cycles.

From Eq. (4), the maximum stress range was calculated as a function of a_i for the 1 to 2-1/2 transition surface crack correction and for threshold stress intensity factors equal to 2, 3.5, and 5 ksi $\sqrt{\text{in.}}$ (2.2, 3.85, and 5.5 MN/m$^{3/2}$). The values of S_r are presented in Table 4.5. The S_r vs. a_i curves of Fig. 4.8 are used to determine for the desired ΔK_{TH} and a_i the maximum stress range below which no fatigue crack will propagate. In the S-N plots presented the horizontal line for that calculated stress range defines the maximum allowable stress range for infinite life design.

The values of C for the 1 to 5 slope transition are presented in Table 4.6. They were used to compute the fatigue life

TABLE 4.4 FATIGUE LIFE - S_{re} = 16 ksi - SEMI-ELLIPTICAL CRACK 1 to 2-1/2 SLOPE

$$\Sigma N = [1/(3.6\times 10^{-10})]\ \Sigma[CS_{re}\sqrt{\pi a_{avg}}\ ]^{-3} \times \Delta a$$

S_{re} = 16 ksi

a_o (in.)	a_f (in.)	a_{avg} (in.)	C	ΔK_I (ksi $\sqrt{in.}$)	ΔN (10^3 cycles)	ΣN (10^3 cycles)
1.80	2.00	1.90	2.82	110	0.4	0.4
1.60	1.80	1.70	1.64	61	2	2
1.40	1.60	1.50	1.27	44	6	9
1.20	1.40	1.30	1.12	36	11	21
1.00	1.20	1.10	1.03	30	19	40
0.90	1.00	0.95	0.99	27	13	53
0.80	0.90	0.85	0.97	25	17	70
0.70	0.80	0.75	0.96	23	21	92
0.60	0.70	0.65	0.96	22	26	118
0.50	0.60	0.55	0.96	20	33	152
0.40	0.50	0.45	0.97	18	44	196
0.30	0.40	0.35	0.99	16	60	256
0.20	0.30	0.25	1.03	14	89	346
0.10	0.20	0.15	1.10	12	157	503
0.08	0.10	0.09	1.22	10	49	553
0.06	0.08	0.07	1.31	10	58	611
0.05	0.06	0.055	1.36	9	37	649
0.04	0.05	0.045	1.41	8	45	694
0.03	0.04	0.035	1.46	8	59	754
0.02	0.03	0.025	1.53	7	86	840
0.01	0.02	0.015	1.62	6	155	996

1 in. = 25.4 mm

1 ksi $\sqrt{in.}$ = 1.1 $MN/m^{3/2}$

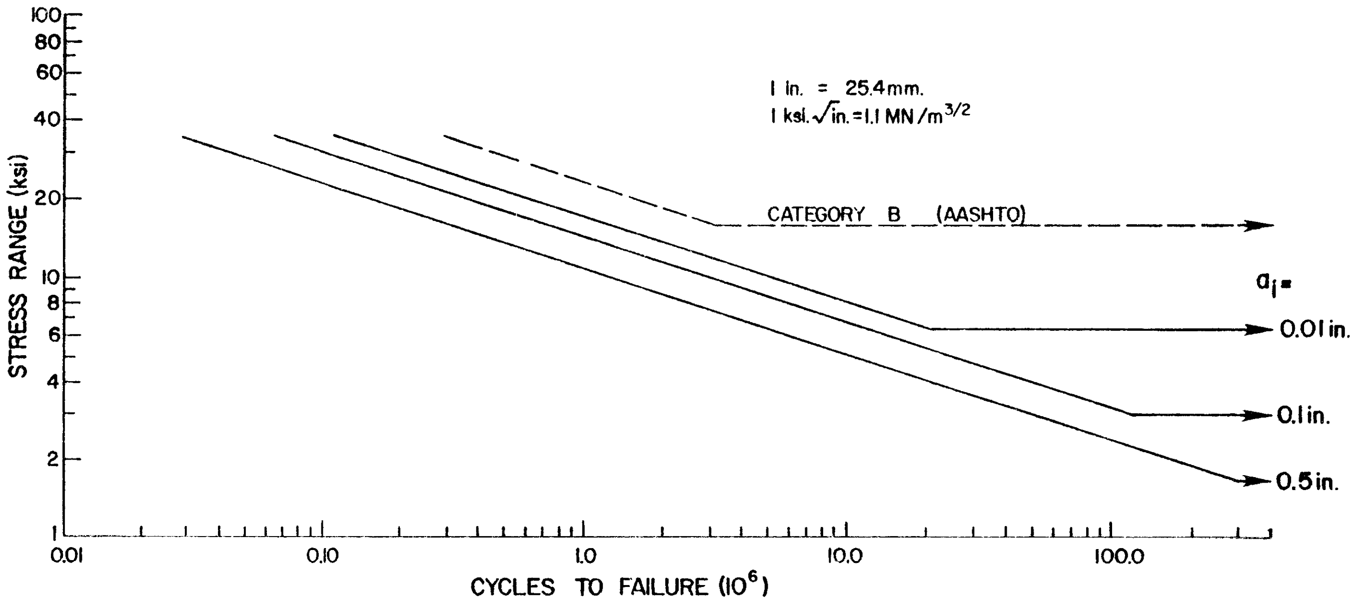

Fig. 4.7 Surface crack - S-N plots - 1 to 2-1/2 slope

TABLE 4.5 ΔK_{TH} SEMI-ELLIPTICAL CRACK - 1 TO 2-1/2 SLOPE

$$\Delta K_{TH} = C\ S_r \sqrt{\pi a_i}$$

a_i (in.)	C	ΔK_{TH} (ksi $\sqrt{in.}$)		
		2	3.5 S_r (ksi)	5
1.90	2.82	0.3	0.5	0.7
1.70	1.64	0.5	0.9	1.3
1.50	1.27	0.7	1.3	1.8
1.30	1.12	0.9	1.5	2.2
1.10	1.03	1.0	1.8	2.6
0.85	0.97	1.3	2.2	3.2
0.65	0.96	1.5	2.6	3.6
0.45	0.97	1.7	3.0	4.3
0.25	1.03	2.2	3.8	5.5
0.09	1.22	3.1	5.4	7.7
0.055	1.36	3.5	6.2	8.8
0.035	1.46	4.1	7.2	10.3
0.025	1.53	4.7	8.2	11.7
0.015	1.62	5.7	10.0	14.2

1 in. = 25.4 mm

1 ksi = 6.89 MPa

1 ksi $\sqrt{in.}$ = 1.1 MN/m$^{3/2}$

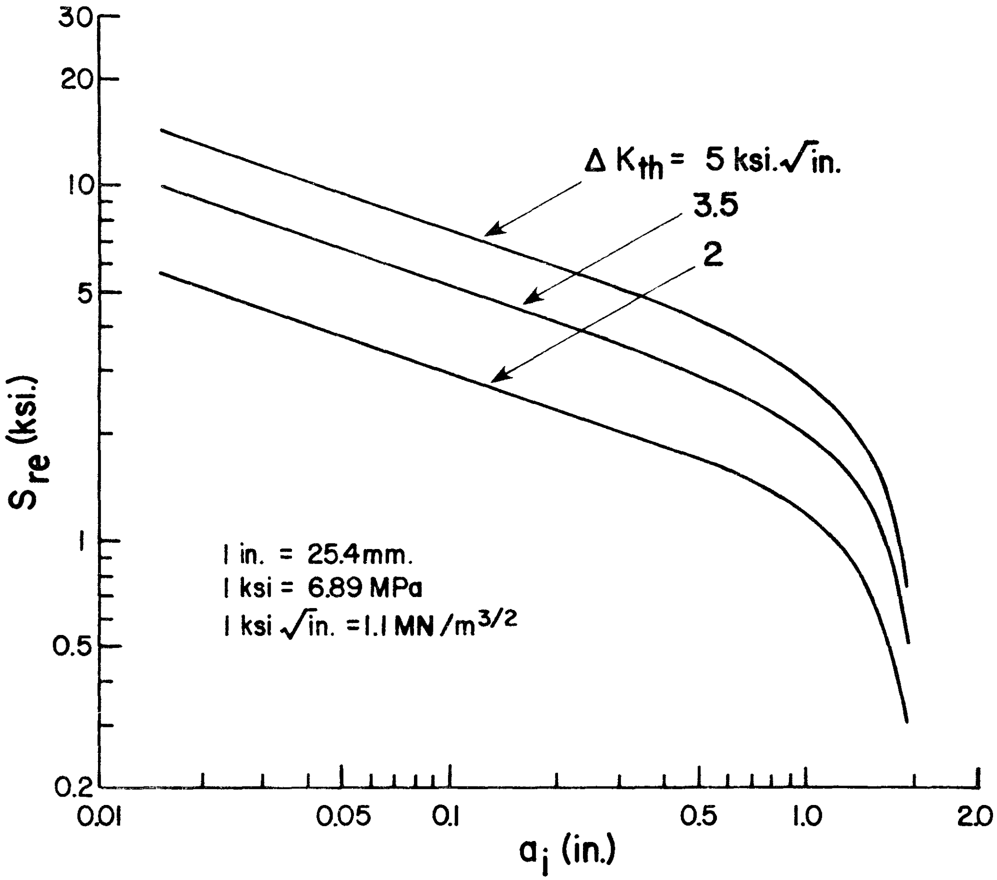

Fig. 4.8 S_r vs. a_i - surface crack - 1 to 2-1/2 slope

TABLE 4.6 SEMI-ELLIPTICAL CRACK CORRECTION - 1 TO 5 SLOPE

$C = F_S F_E F_W F_G$ (a/c = 0.6)

$F_S = 1.05$ $F_E = 0.78$ $F_W = \sqrt{\sec(\pi a/2t)}$ F_G from FEM solution

a (in.)	a/t	F_G	C
0.015	0.012	1.41	1.15
0.025	0.020	1.37	1.12
0.035	0.028	1.33	1.09
0.045	0.036	1.31	1.07
0.055	0.044	1.28	1.05
0.065	0.052	1.27	1.04
0.075	0.060	1.25	1.02
0.085	0.068	1.24	1.02
0.095	0.076	1.22	1.01
0.15	0.12	1.13	0.93
0.25	0.20	1.08	0.91
0.35	0.28	1.06	0.91
0.45	0.36	1.03	0.92
0.55	0.44	1.02	0.95
0.65	0.52	1.01	1.00
0.75	0.60	0.99	1.06
0.85	0.68	0.98	1.16
0.95	0.76	0.98	1.32
1.05	0.84	0.98	1.61
1.175	0.94	0.98	2.62

1 in. = 25.4 mm

as a function of various crack growth intervals for S_{re} equal to 6 ksi (41.34 MPa). The computed values of N are presented in Table 4.7. For a remaining fatigue life of 2.7 million cycles, the initial crack size is 0.4 in. (10.16 mm), which has a surface length of 1.3 in. (33.87 mm) in a 1-1/4-in. (31.75-mm)-thick flange plate. This is the size of surface cracks that would be of concern if missed in an inspection, and that is not likely to occur. The fatigue life for an effective stress range of 16 ksi (110.24 MPa) is presented in Table 4.8. The increase in total life due to the 1 to 5 slope transition is close to twice the number of cycles computed for the 1 to 2-1/2 slope transition for an initial crack size of 0.01 in. (0.25 mm). The S-N plots for initial crack sizes of 0.01 in. (0.25 mm), 0.1 in. (2.54 mm) and 0.5 in. (12.7 mm) are shown in Fig. 4.9 with the Category B (AASHTO) plot. The maximum stress ranges as a function of a_i, C, and ΔK_{TH}, calculated for this transition are presented in Table 4.9 and plotted in Fig. 4.10. For a 0.01-in. (0.25-mm) initial crack size, the maximum stress range for infinite life design is equal to 9 ksi (62.01 MPa) for a ΔK_{TH} value of 2 ksi $\sqrt{in.}$ (2.2 $MN/m^{3/2}$). If that is the case in the bridge being investigated, the splice detail will not fail as the maximum stress range is less than 9 ksi (62.01 MPa). Other S-N plots from any of the initial flaw sizes presented in the previous tables can be drawn similarly.

The correction C for the 1 to 2-1/2 transition corner crack is presented in Table 4.10. The fatigue life as a function of the initial crack size was computed for stress ranges of 6 ksi (41.34 MPa) and 16 ksi (110.24 MPa) and they are presented in Tables 4.11 and 4.12, respectively. For an effective stress range equal to 6 ksi (41.34 MPa), an initial corner crack size of 1 in. (25.4 mm) in a 2-in. (50.8-mm)-thick flange plate will still yield a fatigue life of 2.7 million cycles. That crack size is not

TABLE 4.7 FATIGUE LIFE - S_{re} = 6 ksi - SEMI-ELLIPTICAL CRACK
1 TO 5 SLOPE

$$\Sigma N = [1/(3.6\times10^{-10})]\ \Sigma[CS_{re}\sqrt{\pi a_{avg}}\ ]^{-3} \times \Delta a$$

S_{re} = 6 ksi

a_o (in.)	a_f (in.)	a_{avg} (in.)	C	ΔK_I (ksi $\sqrt{\text{in.}}$)	ΔN (10^3 cycles)	ΣN (10^3 cycles)
1.10	1.25	1.175	2.62	31	15	15
1.00	1.10	1.05	1.61	18	51	66
0.90	1.00	0.95	1.32	14	108	174
0.80	0.90	0.85	1.16	12	188	363
0.70	0.80	0.75	1.06	10	298	662
0.60	0.70	0.65	1.00	9	440	1,103
0.50	0.60	0.55	0.95	8	660	1,763
0.40	0.50	0.45	0.92	7	982	2,745

1 in. = 25.4 mm

1 ksi $\sqrt{\text{in.}}$ = 1.1 MN/$m^{3/2}$

TABLE 4.8 FATIGUE LIFE - S_{re} = 16 ksi - SEMI-ELLIPTICAL CRACK
1 TO 5 SLOPE

$$\Sigma N = [1/(3.6\times10^{-10})]\ \Sigma[CS_{re}\sqrt{\pi a_{avg}}\ ]^{-3} \times \Delta a$$

S_{re} = 16 ksi

a_o (in.)	a_f (in.)	a_{avg} (in.)	C	ΔK_I (ksi $\sqrt{\text{in.}}$)	ΔN (10^3 cycles)	ΣN (10^3 cycles)
1.10	1.25	1.175	2.62	81	1	1
1.00	1.10	1.05	1.61	47	2	3
0.90	1.00	0.95	1.32	37	5	9
0.80	0.90	0.85	1.16	31	9	19
0.70	0.80	0.75	1.06	26	15	34
0.60	0.70	0.65	1.00	23	23	58
0.50	0.60	0.55	0.95	20	34	92
0.40	0.50	0.45	0.92	18	51	144
0.30	0.40	0.35	0.91	16	78	222
0.20	0.30	0.25	0.91	13	129	352
0.10	0.20	0.15	0.93	11	260	612
0.09	0.10	0.095	1.01	9	40	653
0.08	0.09	0.085	1.02	9	46	699
0.07	0.08	0.075	1.02	8	55	755
0.06	0.07	0.065	1.04	8	65	820
0.05	0.06	0.055	1.05	7	81	902
0.04	0.05	0.045	1.07	7	104	1,006
0.03	0.04	0.035	1.09	6	143	1,149
0.02	0.03	0.025	1.12	5	219	1,369
0.01	0.02	0.015	1.15	4	435	1,805

1 in. = 25.4 mm
1 ksi $\sqrt{\text{in.}}$ = 1.1 MN/$\text{m}^{3/2}$

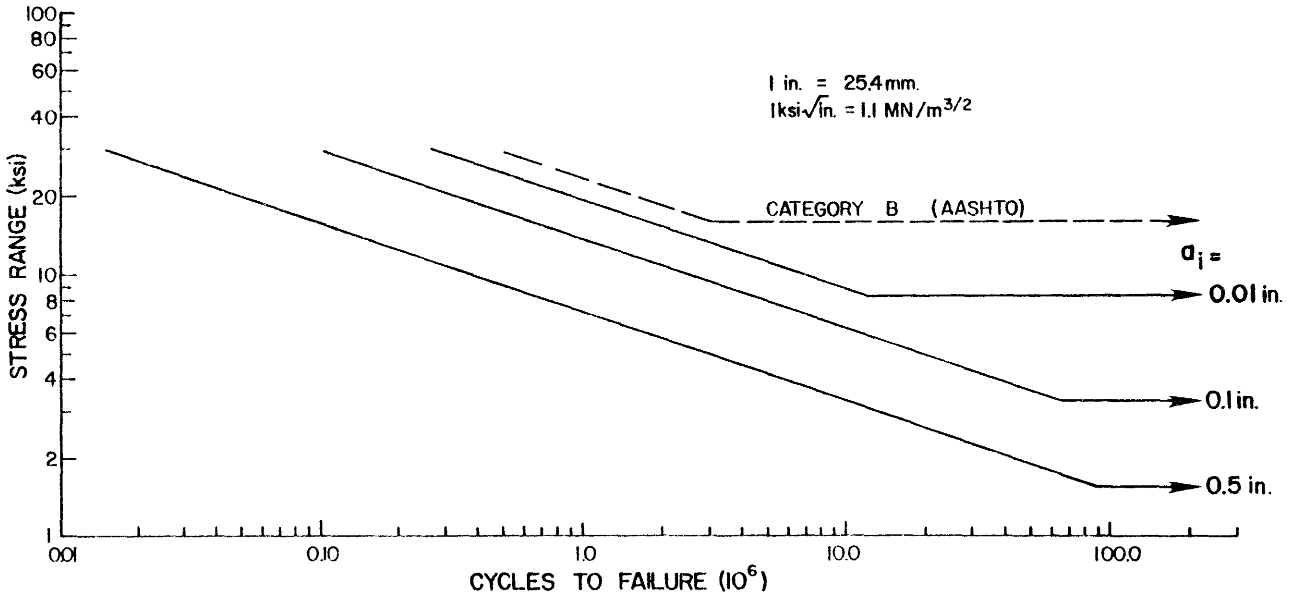

Fig. 4.9 Surface crack - S-N plots - 1 to 5 slope

TABLE 4.9 ΔK_{TH} SEMI-ELLIPTICAL CRACK - 1 TO 5 SLOPE

$$\Delta K_{TH} = C\ S_r \sqrt{\pi a_i}$$

a_i (in.)	C	ΔK_{TH} (ksi $\sqrt{\text{in.}}$)		
		2	3.5 S_r (ksi)	5
1.175	2.62	0.4	0.7	1.0
1.05	1.61	0.7	1.2	1.7
0.95	1.32	0.9	1.5	2.2
0.85	1.16	1.1	1.8	2.6
0.65	1.00	1.4	2.4	3.5
0.45	0.92	1.8	3.2	4.6
0.25	0.91	2.5	4.3	6.2
0.095	1.01	3.6	6.3	9.1
0.075	1.02	4.0	7.1	10.1
0.055	1.05	4.6	8.0	11.5
0.035	1.09	5.5	9.7	13.8
0.025	1.12	6.4	11.2	15.9
0.015	1.15	8.0	14.0	20.0

1 in. = 25.4 mm

1 ksi = 6.89 MPa

1 ksi $\sqrt{\text{in.}}$ = 1.1 $\text{MN/m}^{3/2}$

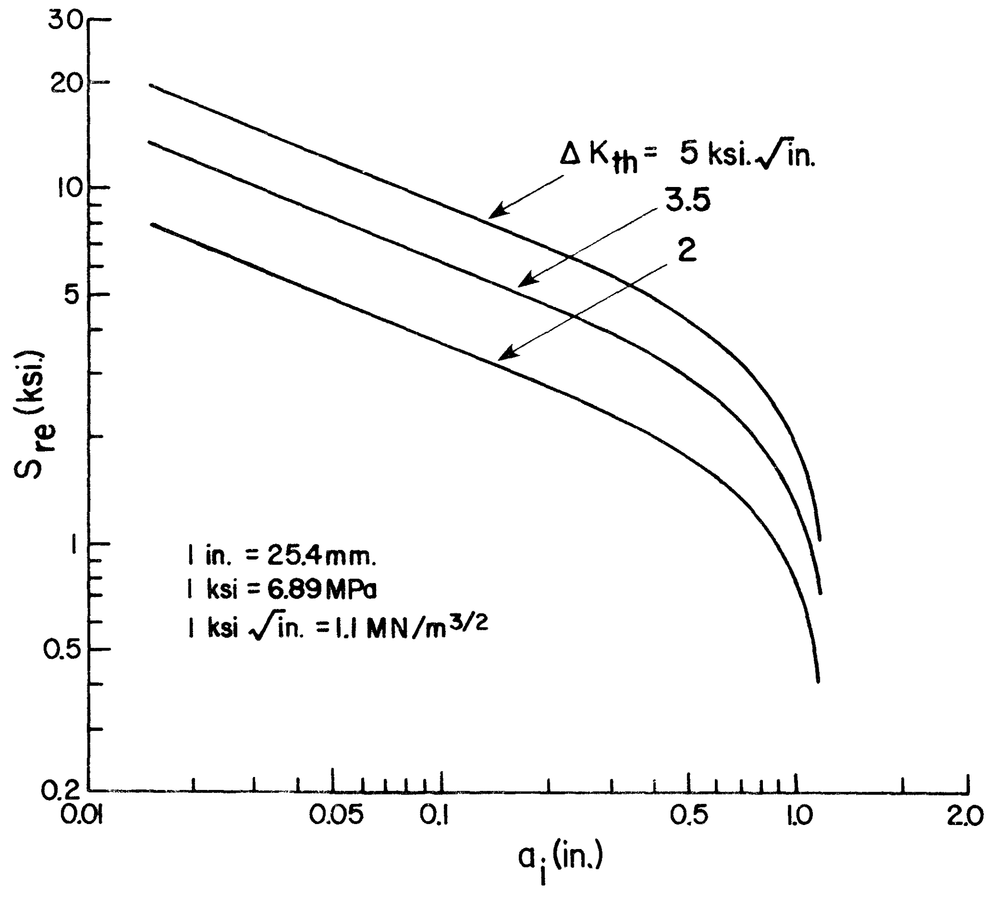

Fig. 4.10 S_r vs. a_i - semi-elliptical surface crack - 1 to 5 slope

TABLE 4.10 CORNER CRACK CORRECTION - 1 TO 2-1/2 SLOPE

$C = F_S F_E F_W F_G$

$F_S = 1.12 \times 1.12$ $F_E = 2/\pi$ $F_W = 1$ F_G from FEM solution

a (in.)	a/t	F_G	C
0.015	0.0075	1.98	1.58
0.025	0.0125	1.87	1.50
0.035	0.0175	1.78	1.42
0.045	0.0225	1.72	1.38
0.055	0.0275	1.66	1.33
0.07	0.035	1.60	1.28
0.09	0.045	1.49	1.19
0.15	0.075	1.34	1.07
0.25	0.125	1.25	1.00
0.35	0.175	1.19	0.95
0.45	0.225	1.15	0.92
0.55	0.275	1.12	0.90
0.65	0.325	1.09	0.87
0.75	0.375	1.07	0.86
0.85	0.425	1.05	0.84
0.95	0.475	1.04	0.83
1.10	0.55	1.02	0.82
1.30	0.65	0.99	0.79
1.50	0.75	0.96	0.77
1.70	0.85	0.97	0.78
1.90	0.95	0.96	0.77

1 in. = 25.4 mm

TABLE 4.11 FATIGUE LIFE - S_{re} = 6 ksi - CORNER CRACK
1 TO 2-1/2 SLOPE

$$\Sigma N = [1/3.6\times10^{-10})]\ \Sigma[C\ S_{re}\ \sqrt{\pi a_{avg}}\ ]^{-3} \times \Delta a$$

$$S_{re} = 6 \text{ ksi}$$

a_o (in.)	a_f (in.)	a_{avg} (in.)	C	ΔK_I (ksi $\sqrt{\text{in.}}$)	ΔN (10^3 cycles)	ΣN (10^3 cycles)
1.80	2.00	1.90	0.77	11	386	386
1.60	1.80	1.70	0.78	11	439	825
1.40	1.60	1.50	0.77	10	551	1,376
1.20	1.40	1.30	0.79	10	632	2,008
1.00	1.20	1.10	0.82	9	726	2,734

1 in. = 2.54 mm

1 ksi = 6.89 MPa

1 ksi $\sqrt{\text{in.}}$ = 1.1 $\text{MN/m}^{3/2}$

TABLE 4.12 FATIGUE LIFE - S_{re} = 16 ksi - CORNER CRACK
1 TO 2-1/2 SLOPE

$$\Sigma N = [1/3.6\times10^{-10})]\ \Sigma[C\ S_{re}\ \sqrt{\pi a_{avg}}\ ]^{-3} \times \Delta a$$

$$S_{re} = 16 \text{ ksi}$$

a_o (in.)	a_f (in.)	a_{avg} (in.)	C	ΔK_I (ksi $\sqrt{\text{in.}}$)	ΔN (10^3 cycles)	ΣN (10^3 cycles)
1.80	2.00	1.90	0.77	31	20	20
1.60	1.80	1.70	0.78	29	23	43
1.40	1.60	1.50	0.77	27	29	72
1.20	1.40	1.30	0.79	26	33	105
1.00	1.20	1.10	0.82	25	38	144
0.90	1.00	0.95	0.83	23	23	167
0.80	0.90	0.85	0.84	22	26	193
0.70	0.80	0.75	0.86	21	29	222
0.60	0.70	0.65	0.87	20	35	258
0.50	0.60	0.55	0.90	19	40	299
0.40	0.50	0.45	0.92	18	51	350
0.30	0.40	0.35	0.95	16	68	419
0.20	0.30	0.25	1.00	15	97	516
0.10	0.20	0.15	1.07	12	171	688
0.08	0.10	0.09	1.19	11	53	741
0.06	0.08	0.07	1.28	10	62	804
0.05	0.06	0.055	1.33	9	40	844
0.04	0.05	0.045	1.38	9	48	893
0.03	0.04	0.035	1.42	8	64	958
0.02	0.03	0.025	1.50	7	91	1,048
0.01	0.02	0.015	1.58	6	168	1,217

1 in. = 25.4 mm

1 ksi = 6.89 MPa

1 ksi $\sqrt{\text{in.}}$ = 1.1 $\text{MN/m}^{3/2}$

likely to be missed and at that level of stress range the detail should not be a problem. The S-N plots for initial crack sizes equal to 0.01 in. (0.25 mm), 0.1 in. (2.54 mm), and 0.5 in. (12.7 mm) are shown in Fig. 4.11. The maximum stress range for infinite life design is presented in Table 4.13 and plotted versus a_i in Fig. 4.12.

Table 4.14 presents the correction C for the 1 to 5 transition corner cracks. The C values were used to compute the fatigue life as a function of initial crack sizes in Tables 4.15 and 4.16. For an effective stress range equal to 6 ksi (41.34 MPa), a 0.80-in. (20.32-mm) initial corner crack in a 1-1/4-in. (31.75-mm)-thick flange plate will yield a fatigue life of over 2 million cycles. That size flaw will not be missed by a careful visual inspection. The results from Table 4.16 were used to plot the S-N curves of Fig. 4.13 for initial crack sizes of 0.01 in. (0.25 mm), 0.1 in. (2.54 mm), and 0.5 in. (12.7 mm). The values of S_r for infinite life design are presented in Table 4.17 and plotted versus a_i in Fig. 4.14. For an initial crack size equal to 0.01 in. (0.25 mm), the maximum S_r for infinite life design is equal to 9.5 ksi (65.46 MPa), but for a 0.5-in. (12.7-mm) initial crack size the value of S_r for no crack growth has to be less than 2 ksi (13.78 MPa) for ΔK_{TH} equal to 2 ksi $\sqrt{in.}$ (2.2 $MN/m^{3/2}$).

The penny-shaped crack is less critical than the surface semi-elliptical or the corner crack studied previously. When it grows to the surface, most of the fatigue life has expired; therefore, only through radiograph, ultrasonic, or other similar method could the cracks be spotted. In Tables 4.18 and 4.19, the fatigue life for penny-shaped crack growth are presented. For S_{re} equal to 6 ksi (41.34 MPa), an initial crack size of 0.90 in. (22.86 mm) in a 1-1/4-in. (31.75-mm)-thick flange will still yield a fatigue

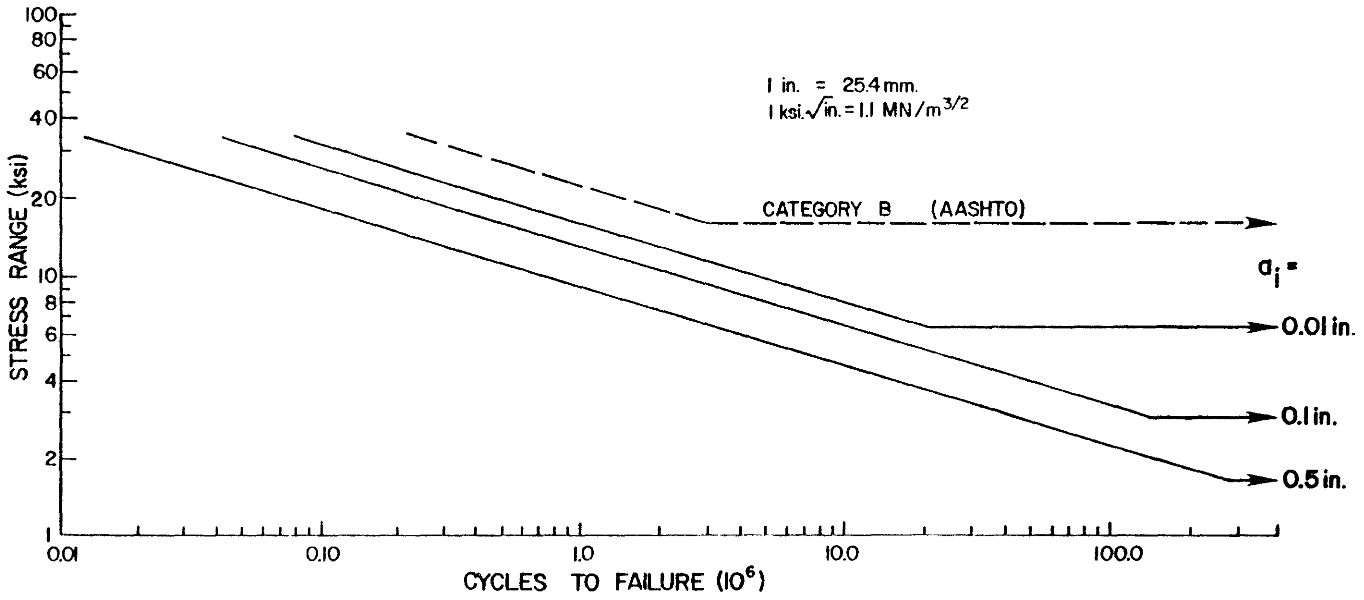

Fig. 4.11 Corner crack - S-N plots - 1 to 2-1/2 slope

TABLE 4.13 ΔK_{TH} CORNER CRACK - 1 TO 2-1/2 SLOPE

$\Delta K_{TH} = C\ S_r$ (ksi $\sqrt{\text{in.}}$)

a_i (in.)	C	ΔK_{TH} (ksi $\sqrt{\text{in.}}$)		
		2	3.5 S_r (ksi)	5
1.90	0.77	1.1	1.9	2.7
1.70	0.78	1.1	1.9	2.8
1.50	0.77	1.2	2.1	3.0
1.30	0.79	1.3	2.2	3.1
1.10	0.82	1.3	2.3	3.3
0.85	0.84	1.5	2.5	3.6
0.65	0.87	1.6	2.8	4.0
0.45	0.92	1.8	3.2	4.6
0.25	1.00	2.3	3.9	5.6
0.09	1.19	3.2	5.5	7.9
0.055	1.33	3.6	6.3	9.0
0.035	1.42	4.2	7.4	10.6
0.025	1.50	4.8	8.3	11.9
0.015	1.58	5.8	10.2	14.6

1 in. = 25.4 mm

1 ksi = 6.89 MPa

1 ksi $\sqrt{\text{in.}}$ = 1.1 $\text{MN/m}^{3/2}$

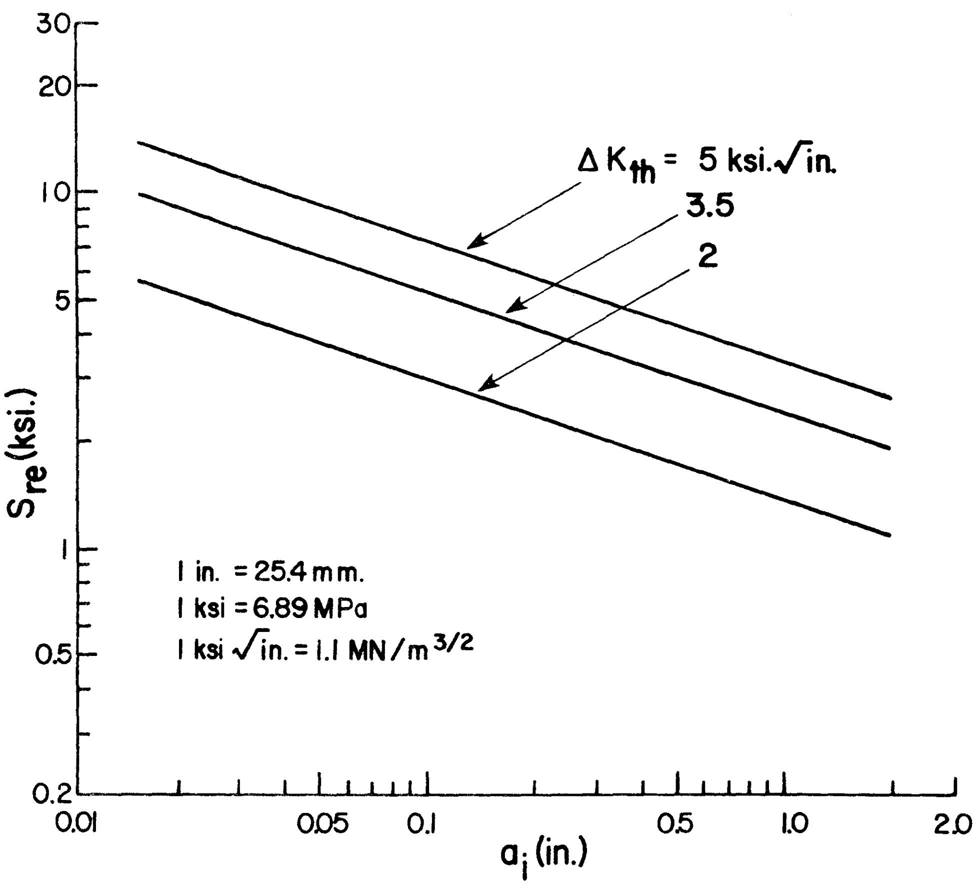

Fig. 4.12 S_r vs. a_i - corner crack - 1 to 2-1/2 slope

TABLE 4.14 CORNER CRACK CORRECTION - 1 TO 5 SLOPE

$$C = F_S F_E F_W F_G$$

$F_S = 1.12\times1.12$ $F_E = 2/\pi$ $F_W = 1$ F_G from FEM solution

a (in.)	a/t	F_G	C
0.015	0.012	1.41	1.13
0.025	0.020	1.37	1.10
0.035	0.028	1.33	1.06
0.045	0.036	1.31	1.05
0.055	0.044	1.28	1.02
0.065	0.052	1.27	1.02
0.075	0.060	1.25	1.00
0.085	0.068	1.24	0.99
0.095	0.076	1.22	0.98
0.15	0.12	1.13	0.90
0.25	0.20	1.08	0.86
0.35	0.28	1.06	0.85
0.45	0.36	1.03	0.82
0.55	0.44	1.02	0.82
0.65	0.52	1.01	0.81
0.75	0.60	0.99	0.79
0.85	0.68	0.98	0.78
0.95	0.76	0.98	0.78
1.05	0.84	0.98	0.78
1.175	0.94	0.98	0.78

1 in. = 25.4 mm

TABLE 4.15 FATIGUE LIFE - S_{re} = 6 ksi - CORNER CRACK
1 TO 5 SLOPE

$$\Sigma N = [1/3.6\times10^{-10})] \Sigma[C\ S_{re} \sqrt{\pi a_{avg}}\ ]^{-3} \times \Delta a$$

$$S_{re} = 6 \text{ ksi}$$

a_o (in.)	a_f (in.)	a_{avg} (in.)	C	ΔK_I (ksi $\sqrt{\text{in.}}$)	ΔN (10^3 cycles)	ΣN (10^3 cycles)
1.10	1.25	1.175	0.78	9	573	573
1.00	1.10	1.05	0.78	9	452	1,025
0.90	1.00	0.95	0.78	8	525	1,551
0.80	0.90	0.85	0.78	8	621	2,172

1 in. = 25.4 mm

1 ksi = 6.89 MPa

1 ksi $\sqrt{\text{in.}}$ = 1.1 $\text{MN/m}^{3/2}$

TABLE 4.16 FATIGUE LIFE - S_{re} = 16 ksi - CORNER CRACK 1 TO 5 SLOPE

$$\Sigma N = [1/3.6\times10^{-10})]\ \Sigma[C\ S_{re}\sqrt{\pi a_{avg}}\ ]^{-3} \times \Delta a$$

S_{re} = 16 ksi

a_o (in.)	a_f (in.)	a_{avg} (in.)	C	ΔK_I (ksi $\sqrt{\text{in.}}$)	ΔN (10^3 cycles)	ΣN (10^3 cycles)
1.10	1.25	1.175	0.78	24	30	30
1.00	1.10	1.05	0.78	23	23	54
0.90	1.00	0.95	0.78	22	27	81
0.80	0.90	0.85	0.78	21	32	114
0.70	0.80	0.75	0.79	20	38	152
0.60	0.70	0.65	0.81	19	43	196
0.50	0.60	0.55	0.82	18	54	250
0.40	0.50	0.45	0.82	16	73	323
0.30	0.40	0.35	0.85	15	95	419
0.20	0.30	0.25	0.86	13	153	572
0.10	0.20	0.15	0.90	10	287	860
0.09	0.10	0.095	0.98	9	44	904
0.08	0.09	0.085	0.99	9	50	954
0.07	0.08	0.075	1.00	8	59	1,014
0.06	0.07	0.065	1.02	8	69	1,083
0.05	0.06	0.055	1.02	7	88	1,172
0.04	0.05	0.045	1.05	7	110	1,282
0.03	0.04	0.035	1.06	6	156	1,438
0.02	0.03	0.025	1.10	5	231	1,670
0.01	0.02	0.015	1.13	4	459	2,129

1 in. = 25.4 mm

1 ksi = 6.89 MPa

1 ksi $\sqrt{\text{in.}}$ = 1.1 $\text{MN/m}^{3/2}$

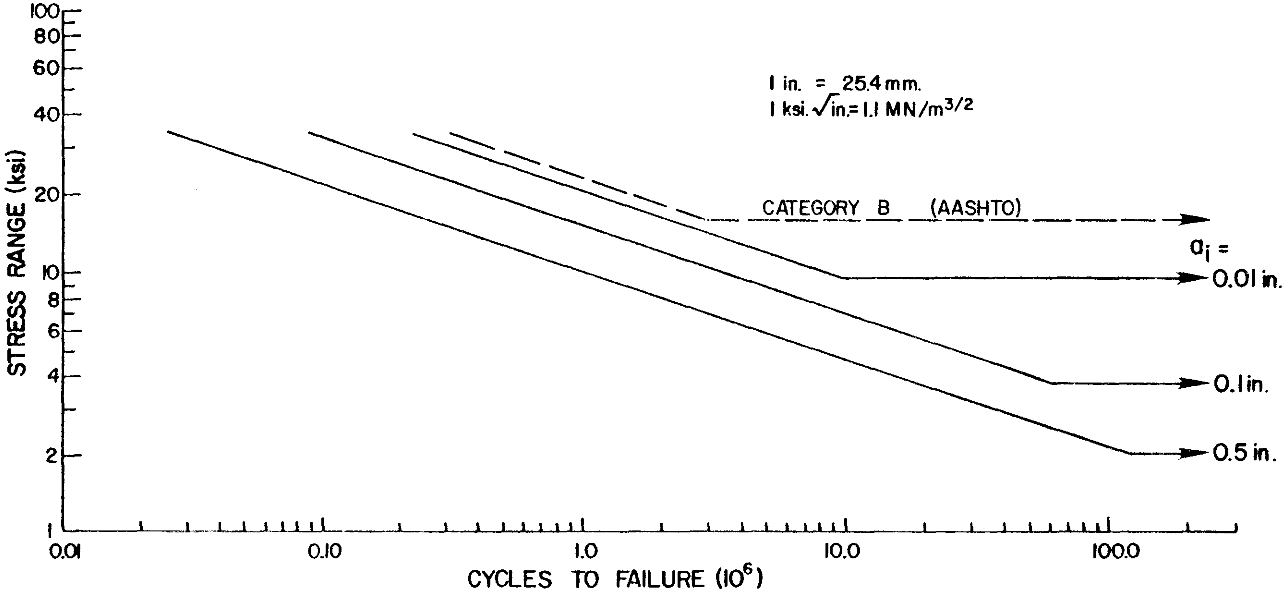

Fig. 4.13 Corner crack - S-N plots - 1 to 5 slope

TABLE 4.17 ΔK_{TH} CORNER CRACK - 1 TO 5 SLOPE

$\Delta K_{TH} = C\ S_r \sqrt{\pi a_i}$

a (in.)	C	ΔK_{TH} (ksi $\sqrt{in.}$)		
		2	3.5	5
1.175	0.78	1.3	2.3	3.3
1.05	0.78	1.4	2.5	3.5
0.95	0.78	1.5	2.6	3.7
0.85	0.78	1.6	2.7	3.9
0.65	0.81	1.7	3.0	4.3
0.45	0.82	2.1	3.6	5.1
0.25	0.86	2.6	4.6	6.6
0.095	0.98	3.7	6.5	9.3
0.075	1.00	4.1	7.2	10.3
0.055	1.02	4.7	8.3	11.8
0.035	1.06	5.7	10.0	14.2
0.025	1.10	6.5	11.4	16.2
0.015	1.13	8.2	14.3	20.4

1 in. = 25.4 mm

1 ksi = 6.89 MPa

1 ksi $\sqrt{in.}$ = 1.1 $MN/m^{3/2}$

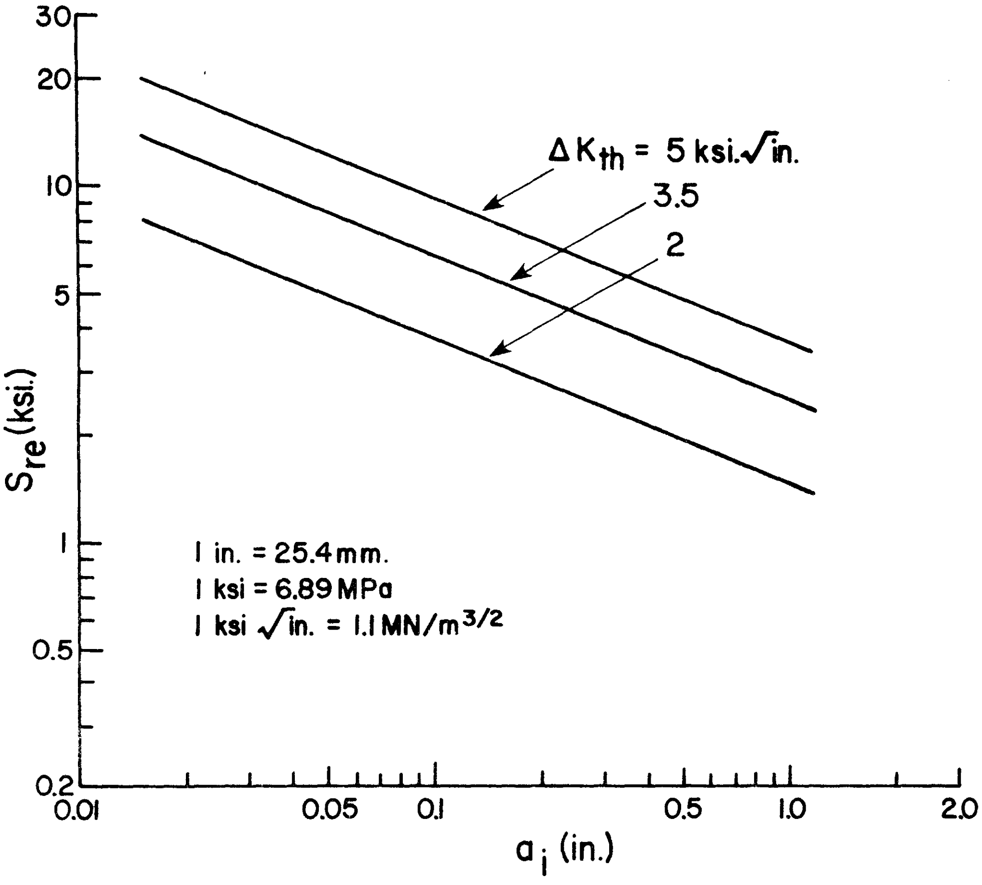

Fig. 4.14 S_r vs. a_i - corner crack - 1 to 5 slope

TABLE 4.18 FATIGUE LIFE - S_{re} = 6 ksi - PENNY-SHAPED CRACK

$$\Sigma N = [1/3.6\times10^{-10})] \ \Sigma[C \ S_{re} \sqrt{\pi a_{avg}} \ ]^{-3} \times \Delta a$$

S_{re} = 6 ksi

a_o (in.)	a_f (in.)	a_{avg} (in.)	C	ΔK_I (ksi $\sqrt{in.}$)	ΔN (10^3 cycles)	ΣN (10^3 cycles)
1.10	1.25	1.175	2/π	8	1,054	1,054
1.00	1.10	1.05		7	832	1,886
0.90	1.00	0.95		7	966	2,852

1 in. = 25.4 mm

1 ksi = 6.89 MPa

1 ksi $\sqrt{in.}$ = 1.1 $MN/m^{3/2}$

TABLE 4.19 FATIGUE LIFE - S_{re}= 16 ksi - PENNY-SHAPED CRACK

$$\Sigma N = [1/3.6\times 10^{-10})] \, \Sigma[C \, S_{rc} \sqrt{\pi a_{avg}} \,]^{-3} \times \Delta a$$

S_{re} = 16 ksi

a_o (in.)	a_f (in.)	a_{avg} (in.)	C	ΔK_I (ksi $\sqrt{\text{in.}}$)	ΔN (10^3 cycles)	ΣN (10^3 cycles)
1.80	2.00	1.90	2/π	25	36	36
1.60	1.80	1.70		24	45	81
1.40	1.60	1.50		23	51	133
1.20	1.40	1.30		21	63	196
1.00	1.20	1.10		19	81	278
0.90	1.00	0.95		18	50	329
0.80	0.90	0.85		17	60	389
0.70	0.80	0.75		16	72	462
0.60	0.70	0.65		15	90	552
0.50	0.60	0.55		14	115	668
0.40	0.50	0.45		13	156	824
0.30	0.40	0.35		11	227	1,052
0.20	0.30	0.25		9	377	1,430
0.10	0.20	0.15		7	812	2,242
0.08	0.10	0.09		6	349	2,592
0.06	0.08	0.07		5	509	3,102
0.05	0.06	0.055		5	365	3,468
0.04	0.05	0.045		4	494	3,962
0.03	0.04	0.035		4	720	4,683

1 in. = 25.4 mm

1 ksi = 6.89 MPa

1 ksi $\sqrt{\text{in.}}$ = 1.1 $\text{MN/m}^{3/2}$

life of 2.8 million cycles. An internal defect with that size diameter will not be missed by any of the nondestructive testing methods used. For the allowable S_{re} equal to 16 ksi (110.24 MPa), an initial flaw size of 0.05 in. (1.27 mm) yields over 3.4 million cycles. This is the size of initial defects we should look for in the required nondestructive inspection. The S-N plots for penny-shaped flaws are shown in Fig. 4.15. The curves for initial crack size equal to 0.05 in. (1.27 mm), 0.1 in. (2.54 mm), and 0.5 in. (12.7 mm) are compared with Category B (AASHTO) provisions. The S_r for infinite life design is presented in Table 4.20 and plotted versus a_i in Fig. 4.16. For an initial flaw size equal to 0.05 in. (1.27 mm), the maximum stress range for no crack growth has to be less than 7.8 ksi (53.74 MPa) for a ΔK_{TH} of 2 ksi $\sqrt{in.}$ (2.2 $MN/m^{3/2}$). The region we find internal defects is not affected by the stress concentration from change in the transition slope and the same results are valid for the 1 to 2-1/2 and the 1 to 5 transition.

In order to establish the fatigue life as a function of crack growth intervals, Tables 4.21 through 4.25 have been prepared for the 1 to 2-1/2 and the 1 to 5 transition slope geometries. For any of the cracks being studied, the number of cycles to failure can be found if we divide the corresponding columns by the applied stress range raised to the third power. In doing so the tables will apply for any stress range.

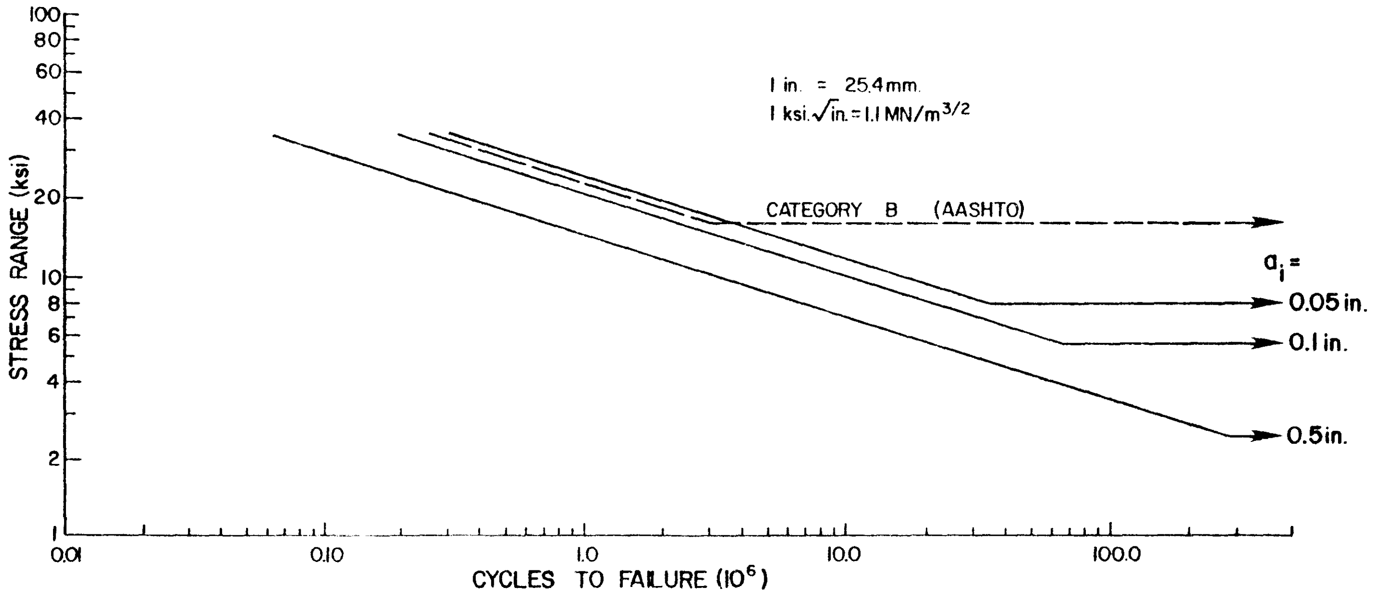

Fig. 4.15 Penny-shaped crack - S-N plots

TABLE 4.20 ΔK_{TH} PENNY-SHAPED CRACK

$$\Delta K_{TH} = C\ S_r \sqrt{\pi a_i}$$

a (in.)	C	ΔK_{TH} (ksi $\sqrt{\text{in.}}$)		
		2	3.5	5
1.90	$2/\pi$	1.3	2.3	3.2
1.70		1.4	2.4	3 4
1.50		1.4	2.5	3.6
1.30		1.6	2.7	3.9
1.10		1.7	3.0	4.2
0.85		1.9	3.4	4.8
0.65		2.2	3.8	5.5
0.45		2.6	4.6	6.6
0.25		3.5	6.2	8.9
0.009		5.9	10.3	14.8
0.055		7.6	13.2	18.9
0.035		9.5	16.6	23.7

1 in. = 25.4 mm

1 ksi = 6.89 MPa

ksi $\sqrt{\text{in.}}$ = 1.1 $\text{MN/m}^{3/2}$

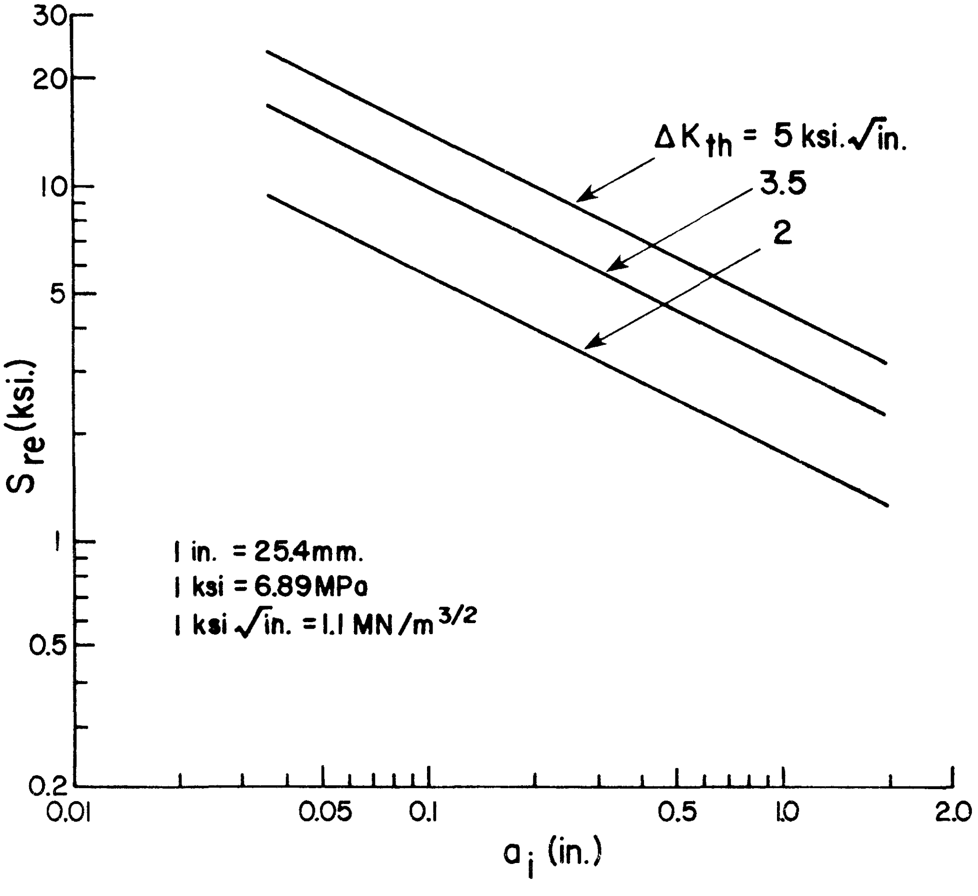

Fig. 4.16 S_r vs. a_i - penny-shaped crack

TABLE 4.21 FATIGUE LIFE - SEMI-ELLIPTICAL CRACK - 1 TO 2-1/2 SLOPE

$$\Sigma N(S_{re})^3 = [1/(3.6\times 10^{-10})]\ \Sigma[C\sqrt{\pi a_{avg}}]^{-3} \times \Delta a$$

a_o (in.)	a_f (in.)	a_{avg} (in.)	C	$\Delta N(S_{re})^3$ (10^6 cycles×ksi^3)	$\Sigma N(S_{re})^3$ (10^6 cycles×ksi^3)
1.80	2.00	1.90	2.82	1	1
1.60	1.80	1.70	1.64	10	11
1.40	1.60	1.50	1.27	26	38
1.20	1.40	1.30	1.12	47	86
1.00	1.20	1.10	1.03	79	165
0.90	1.00	0.95	0.99	55	220
0.80	0.90	0.85	0.97	69	290
0.70	0.80	0.75	0.96	86	377
0.60	0.70	0.65	0.96	107	485
0.50	0.60	0.55	0.96	138	623
0.40	0.50	0.45	0.97	181	804
0.30	0.40	0.35	0.99	248	1,052
0.20	0.30	0.25	1.03	365	1,418
0.10	0.20	0.15	1.10	645	2,063
0.08	0.10	0.09	1.22	203	2,266
0.06	0.08	0.07	1.31	239	2,506
0.05	0.06	0.055	1.36	153	2,660
0.04	0.05	0.045	1.41	186	2,846
0.03	0.04	0.035	1.46	244	3,091
0.02	0.03	0.025	1.53	352	3,443
0.01	0.02	0.015	1.62	638	4,082

1 in. = 25.4 mm
1 ksi = 6.89 MPa

TABLE 4.22 FATIGUE LIFE - SEMI-ELLIPTICAL CRACK - 1 TO 5 SLOPE

$$\Sigma N(S_{re})^3 = [1/(3.6\times10^{-10})]\ \Sigma[C\sqrt{\pi a_{avg}}]^{-3} \times \Delta a$$

a_o (in.)	a_f (in.)	a_{avg} (in.)	C	$\Delta N(S_{re})^3$ (10^6 cycles×ksi^3)	$\Sigma N(S_{re})^3$ (10^6 cycles×ksi^3)
1.10	1.25	1.175	2.62	3	3
1.00	1.10	1.05	1.61	9	12
0.90	1.00	0.95	1.32	23	36
0.80	0.90	0.85	1.16	40	77
0.70	0.80	0.75	1.06	64	141
0.60	0.70	0.65	1.00	95	236
0.50	0.60	0.55	0.95	142	379
0.40	0.50	0.45	0.92	212	591
0.30	0.40	0.35	0.91	319	911
0.20	0.30	0.25	0.91	529	1,441
0.10	0.20	0.15	0.93	1,068	2,508
0.09	0.10	0.095	1.01	165	2,674
0.08	0.09	0.085	1.02	189	2,864
0.07	0.08	0.075	1.02	228	3,092
0.06	0.07	0.065	1.04	267	3,360
0.05	0.06	0.055	1.05	334	3,694
0.04	0.05	0.045	1.07	426	4,121
0.03	0.04	0.035	1.09	588	4,709
0.02	0.03	0.025	1.12	898	5,607
0.01	0.02	0.015	1.15	1,785	7,393

1 in. = 25.4 mm
1 ksi = 6.89 MPa

TABLE 4.23 FATIGUE LIFE - CORNER CRACK - 1 TO 2-1/2 SLOPE

$$\Sigma N(S_{re})^3 = [1/(3.6\times10^{-10})]\ \Sigma[C\sqrt{\pi a_{avg}}]^{-3}\times\Delta a$$

a_o (in.)	a_f (in.)	a_{avg} (in.)	C	$\Delta N(S_{re})^3$ (10^6 cycles×ksi^3)	$\Sigma N(S_{re})^3$ (10^6 cycles×ksi^3)
1.80	2.00	1.90	0.77	83	83
1.60	1.80	1.70	0.78	94	178
1.40	1.60	1.50	0.77	119	297
1.20	1.40	1.30	0.79	136	433
1.00	1.20	1.10	0.82	156	590
0.90	1.00	0.95	0.83	94	684
0.80	0.90	0.85	0.84	107	792
0.70	0.80	0.75	0.86	120	913
0.60	0.70	0.65	0.87	144	1,058
0.50	0.60	0.55	0.90	167	1,225
0.40	0.50	0.45	0.92	212	1,438
0.30	0.40	0.35	0.95	281	1,719
0.20	0.30	0.25	1.00	399	2,118
0.10	0.20	0.15	1.07	700	2,819
0.08	0.10	0.09	1.19	219	3,038
0.06	0.08	0.07	1.28	256	3,295
0.05	0.06	0.055	1.33	164	3,459
0.04	0.05	0.045	1.38	198	3,658
0.03	0.04	0.035	1.42	266	3,924
0.02	0.03	0.025	1.50	373	4,298
0.01	0.02	0.015	1.58	688	4,906

1 in. = 25.4 mm
1 ksi = 6.89 MPa

TABLE 4.24 FATIGUE LIFE - CORNER CRACK - 1 TO 5 SLOPE

$$\Sigma N(S_{re})^3 = [1/(3.6\times 10^{-10})]\ \Sigma [C\ \sqrt{\pi a_{avg}}]^{-3} \times \Delta a$$

a_o (in.)	a_f (in.)	a_{avg} (in.)	C	$\Delta N(S_{re})^3$ (10^6 cycles×ksi^3)	$\Sigma N(S_{re})^3$ (10^6 cycles×ksi^3)
1.10	1.25	1.175	0.78	123	123
1.00	1.10	1.05	0.78	97	221
0.90	1.00	0.95	0.78	113	335
0.80	0.90	0.85	0.78	134	469
0.70	0.80	0.75	0.79	155	624
0.60	0.70	0.65	0.81	179	804
0.50	0.60	0.55	0.82	221	1,026
0.40	0.50	0.45	0.82	299	1,326
0.30	0.40	0.35	0.85	392	1,718
0.20	0.30	0.25	0.86	627	2,345
0.10	0.20	0.15	0.90	1,178	3,523
0.09	0.10	0.095	0.98	181	3,704
0.08	0.09	0.085	0.99	207	3,912
0.07	0.08	0.075	1.00	242	4,155
0.06	0.07	0.065	1.02	283	4,438
0.05	0.06	0.055	1.02	364	4,803
0.04	0.05	0.045	1.05	451	5,254
0.03	0.04	0.035	1.06	639	5,894
0.02	0.03	0.025	1.10	948	6,842
0.01	0.02	0.015	1.13	1,882	8,724

1 in. = 25.4 mm
1 ksi = 6.89 MPa

TABLE 4.25 FATIGUE LIFE - PENNY-SHAPED CRACK

$$\Sigma N(S_{re})^3 = [1/(3.6\times10^{-10})]\ \Sigma[C\sqrt{\pi a_{avg}}]^{-3} \times \Delta a$$

a_o (in.)	a_f (in.)	a_{avg} (in.)	C	$\Delta N(S_{re})^3$ (10^6cycles×ksi^3)	$\Sigma N(S_{re})^3$ (10^6cycles×ksi^3)
1.80	2.00	1.90	$2/\pi$	147	147
1.60	1.80	1.70		174	322
1.40	1.60	1.50		210	532
1.20	1.40	1.30		260	793
1.00	1.20	1.10		335	1,129
0.90	1.00	0.95		208	1,337
0.80	0.90	0.85		246	1,584
0.70	0.80	0.75		297	1,882
0.60	0.70	0.65		368	2,251
0.50	0.60	0.55		474	2,725
0.40	0.50	0.45		640	3,365
0.30	0.40	0.35		933	4,299
0.20	0.30	0.25		1,547	5,846
0.10	0.20	0.15		3,328	9,174
0.08	0.10	0.09		1,432	10,606
0.06	0.08	0.07		2,087	12,694
0.05	0.06	0.055		1,499	14,193
0.04	0.05	0.045		2,025	16,218
0.03	0.04	0.035		2,952	19,171

1 in. = 25.4 mm
1 ksi = 6.89 MPa

CHAPTER 5

SUMMARY AND CONCLUSIONS

(1) Analytical solutions for C, the stress gradient and geometry correction applied to the stress intensity factor for flange thickness transition, were estimated using the superposition approach. The stress gradient correction, F_G, was calculated using a finite element method solution for the AASHTO 1 to 2-1/2 transition slope and for the 1 to 5 slope used in the bridge being investigated. The generated F_G solution should be very accurate for a/t ratios greater than 0.01. These solutions are applied to surface and corner cracks at the toe or end of the transition weld.

(2) The bridge under investigation was modeled using a direct stiffness method computer program. The load was assumed to be carried solely by one of the two main girders. The measured influence lines showed part of the load was transferred to the "unloaded" girder. The redistribution was not the same for different sections.

(3) The bridge response under increasing speed showed a significant increase in stress range due to increased vibrations. At the 55 MPH normal traffic speed, the vibration cycles had amplitudes of the same magnitude as the static stress range. These dynamic vibrations had a frequency equal to the bridge's natural frequency.

(4) Due to the induced vibrations, the measured effective stress range at the splice section was close to two times the

stress range calculated by applying the total load to a single girder. However, for the calculated effective stress range of 6 ksi (41.34 MPa), only cracks bigger than 0.40 in. (10.16 mm) in the 1-3/4-in. (31.75-mm)-thick plate will yield fatigue lives below 2 million cycles. This size of cracks is not likely to be missed in an inspection. Consequently, this detail should not be a critical problem on the bridge studied if it is adequately inspected.

(5) The 1 to 5 slope transition yields close to two times the fatigue life calculated for the 1 to 2-1/2 transition for the same initial crack size. The change in cost between the details is not significant. The 1 to 5 slope transition is recommended due to the less severe stress concentration and longer fatigue life.

(6) Solutions for the fatigue life of surface, corner, and interior cracks are presented in tabular form. The fatigue life as a function of the initial crack sizes can be estimated from these tables. They can be applied to any desired stress range. S-N plots for the various crack geometries and both transition slopes are presented for small crack sizes. They are compared to the experimental S-N plot for Category B details. The effective stress ranges were plotted versus initial flaw sizes for ΔK_{TH} equal to 2, 3.5, and 5 ksi $\sqrt{\text{in.}}$*; the stress range below which no crack growth will occur can be determined using the appropriate values of ΔK_{TH} and a_i.

(7) Recommended Studies

7.1 The accuracy of the analytical solutions should be checked against experimental data. The initial crack sizes should

---

*1 ksi $\sqrt{\text{in.}}$ = 1.1 $\text{MN/m}^{3/2}$

be measured accurately as the value of a_i has a significant influence upon fatigue life.

7.2 The detail response under a large number of low fatigue cycles should be determined. Each major cycle due to a single truck has superimposed vibration cycles at the bridge's natural frequency. Over twenty of these low amplitude cycles occur with a single vehicle passage.

APPENDIX A

FINITE ELEMENT SOLUTION AND F_G DETERMINATION

Stress intensity factor solutions for practical problems must be obtained to allow a design solution using fracture mechanics principles. Closed-formed solutions for idealized geometries will not always be found in the design of structures. One approach to the problem is to use the superposition of accepted solutions, as it has been done in the estimation of K value expressions for semi-elliptical surface flaws, corner flaws, and interior penny-shaped flaws. When the point of interest falls in a region of change in geometry, the nonuniform stress fields have to be accounted for; this can be achieved by the superposition of a stress gradient correction, F_G.

When cracks are present in the regions of geometrical discontinuities special crack tip elements with inverse square root singularity will yield very accurate results in the finite element method solution. When the K values are needed for various crack sizes as in fatigue design, this direct approach becomes prohibitive in terms of computer time.

An alternate approach proposed in Ref. 14 and used in this study requires only one finite element solution at the section where the cracks shall be inserted. The integration of the stresses along the crack can be obtained by the use of Eq. (15) and the summation of discrete stresses, as in Fig. 2.11, gives results well within the desired accuracy.

An available two-dimensional finite element program [19] was used to determine the distribution of stresses at the AASHTO 1 to 2-1/2 thickness transition slope and at the 1 to 5 slope used in the bridge being investigated. The overall dimensions of the flange thickness transition models are shown in Figs. A1 and A2, along with the boundary conditions. The nominal stresses were applied at a distance over three times the flange thickness so as not to influence the stress field distribution. The stress along the flange thickness was taken as a constant rather than the actual trapezoidal distribution. The difference in the stress on the top and bottom of the flange in the girder studied was 3 percent; this small variation was felt to be insignificant.

A nonreformulated quadratic displacement subparametric isotropic quadrilateral element, QUAD8, and a reformulated isotropic quadratic displacement triangular element, TRI, were used as the 174 quadrilateral and the four triangular elements in which the models were subdivided. The nine quadrilateral elements at the region of interest (see the dashed elements in the models) were rezoned in a much finer grid, with 25×9 elements from a subdivision of five for each dimension. Plane stress solutions were used for both geometries.

Right at the point of change in geometry where the two quadrilateral and the two triangular elements are connected, the stress concentration factor is dependent upon mesh size. At this point, the solution does not converge as we change to finer meshes due to the singularity at that node. From the solution at the neighborhood of that node, a smooth curve could be used to extrapolate that solution to the point of maximum stress concentration. A more refined procedure was used without employing much more effort, due to the automatic node spacing generation feature built in the TEXGAP finite element program. The mesh in the area of interest was refined and the convergence criteria defined as acceptable when the difference in stress between the two finer meshes at a distance a/t equal to 0.01 was less than 5 percent,

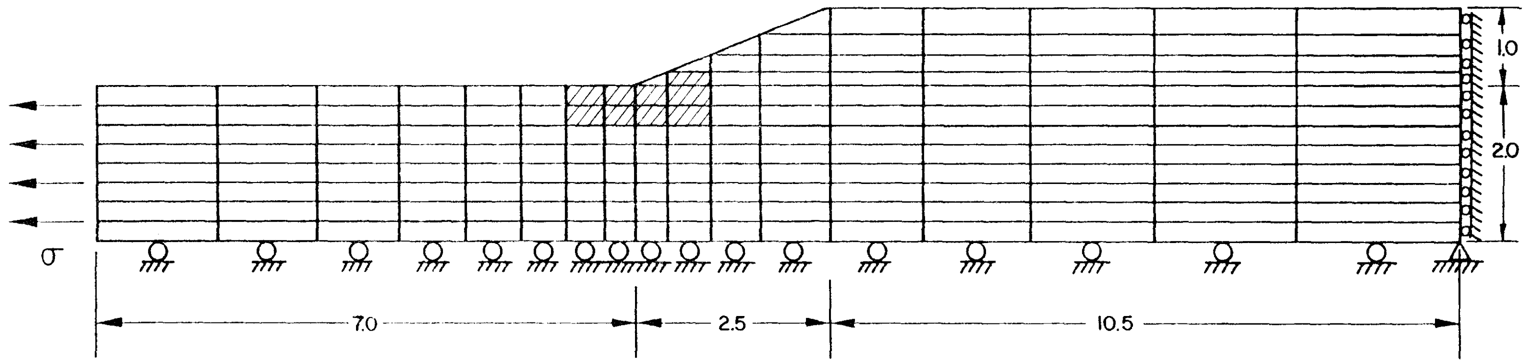

Fig. A1 FEM model - 1 to 2-1/2 slope

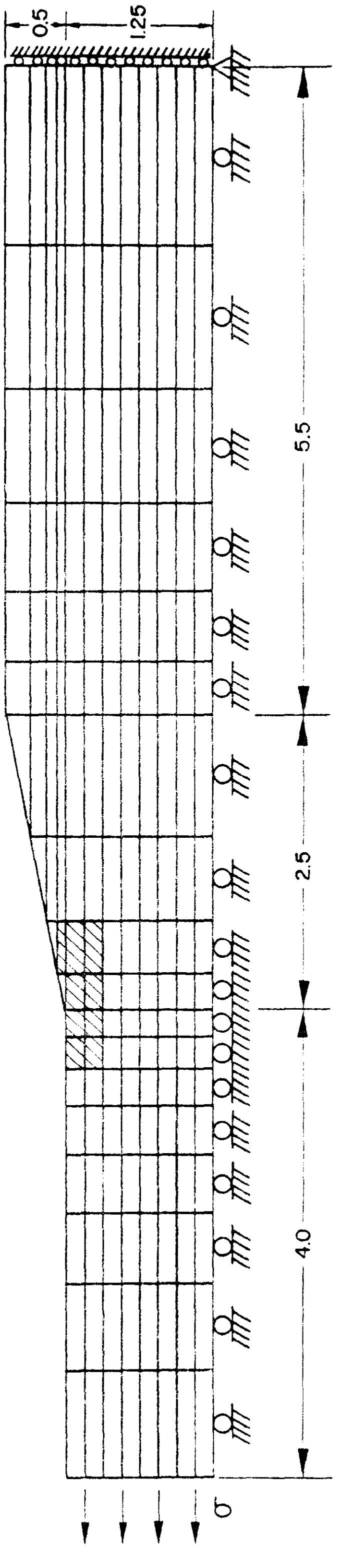

Fig. A2 FEM model - 1 to 5 slope

where a is the crack length measured at the point of stress concentration and t is the flange thickness, as in Fig. A1. When the above criteria were met, the finer mesh stress concentration decay was then used to calculate the F_G correction. The influence of the stress concentration on F_G is the greatest at the crack tip; therefore, for crack sizes greater than 0.01 of a/t, the F_G values are very accurate.

For the 1 to 2-1/2 thickness transition slope, four refinements were necessary to meet the 5 percent difference criterion at a/t equal to 0.01. The solutions for each mesh gradient used are presented in Tables A1 through A4. The finest rezone gave a value of a/t equal to 0.0043. The values presented in the tables are node stress values from the finite element plane-stress solution. The gradient ℓ_1/ℓ_8 for each solution defines the ratio of the bottom element in the vertical dimension to the top element. The ratios used were 1, 4, 8, and 16. In Figs. A1 and A2, the gradient ratio equal to 1 was used, and the 4, 8, and 16 gradient ratios are shown in Figs. A3, A4, and A5.

For each vertical gradient solution table, the stress concentration values for the rezone solution are also presented. They are all node values. The stress concentration factor at the point of change in geometry is the average from the two quadrilateral node solutions.

The stress concentration decay as a function of a/t is plotted in Figs. A6 through A8 for the 1, 4, and 8 gradient ratio solutions. The 16 gradient ratio solution was presented in Fig. 2.24. We can see the decay is steeper for the finer meshes for a/t values close to zero. The curves converge for very small a/t ratios.

TABLE A1 FEM NODE STRESSES - 1 TO 2-1/2 SLOPE

$\ell_1/\ell_8 = 1$

1st Solution		Rezone	
a/t	SC	a/t	SC
0.0000	1.60*	0.0000	1.60*
0.1250	1.11	0.0250	1.39
0.2500	1.02	0.0500	1.30
0.3750	0.96	0.0750	1.23
0.5000	0.93	0.1000	1.17
0.6250	0.91	0.1250	1.13
0.7500	0.90	0.1500	1.10
0.8750	0.90	0.1750	1.07
1.0000	0.90	0.2000	1.05
		0.2250	1.03
		0.2500	1.02

*Average stress at singularity from the two quadrilateral element nodes, 1.49 and 1.71. The triangular node stress concentration is 1.21.

TABLE A2 FEM NODE STRESSES - 1 TO 2-1/2 SLOPE

$\ell_1/\ell_8 = 4$

1st Solution		Rezone	
a/t	SC	a/t	SC
0.0000	1.78*	0.0000	1.78*
0.0565	1.30	0.0113	1.58
0.1254	1.13	0.0226	1.49
0.2094	1.04	0.0339	1.41
0.3117	0.98	0.0452	1.35
0.4365	0.94	0.0565	1.30
0.5886	0.92	0.0703	1.25
0.7740	0.90	0.0841	1.21
1.0000	0.90	0.0978	1.18
		0.1116	1.15
		0.1254	1.13

*Average stress at singularity from the two quadrilateral element nodes, 1.63 and 1.93. The triangular node stress concentration is 1.33.

TABLE A3 FEM NODE STRESSES - 1 TO 2-1/2 SLOPE

$\ell_1/\ell_8 = 8$

1st Solution		Rezone	
a/t	SC	a/t	SC
0.0000	1.96*	0.0000	1.96*
0.0354	1.40	0.0071	1.73
0.0886	1.22	0.0142	1.63
0.1473	1.10	0.0212	1.54
0.2336	1.02	0.0283	1.47
0.3498	0.97	0.0354	1.41
0.5062	0.93	0.0460	1.36
0.7167	0.91	0.0567	1.31
1.0000	0.90	0.0673	1.27
		0.0780	1.24
		0.0886	1.21

*Average stress at singularity from the two quadrilateral element nodes, 1.80 and 2.12. The triangular node stress concentration is 1.47.

TABLE A4 FEM NODE STRESSES - 1 TO 2-1/2 SLOPE

$\ell_1/\ell_8 = 16$

1st Solution		Rezone	
a/t	SC	a/t	SC
0.0000	2.24*	0.0000	2.24*
0.0214	1.54	0.0043	1.94
0.0531	1.32	0.0085	1.81
0.1002	1.17	0.0128	1.70
0.1702	1.07	0.0171	1.62
0.2743	1.00	0.0214	1.56
0.4289	0.95	0.0277	1.48
0.6586	0.91	0.0340	1.43
1.0000	0.90	0.0404	1.38
		0.0467	1.35
		0.0531	1.31

*Average stress at singularity from the two quadrilateral element nodes, 2.07 and 2.40. The triangular node stress concentration is 1.70.

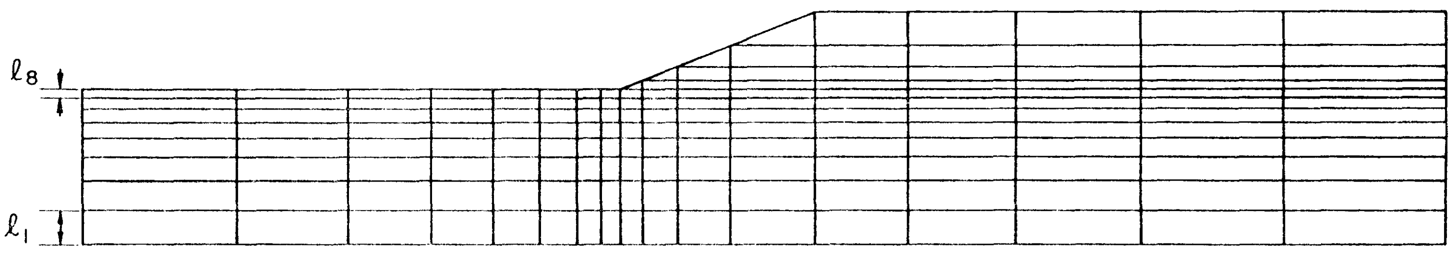

Fig. A3 FEM gradient ratio $\ell_1/\ell_8 = 4$

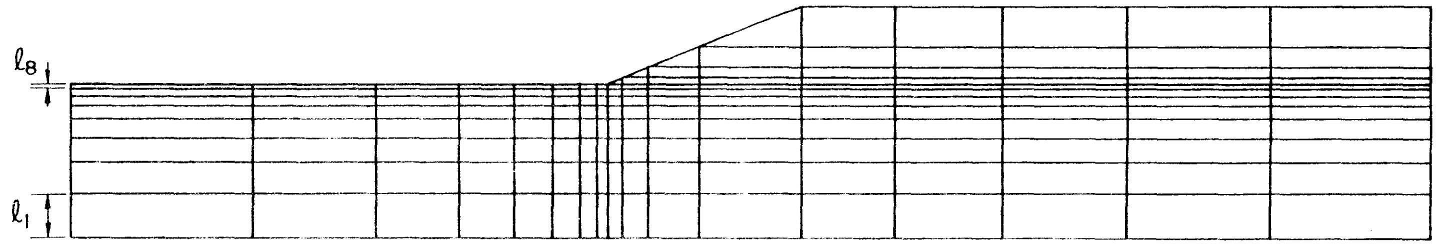

Fig. A4 FEM gradient ratio $\ell_1/\ell_8 = 8$

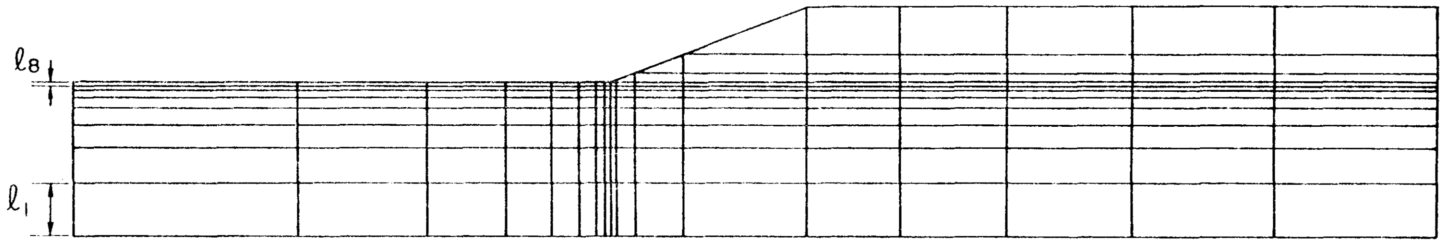

Fig. A5 FEM gradient ratio $\ell_1/\ell_8 = 16$

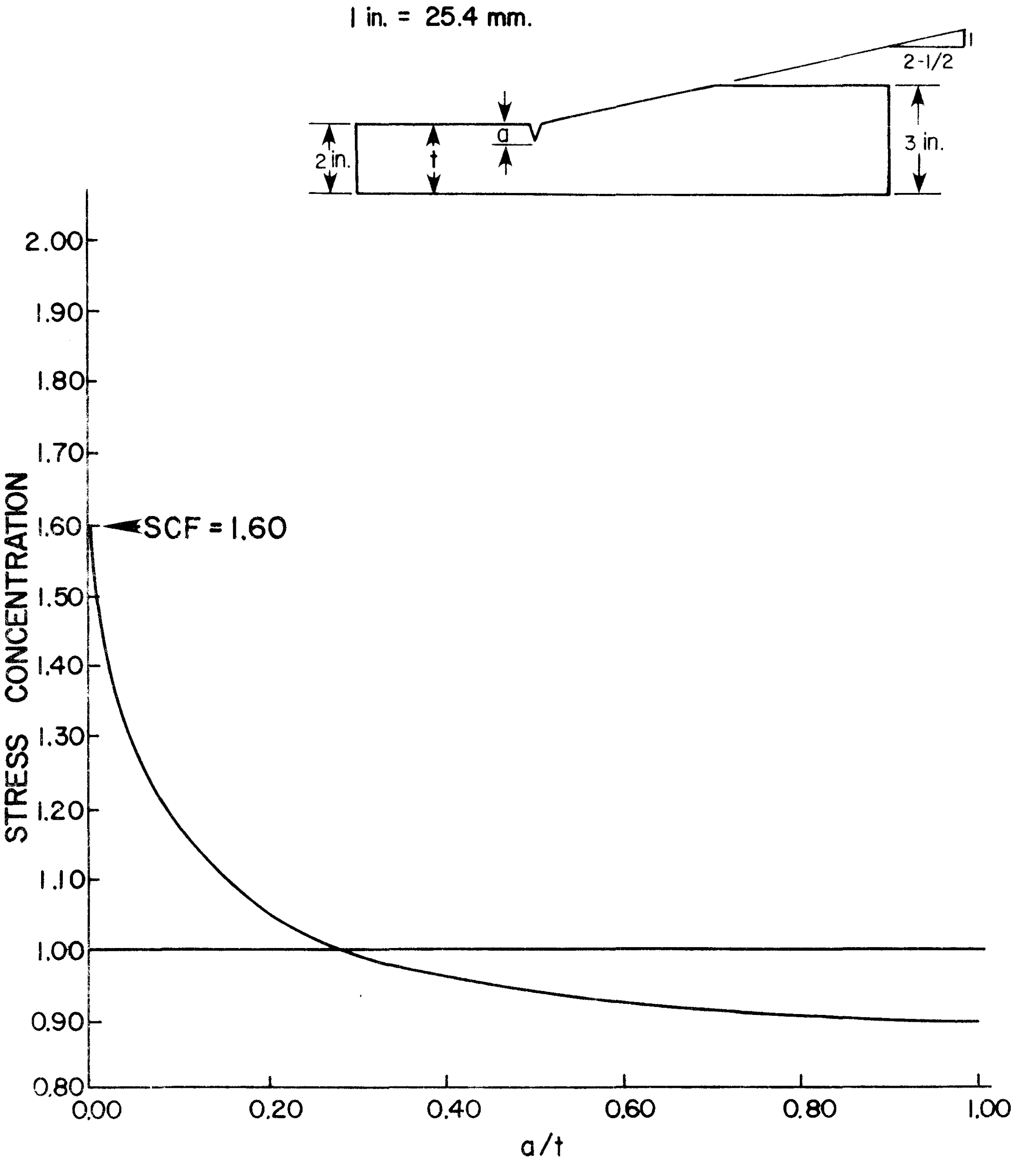

Fig. A6 Stress concentration decay - 1 to 2-1/2 slope $\ell_1/\ell_8 = 1$

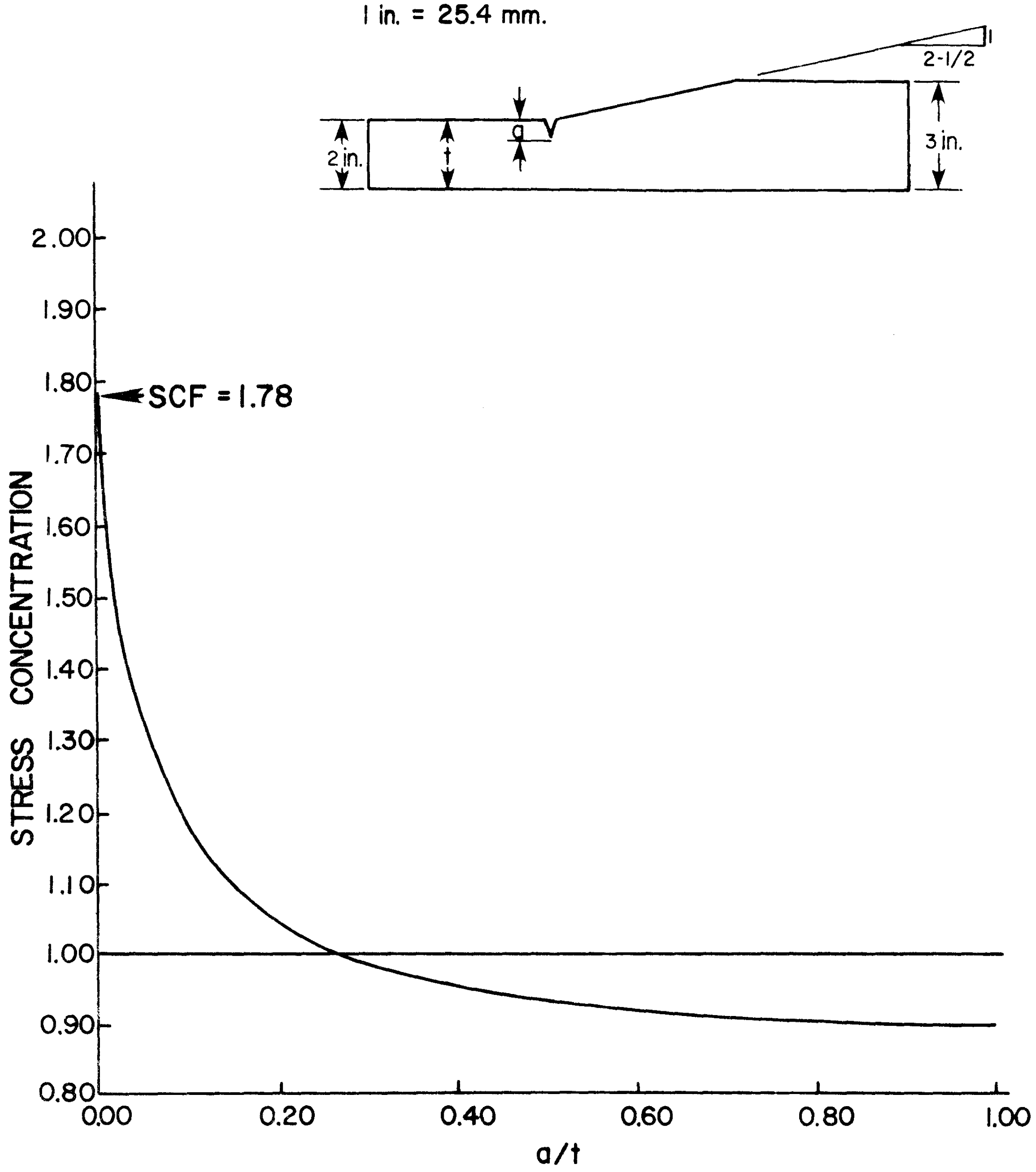

Fig. A7 Stress concentration decay - 1 to 2-1/2 slope $\ell_1/\ell_8 = 4$

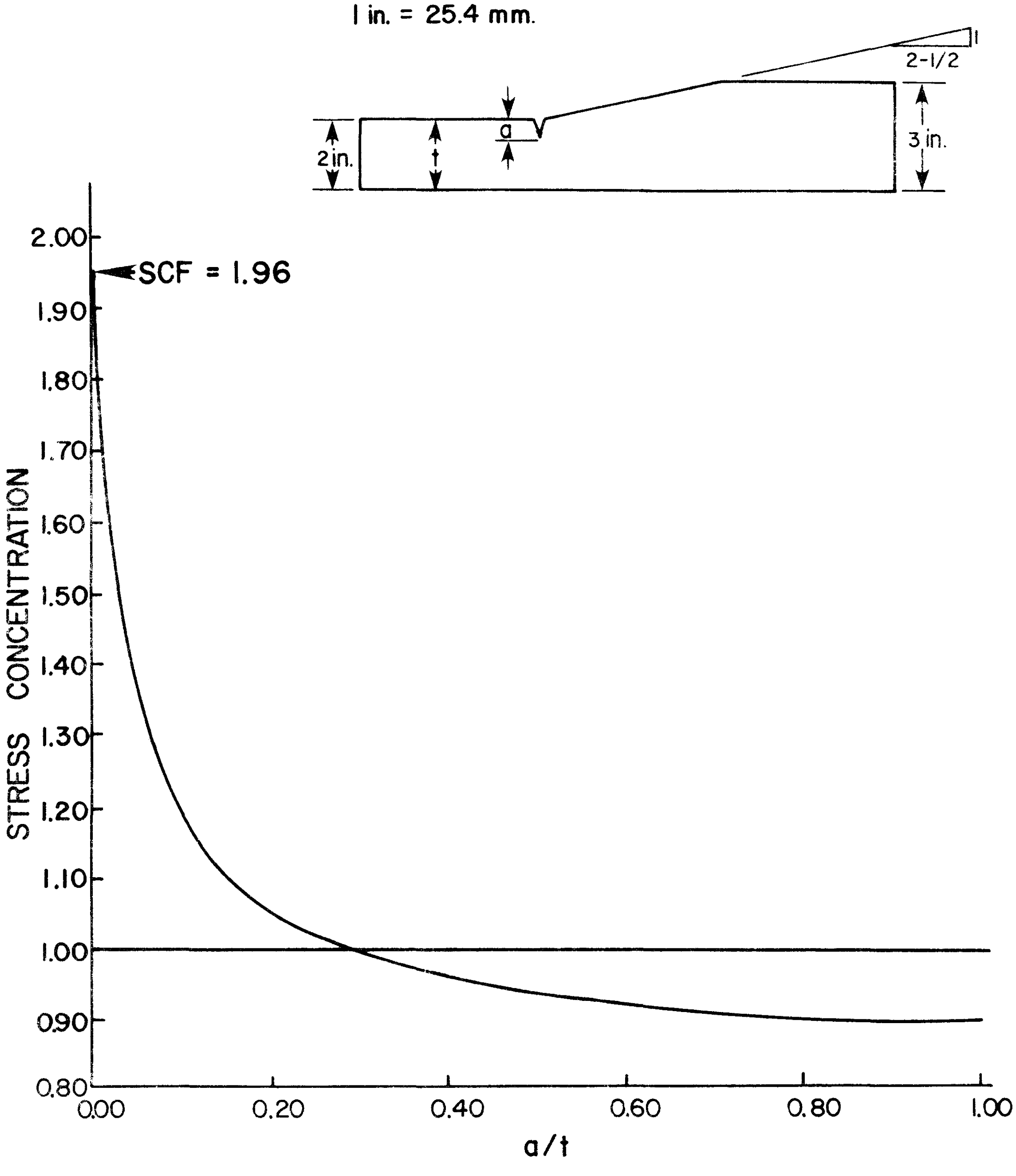

Fig. A8 Stress concentration decay - 1 to 2-1/2 slope
$\ell_1/\ell_8 = 8$

For the 1 to 5 thickness transition slope, three refinements were necessary to meet the 5 percent difference criteria at a/t of 0.01. The solutions for each mesh gradient used are presented in Tables A5 through A7 for the mesh gradient ratio, ℓ_1/ℓ_8, equal to 1, 4, and 8. The finest rezone for this slope gave a value of a/t equal to 0.0071. The stress concentration decay for gradients 1 and 4 is shown in Figs. A9 and A10. The decay for the gradient ratio equal to 8 was presented in Fig. 2.24. The same comments for the 1 to 2-1/2 slope solution apply to this one, but because of the less severe geometry change, the 1 to 5 slope solution converged more rapidly.

Tables A8 and A9 and Figs. A11 and A12 show the stress concentration at the flange surface for the 1 to 2-1/2 and the 1 to 5 slope thickness transition. The stress concentration decay is again very steep and at about 1 in. (25.4 mm) into the flange the value of the stress concentration equals the applied nominal stress. The solutions used for the surface decay were the last refined meshes with ℓ_1/ℓ_8 equal to 16 and 8 for the 1 to 2-1/2 and 1 to 5 slope, respectively.

The values of F_G were calculated from the stress concentration decay node stresses and linearly interpolated for intermediate values. The F_G values for all mesh refinements and for both slopes are presented in Tables A10 through A16. The values of a and b_i refer to Eq. (15) and Fig. 2.11, where the nodes SC refer to σ_{b_i}/σ, the stress concentration to nominal stress ratio. The F_G solutions were presented in Figs. 2.13 and 2.15.

TABLE A5 FEM NODE STRESSES - 1 TO 5 SLOPE

$\ell_1/\ell_8 = 1$

1st Solution		Rezone	
a/t	SC	a/t	SC
0.0000	1.34*	0.0000	1.34*
0.1250	1.08	0.0250	1.23
0.2500	1.02	0.0500	1.18
0.3750	0.98	0.0750	1.14
0.5000	0.96	0.1000	1.11
0.6250	0.95	0.1250	1.09
0.7500	0.94	0.1500	1.07
0.8750	0.94	0.1750	1.05
1.0000	0.94	0.2000	1.04
		0.2250	1.03
		0.2500	1.02

*Average stress at singularity from the two quadilateral element nodes, 1.29 and 1.39. The triangular node stress concentration is 1.13.

TABLE A6 FEM NODES STRESSES - 1 TO 5 SLOPE

$\ell_1/\ell_8 = 4$

1st Solution		Rezone	
a/t	SC	a/t	SC
0.0000	1.43*	0.0000	1.43*
0.0565	1.18	0.0113	1.33
0.1254	1.09	0.0226	1.28
0.2094	1.03	0.0339	1.24
0.3117	1.00	0.0452	1.20
0.4365	0.97	0.0565	1.18
0.5886	0.95	0.0703	1.15
0.7740	0.94	0.0841	1.13
1.0000	0.94	0.0978	1.11
		0.1116	1.10
		0.1254	1.08

*Average stress at singularity from the two quadrilateral element nodes, 1.37 and 1.49. The triangular node stress concentration is 1.20.

TABLE A7 FEM NODE STRESSES - 1 TO 5 SLOPE

$\ell_1/\ell_8 = 8$

1st Solution		Rezone	
a/t	SC	a/t	SC
0.0000	1.50*	0.0000	1.50*
0.0354	1.23	0.0071	1.39
0.0886	1.13	0.0142	1.34
0.1473	1.07	0.0212	1.30
0.2336	1.02	0.0283	1.27
0.3498	0.99	0.0354	1.24
0.5062	0.96	0.0460	1.21
0.7167	0.94	0.0567	1.18
1.0000	0.94	0.0673	1.16
		0.0780	1.15
		0.0886	1.13

*Average stress at singularity from the two quadrilateral element nodes, 1.42 and 1.58. The triangular node stress concentration is 1.24.

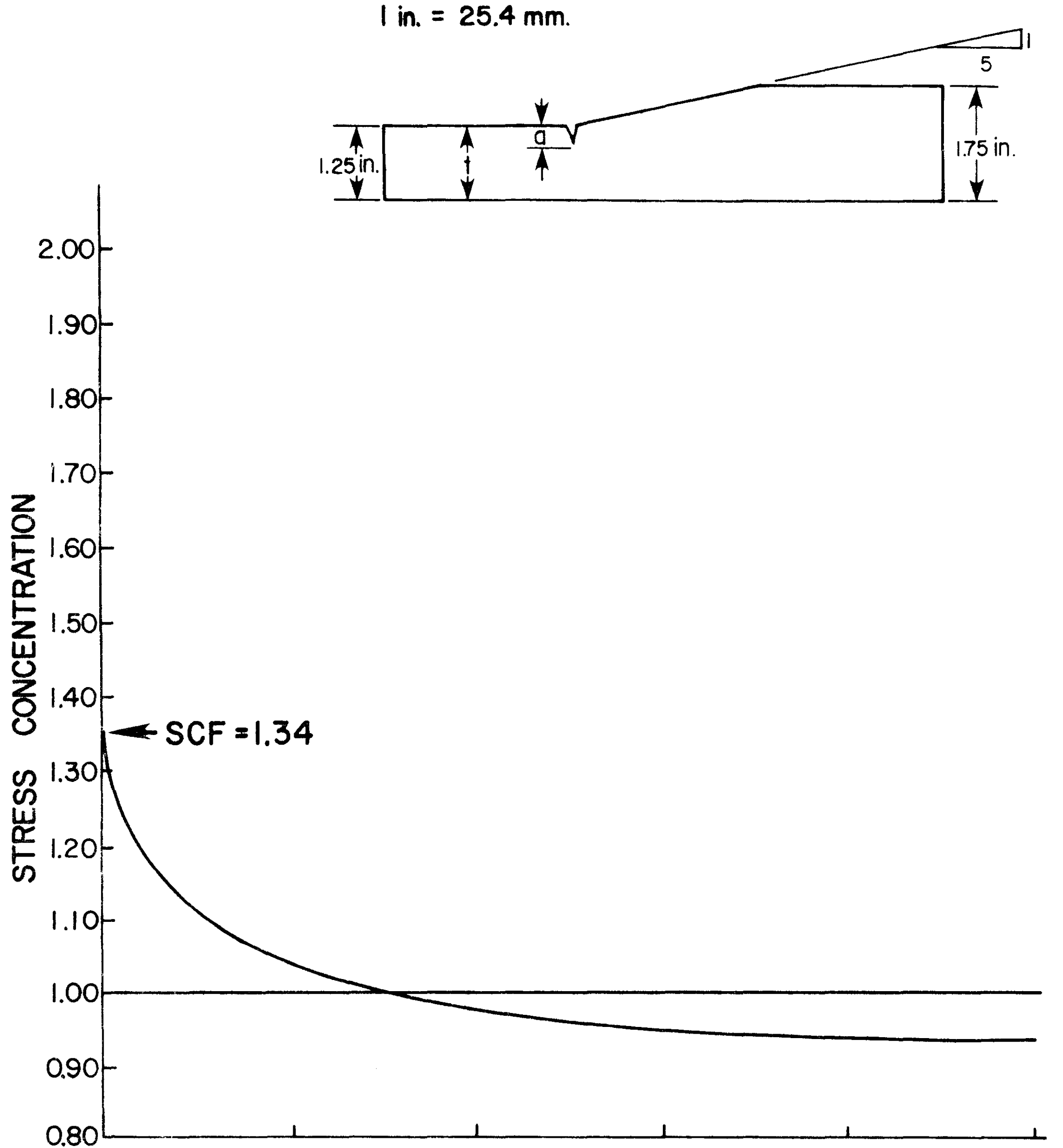

Fig. A9 Stress concentration decay - 1 to 5 slope $\ell_1/\ell_8 = 1$

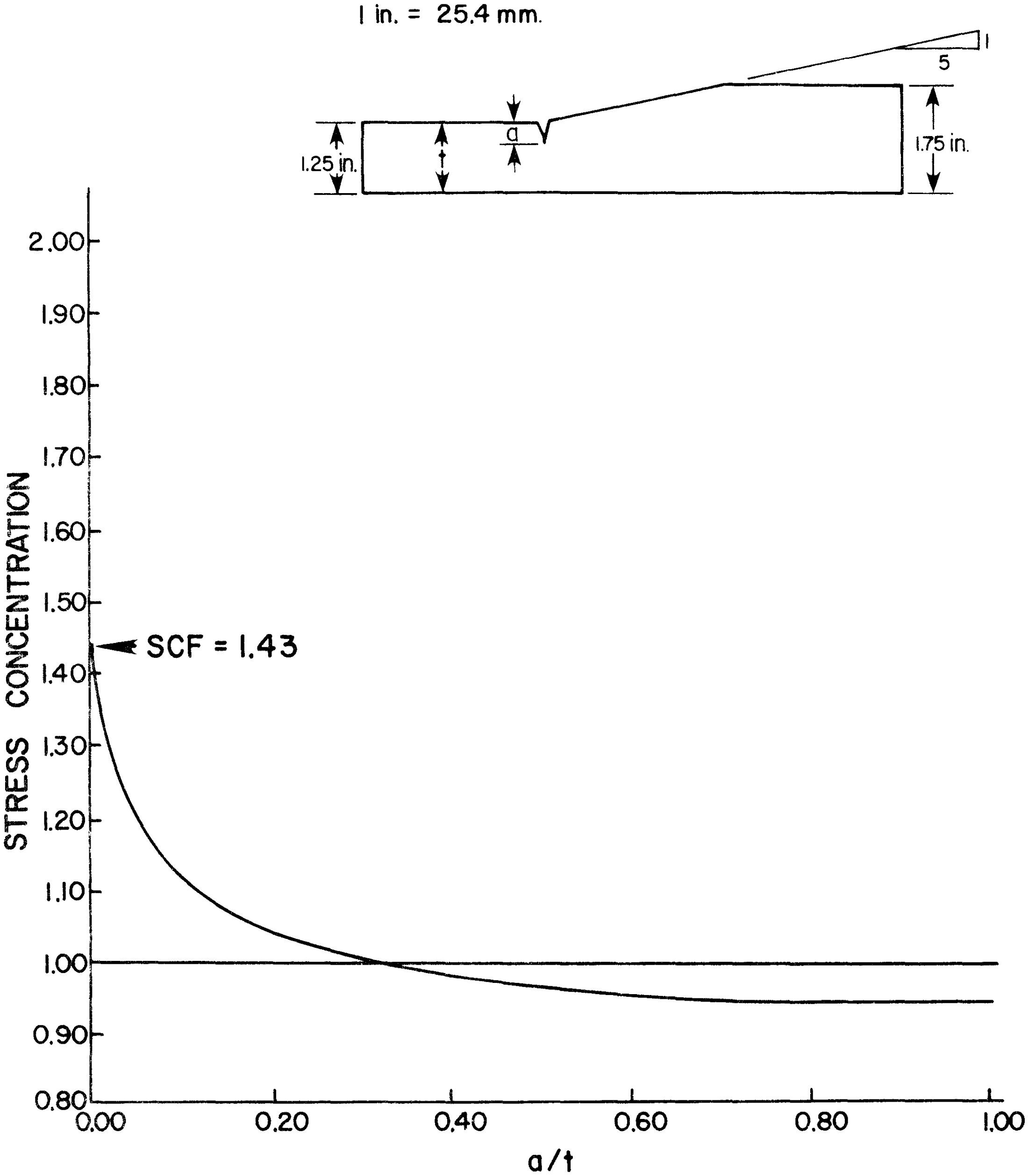

Fig. A10 Stress concentration decay - 1 to 5 slope
$\ell_1/\ell_8 = 4$

TABLE A8 FEM NODE SURFACE STRESSES - 1 TO 2-1/2 SLOPE

1st Solution		Rezone	
x (in.)	SC	x (in.)	SC
0.0000	2.24*	0.0000	2.24*
0.0728	1.54	0.0146	2.18
0.1960	1.31	0.0291	2.02
0.4047	1.16	0.0437	1.86
0.7583	1.07	0.0582	1.71
1.3572	1.01	0.0728	1.54
2.3711	0.99	0.0974	1.49
4.0897	1.00	0.1221	1.43
7.0000	1.00	0.1467	1.38
		0.1714	1.33
		0.1960	1.28

1 in. = 25.4 mm

*Average stress at singularity from the two quadrilateral element nodes, 2.07 and 2.40. The triangular node stress concentration is 1.70.

TABLE A9 FEM NODE SURFACE STRESSES - 1 TO 5 SLOPE

1st Solution		Rezone	
x (in.)	SC	x (in.)	SC
0.0000	1.50*	0.0000	1.50*
0.0854	1.21	0.0171	1.49
0.2122	1.12	0.0342	1.42
0.4007	1.05	0.0512	1.35
0.6807	1.02	0.0683	1.28
1.0964	1.00	0.0854	1.21
1.7154	1.00	0.1108	1.19
2.6344	1.00	0.1361	1.17
4.0000	1.00	0.1615	1.15
		0.1868	1.13
		0.2122	1.10

1 in. = 25.4 mm

*Average stress at singularity from the two quadrilateral element nodes, 1.42 and 1.58. The triangular node stress concentration is 1.24.

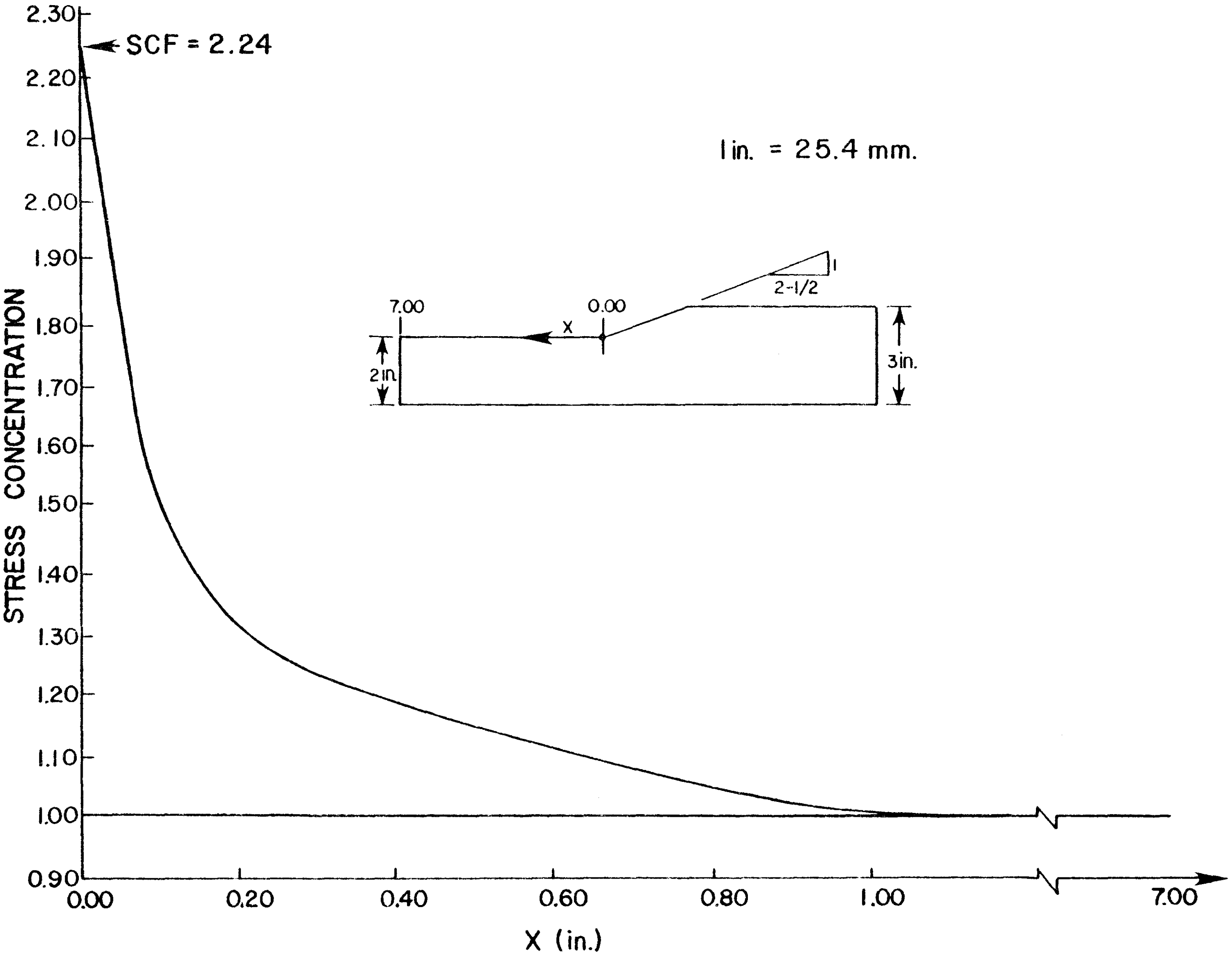

Fig. All Surface stress concentration decay - 1 to 2-1/2 slope

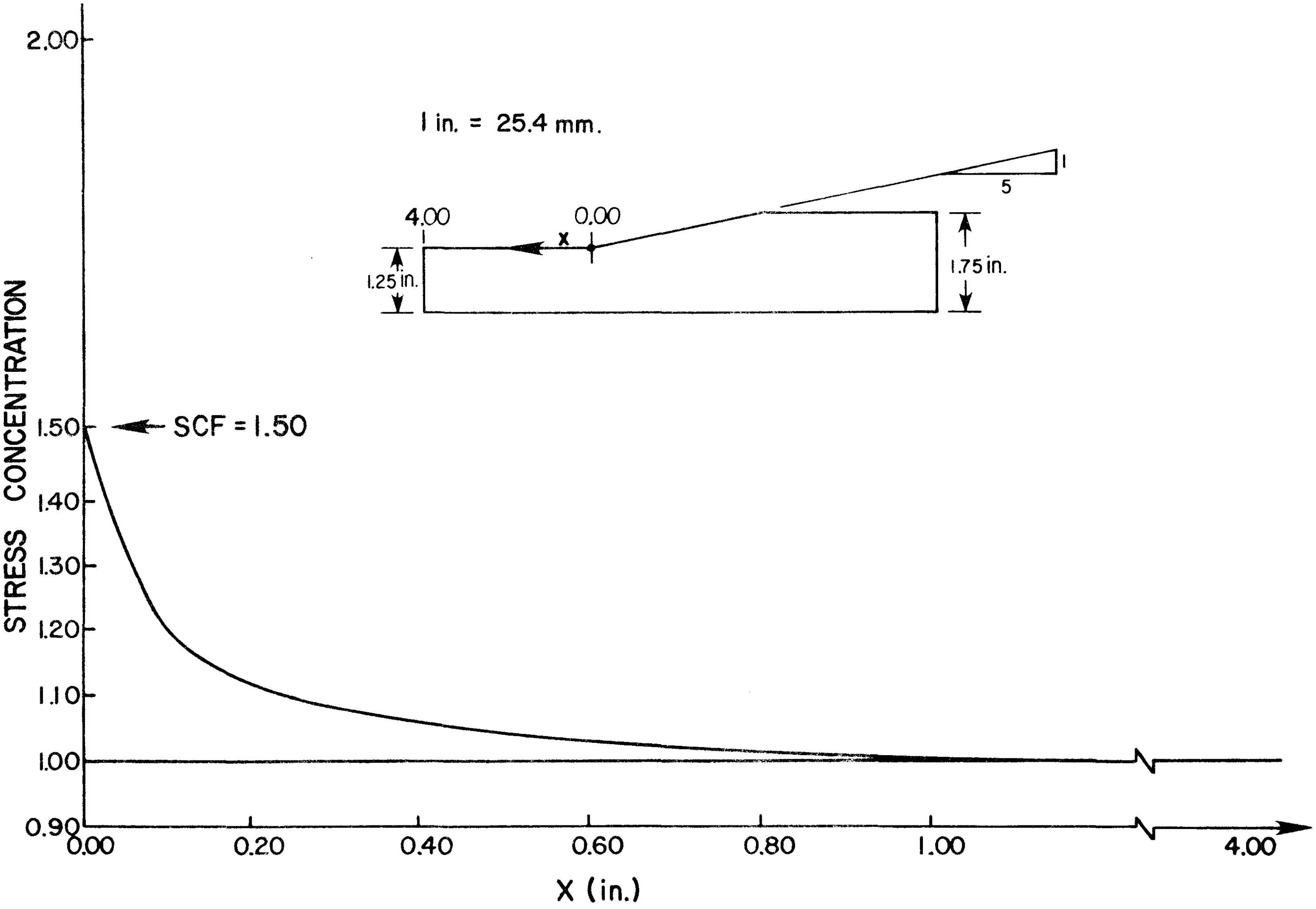

Fig. A12 Surface stress concentration decay - 1 to 5 slope

TABLE A10 STRESS GRADIENT CORRECTION FACTOR - 1 TO 2-1/2 SLOPE

$\ell_1/\ell_8 = 1$

a	a/t	b_i	SC	F_G
0.05	0.025	0.05	1.400	1.50
0.10	0.050		1.303	1.40
0.15	0.075		1.227	1.34
0.20	0.100		1.173	1.29
0.25	0.125		1.131	1.25
0.30	0.150		1.098	1.22
0.35	0.175		1.071	1.19
0.40	0.200		1.049	1.17
0.45	0.225		1.030	1.15
0.50	0.250		1.015	1.13
0.75	0.375	0.25	0.961	1.07
1.00	0.500		0.931	1.03
1.25	0.625		0.914	1.00
1.50	0.750		0.904	0.96
1.75	0.875		0.899	0.97
2.00	1.000		0.897	0.96

TABLE A11 STRESS GRADIENT CORRECTION FACTOR - 1 TO 2-1/2 SLOPE

$\ell_1/\ell_8 = 4$

a	a/t	b_i	SC	F_G
0.0226	0.0113	0.0226	1.580	1.68
0.0452	0.0226		1.480	1.58
0.0678	0.0339		1.405	1.52
0.0904	0.0452		1.345	1.47
0.1130	0.0565		1.297	1.42
0.1406	0.0703	0.0276	1.249	1.38
0.1682	0.0841		1.211	1.35
0.1958	0.0979		1.179	1.31
0.2234	0.1117		1.152	1.29
0.2510	0.1255		1.120	1.26

TABLE A12 STRESS GRADIENT CORRECTION FACTOR - 1 TO 2-1/2 SLOPE

$\ell_1/\ell_8 = 8$

a	a/t	b_i	SC	F_G
0.0142	0.0071	0.0142	1.740	1.85
0.0284	0.0142		1.620	1.74
0.0426	0.0213		1.535	1.66
0.0568	0.0284		1.468	1.60
0.0710	0.0355		1.414	1.56
0.0900	0.0450	0.0190	1.355	1.51
0.1090	0.0545		1.308	1.46
0.1280	0.0640		1.270	1.43
0.1470	0.0735		1.238	1.39
0.1660	0.0830		1.210	1.37

TABLE A13 STRESS GRADIENT CORRECTION FACTOR - 1 TO 2-1/2 SLOPE

$\ell_1/\ell_8 = 16$

a	a/t	b_i	SC	F_G
0.0085	0.0043	0.0085	1.940	2.09
0.0170	0.0085		1.811	1.95
0.0255	0.0128		1.701	1.86
0.0340	0.0170		1.621	1.79
0.0425	0.0213		1.558	1.73
0.0552	0.0276	0.0127	1.484	1.66
0.0679	0.0340		1.427	1.61
0.0807	0.0403		1.382	1.52
0.0934	0.0467		1.345	1.48
0.1061	0.0530		1.314	1.45

TABLE A14 STRESS GRADIENT CORRECTION FACTOR - 1 TO 5 SLOPE

$\ell_1/\ell_8 = 1$

a	a/t	b_i	SC	F_G
0.03125	0.025	0.03125	1.230	1.29
0.06250	0.050		1.182	1.23
0.09375	0.075		1.141	1.20
0.12500	0.100		1.111	1.18
0.15625	0.125		1.087	1.15
0.18750	0.150		1.067	1.13
0.21875	0.175		1.051	1.12
0.25000	0.200		1.038	1.10
0.28125	0.225		1.027	1.09
0.31250	0.250		1.017	1.08
0.46875	0.375	0.15625	0.982	1.05
0.62500	0.500		0.962	1.02
0.78125	0.625		0.949	1.01
0.93750	0.750		0.941	0.99
1.09375	0.875		0.937	0.98
1.25000	1.000		0.935	0.98

TABLE A15 STRESS GRADIENT CORRECTION FACTOR - 1 TO 5 SLOPE

$\ell_1/\ell_8 = 4$

a	a/t	b_i	SC	F_G
0.01412	0.0113	0.01412	1.326	1.38
0.02824	0.0226		1.277	1.33
0.04236	0.0339		1.236	1.29
0.05648	0.0452		1.204	1.27
0.07060	0.0565		1.178	1.24
0.08782	0.0703	0.01722	1.152	1.22
0.10504	0.0840		1.131	1.20
0.12226	0.0978		1.114	1.19
0.13948	0.1116		1.099	1.17
0.15670	0.1254		1.084	1.16

TABLE A16 STRESS GRADIENT CORRECTION FACTOR - 1 TO 5 SLOPE

$\ell_1/\ell_8 = 8$

a	a/t	b_i	SC	F_G
0.00886	0.0071	0.00886	1.389	1.44
0.01772	0.0142		1.341	1.39
0.02658	0.0213		1.298	1.36
0.03544	0.0284		1.265	1.33
0.04430	0.0354		1.238	1.31
0.05620	0.0450	0.01190	1.208	1.28
0.06810	0.0545		1.184	1.26
0.08000	0.0640		1.164	1.24
0.09190	0.0735		1.147	1.23
0.10380	0.0830		1.131	1.21

REFERENCES

1. Point Pleasant Bridge, National Transportation Safety Board, "Collapse of U.S. 35 Highway Bridge, Point Pleasant, West Virginia, December 15, 1967," Report No. NTSB-HAR-71-1, Washington, D.C., 1971.

2. AASHTO Subcommittee on Bridges and Structures, Standard Specifications for Highway Bridges, American Association of State Highway and Transportation Officials, Twelfth Edition, Washington, D.C., 1977.

3. Fisher, J. W., Frank, K. H., Hirt, M. A., and McNamee, B. M., "Effect of Weldments on the Fatigue Strength of Steel Beams," NCHRP Report No. 102, Highway Research Board, 1970.

4. Fisher, J. W., Albrecht, P. A. Yeu, B. T., Klingerman, D. J., and McNamee, B. M., "Fatigue Strength of Steel Beams with Welded Stiffeners and Attachments," NCHRP Report No. 147, Transportation Research Board, 1974.

5. Roberts, R., Fisher, J. W., Irwin, G. R. Boyer, K. D., Hansammann, H., Krishna, G. V., Morf, V., and Slockbower, R. E., "Determination of Tolerable Flaw Sizes in Full Size Welded Bridge Details," Report No. FHWA-77-170, Federal Highway Administration, 1977.

6. Schilling, C. G., Klippstein, K. H., Barsom, J. M., and Blake, G. T., "Fatigue of Welded Steel Bridge Members under Variable-Amplitude Loading," Final Report, NCHRP Project 12-12, Transportation Research Board, 1975.

7. Irwin, G. R., "Analysis of Stress and Strains near the End of a Crack Transversing Plate," Journal of Applied Mechanics, Transactions, ASME, Vol. 24, 1957.

8. Cudney, G. R., "Stress Histories of Highway Bridges," Journal of the Structural Division, ASCE, December 1968.

9. Rolfe, S. T., and Barsom, J. M., Fracture and Fatigue Control in Structures--Applications of Fracture Mechanics, Prentice-Hall, Inc., 1977.

10. American Society for Testing and Materials, "Standard Test Method for Plane-Strain Fracture Toughness of Metallic Materials," ASTM Designation E399-74, Part 10, ASTM Annual Standards.

11. Barsom, J. M., "Fatigue Crack Propagation in Steels of Various Yield Strengths," Journal of Engineering for Industry, Transactions, ASME, Series B, 93, No. 4, November 1971.

12. Lawrance, F. V., Jr., and Munse, W. H., "Fatigue Crack Propagation in Steel Weldments," Society of Automotive Engineers, Automotive Engineering Congress, Detroit, Michigan, January 10-14, 1972, 720267.

13. Miner, M. A., "Cumulative Damage in Fatigue," Journal of Applied Mechanics, ASME, Vol. 12, September 1945.

14. Albrecht, P., and Yamada, K., "Rapid Calculation of Stress Intensity Factors," Journal of the Structural Division, ASCE, February 1977.

15. Paris, P. C., and Sih, G. C., "Stress Analysis of Cracks," Fracture Toughness Testing and Its Applications, ASTM, STP381, 1965.

16. Smith, F. W., Kobayashi, A. S., and Emery, A. F., "Stress Intensity Factors for Penny-Shaped Cracks. Part 2 - Semi-Infinite Solid," Journal of Applied Mechanics, ASME, December 1967.

17. Irwin, G. R., Liebowitz, H., and Paris, P. C., "A Mystery of Fracture Mechanics," Engineering Fracture Mechanics, Vol. 1, 1968.

18. Irwin, G. R., "The Crack Extension Force for a Part through Crack in a Plate," Journal of Applied Mechanics, Transactions, ASME, 1962.

19. Dunham, R. S., and Becker, E. B., "Texas Grain Analysis Program (TEXGAP)," Texas Institute for Computation Mechanics, The University of Texas at Austin, 1973.

20. Peterson, R. E., Stress Concentration Factors, J. Wiley & Sons, New York, 1974.

21. Liu, A. F., "Stress Intensity Factor for a Corner Flaw," Engineering Fracture Mechanics, Vol. 4, 1972.

22. Sneddon, I. N., "The Distribution of Stress in the Neighborhood of a Crack in an Elastic Solid," Proceedings, Physical Society of London, 187, 1946.

23. Hirt, M. A., and Fisher, J. W., "Fatigue Crack Growth in Welded Beams," Engineering Fracture Mechanics, Vol. 5, 1973.

24. Fisher, J. W., "Bridge Fatigue Guide--Design and Details," American Institute of Steel Construction (AISC), New York, 1977.

25. Payne, W. F., "Fracture Toughness Testing and Its Application," ASTM, STP381, 1965.

26. American Society of Mechanical Engineers, "Rules for In-Service Inspection of Nuclear Power Plant Components," ASME Boiler and Pressure Vessel Code, Section XI, 1974.

(Continued from inside front cover)

183-8	"The Resilient and Fatigue Characteristics of Asphalt Mixtures Processed by the Dryer-Drum Mixer," by Manuel Rodriguez and Thomas W. Kennedy, December 1976.
183-9	"Fatigue and Repeated-Load Elastic Characteristics of Inservice Portland Cement Concrete," by John A. Crumley and Thomas W. Kennedy, June 1977.
183-10	"Development of a Mixture Design Procedure for Recycled Asphalt Mixtures," by Ignacio Perez, Thomas W. Kennedy, and Adedare S. Adedimila, November 1978.
183-11	"An Evaluation of the Texas Blackbase Mix Design Procedure Using the Indirect Tensile Test," by David B. Peters and Thomas W. Kennedy, March 1979.
183-12	"The Effects of Soil Binder and Moisture on Blackbase Mixtures," by Wei-Chou V. Ping and Thomas W. Kennedy, May 1979.
184-1	"The TEXAS Model for Intersection Traffic—Development," by Clyde E. Lee, Thomas W. Rioux, and Charlie R. Copeland, December 1977.
184-2	"The TEXAS Model for Intersection Traffic — Programmer's Guide," by Clyde E. Lee, Thomas W. Rioux, Vivek S. Savur, and Charlie R. Copeland, December 1977.
184-3	"The TEXAS Model for Intersection Traffic—User's Guide," by Clyde E. Lee, Glenn E. Grayson, Charlie R. Copeland, Jeff W. Miller, Thomas W. Rioux, and Vivek S. Savur, July 1977.
184-4F	"Application of the TEXAS Model for Analysis of Intersection Capacity and Evaluation of Traffic Control Warrants," by Clyde E. Lee, Vivek S. Savur, and Glenn E. Grayson, July 1978.
188-1	"Behavior of Stage-Cast Inverted T-Beams with the Precast Flange in Tension," by S. A. A. Wahidi and R. W. Furlong, August 1976.
188-2F	"Strength and Behavior of Stage-Cast Inverted T-Beams," by Richard W. Furlong, August 1978.
196-1F	"Design of Reinforcement for Notched Ends of Prestressed Concrete Girders," by Gangadharan Menon and Richard W. Furlong, August 1977.
198-1F	"Control of Cracking on the Side Faces of Large Reinforced Concrete Beams," by G. C. Frantz and J. E. Breen, September 1978.
209-1F	"Fatigue Loading of Cantilever Sign Structures from Truck Wind Gusts," by Bruce M. Creamer, Karl H. Frank, and Richard E. Klingner, April 1979.
212-1F	"Design Criteria for Median Turn Lanes," by C. Michael Walton, Thomas W. Horne, and William K. Fung, March 1978.
244-1	"Analysis of Single Piles Under Lateral Loading," by Barry J. Meyer and Lymon C. Reese, December 1979.
245-1F	"Texas Traffic Data Acquisition Program," by Han-Jei Lin, Clyde E. Lee, and Randy Machemehl, February 1980.
514-1F	"Effects of Temperature Change on Plastic Crash Cushions," by Victor N. Toth and Clyde E. Lee, January 1976.
1053-1F	"Social Service Agency Transportation Services: Current Operations and the Potential for the Increased Involvement of the Taxi Industry," by Walter L. Cox and Sandra Rosenbloom, August 1977.
RR 16	"The Prediction of Passenger Riding Comfort from Acceleration Data," by Craig C. Smith, David Y. McGehee, and Anthony J. Healey, March 1976.
RR 35	"Perceived Environmental Utility Under Alternative Transportation Systems: A Framework for Analysis," by Pat Burnett, March 1976.
RR 36	"Monitoring the Effects of the Dallas/Fort Worth Regional Airport — Volume I: Ground Transportation Impacts," by William J. Dunlay, Jr., Lyndon Henry, Thomas G. Caffery, Douglas W. Wiersig, and Waldo A. Zambrano, December 1976.
RR 37	"Monitoring the Effects of the Dallas/Fort Worth Regional Airport — Volume II: Land Use and Travel Behavior," by Pat Burnett, David Chang, Carl Gregory, Arthur Friedman, Jose Montemayor, and Donna Prestwood, July 1976.
RR 38	"The Influence on Rural Communities of Interurban Transportation Systems, Volume II: Transportation and Community Development: A Manual for Small Communities," by C. Michael Walton, John Huddleston, Richard Dodge, Charles Heimsath, Ron Linehan, and John Betak, August 1977.
RR 39	"An Evaluation of Promotional Tactics and Utility Measurement Methods for Public Transportation Systems," by Mark Alpert, Linda Golden, John Betak, James Story, and C. Shane Davies, March 1977.
RR 40	"A Survey of Longitudinal Acceleration Comfort Studies in Ground Transportation Vehicles," by L. L. Hoberock, July 1976.
RR 43	"A Pavement Design and Management System for Forest Service Roads — A Working Model," by Freddy L. Roberts, B. Frank McCullough, Hugh J. Williamson, and William R. Wallin, February 1977.
RR 45	"Characteristics of Local Passenger Transportation Providers in Texas," by Ronald Briggs, January 1977.
RR 46	"The Influence on Rural Communities of Interurban Transportation Systems, Volume I: The Influence on Rural Communities of Interurban Transportation Systems," by C. Michael Walton, Richard Dodge, John Huddleston, John Betak, Ron Linehan, and Charles Heimsath, August 1977.
RR 47	"Effects of Visual Distraction on Reaction Time in a Simulated Traffic Environment," by C. Josh Holahan, March 1977.
RR 48	"Personality Factors in Accident Causation," by Deborah Valentine, Martha Williams, and Robert K. Young, March 1977.
RR 49	"Alcohol and Accidents," by Robert K. Young, Deborah Valentine, and Martha S. Williams, March 1977.
RR 50	"Alcohol Countermeasures," by Gary D. Hales, Martha S. Williams, and Robert K. Young, July 1977.
RR 51	"Drugs and Their Effect on Driving Performance," by Deborah Valentine, Martha S. Williams, and Robert K. Young, May 1977.
RR 52	"Seat Belts: Safety Ignored," by Gary D. Hales, Robert K. Young, and Martha S. Williams, June 1978.
RR 53	"Age-Related Factors in Driving Safety," by Deborah Valentine, Martha Williams, and Robert K. Young, February 1978.
RR 54	"Relationships Between Roadside Signs and Traffic Accidents: A Field Investigation," by Charles J. Holahan, November 1977.
RR 55	"Demographic Variables and Accidents," by Deborah Valentine, Martha Williams, and Robert K. Young, January 1978.
RR 56	"Feasibility of Multidisciplinary Accident Investigation in Texas," by Hal L. Fitzpatrick, Craig C. Smith, and Walter S. Reed, September 1977.
RR 60	"A Pavement Design and Management System for Forest Service Roads — Implementation," by B. Frank McCullough and David R. Luhr, January 1979.
RR 61	"Multidisciplinary Accident Investigation," by Deborah Valentine, Gary D. Hales, Martha S. Williams, and Robert K. Young, October 1978.
RR 62	"Psychological Analysis of Degree of Safety in Traffic Environment Design," by Charles J. Holahan, February 1979.
RR 63	"Automobile Collision Reconstruction: A Literature Survey," by Barry D. Olson and Craig C. Smith, December 1979.
RR 64	"An Evaluation of the Utilization of Psychological Knowledge Concerning Potential Roadside Distractors," by Charles J. Holahan, December 1979.